ABSTRACT

PROGL, CURTIS LORENZ. High Resolution Electron Beam Testing of Gallium Nitride Based Light Emitting Diodes. (Under the direction of Phillip E. Russell.)

This research was undertaken to address questions related to luminescence from Gallium Nitride (GaN) based light emitting diodes (LEDs) and the challenges related to their investigation. The work describes development and characterization of sample preparation methods, and application of electron beam induced current (EBIC) and cathodoluminescence (CL) experimental techniques for a scanning transmission electron microscope (STEM). The methods were used to directly correlate electrical and optical behavior to device structure in commercial multi quantum well (MQW) GaN based blue and green LEDs.

In situ current-voltage characterization of focused ion beam (FIB) processed STEM samples showed increased current at low voltages. Further investigations confirmed that the increase is associated with a FIB induced damage of the exposed pn-junction, and the leakage current profile corresponds to the Poole-Frenkel mechanism.

Cross-sectional STEM-EBIC enabled direct correlation between charged carrier behavior and V-defects in MQW GaN based LEDs. Defect contrast measurements for V-defects in blue and green LEDs ranged from 50% – 80% confirming these defects suppress EBIC. Correlation with plan view SEM-EBIC indicated that V-defect density in the bright EBIC contrast region at 0.8×10^9 per cm^2 was lower than V-defect density in the dark region at 2.6×10^9 per cm^2.

Location of the pn-junction in both blue and green MQW LEDs was achieved with nanometer resolution. For a blue LED the pn-junction was at 21 ± 2 nm while for a green LED it was located at 28 ± 21 nm both measured from the first QW on the n-GaN side. Analysis of STEM-EBIC profiles suggests that minority carrier diffusion length for holes is less than that for electrons with both increasing inside V-defects.

Improvements were implemented to an existing STEM-CL in-lens rig that resulted in a 90-95% reduction in dataset time while increasing signal-to-noise. Resolution of QW, GaN and defect emission was demonstrated, CL spectroscopy

performed on different regions of the sample, and results correlated to device structure.

Results from STEM-EBIC/CL suggest V-defects enhance unwanted Mg diffusion into the active layer. Diffusion at V-defect reduces field strength resulting in reduced EBIC while clustering of V-defects enables sufficient Mg diffusion to produce a pn-junction shift.

High Resolution Electron Beam Testing of Gallium Nitride Based Light Emitting Diodes

by
Curtis Lorenz Progl

A dissertation submitted to the Graduate Faculty of
North Carolina State University
In partial fulfillment of the
Requirements for the degree of
Doctor of Philosophy

Materials Science and Engineering

Raleigh, North Carolina

2008

Approved by:

_____	_____
Prof. C. M. Osburn	Prof. M. A. Johnson
_____	_____
Prof. G. J. Duscher	Prof. P. E. Russell (Chair of the Advisory Committee)

BIOGRAPHY

Curtis L. Progl was born in New York City, New York, in 1958, and lived there for eighteen years. He graduated from Francis Lewis High School in Flushing, New York in 1976 and at the end of the summer moved to Raleigh, North Carolina to attend North Carolina State University. In 1980 he earned a Bachelors of Science in Chemical Engineering. He then earned a Masters of Science in Mechanical Engineering from North Carolina State University in 1983, for work performed on the reduction of noise from an air-jet loom.

In July of 1983 Curt was employed by Data General in Clayton, North Carolina and worked as a manufacturing engineering for the fabrication of printed circuit boards. After seven years and rising to the level of senior advanced manufacturing engineer Curt accepted a senior mechanical engineering position with Exide Electronics in Raleigh, North Carolina. The position involved mechanical packaging and thermal management of uninterruptible power supply systems. This eventually led to an opportunity in the fall of 1996 to work for Compaq Computer Corporation in Houston, Texas on thermal solutions for notebook computers. While at Compaq Curt was given an opportunity to further his education and in 2000 earned a Masters of Business Administration from the University of Texas at Austin.

To gain an understanding of the business side of industry Curt accepted a product marketing position in early 2000 with Dell Computers in Austin, Texas. For two years he managed software and peripheral products for the workstation group. Reorganization then put him back into an advanced engineering group where he worked until returning to graduate school in fall of 2004. There he began the Ph.D. program in Materials Science and Engineering at North Carolina State University under the direction of Dr. Phillip E. Russell.

ACKNOWLEDGMENTS

I wish to thank the following for their time and support:

- Cree, Inc. for financial support
- Professor Russell; for accepting me into his group and teaching me the scientific method.
- My Ph.D committee members: Professor Johnson; for teaching me about gallium nitride, Professor Duscher; for teaching me about TEM and Professor Osburn; for teaching me about electronic characterization of devices.
- The staff at AIF: Dieter Griffis, Dale Batchelor, Fred Stevie, Roberto Garcia and Chuck Mooney – for your help in resolving all the problems that came up big and small.
- Kristin Bunker, for helping me to extend the work that started with you.
- The AIF graduate students: Anthony Garetto, Mike Salmon, Chris Penley and Wingo Wong – for the fellowship and support as my graduate student brothers in arms.
- Edna Deas, for being the Material Science student's administration god send
- Chad Parish, especially, for providing support in both academic and research areas that I could not have done without.
- Jim Vitarelli, especially, for teaching me sample prep, FIB, STEM and whose support and assistance I could not have done without.

Lastly, I would like to acknowledge my family for supporting my decision to return to school to pursue my goal of earning a Ph.D.

TABLE OF CONTENTS

LIST OF TABLES vii
LIST OF FIGURES viii
1. Introduction 1
2. Gallium Nitride Based Material System and Devices 3
2.1 Gallium nitride 3
2.2 Gallium nitride growth 5
2.3 Gallium nitride based LEDs 8
2.4 Challenges 10
2.4.1 Substrate lattice mismatch 10
2.4.2 Compositional variation 13
2.4.3 Quantum-confined stark effect 15
2.4.4 Defect tolerant emission 17
2.4.5 Research motivation 18
3. Analytical Techniques 20
3.1 Electron beam induced signals of interest 20
3.2 Electron beam induced current 22
3.3 Cathodoluminescence 24
3.4 Electron-hole pairs 26
3.5 High-resolution electron beam testing 28
3.6 STEM EBIC 33
3.5.1 Introduction 33
3.5.2 STEM-EBIC systems 33
3.5.3 Applications to GaN 34
3.6 STEM CL 36
3.6.1 Introduction 36
3.6.2 STEM-CL systems 36
3.6.3. Applications to GaN 38
3.7 Focused ion beam 39
3.7.1 Introduction 39
3.7.2 Milling and deposition 40
3.7.3 Artifacts 41
4. Sample Preparation Methods and Results 43
4.1 Introduction 43
4.2 Sample characterization 43
4.2.1 Current-voltage characterization 43
4.2.2 In situ current-voltage characterization 48
4.2.3 Electroluminescence characterization 49
4.3 Lift-out prep method 50
4.3.1 Motivation 50
4.3.2 Concept 51
4.3.3 Ohmic contacts 52
4.3.4 Bridging interconnect 56
4.3.4.1 Introduction 56

4.3.4.2 Tungsten wire interconnect 57
4.3.4.3 Copper micro-trace interconnect 61
4.3.4.4 Thin foil interconnect 65
4.3.5 Contact characterization 68
4.3.5.1 Introduction 68
4.3.5.2 I-V characterization of lift-out sample contacts 69
4.3.6 Contact options n-SiC 73
4.3.6.1 Introduction 73
4.3.6.2 Metallization experiment 73
4.3.6.3 Metallization results 75
4.3.7 Summary lift-out method 78
4.4 Cross-rib prep method 79
4.4.1 Introduction 79
4.4.2 Sample holder 80
4.4.3 Expected I-V results 83
4.4.4 Prep results 87
4.4.5 Etch damaged leakage current 94
4.4.6 Poole-Frenkel effect 96
4.4.7 Progressive mill 99
4.4.8 FIB damage removal 102
4.4.8.1 Damage thickness 102
4.4.8.2 Low energy FIB polish 103
4.4.8.3 Wet etch 104
4.4.8.4 Additional damage removal options 106
4.4.9 Cross-rib prep summary 107
4.5 Mechanical pre-thin 108
4.5.1 Introduction 108
4.5.2 Pre-thin process 108
4.5.3 Attaching pre-thinned sample 110
4.5.4 Characterization results 112
4.5.5 Offset mounting jig 114
4.6 Sample prep methods and results summary 115
5. STEM-EBIC Experiments and Results 118
5.1 Motivation 118
5.2 Surface effect investigation 124
5.3 Experiment design 126
5.4 Samples 129
5.5 UltraThin Blue LED 130
5.5.1 Plan-view SEM-EBIC mapping 130
5.5.2 FIB prep of cross-section 133
5.5.3 Electro-optical characterization 135
5.5.4 STEM-EBIC setup 140
5.5.5 STEM-EBIC mapping 142
5.5.6 STEM-EBIC line scans 152
5.5.6.1 Results 152

5.5.6.2 Discussion 158
5.5.7 Blue UltraThin LED summary 162
5.6 UltraThin Green LED 163
5.6.1 Plan-view SEM-EBIC mapping 163
5.6.2 FIB prep of cross-section 166
5.6.3 Electro-optical characterization 167
5.6.4 STEM-ZC 172
5.6.5 STEM-EBIC mapping 175
5.6.6.1 Results 180
5.6.6.2 Discussion 185
5.6.7 Green LED summary 186
5.7 STEM-EBIC summary 187
6. STEM-CL Experiments and Results 189
6.1 Motivation 189
6.2 STEM-CL set-up 190
6.3 Samples 193
6.4 UltraThin Blue LED results and discussion 193
6.6 STEM-CL summary 203
7. Conclusions 204
7.1 Contribution 204
7.1.1 Summary 204
7.1.2 Contribution: Methods and techniques 205
7.1.3 Contribution: GaN-alloy LED characterization 206
7.2 Future work 207
8. References 209
Appendices 222
A.1 FIB sputter rate calculations 223
A.2 LabView current-voltage data collection program 225
A.3 Metal to p-semiconductor contact 232
A.4 Injection estimates 234

LIST OF TABLES

Table 1: Physical properties of III-nitrides[8]..... 5
Table 2: Common problems due to heteroepitaxy[15]..... 7
Table 3: Extracted minority carrier diffusion lengths using VanRoosbroeck model[121]. 160
Table 4: Extracted minority carrier diffusion lengths using VanRoosbroeck model[121] 185

LIST OF FIGURES

Figure 1: Band gap energy vs. lattice constant for III-nitrides (Adapted from Schubert[6]). 3
Figure 2: GaN wurtzite crystal structure[7] 4
Figure 3: Schematic of double heterostructure. 9
Figure 4: Schematic of QW structure showing discrete energy states. 9
Figure 5: Threading dislocations in GaN. 11
Figure 6: Typical V-defect. 13
Figure 7: Schematic of phase separation in InGaN QW (Adapted from Ponce[34]). 14
Figure 8: Schematic of spontaneous and piezoelectric polarization in wurtzite GaN. 15
Figure 9: Schematic of band structure (a) with and (b) without band bending due to quantum confined stark effect. 16
Figure 10: General structure of MQW $In_xGa_{1-x}N$ based LED (Figure not to scale). 19
Figure 11: Electron beam generated signals of interest (Adapted from Williams and Carter[56]). 20
Figure 12: Casino data of a 30 keV electron beam incident on bulk GaN. 22
Figure 13: Schematic of cross-sectional EBIC experiment. 23
Figure 14: Schematic of plan-view EBIC experiment. 24
Figure 15: Schematic of CL collection system. 25
Figure 16: Schematic of electron beam induced EHP generation in (a) band energy and (b) bond diagrams. 27
Figure 17: Effect of beam energy and sample thickness on interaction volume (figure not to scale). 29
Figure 18: Comparison of SEM and TEM configurations. 30
Figure 19: Schematic of a STEM. 31
Figure 20: Schematic STEM based characterization. 32
Figure 21: Isometric drawing of STEM-EBIC holder (From Perrreault and Ast[69]). 34
Figure 22: EBIC and Z-contrast line scans showing relative location of pn-junction. (From Bunker et al.,[70]). 35
Figure 23: (a) Schematic of lens based STEM-CL system (b) Lens assembly mounted to vacuum feed through flange (From Bunker[75]). 38
Figure 24: Equivalent LED circuit with parasitic resistances. 45
Figure 25: Effect of series and parallel resistance on pn-junction I-V curves. 46
Figure 26: Semi log plot of I-V data for blue MQW InGaN LED. 47
Figure 27: Detailed view of Hitachi 2100 FIB. 49
Figure 28: STEM-EBIC holder with sample. 49
Figure 29: STEM-EBIC lift-out sample prep. 51
Figure 30: Metal to n-type semiconductor ohmic contact. 54
Figure 31: Metal to n-type semiconductor Schottky contact. 55
Figure 32: Lift-out sample attached to cross hatched grid. 57
Figure 33: Preparation of tungsten needle for use as interconnect. 57
Figure 34: a) Tungsten wire interconnect. b) Attach points on lift-out sample. 58

Figure 35: Placement and connection of tungsten wire interconnect to slotted grid. 59
Figure 36: a) Lift-out probe holding interconnect to sample. b) Completed interconnect with additional stress relief. 60
Figure 37: a) Cleaned lift-off sample showing completed contacts. b) Sample ready for formation of electron transparent section. 61
Figure 38: Cross-section schematic of Damascene micro-trace wafer. 62
Figure 39: a) Planar view of partially polished wafer. b) Processed wafer ready for trace extraction. 62
Figure 40: a) Area with undercut micro-traces. b) Targeted micro-trace for lift-off. . 63
Figure 41: a) Initiation of trace removal. b) Extracted trace. 64
Figure 42: a) Grid side attach of micro-trace. b) Micro-trace held to lift-out probe by surface contact. 64
Figure 43: a) Extending micro-trace to sample. b) Micro-trace interconnect. 65
Figure 44: Cross section schematic of foil support jig. 66
Figure 45: a) Foil and support jig. b) FIB processing to form foil interconnect. 66
Figure 46: Placement of foil interconnect. 67
Figure 47: a) Top-view. b) Angled-view of completed interconnect. 68
Figure 48: Modified alligator clip for electrical testing with LED emitting under bias. 69
Figure 49: I-V curve interconnect to grid contact. 70
Figure 50: I-V curve LED die vs. lift-out. 71
Figure 51: (a) Physical sample and (b) equivalent circuit schematic. 72
Figure 52: LED wafer mounted on TO-header. 73
Figure 53: Wafer mounted in crystal bond with n-side metallization polished off. 74
Figure 54: Sputter coated metallization. 75
Figure 55: a) Wafer-1 initial I-V. b) Wafer-1 Mo/Au metallization I-V. 76
Figure 56: a) Wafer-2 initial I-V. b) Wafer-2 Ti/Au metallization I-V. 76
Figure 57: a) Wafer-3 initial I-V. b) Wafer-3 Ta/Au metallization I-V. 77
Figure 58: Sputter coated metallization a) Ta/Au. b) Ti/Au. c)Mo/Au. 78
Figure 59: Schematic of Cross-rib sample prep. 80
Figure 60: a) Cross-section schematic of sandwich style holder. b) Assembled holder with sample. (From Bunker[75]). 81
Figure 61: Top-view of modified holder with sample in place. 81
Figure 62: Side-view of sample holder. 83
Figure 63: Expected effect of reduced planar area on I-V relation. 84
Figure 64: Expected effect of reduced parallel resistance on I-V relation. 86
Figure 65: Sample in STEM-EBIC holder emitting under bias. 87
Figure 66: Sample in FIB prior to milling. 88
Figure 67: Initial sample in-situ FIB I-V. a) Linear plot. b) Semi-log plot. 89
Figure 68: FIB image of sample after cut. 90
Figure 69: I-V results after initial cut. a) Linear plot. b) Semi-log plot. 91
Figure 70: FIB image of sample after second cut. 92
Figure 71: I-V results after second cut. a) Forward bias. b) Reverse bias. 93
Figure 72: Forward (top) and reverse (bottom) I-V characteristics from GaN diodes exposed to Ar discharges (From Dang et. al.[101]). 95

Figure 73: Energy diagram of trapping center with Poole-Frenkel emission (Adapted from Mitrofanov and Manfra[104]). 97
Figure 74: Low bias linear dependence of log(I) versus $V^{1/2}$. 98
Figure 75: Progressive mill SiC cut. a) Schematic-cross section. b) Top-view of cut. 100
Figure 76: I-V characteristic after milling SiC. 100
Figure 77: Progressive mill GaN cut. a) Schematic cross-section. b) Top-view cut. 101
Figure 78: I-V characteristic after milling into GaN mesa. 101
Figure 79: Simulations of ion ranges of Ga^+ beams with GaN substrate for 10 and 40 keV. 102
Figure 80: I-V characteristic of low energy FIB damage removal. 103
Figure 81: I-V characteristic of KOH wet etch FIB damage removal. 105
Figure 82: Schematic of pre-thin sample prep. 108
Figure 83: Mounting and test of pre-thinned sample. a) Mechanically polished die secured to glass slide. b) Sample holder attached to thinned sample. c) Cathode side of holder showing Ag epoxy attach. d) Sample in STEM-EBIC holder emitting under bias. 111
Figure 84: Current density versus voltage characteristics for pre-thin sample prep. 113
Figure 85: Mechanical pre-thinned sample with FIB formed cross-section. 114
Figure 86: a) Schematic cross-section of mounting jig. b) Jig assembly. 115
Figure 87: Cross-sectional view SEM-EBIC polished LED showing inhomogeneous EBIC signal. 118
Figure 88: Plan view SEM-EBIC showing inhomogeneous EBIC signal (From Parish[114]. 119
Figure 89: Cross-sectional EBIC images. a) Sapphire substrate. b) GaN substrate. (From Kuroda et. al.[115]). 121
Figure 90: Low-voltage (7 keV) cross-sectional (a) SE and (b) CL images (From Moldovan et. al.[116]). 122
Figure 91: Low-voltage (4 keV) cross-sectional (a) SE and (b) EBIC images (From Moldovan et. al.[116]). 123
Figure 92: Cross-section SEM-EBIC mapped to SE image indicates that contrast variations in EBIC signal are not due to visible surface artifacts. 124
Figure 93: Oxygen plasma illuminated IR image of sample in SEM during Evactron clean. Sample is highlighted by dashed box. 125
Figure 94: EBIC signal comparison along junction before and after plasma clean. Insert at bottom shows pn-junction along which intensity measurements taken. ... 126
Figure 95: Mapping regions of interest identified by plan-view EBIC. 128
Figure 96: Initial FIB based milling isolates region of interest which is then followed by final thinning to form electron transparent cross-section at selected areas of interest. 128
Figure 97: Schematic UltraThin LED (From Cree[117]). 129
Figure 98: As received LED samples mounted on a TO-header with silver paste. 130

Figure 99: SE plan-view image of mechanical polished blue LED mounted on sample holder. 131
Figure 100: SE plan-view image of blue LED showing area to be mapped. 131
Figure 101: Plan-view EBIC to identify region of interest. 132
Figure 102: SE plan-view image blue LED with region of interest denoted..... 132
Figure 103: Placement of alignment fiducial and Pt protective strap..... 134
Figure 104: Formation of cross-rib isolating region of interest. 134
Figure 105: Electron transparent cross-section ~ 0.2 μm thick. 135
Figure 106: I-V data taken at various stages of sample preparation for STEM-EBIC a) Linear scale b) Semi-log scale. 136
Figure 107: EL spectra normalized to the mechanical polished UltraThin blue LED under 2.4 V forward bias in STEM shows little change to FWHM after FIB prep. .. 138
Figure 108: Short wavelength detail of UltraThin blue LED EL spectra under 2.4 V forward bias in STEM reveals GaN emission. 139
Figure 109: Long wavelength detail of UltraThin blue LED EL spectra under 2.4 V forward bias in STEM. 140
Figure 110: STEM-EBIC setup for Hitachi HD-2000 dedicated STEM. 141
Figure 111: SE image of blue UltraThin sample in STEM. 142
Figure 112: a) ZC image acquired with HD-2000 STEM b) ZC map & c) EBIC map acquired simultaneously using Noran with 128x128 pixels and 0.03 sec dwell time per pixel. d) Composite image of EBIC map overlaid on ZC map. 144
Figure 113: a) ZC image acquired with HD-2000 STEM b) ZC map & c) EBIC map acquired simultaneously using Noran with 128x128 pixels and 0.03 sec dwell time per pixel. d) Composite image of EBIC map overlaid on ZC map. White line in a) and c) shows location local induced peak current measured for defect capture range. 145
Figure 114: Changes in peak induced current along junction. 146
Figure 115: a) ZC image acquired with HD-2000 STEM b) ZC map & c) EBIC map acquired simultaneously using Noran with 256x256 pixels and 0.01 sec dwell time per pixel. d) Composite image of EBIC map overlaid on ZC map. 148
Figure 116: a) ZC image acquired with HD-2000 STEM b) ZC map & c) EBIC map acquired simultaneously using Noran with 128x128 pixels and 0.03 sec dwell time per pixel. d) Composite image of EBIC map overlaid on ZC map. 149
Figure 117: a) ZC image acquired with HD-2000 STEM b) ZC map & c) EBIC map acquired simultaneously using Noran with 128x128 pixels and 0.03 sec dwell time per pixel. d) Composite image of EBIC map overlaid on ZC map. 150
Figure 118: a) ZC image acquired with HD-2000 STEM b) ZC map & c) EBIC map acquired simultaneously using Noran with 256x256 pixels and 0.02 sec dwell time per pixel. d) Composite image of EBIC map overlaid on ZC map. 151

Figure 119: EBIC line scans taken traversing into a sectioned V-defect. Signal suppression observed as line scan cuts across more of the defect. A defect contrast of 0.84 was measured from the change in peak to trough spread between line scans (a) and (d). A defect related shift in pn-junction location is also observed. From line scan (a) with junction located 22± 2 nm from QW-1 to line scan (d), junction shifted 77 nm toward p-GaN..... 154
Figure 120: EBIC line scans taken traversing out of a sectioned V-defect. Signal suppression decreases as line scan cuts across less of the defect. A defect contrast of 0.73 was measured from the change in peak to trough spread between line scan (c) and (a). A defect related shift in pn-junction location is also observed. From line scan (a) to (c) the junction shifted 67 nm toward n-GaN layer and was located 30± 2 nm left of QW-1..... 155
Figure 121: EBIC line scans taken traversing region between V-defects. Signal strength measured from the change in peak to trough spread increased as scan location moved away from sectioned V-defect. A slight shift in pn-junction is observed as line scan location is moved further away from sectioned V-defect. From line scan (a) to (c) the junction shifted 8 nm toward n-GaN layer and was located from (c) 22± 2 nm left of QW-1..... 156
Figure 122: EBIC line scans taken traversing into an embedded V-defect. Signal suppression observed as line scan cuts across more of the defect. A defect contrast of 0.50 was measured from the change in peak to trough spread between line scan (a) and (d). A defect related shift in pn-junction location is also observed. From line scan (a) with junction located 20± 2 nm left of QW-1 to line scan (c), the junction shifted 12 nm toward the p-GaN layer. 157
Figure 123: SE plan-view image of mechanical polished green LED mounted on sample holder. 164
Figure 124: Plan-view EBIC to identify region of interest. 164
Figure 125: SE plan-view image green LED with region of interest denoted. 165
Figure 126: Formation of cross-rib isolating region of interest. 166
Figure 127: I-V data taken at various stages of sample preparation for STEM-EBIC a) Linear scale b) Semi-log scale..... 168
Figure 128: EL spectra normalized to mechanically polished UltraThin green LED under 2.4 V forward bias in STEM shows little change to FWHM after FIB prep.. 170
Figure 129: Short wavelength detail of UltraThin green LED EL spectra under 2.4 V forward bias in STEM reveals GaN emission..... 171
Figure 130: Long wavelength detail of UltraThin green LED EL spectra under 2.4 V forward bias in STEM..... 172
Figure 131: Composite image of continuous bright contrast region in cross-section. 173
Figure 132: Composite image of continuous dark contrast region in cross-section. 174
Figure 133: a) ZC image acquired with HD-2000 STEM b) ZC map & c) EBIC map acquired simultaneously using Noran with 128x128 pixels and 0.03 sec dwell time per pixel. d) Composite image of EBIC map overlaid on ZC map..... 177

Figure 134: a) ZC image acquired with HD-2000 STEM b) ZC map & c) EBIC map acquired simultaneously using Noran with 128x128 pixels and 0.02 sec dwell time per pixel. d) Composite image of EBIC map overlaid on ZC map. 178
Figure 135: a) ZC image acquired with HD-2000 STEM b) ZC map & c) EBIC map acquired simultaneously using Noran with 128x128 pixels and 0.02 sec dwell time per pixel. d) Composite image of EBIC map overlaid on ZC map. 179
Figure 136: EBIC line scans taken from bright contrast region. Location is far right of V-defect #10 in Figure 131. From line scan (a) with junction located 49± 2 nm left of QW-1 and shows little variation in location between (a) and (b). 182
Figure 137: EBIC line scans taken from V-defect #24 in dark EBIC contrast region shown in Figure 132. A defect contrast of 0.70 to 0.80 was measured from the change in peak to trough spread between line scans (a)-(b) and (c)-(b). Little defect related shift in pn-junction location is observed. From line scan (c) the junction is junction located 20± 2 nm left of QW-1. Increase in EBIC signal in p-GaN layer indicates presence of additional rectifying peak. 183
Figure 138: EBIC line scans taken from embedded V-defect. A defect contrast of 0.70 was measured from the change in peak to trough spread between line scans (a) and (b). At the defect core the pn-junction was located 13± 2 nm left of QW-1. From line scan (a) the junction is junction located 7± 2 nm left of QW-1. 184
Figure 139: STEM-CL spectra for 10000 ms integration time with average of three in 300 nm region cross-section. (From Bunker[75]). 190
Figure 140: an Acton SpectraPro 2150i monochromator/spectrometer. 191
Figure 141: Acton SpectraHub monochromator/spectrometer controller. 192
Figure 142: Schematic of STEM-CL spectroscopy system set-up. 192
Figure 143: STEM-CL set-up for Hitachi HD-2000 dedicated STEM. 193
Figure 144: a) Previous STEM-CL holder. b) Modified STEM-EBIC/CL holder. 194
Figure 145: ZC image showing location of scan box used for STEM-CL. 196
Figure 146: STEM-CL spectra results versus (a) wavelength and (b) energy for 500 ms integration time averaged over three scans (red line is moving average of 3). 197
Figure 147: ZC image showing location of various scan boxes on different regions of blue LED sample 201
Figure 148: STEM-CL spectra results (a) QW, V-defect and (b) QW, n-GaN taken from scan box regions shown in Figure 147 (moving average of 3 applied). 202

1. Introduction

This research was undertaken to address questions related to luminescence from Gallium Nitride (GaN) based light emitting diodes (LEDs) and the challenges related to their investigation. Interest in the GaN material system has grown rapidly since the mid-1990's driven primarily by applications in optoelectronic devices[1]. Compared to standard incandescent lighting LEDs offer potential longer lifetimes and less energy consumption[2]. Although, fluorescent lights have been available for years and are about as efficient as LEDs, they contain as much as 20 mg of mercury and spent lamps are classified as hazardous waste. The U.S. Environmental Protection Agency estimates that over 800 million florescent lamps are produced each year to replace spent lamps that are then disposed[3]. The FDA sets mercury limits in water at 0.002 mg/L and if spent florescent lamps are not disposed of properly, there is enough mercury in those lamps to contaminate $2x10^{12}$ gallons of water per year[4]. GaN based LEDs contain no mercury and are not classified as a hazardous waste.

Over time LEDs have evolved from simple homojunction devices to complex structures with improved efficiency and luminescence properties. GaN based LEDs are often alloyed with aluminum or indium to tune performance and color. However, optoelectronic properties of GaN alloy LEDs as related to device composition and structure are still not completely understood. Nano-characterization techniques are required to directly correlate structural, chemical, electrical and optical properties. In addition rapid, robust sample preparation methods are needed that maintain an electrically functionally device while ensuring the probed region is indicative of the bulk material.

The driving force of this work is to advance the understanding of optoelectronic properties in GaN based LEDs. In particular the focus is on direct correlation of electrical and optical properties to device structure. To achieve this required the development and characterization of sample preparation methods, and application of electron beam induced current (EBIC) and cathodoluminescence (CL) experimental techniques for a scanning transmission electron microscope (STEM).

The methods were then used to investigate defect influence on electrical and optical behavior of fully processed GaN based blue and green LEDs.

The dissertation is structured as follows. Chapter 2 reviews the GaN based LED material system and identifies device challenges that require investigation. Chapter 3 is discussion of applicable electron beam analytical techniques. Chapter 4 covers development and characterization of sample preparation methods in support of the analytical techniques. Chapters 5 and 6 present electrical and optical investigations respectively and cover experimental design, results and discussion. Chapter 7 concludes the dissertation with a summary of the key contributions and suggested future investigations.

2. Gallium Nitride Based Material System and Devices

2.1 Gallium nitride

Gallium nitride is a binary III/V direct band gap semiconductor that along with aluminum nitride (AlN), indium nitride (InN) and their alloys are commonly known as III-nitrides. Due primarily to their wide energy band gap these materials have excellent physical properties, which make them ideal building blocks for optical and power electronic devices[5]. The III-nitride materials form a continuous alloy system yielding semiconductors with direct band gaps that range from 0.9 eV to 6.2 eV. From an optical standpoint this allows the fabrication of red to deep ultraviolet light emitting diodes from (In, Ga, Al)N alloys. Figure 1 shows band gap energy for III-nitrides as a function lattice constant.

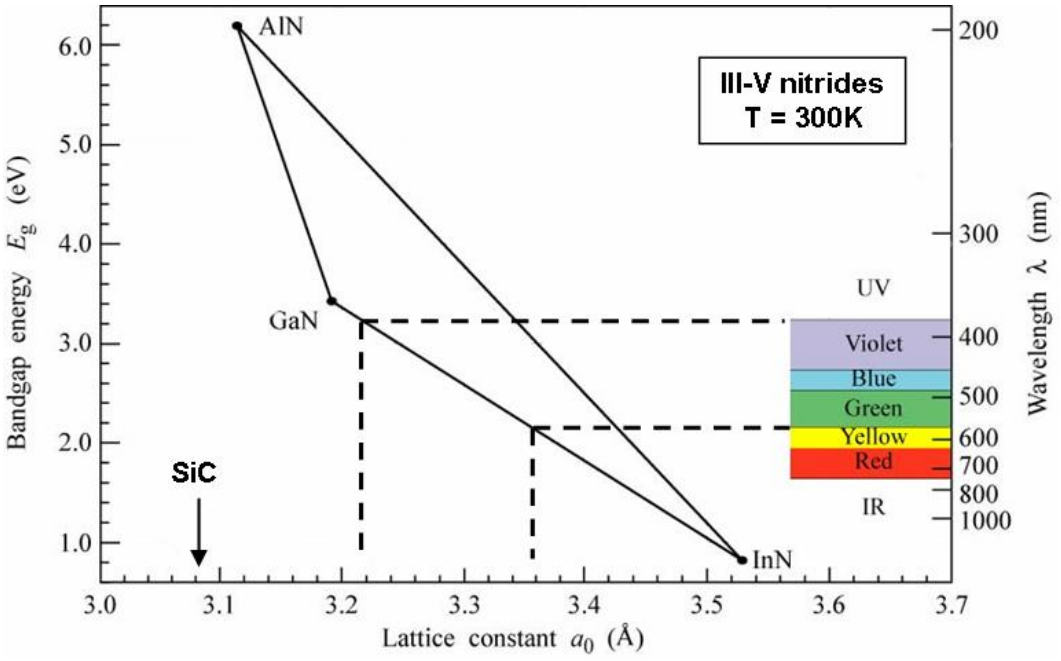


Figure 1: Band gap energy vs. lattice constant for III-nitrides (Adapted from Schubert[6]).

The driving force behind interest in III-nitrides is their potential for numerous device applications as dictated by their physical properties. In their stable form at room temperature and pressure III-nitrides have a wurtzite crystal structure with

hexagonal symmetry. For reference other common semiconductor materials such as silicon (Si) and gallium arsenide (GaAs) have a diamond or zinc-blende structure. A representation of the GaN wurtzite crystal structure is presented in Figure 2.

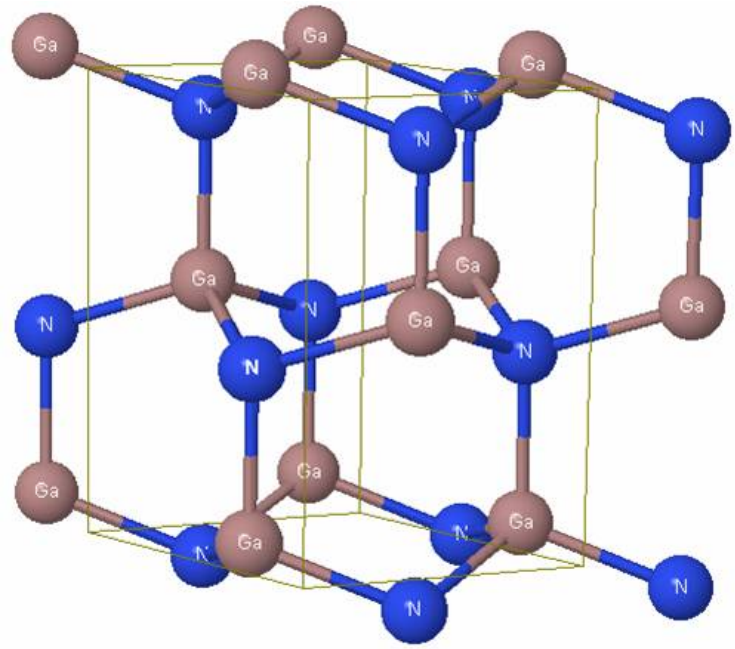


Figure 2: GaN wurtzite crystal structure[7].

III-nitrides do not have a center of symmetry and as such are polar crystals. Thus they possess piezoelectric properties the impact of which will be discussed in a later section. The large difference in electronegativity between group III elements and nitrogen yields strong bond strengths. This results in the wide band gap energies shown in Figure 1. Because the intrinsic carrier concentration is an exponential function of the band gap energy and temperature, wide band gap materials have lower leakage and dark currents.

$$n_i = 4.9x10^{15}\left(\frac{m_e m_h}{m_0^2}\right)^{3/4} T^{3/2} \exp\left(\frac{-E}{2kT}\right) \qquad (2\text{-}1)$$

In addition, III-nitrides have high thermal conductivity and electron mobility. A summary of the key physical properties of III-nitrides are listed in Table 1. Because

of these properties and the ability to tune emission, GaN alloy devices are being commercialized for light-emitting diode and laser diode applications.

Table 1: Physical properties of III-nitrides[8].

Property	GaN	AlN	InN
Room temperature band gap (eV)	3.4	6.2	0.9
Bond strength (eV)	2.20	2.88	1.93
Thermal Conductivity (W/cm-K)	1.3	3.2	0.8
Lattice constant a (Å)	3.189	3.112	3.545
Lattice constant c (Å)	5.186	4.982	5.703

2.2 Gallium nitride growth

The synthesis of GaN was first described in 1932 by Johnson et al.[9]. However, the resulting material was polycrystalline and as such not useful for semiconductor devices. It was not until 1980-1990's that two major breakthroughs led to resurgence in GaN research: development of a buffer layer technique to obtain smooth non-polycrystalline films and demonstration of p-type doping. This was followed in the mid 1990s by the development of the two-flow MOCVD process that yielded improved growth uniformity. Currently research in GaN has become a field of its own as the growth in commercial devices continues. A list of several key developments that laid the technological framework for the current commercial success of GaN are listed presented below.

- Epitaxial deposition of GaN using hydride VPE[10]
- Employment of nucleation buffer layers[11]
- Use of magnesium to achieve p-type GaN[12]
- Development of the two-flow MOCVD process[13]

Over the years many crystal synthesis techniques have been investigated for the

epitaxial growth of GaN. Among them, metal-organic chemical vapor deposition (MOCVD), molecular beam epitaxy (MBE) and hydride vapor phase epitaxy (HVPE) are the most common[14].

One of the major challenges faced in the growth of GaN is availability of suitable substrates. With the exception of silicon on sapphire no other semiconductor has been commercialized exclusively using heteroepitaxial materials[15]. This is because bulk GaN has proven difficult to grow, in part due to the low solubility of nitrogen in gallium and the high vapor pressure of nitrogen on GaN. Recently bulk GaN has been grown by HVPE, but cost and availability make it prohibitive for use in LED applications.

Typically the lattice constant mismatch has been used to determine the suitability of a material as a substrate for GaN epitaxy. In practice a substrate must satisfy several properties in order to be suitable for epitaxial growth. This includes the material structure, surface quality, chemical, electrical and thermal properties as these will influence the quality of the epitaxial layer. Selection of the substrate thereby impacts the crystal orientation, polarity, strain and defect concentration of the epitaxy layer. A summary of problems arising from heteroepitaxy is presented below in Table 2.

Table 2: Common problems due to heteroepitaxy[15].

Substrate property	Problem
Horizontal mismatch (a-lattice)	High misfit dislocation densities causing: high leakage currents, reduced thermal
Vertical mismatch (c-lattice)	Antiphase boundaries, inversion domain boundaries
Coefficient of thermal expansion mismatch	Thermally induced stress in both the epitaxy film and substrate
Low thermal conductivity	Poor heat dissipation
Different chemical composition	Contamination of the epitaxy film, electronic interface states created by dangling bonds
Non-polar surface	Mixed polarity in the epitaxial film, inversion domains

A wide variety of substrates have been studied for GaN epitaxy a summary of which can be found in Liu and Edgar[15]. For GaN alloy LEDs the typical substrates are α-Al_2O_3 sapphire or 6H-SiC silicon carbide. Both substrates produce [0001] orientated GaN. Of the two, sapphire is the most used substrate for III-nitride growth primarily because of cost. It has high thermal and chemical stability, and availability of large high quality wafers. Its drawbacks are large lattice and thermal conductivity mismatches to GaN and poor electrical conductivity. Silicon carbide has the closest match with GaN in regards to crystal symmetry, lattice and thermal conductivity. Electrically conductive substrates are available thereby allowing backside contacts simplifying the LED device structure compared to sapphire substrates. The primary drawback of silicon carbide is cost.

With any semiconductor material, understanding how to control electrical properties through intentional doping is a key requirement. For n-type GaN, doping with Si is well established method for both vapor phase and vacuum deposition

processes[8]. On the other hand, p-type doping of GaN has been problematic. This obstacle was overcome by the addition of Mg as a dopant followed by post-growth irradiation by electron beam, which converted the Mg-compensated GaN into p-type GaN. Later, it was discovered that high-temperature annealing under nitrogen ambient works equally well to form p-GaN. However, Mg is a deep dopant and full ionization is not achieved. Nevertheless no other impurity has been as successful in yielding p-type GaN[8].

In summary, the direct band gap energy range of GaN and its alloys make III-nitrides ideally suited for use in optoelectronic devices and are beginning to see acceptance in high power and high frequency applications. Cost and availability of a native substrate has required the use of heteroepitaxial materials for LED devices. The two most common substrates for GaN epitaxy are sapphire and silicon carbide. To achieve desired electrical properties GaN is typically doped with Si (n-type) and Mg (p-type).

2.3 Gallium nitride based LEDs

The achievement of p-type doping was critical in enabling the development of GaN based pn-junction LEDs. The first such device was reported in 1992 by Akasaki et al.[16] and emitted light in the ultraviolet range at a power of 42 μW. The LED was based on a pn-homojunction meaning that p- and n-sides were GaN just doped differently. In this configuration the recombination of injected carriers is governed by the diffusion length and occurs over a large region with a strongly changing minority carrier concentration. As radiative recombination is a function of free carrier concentration, it is critical that the region in which recombination occurs has a high carrier concentration[6].

Increased carrier confinement can be achieved using double heterostructures that consist of two barrier layers sandwiched around the active layer. The barrier layers have a larger band gap than the active region shown schematically in Figure 3. In 1993 the first GaN based heterostructure, p-GaN/InGaN/n-GaN, was reported and showed an order of magnitude improvement in output power,125 μW, compared

to the homojunction device[17]. In addition, by varying the indium mole relation, $In_xGa_{1-x}N$ and doping the active layer with Zn, blue to blue-green emission was possible. However, poor crystal quality at indium mole fractions necessary for green band-edge emission limited application of double heterostructures devices.

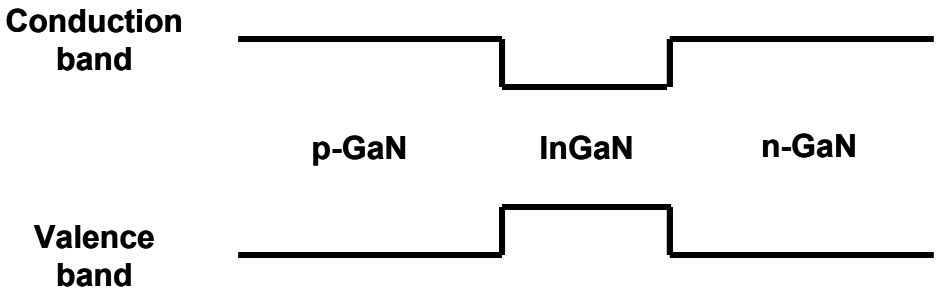


Figure 3: Schematic of double heterostructure.

Drawbacks associated with double heterostructures were overcome by reducing the thickness of the active layer. First, if the active layer is sufficiently thin lattice-mismatch between the active and barrier layers is taken up by pseudomorphic strain and not by the formation of dislocations. Second, as the active layer width approaches the De-Broglie wavelength (≅ 3 nm for InGaN) quantum effects become apparent. When then the thickness is comparable to the De-Broglie wavelength the conduction and valence band energy states no longer behave as a continuum but become discreet and quantized (Figure 4). Under these conditions the active layer is now termed a quantum well (QW).

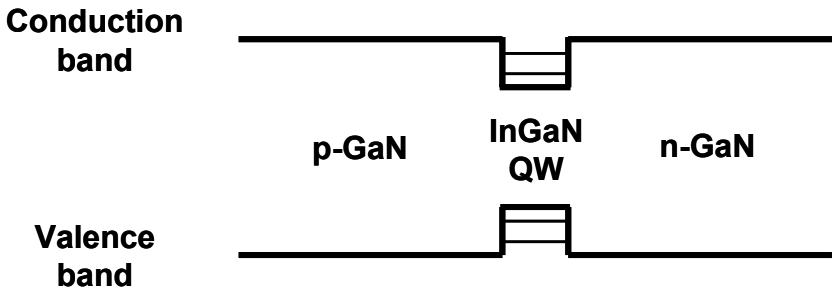


Figure 4: Schematic of QW structure showing discrete energy states.

In 1994 Nakamura reported the first single quantum well (SQW) GaN based LED[18]. By varying the indium mole fraction in the $In_xGa_{1-x}N$ active layer from 0.2 to 0.7 the peak wavelength was varied from blue to yellow. Output powers ranged from 4 mW for blue, 1 mW for green and 0.5 mW for yellow LEDs. The drop in output power with increased wavelength reflects the decrease in crystal quality between the QW and barrier layers as both lattice mismatch and differences in thermal expansion coefficient increase with indium concentration. Lastly, the spectral width of QW based LEDs is significantly narrower than the first generation Zn doped heterostructure LEDs resulting in improved color purity. As such, the SQW and multiple quantum well (MQW) structures serve as the basis for today's high-brightness GaN based LEDs.

2.4 Challenges

While the use of QW structures has improved several key LED performance metrics, several challenges still remain. GaN epilayers exhibit high dislocation densities whose impact on optoelectronic properties is still controversial. There is no consensus on how defects influence luminescence. As such an improved understanding of the defect behavior in GaN and impact on luminescence is necessary in order to continue to advance the performance of LEDs. A summary of the major defects in GaN devices follows.

2.4.1 Substrate lattice mismatch

Cost and availability constraints of native substrates necessitated the commercialization of GaN LEDs with heteroepitaxial materials. Typically grown on sapphire and silicon carbide, GaN epilayers contain large dislocation densities due primarily to lattice mismatch. With respect to GaN, Al_2O_3 has a 13% mismatch and 6H-SiC has a 3.5% mismatch. Because of this mismatch GaN nucleates at discrete sites across the substrate. As these sites grow they eventually interact with one another leading to the formation of threading dislocations. The implementation of an AlGaN buffer layer to take up some of the mismatch induced strain has helped

reduce the defect density. Never the less, in a typical GaN LED dislocation densities ranging from 10^8 – 10^{10} cm^{-2} are expected[19]. Figure 5 shows typical threading dislocations observed in a GaN LEDs.

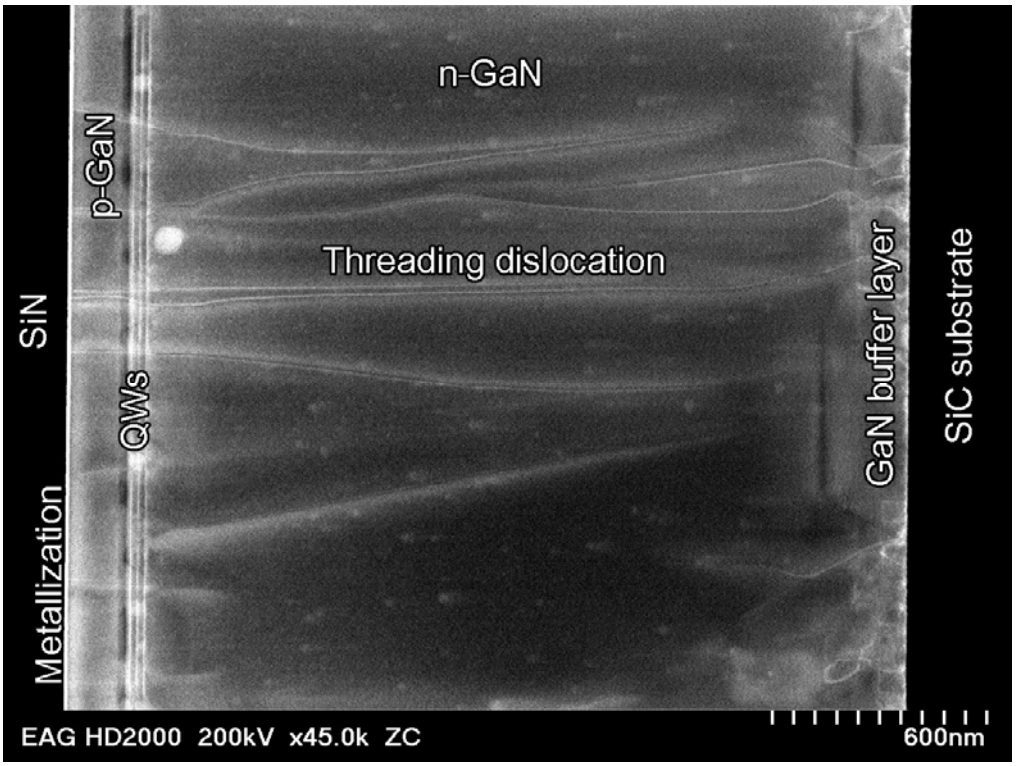


Figure 5: Threading dislocations in GaN.

In addition, threading dislocations have been associated with a defect termed the 'V-defect' observed in the growth of InGaN MQW stacks. The structure of V-defects has been studied extensively and characterized as a hexagonal inverted pyramid that forms on the (0001) plane and the pyramid sidewalls are {10-11}[20-25]. Recently Liu et al.[26] proposed a new method to determine the exact three-dimensional geometry of V-defects in AlN. The method correlates cross-section profiles to different cut positions through the V-defect. Application of the method can be used to identify the V-defect facets. A typical V-defect observed for InGaN MQW structures is shown in Figure 6.

The formation mechanism for V-defects is still being investigated, but is often reported to be induced by mixed threading dislocations, **b**=1/3<11-23>, during MQW growth. Liliental-Weber et al.[27] proposed that formation of the defect is caused by gettering. Impurities or dopant elements tend to congregate at dislocation sites and at high enough concentrations may locally inhibit crystal growth in the area of the dislocation, initiating V-defect formation. Cho et al.[23] found that not all V-defects are connected with a threading dislocation. Instead stacking mismatch boundaries induced by stacking faults were proposed as an alternative origin for V-defects. Wu et al.[22] proposed that V-defect formation is controlled kinetically by reduced GaN incorporation at lower growth temperatures. To suppress re-evaporation of indium, the growth temperature is lowered which reduces GaN surface diffusion, and thus the defect morphology is kinetically governed. As temperatures are increased for growth of p-GaN, surface diffusion rates are sufficiently high that the V-defects are back-filled/planarized by GaN.

While the structure and formation of V-defects has been investigated, little is know about their optoelectronic activity. It has been proposed that the V-defects contribute to carrier localization away from non-radiative sites. Hangleiter et al.[28] and Netzel et al.[29] reported that narrow QWs on the sidewalls of V-defects have higher band gap energy that effectively localizes carriers by providing an energy barrier around every defect. However, it has also been reported that V-defects have lower band gap energy and result in loss of light output[22, 30]. In short more studies are needed.

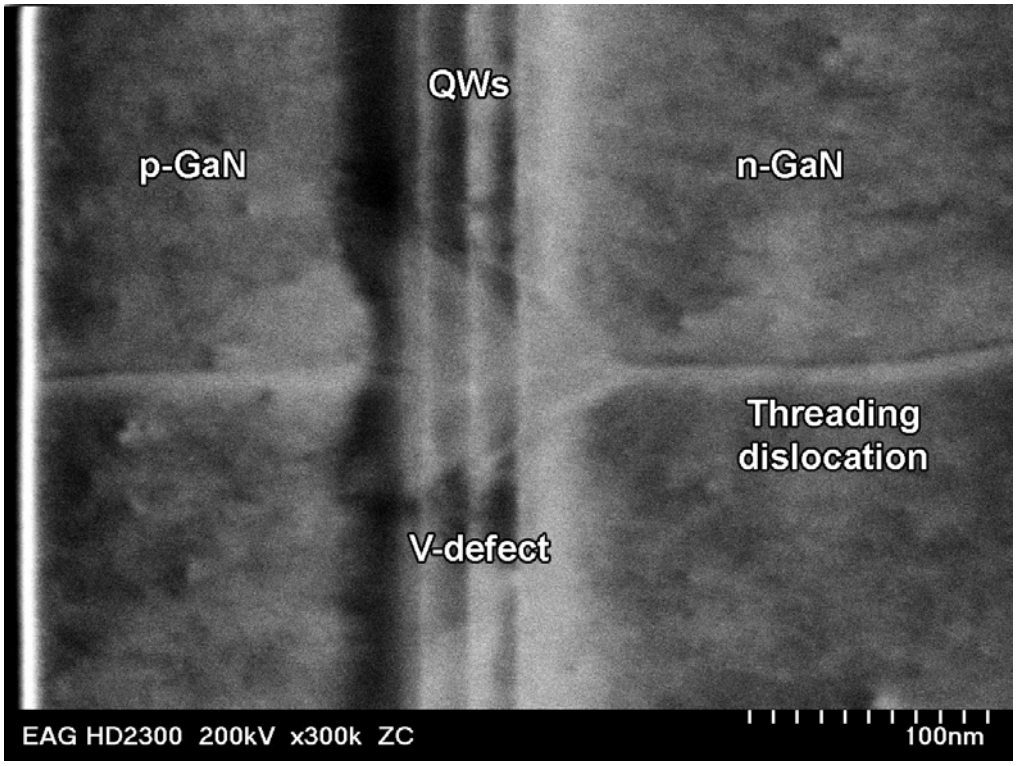


Figure 6: Typical V-defect.

Despite the large dislocation density, GaN based LEDs exhibit high optical efficiencies whereas for GaAs based LEDs dislocation densities > 10^6 cm^{-2} quench light emission[2, 31, 32]. As dislocations are thought to be non-radiative recombination sites, strong luminescence from GaN-based LEDs was surprising. This led to questions regarding the nature of dislocations and there interaction with other defects in the GaN material system.

2.4.2 Compositional variation

A spinodal is predicted in the InN-GaN phase diagram. Theoretical calculations by Ho and Stringfellow[33] suggest that InGaN alloys are unstable over most of the compositional range and typical temperatures (600 – 800 C) used for epitaxial growth. They showed that for indium compositions between the spinodal limit and the miscibility gap (6%-22% indium at 800 C) the system is metastable and phase separation occurs. This indium concentration is in the range of blue to blue-green

devices and the potential exists that the InGaN alloy will not be homogeneous. Thus the predicted spinodal has the potential to yield InN-rich and GaN-rich regions within InGaN QWs. The result of this phase separation would produce band gap variation as InN regions reduce the intended band gap as shown below in Figure 7.

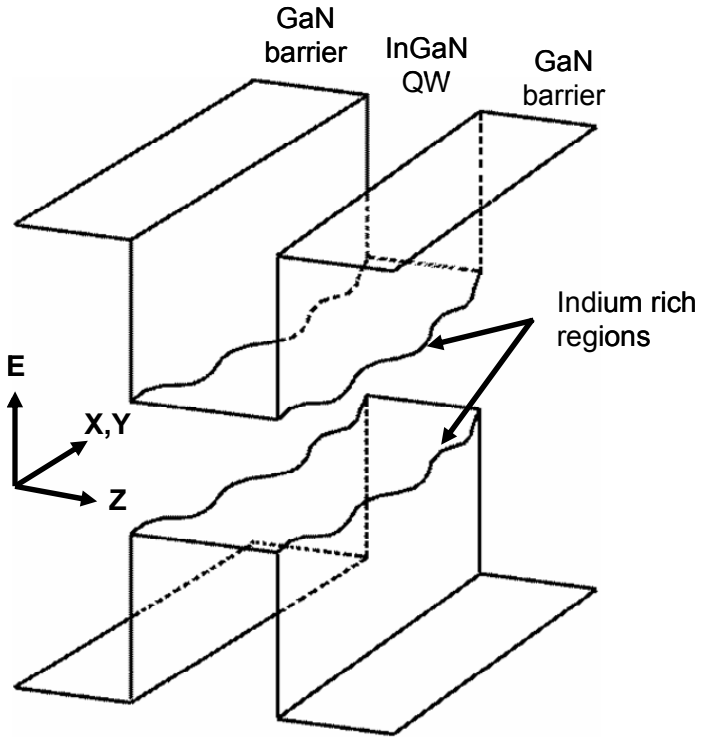


Figure 7: Schematic of phase separation in InGaN QW (Adapted from Ponce[34]).

One of the potential artifacts from phase separation is emission broadening. This is due to longer wavelength (red shift) emission from the In-rich sites termed quantum dots (QD). However, any additional impact on luminescence from the QDs is still a subject of significant research. Recent work suggests that stress present in the QWs may suppress the spinodal such that phase separation is no longer an issue at the growth temperatures for LEDs[35, 36]. What may result from the potential immiscibility will be discussed further in section 2.4.4.

2.4.3 Quantum-confined stark effect

GaN alloy devices exhibit polarization effects due to the polarity difference between cation sites (Ga, In) and anion sites (N). Furthermore, wurtzite GaN is non-centrosymmetric which enables a polarization charge to manifest itself at hetero-interfaces. This is termed spontaneous polarization (P_{sp}) as it is not induced by strain, but by the difference in polarization constants across an interface. For our devices of interest we need to consider the polarization constants for GaN (-0.029 C/m^2) and InN (-0.032 C/m^2)[8]. Since the polarization constants are close, the effect of spontaneous polarization for InGaN/GaN structures is relatively small compared to the piezoelectric effect (Figure 8) which will now be discussed.

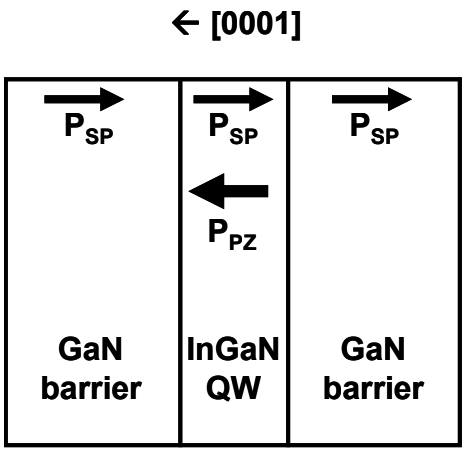


Figure 8: Schematic of spontaneous and piezoelectric polarization in wurtzite GaN.

Piezoelectric polarization (P_{pz}) results from lattice mismatch strain between InGaN QWs and GaN barrier layers. Recall from section 2.1 that for InGaN LEDs emission is tuned by varying the indium mole fraction. Consequently, increasing the percentage of indium in the QW also increases the lattice mismatch to the barrier layer. If the QW thickness is less than the critical thickness, lattice mismatch is accommodated by pseudomorphic strain. Above the critical thickness lattice mismatch is accommodated by a combination of strain and misfit dislocations[37]. From Pereira et al.[38] critical thickness is not a constant and for $In_xGa_{1-x}N$ alloys

varies inversely with indium concentration; 3 nm for x = 0.1 to 1 nm for x = 0.2. Thus piezoelectric polarization is expected to increase as indium concentration is increased to achieve longer wavelength emission.

At issue is an electric field (E_{pz}) induced by piezoelectric polarization that can affect the desired band structure and thus the optical and electrical properties of the device. Termed the quantum confined stark effect (QCSE) the presence of an electric field results in the band bending shown schematically in Figure 9.

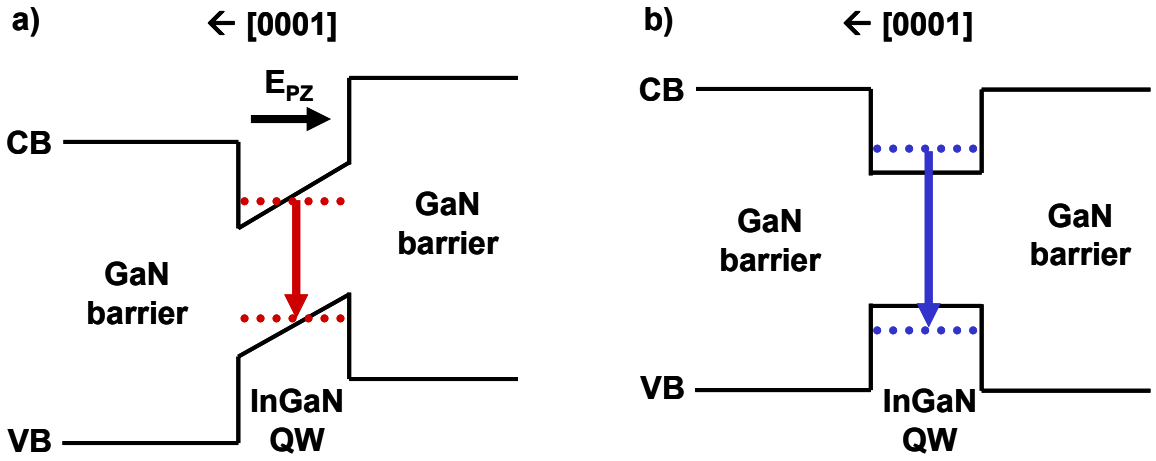


Figure 9: Schematic of band structure (a) with and (b) without band bending due to quantum confined stark effect.

The effect of band bending is two fold. First, the QCSE lowers the effective electron-hole pair recombination energy (dotted lines in Figure 9). This yields a red-shift in quantum well emission energy. The amount of shift is determined by the magnitude of the induced piezoelectric field which in turn is related to the lattice mismatch strain. Second, electrons and holes 'pool' in the energy minima resulting in a separation of their respective wavefunctions. The result is an increase in recombination time which potentially is a greater problem than the aforementioned red-shift. Increased recombination time allows carriers to find non-radiative recombination sites which results in reduced luminescence. Thus the QCSE has the

potential to negatively impact both emission efficiency and desired emission wave length.

2.4.4 Defect tolerant emission

GaN based LEDs exhibit strong emission despite a high density of threading dislocations, compositional fluctuations, and quantum confined stark effect[2, 31, 39]. Thus the question why is luminescence from GaN based LEDs relatively insensitive to defects. The answer to this is still open to debate and research continues.

At the heart of the question is the high dislocation density 10^8 – 10^{10} cm^{-2} associated with GaN devices. Because GaN LEDs have strong emission, initially it was thought that dislocations in GaN were not electrically active. That is to say dislocations do not act as carrier traps by forming mid-level states within the band gap. Attempts to correlate defects to luminescence have been made by numerous research groups [40-43]. Results are still contradictory with some groups asserting dislocations are electrically active[44] while others report the opposite[45, 46]. This is due to the difficulty of directly correlating defects to optical and electrical properties which will be discussed further in the next chapter. While the optoelectronic behavior of threading dislocations is still unclear, there is strong correlation between non-radiative recombination sites and threading dislocation density[39]. If dislocations are non-radiative recombination sites, then some characteristic of the GaN alloy system is impeding charge carriers from reaching those sites.

The most common explanation for how charge carriers avoid nonradiative defects is compositional inhomogeneity within the QWs. In 1996 Chichibu et al.[40] attributed the electroluminescence peak for an InGaN LED to recombination of EHPs localized at energy minima due to InN-rich regions less than 60 nm in size. Localization of the carriers in the indium enriched region helps keep them away from non-radiative recombination sites. Several groups attempted to investigate compositional fluctuations within the QWs and have reported the presence of In-rich regions[47, 48]. On the other hand it has been proposed the high-energy electron beam testing such as that seen with transmission electron microscopy (TEM) can induce

the formation of In-rich regions[49]. Pooling due to the QCSE has been proposed as the localization mechanism impeding carriers from reaching non-radiative sites[50-52]. However, InGaN QWs grown on non-polar GaN which does not exhibit the QCSE, yielded recombination dynamics similar to those observed with polar GaN. Recently, Chichibu et al. proposed that localization occurs on a much smaller scale and is due to atomic condensates of In-N spontaneously formed in statistically homogeneous InGaN alloys[39]. Observations of extremely short positron diffusion lengths (~ 4 nm) in indium alloys lead the authors to conclude the presence of a high density of sites capable of efficiently capturing positrons and thus, holes. Identification of the sites came from two independent studies. Both Kent and Zunger[53] and Wang[54] using large-scale atomistic empirical pseudopotential calculations predicted strong hole localization due to randomly formed condensates of In-N, which form deep acceptors. At this size scale direct observation of the atomic condensates will be difficult and has yet to be reported in literature.

2.4.5 Research motivation

While many different theories have been proposed, the origin of high luminescence efficiency of GaN alloy LEDs still remains elusive. This research was undertaken to address questions related to the relatively defect tolerant optical and electrical properties of GaN based LEDs. The focus is on direct correlation of defects to optoelectronic behavior. This work also supports the advancement of optoelectronic analytical techniques using electron beam testing which is the topic of the next chapter. Lastly, it is fitting to conclude this chapter by describing the specific device of interest. The work in this dissertation involves the characterization of GaN based MQW blue and green LEDs grown on silicon carbide substrates. The typical structure of the devices investigated is shown in Figure 10.

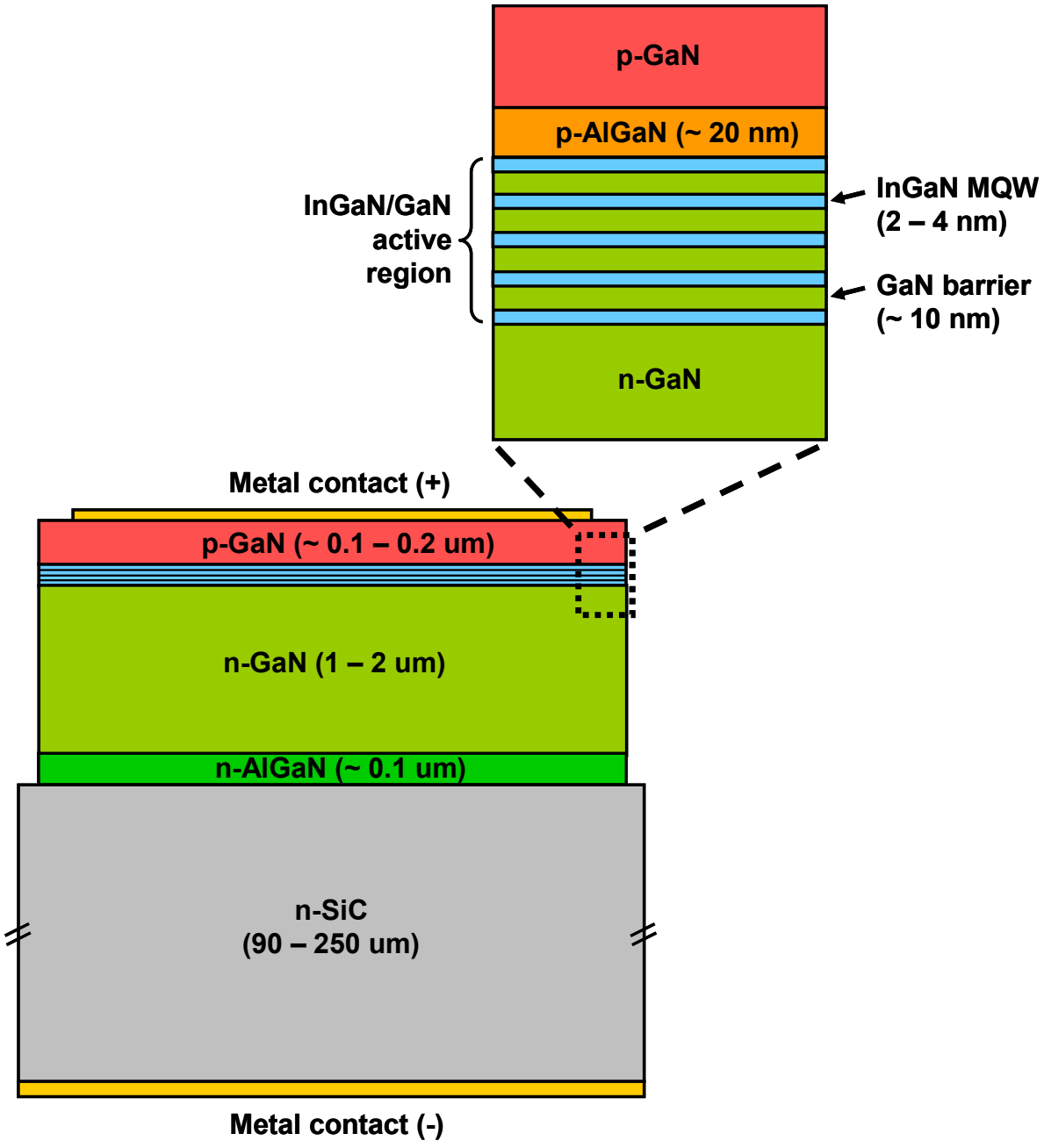


Figure 10: General structure of MQW $In_xGa_{1-x}N$ based LED (Figure not to scale).

3. Analytical Techniques

3.1 Electron beam induced signals of interest

The interaction of an electron beam with a sample produces a rich set of signals of interest which are summarized in Figure 11. The electron beam-specimen interactions are a result of elastic and inelastic scattering processes that occur simultaneously within the sample[55].

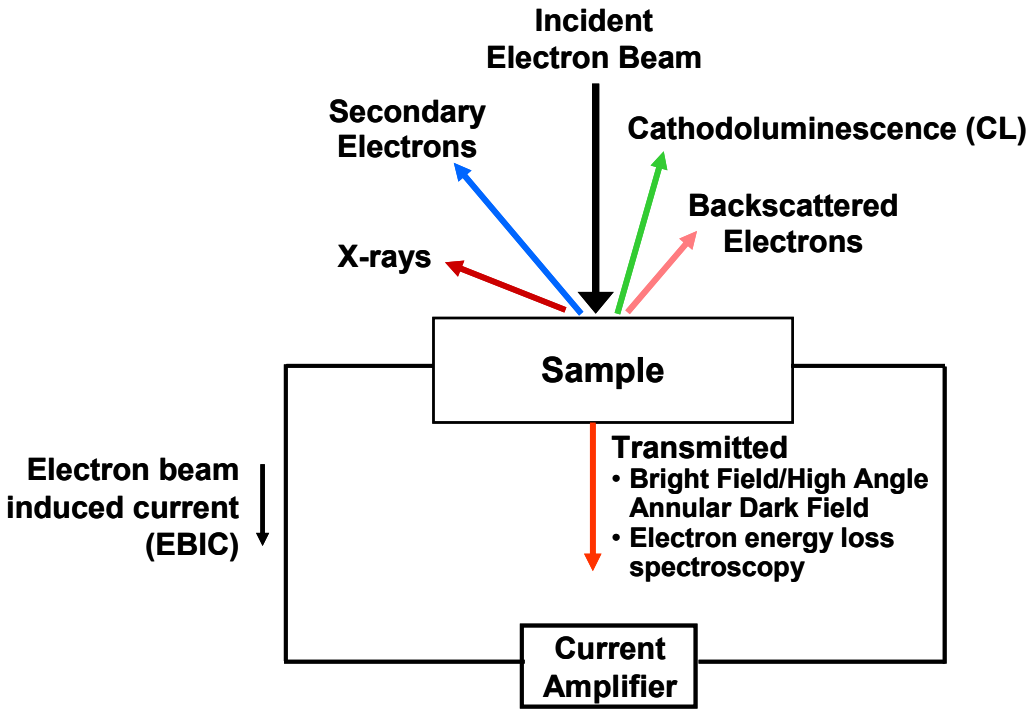


Figure 11: Electron beam generated signals of interest (Adapted from Williams and Carter[56]).

An elastic scattering event is characterized by directional change to the electron trajectory with little or no energy loss. Elastic scattering primarily gives rise to backscattered electrons (BSE). Inelastic scattering events are characterized by

small angular changes to the electron trajectory with energy loss. The transfer of energy from incident electrons to the tightly bound inner-shell electrons and loosely bound outer-shell electrons of the atoms in the specimen gives rise to phonons (lattice vibrations), plasmons (electron oscillations), auger electrons, x-rays, photons, secondary electrons (SE), and electron-hole pair (EHP) generation[55]. During any given inelastic scattering event the incident electron can transfer an amount of energy ranging from less than 1 eV to the full energy carried by the electron. As inelastic scattering is an energy loss event it limits the distance traveled by the incident electrons within the sample.

The region in which the electrons interact with the sample, deposit energy and generate signals is called the interaction volume. The size of the interaction volume is a function of the mean atomic number, weight and density of the sample, the electron energy, spot size and incident angle[55]. Depending on these parameters the interaction volume can extend from a few nanometers to a few microns below the surface.

Understanding the size and shape of the interaction volume is crucial to understanding and interpretation of electron microscopy data. Estimates of the interaction volume are made by determining the distance traveled by incident electrons within the sample (electron range). The most common approach is to use Monte Carlo modeling based of an established energy-loss law for electron beam interactions with a solid[57]. Monte Carlo simulations generate plots of the probable electron paths within a sample. By running several thousand simulations an estimate of interaction volume is obtained. Figure 12 shows a simulation from the Monte Carlo software Casino[58], which illustrates the interaction volume resulting from a 30 keV electron beam interacting with bulk GaN.

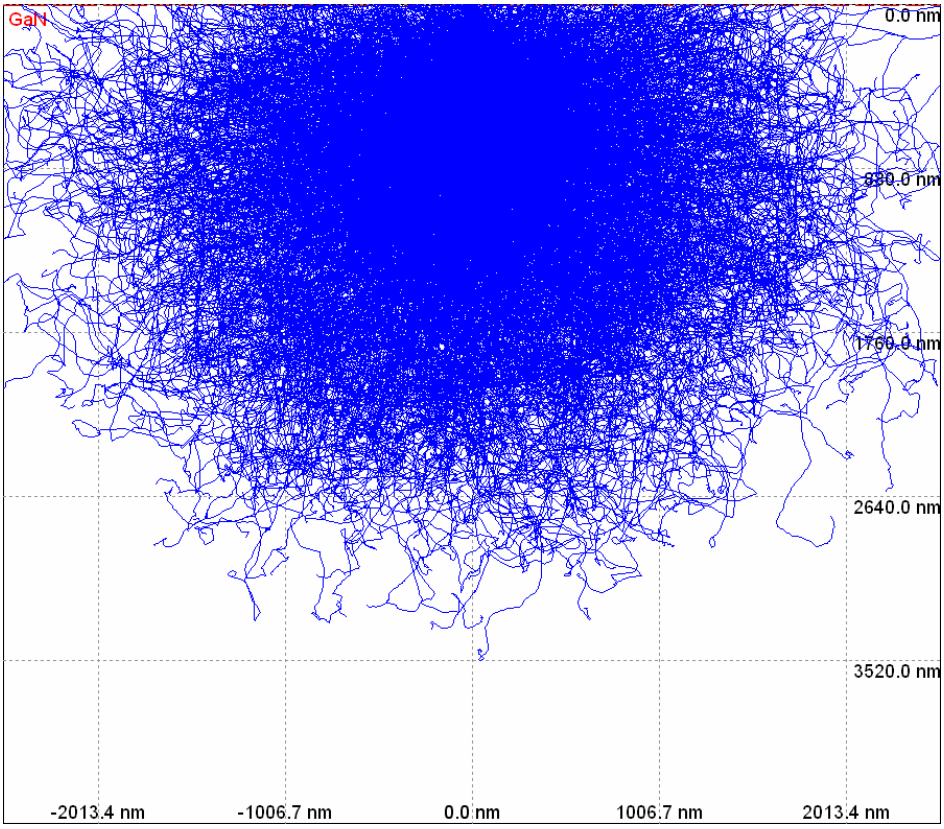


Figure 12: Casino data of a 30 keV electron beam incident on bulk GaN.

From this result we can get an estimate of the depth ~ 2.6 μm and width ~ 4 μm of the interaction volume. As this is the region within which electrons interact with the sample the figure above underlines to importance of knowing where signals of interest are generated as that will impact resolution limits.

3.2 Electron beam induced current

As discussed above the interaction of an electron beam with a sample produces electron-hole pairs. EHP generation in a material with a band gap is the basis for an electron microscopy technique called electron beam induced current (EBIC) analysis. This technique can provide information on electrical properties of defects, minority carrier diffusion lengths, recombination mechanisms both surface and bulk, pn-junction location and homogeneity[59-61].

In the absence of a separating force, EHPs will either recombine amongst themselves or due to localized concentration gradients diffuse to recombination sites. Under these conditions an EBIC signal is not produced. Alternatively, the presence of an electric field causes drift of nearby EHPs. The field applied either externally or internally will separate electrons and holes creating a current I_{EBIC} which can then be detected by an external circuit. Collection and imaging of a sample with the induced current is known as EBIC microscopy.

As an electric field is required, semiconductors devices that exhibit rectifying junctions are perfect candidates for EBIC analysis. Rectifying junctions have a 'built-in' electric field resulting from the depletion of free carriers in the space charge region. Beam injected EHPs within a diffusion length (L) of the space charge region will get separated with electrons swept to the n-side and holes to the p-side generating I_{EBIC}. A schematic of a typical cross-sectional EBIC experiment is shown below in Figure 13 with the electron beam scanned parallel to the junction.

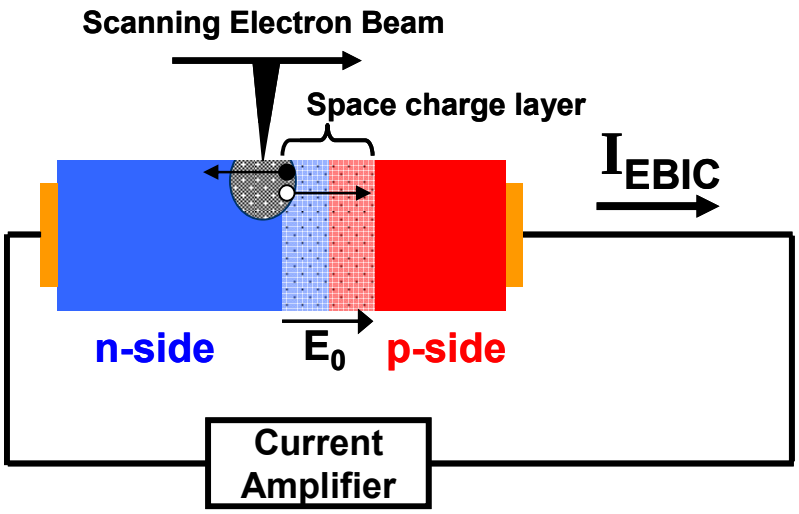


Figure 13: Schematic of cross-sectional EBIC experiment.

The magnitude of I_{EBIC} depends on the number of EHPs generated and position relative to the electric field. EHPs generated beyond the diffusion length will not feel the effect of the electric field and will eventually recombine. EHPs

generated within diffusion length of the space charge region feel the effect of the built-in electric field. As the field strength reaches a maximum at the pn-junction, the probability of EHP separation reaches a maximum as well. Therefore the EBIC signal is expected to peak at the pn-junction and then drop off. The signal can also be affected by the presence of defects which trap charge carriers and prevent them from contributing to I_{EBIC}. Defects increase recombination rate, and reduce the recombination lifetime, of minority carriers. As such, areas near a recombination-enhancing defect have a high contrast and appear dark in an EBIC micrograph.

For the evaluation of defects it is also useful to scan the electron beam perpendicular to the pn-junction in what is called plan-view EBIC. This allows planar mapping of defects as recombination sites will appear dark due to lower I_{EBIC} from those regions. An example of a typical plan-view EBIC experiment is shown below in Figure 14.

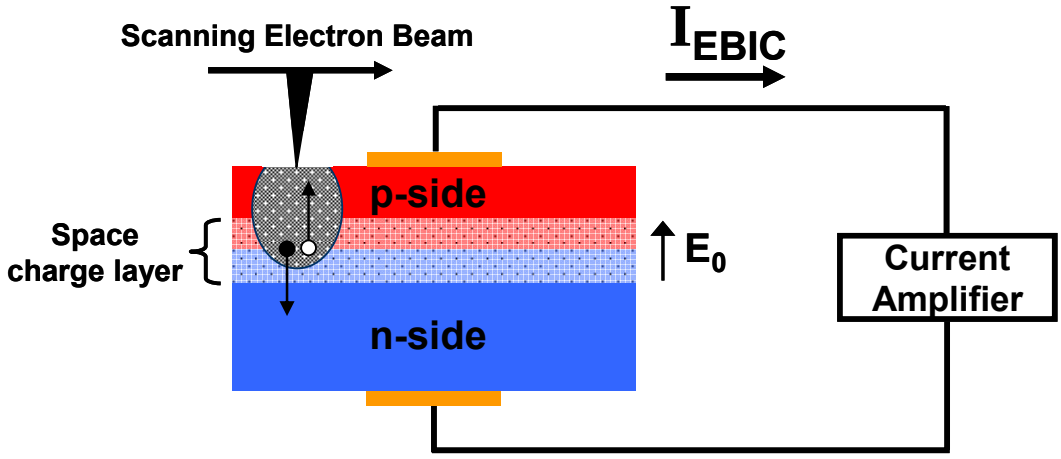


Figure 14: Schematic of plan-view EBIC experiment.

3.3 Cathodoluminescence

As opposed to the separation of carriers, recombination of EHPs can result in photon emission. If the method of exciting emission is via electron bombardment the process is called cathodoluminescence (CL). The emitted photons can be collected and used for both imaging and spectral analysis. This yields information on the

optoelectronic behavior of the sample. Other forms of luminescence exist and are classified according to their excitation method. Electroluminescence (EL) is the emission of photons due to an applied electrical field and is the operational mode for LEDs. Photoluminescence (PL) is due to photoexcitation excitation. As the most common way to perform CL experiments is with an electron microscope the remainder of this discussion will concentrate on cathodoluminescence.

CL microscopy can be broken into three broad categories; spectroscopy, panchromatic imaging and spectroscopic imaging. Spectroscopy is performed by investigating the spectral distribution of light. This yields information on the energies of different transitions in the sample. A number of transitions are possible that include but are not limited to; band-to-band, sub-band gap, excitonic and defect assisted. Panchromatic imaging spatially maps all the emitted wavelengths within the response of the detector. This enables the identification of high and low radiative recombination areas. As defects typically arrest radiative recombination, panchromatic imaging is used to target areas of interest for further investigation. Spectroscopic imaging combines spectral response with imaging to map emission from a particular wavelength band. This allows a particular emission to be mapped and spatially related to the sample structure.

In order to perform CL microscopy requires the electron microscope be specially equipped with some form of high efficiency light collection and detection apparatus. An example of a typical CL collection set-up is shown in Figure 15.

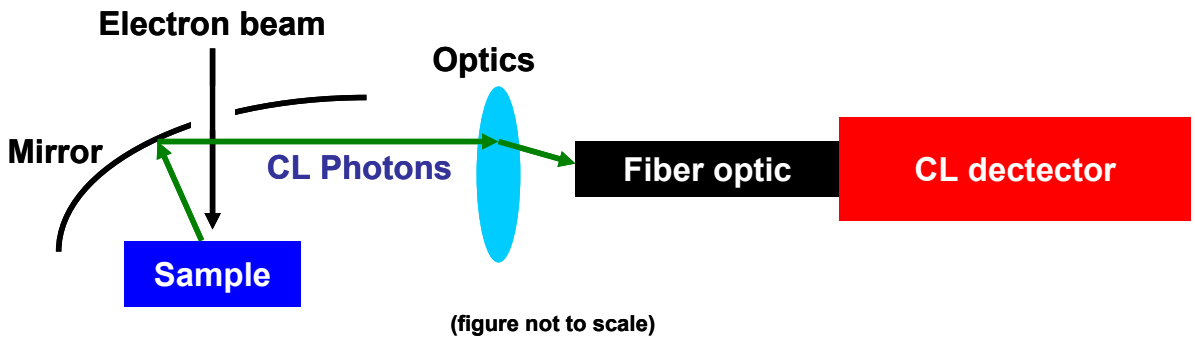


Figure 15: Schematic of CL collection system.

Ideally the sample is positioned at the focal point of a large collection mirror. Emitted photons are collected and focused onto a fiber optic feed through to an ex-vacuo detector. The detector typically consists of a monochromator with a photomultiplier or CCD array.

In addition CL set-ups often include cold-stages to suppress non-radiative processes which are typically thermally activated. This is important because the internal quantum efficiency η defined by Yacobi and Holt[62] affects emission intensity.

$$\eta = \frac{R^R}{R^N} = \frac{1}{1+\exp\left[-\frac{E_A}{kT}\right]} \tag{3-1}$$

Where R^R and R^N are the radiative and non-radiative recombination rates respectively, E_A is activation energy, k is Boltzmann constant and T is temperature. Equation (3-1) indicates that emission is stronger at low temperatures than higher temperatures.

3.4 Electron-hole pairs

The magnitude of I_{EBIC} and CL intensity is a function of the number of EHPs generated and therefore it is important to understand this process. The interaction of an electron beam with a semiconductor can result in promotion of an electron across the band gap. This yields an electron in the conduction band and a hole in the conduction both free to drift and diffuse. A schematic of this process is shown below in Figure 16.

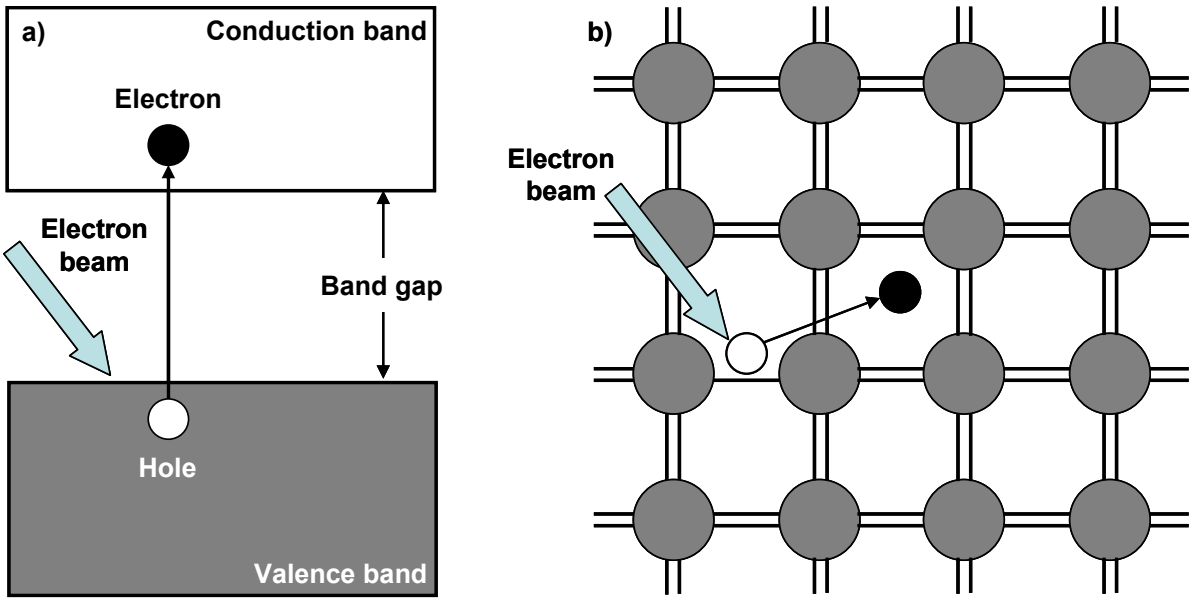


Figure 16: Schematic of electron beam induced EHP generation in (a) band energy and (b) bond diagrams.

There are various methods to estimate the rate of EHP generation G. In general any method for determining G must account for recombination and scattering losses. From Newbury[63] the most common method for determining G at SEM energies starts by calculating the number of EHPs created per second, G_0.

$$G_0 = \frac{E(1-n)}{qE_{eh}} i_b \qquad (3\text{-}2)$$

Where E is incident electron beam energy, n is bulk backscattering coefficient, q is electron charge, E_{eh} is average energy required to produce an EHP and i_b is incident electron beam current. While E and i_b are determined from the microscope set-up, n and E_{eh} are obtained by other methods. Estimates for the bulk backscattering coefficient can be obtained from Monte Carlo simulations. Determining E_{eh} is more challenging as it is a reflection of the complete electron interaction process. To simplify it is common practice to assume $E_{eh} = 3E_{bandgap}$. As n accounts for scattered electrons lost to EHP formation we now need to account for EHPs lost to recombination. This is done by multiplying G_0 by the estimated minority carrier diffusion length. The resulting number is an estimate for EHP generation. It should

be noted that this estimate for G is based on SEM energies. At higher accelerating voltages relativistic effects appear and estimates for G based on Newbury's method are suspect. The question of EHP generation at high electron energies will be discussed in a later section on high-resolution electron beam testing.

Semiconductors are doped to achieve specific electrical properties and the generation of EHPs can affect the engineered carrier concentrations. This can potentially alter the electrical behavior of the sample and leads to a discussion on low/high-injection conditions. First, consider an n-doped semiconductor. At equilibrium the concentration of electrons, majority carriers, is much greater than holes, minority carriers. Under low-injection conditions EHP generation of minority carriers (holes in this case) is less than the initial number of majority carriers. Now recall that EHP formation generates an equal number of electron and holes. In order to maintain charge neutrality, the relatively small number of excess majority carriers will drift to follow the diffusive motion of these minority carriers. Consequently the motion of both majority and minority carriers can be characterized by one parameter, the minority diffusion coefficient. This greatly simplifies modeling of carrier behavior. Under high-injection conditions EHP generation of minority carriers exceeds the initial number of majority carriers. This complicates the diffusion model by requiring the use of coefficients for both majority and minority carries. In addition, the large number of minority carriers may saturate defect sites resulting in changes to the sample behavior.

3.5 High-resolution electron beam testing

As discussed in the previous chapter the relative defect insensitive emission characteristics of GaN alloy LEDs are not yet well understood. In part this is due to the difficulty of directly correlating defects to optical and electrical properties. In an SEM the beam excited volume of EHP generation limits spatial resolution. This can be seen below in Figure 17 based on results from Monte Carlo simulations. Figure 17 (a) and (b) show for a 5 and 30 keV beam on bulk GaN the interaction volume is on the order of 0.2 and 4.2 μm respectively. This is too large to resolve the fine

features of the QWs within the active layer. On the other hand Figure 17 (c) shows that the combination of high energy electron beam and thin sample decrease the size of the interaction volume and nanometer spatial resolution is possible.

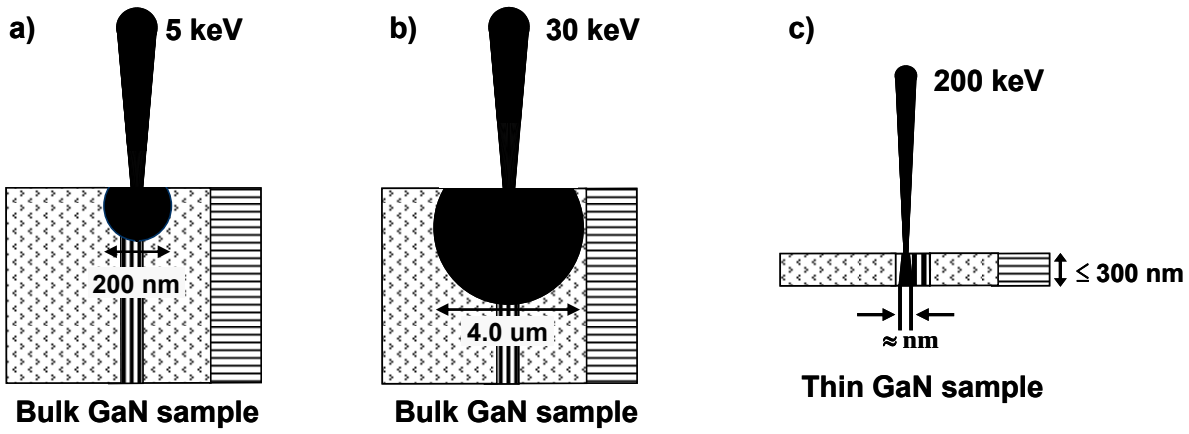


Figure 17: Effect of beam energy and sample thickness on interaction volume (figure not to scale).

High-resolution electron microscopy is defined in this work as transmission electron microscopy (TEM) and scanning transmission microscopy (STEM). In traditional TEM imaging mode, the thin specimen is illuminated with a nearly parallel beam of electrons, and the transmitted electrons are then focused by the objective lens to form an image. This is analogous to the operation of a light microscope with the exception the focal length of an electromagnetic lens is changed by varying the lens current. Figure 18 below shows the configuration differences between a standard SEM and TEM.

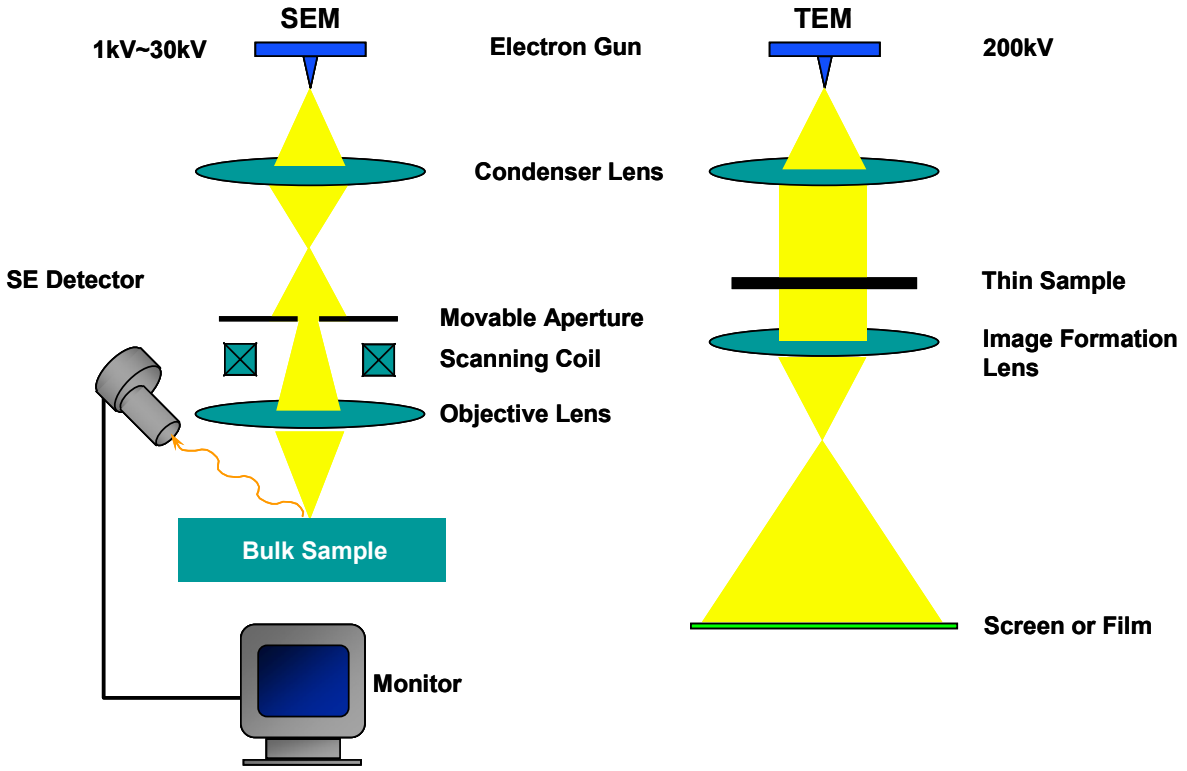


Figure 18: Comparison of SEM and TEM configurations.

In a STEM the electron beam is focused on and rastered across the sample. In addition to SE, BSE, x-rays, photons, and EHPs, electrons transmitted through the sample can be detected with a high-angle annular dark field (HAADF) detector or a bright field (BF) detector. The HAADF detector is an annular detector placed concentrically about the post-specimen optical axis. The HAADF detector detects transmitted electrons that have been scattered through high angles. The acceptance angle of the HAADF detector is typically between 50mrad-200mrad, but can often be controlled with a projector lens. HAADF images are often called 'Z-contrast' images because the cross section for Rutherford elastic scattering is proportional to Z^2. Consequently, high-Z regions of a specimen would scatter more electrons and have a higher intensity than low-Z regions[64, 65]. The BF detector is an axial detector that is usually placed after the HAADF detector and detects transmitted electrons that have undergone low angles of scatter. A schematic of a typical STEM is shown below in Figure 19.

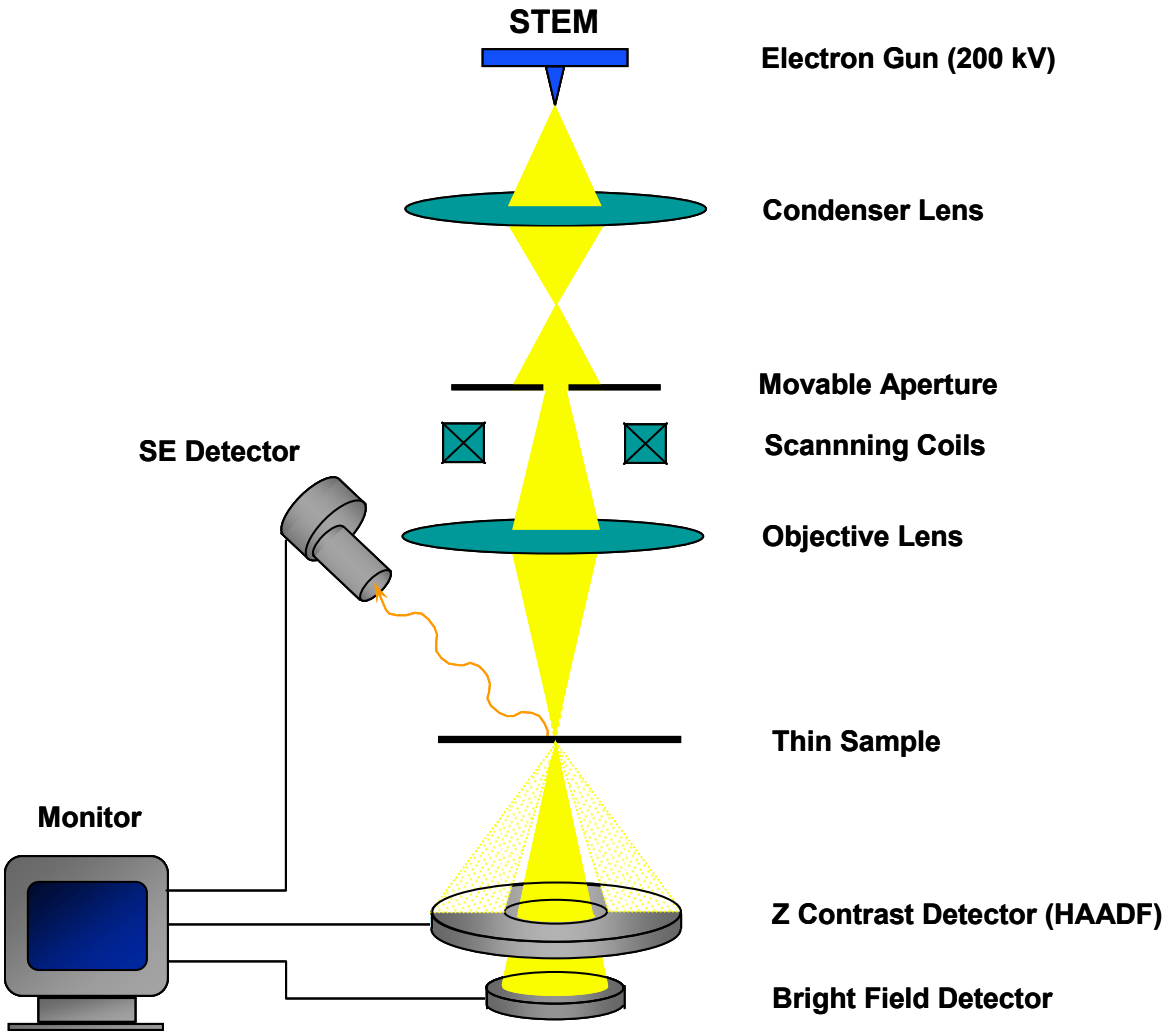


Figure 19: Schematic of a STEM.

Intended for applications requiring highly localized nanoanalysis with energy dispersive x-ray spectroscopy (EDS) and electron energy loss spectroscopy (EELS), the first dedicated STEM was produced in 1963 by Vacuum Generators Microscopies Ltd. Since then the use of dedicated STEMs has increased partly in response of support to the thin film semiconductors industry. For the work in this dissertation a Hitachi HD-2000 STEM was used. The column design is more analogous to a field emission SEM than a conventional TEM. An electron beam is produced from a field emission source and accelerated to 200 keV. The HD-2000

STEM is capable of operation under several different modes (beam currents). An example of one such setting is 'normal' mode with a beam current of ~1 nA and a final spot size of ~ 0.5 nm.

Transmission electron microscopy and scanning transmission microscopy overcome the resolutions limits of conventional standard electron microscopies. These techniques are utilized to examine the internal structure of thin samples, which are electron transparent (Figure 20). For this application a 'thin' sample is one that is on the order of a few hundred nanometers thick. To simultaneously measure electro-optical properties with techniques such as EBIC or CL requires specialized TEM/STEM set-ups and sample prep. A discussion on instrument set-up for STEM-EBIC and –CL follows. A discussion on sample prep is reserved for chapter 4.

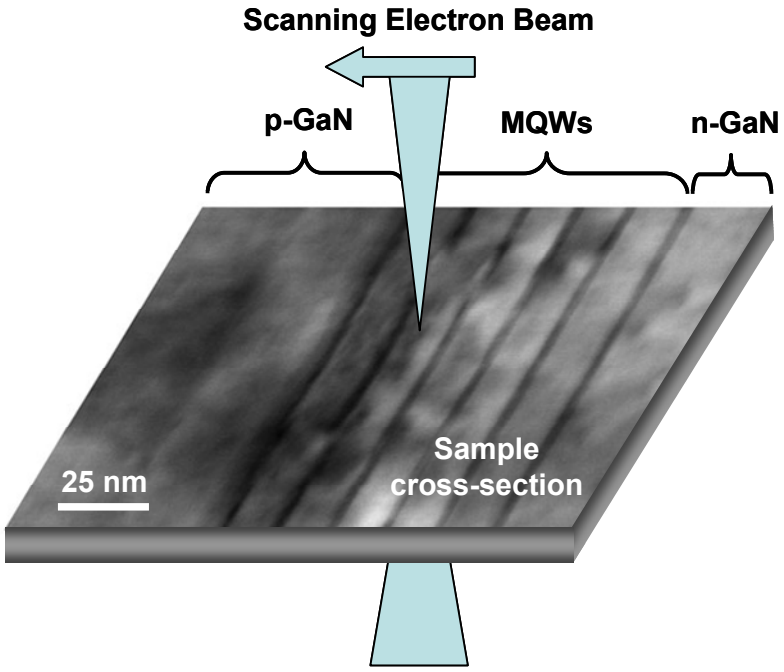


Figure 20: Schematic STEM based characterization.

3.6 STEM EBIC

3.5.1 Introduction

While EBIC identifies electrical activity of defects it is not effective in identifying the crystallographic nature of defects. On the other hand TEM/STEM techniques are capable of nanometer spatial resolution and the identification of defect structure. To fully characterize a defect, EBIC must be combined with either TEM or STEM techniques. The resulting STEM-EBIC technique is a powerful tool for the direct characterization of electrical transport properties to defects in semiconductor materials[66].

3.5.2 STEM-EBIC systems

The first TEM-EBIC system was demonstrated in 1977 by Sparrow and Valde on a Cambridge TEM equipped with a scanning attachment. Results correlated crystal defects with electrical properties in silicon transistors[67]. In 1978 Petroff et al. modified a TEM to perform simultaneous structural- EBIC analysis of dislocation cores and nonradiative recombination properties in GaAlAsP[59]. The first STEM-EBIC system was developed in 1980 by Fathy et al[68]. Interestingly, neither group published instrumentation details. The first description of a STEM-EBIC holder was provided in 1988 by Perrault and Ast[69]. A reprint of their holder design for a JEOL 200CX STEM is shown in Figure 21. Electrical contact to the sample is made on one side through the body of the holder and on the other side by wire bonding to one of the three isolated bonding pads.

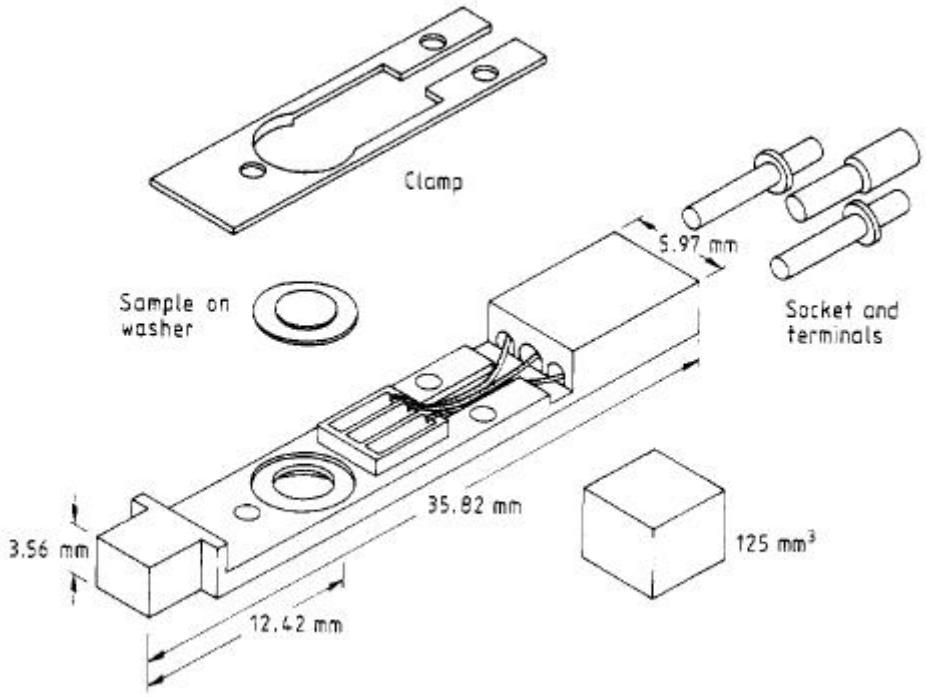


Figure 21: Isometric drawing of STEM-EBIC holder (From Perrreault and Ast[69]).

The unshielded signal wires passed to a BNC cable which transferred the signal from the sample to a Keithley 427, low-noise current amplifier. Functionality of the holder was demonstrated with the observation of electrically active defects in silicon Schottky diodes. In 2003 Bunker et al. developed a STEM-EBIC holder for the Hitachi HD-2000 series of microscopes[70]. Unlike the design by Perreault and Ast, the design by Bunker et al. electrically isolated the sample from the body of the holder. This was done to reduce potential noise from scattered electrons hitting the body of the holder. From the electrically isolated sample two Kapton insulated wires were connected to a subminiature A (SMA) connector that transferred the EBIC signal to a Keithley 614 electrometer.

3.5.3 Applications to GaN

Given the usefulness of STEM-EBIC it is surprising to find little in the literature on the use of this technique for the investigation of GaN alloy devices. Perhaps this is due in part to the challenging sample preparation and formation of

electrical connections necessary for STEM-EBIC. To our knowledge the only specific application was by Bunker et al. in 2003. In their paper they reported on an application of the STEM-EBIC technique for determining pn-junction location in InGaN SQW LEDs. Using simultaneous collection of Z-contrast and EBIC images they were able to position the pn-junction with nanometer resolution. Comparing the peak in the Z-contrast image to the peak in the EBIC image the pn-junction was located 19 ± 3 nm from the center of the InGaN QW (Figure 22).

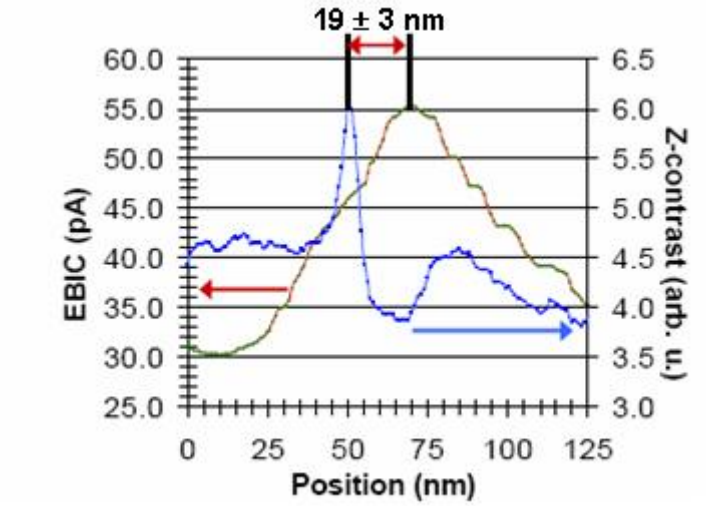


Figure 22: EBIC and Z-contrast line scans showing relative location of pn-junction. (From Bunker et al.,[70]).

The results reported by Bunker et al. invite further investigations by STEM-EBIC of GaN based devices and in particular LEDs. Their investigation was limited to SQW devices, but most commercial LEDs now incorporate MQWs. In this dissertation the STEM-EBIC technique is first extended to investigate the relation between multiple quantum wells and the pn-junction. Then STEM-EBIC is applied to the investigation of V-defects in order to obtain information regarding the electrical activity of these defects. The end result is the first known direct correlation of electrical properties to individual V-defects. The complimentary approach for investigating optical properties will now be discussed.

3.6 STEM CL

3.6.1 Introduction

TEM and STEM are the most powerful techniques for observation and identification of defects in crystals. Combined with CL these techniques are invaluable for directly correlating optical properties to individual defects. However, thin samples are required and therefore the signals generated are lower than attainable with SEM-CL analysis of bulk samples. Furthermore, the space available to put a CL collection apparatus in a high-resolution microscope such as a STEM is limited. Compromises to the collection apparatus will adversely impact the detected signal. Lastly, since the areas analyzed are small they must be selected with care or repeated observations taken in order to ensure a true representation of the sample is achieved.

3.6.2 STEM-CL systems

Faced with these challenges it is not surprising that dedicated STEM-CL systems have seen limited development. A review of some of those systems now follows. In 1978 Petroff et al. developed a CL apparatus using an elliptical mirror for light collection and two planar mirrors plus an optical fiber for transmission of the signal[62]. The collection mirror fit within an 8 mm gap between the two halves of the objective pole piece. The two planar mirrors were offset to the side and used to direct CL onto the optical fiber. Other implementations of mirror based collection systems have since been developed. In 1981 Roberts developed multiple versions of concave mirror collection schemes with at least one 7 mm mirror positioned within the pole piece gap[71]. Collection efficiencies were estimated at ~20%. The highest reported efficiency for a STEM-CL mirror based system, 45% was reported by Yamamoto[72] in 1983. This was achieved with an elliptical mirror that fit within a 12 mm pole piece gap and directed the CL signal onto a light guide. Non-ellipsoid mirror based collection systems have also been developed. Most notably Pennycook et al. in 1981 reported using a tapered, internally reflecting silver quartz

light tube[73]. The key advantage of this system was its profile allowing it to be used with pole pieces having less than a 3 mm gap. The trade-off is collection efficiency which was estimated at ~10%. In 2002 Tanabe et al. reported on development of a compact CL system that requires no modification to the microscope[74]. The authors designed a specimen holder that accommodates a flat light collecting mirror below the sample. CL signals are guided outside the microscope through a quartz optical fiber embedded within the barrel of the specimen holder. At the time of the article no estimates of collection efficiency were provided as issues with background intensities were being resolved. In 2004 Bunker reported on the design and test of a lens based implemented on a STEM in which the pole piece spacing was too narrow to allow insertion of an ellipsoid mirror (Figure 23)[75]. Preliminary results showed that detection of CL was possible and collection efficiency was estimated at ~5%.

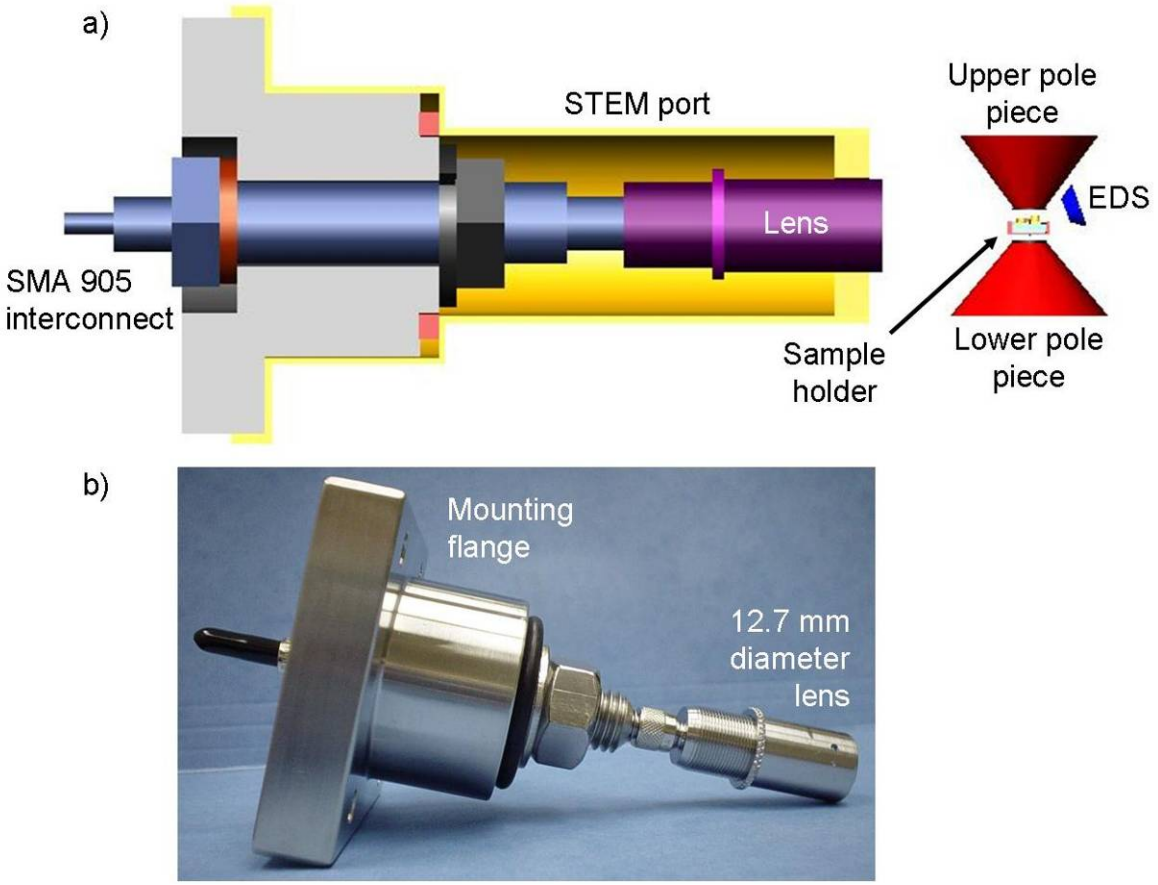


Figure 23: (a) Schematic of lens based STEM-CL system (b) Lens assembly mounted to vacuum feed through flange (From Bunker[75]).

3.6.3. Applications to GaN

While the direct correlation of defects to luminescence is difficult, several groups have studied GaN based devices with STEM-CL. Indium composition fluctuations in SQW and MQW InGaN devices were investigated by Albrecht et al[76]. Results did not show any indication of phase separation for either type of samples. In 2002, Boyall et al. used CL imaging and spectroscopy to investigate emission from a SQW InGaN device[77]. In this case both panchromatic and monochromatic imagining indicated the presence of indium fluctuations on the order of 1%. More recently in 2003, Zhang et al. reported monochromatic TEM-CL results that also supported the existence of indium fluctuations[78]. However, it has also been reported that high-energy electron beam damage can induce phase separation[49].

Threading dislocations have also been investigated most notably by Yamamoto et al[44, 79, 80]. Using plan view STEM-CL techniques they were able to associate threading dislocations with the suppression of CL emission. Their results also indicated that dislocations were not associated with yellow band emission. However, it has been proposed that TEM/STEM beam energies are high enough to cause lattice damage which can quench the CL emission of the sample. This was reported by Boyall et al. for InGaN quantum wells devices when they observed CL signal quenching after a few hundred seconds at 120 keV and 100 K[81]. Continuing with dislocations, Nakaji et al. in 2005 developed a theory to describe expected changes in the full width half max (FWHM) of dislocation images in STEM-CL[79]. They predicted that the FWHM would increase with sample thickness and decrease with increasing voltage, which was later confirmed by experiment. Lastly, Wu et al. in 1998 reported on the investigation of V-defects by planar STEM-CL. CL studies were performed on a back-side wedge polished MQW InGaN sample. CL spectra taken at 10 K and 300 K showed a long-wavelength shoulder in addition to the expected InGaN QW peak. The feature was correlated with V-defects and attributed to formation of In-rich structures either at the apex of the V-defect or along the defect side walls. As planar STEM-CL was used in this investigation it is difficult to resolve the source long-wavelength shoulder. To do so requires cross-section STEM-CL but to our knowledge, no such study is reported in the literature.

3.7 Focused ion beam

3.7.1 Introduction

A focused ion beam (FIB) can be thought of as an SEM that utilizes a focused probe of ions instead of electrons for both imaging the surface of the sample as well as physically sputtering material with high levels of precision. A FIB uses a liquid metal ion source (LMIS) to generate a beam of ions. Gallium is the most common LMIS as it has several favorable properties; namely low melting temperature, volatility and free surface energy.

To form a beam, the gallium source is heated allowing it to flow and wet a field emission needle. An electric field on the order of 10^8 V/cm is applied causing the liquid gallium to form a point source ~ 2 – 5 nm. An extraction voltage then 'pulls' gallium from the needle tip and ionizes by field evaporation yielding a Ga+ current density ~ 10^8 A/cm^2. The ions are then accelerated to a typical energy of 0.5 – 40 keV, sent down a column, focused with electrostatic lens and rastered across the surface of the sample. Typical beam currents range from 1 pA to 30 nA for beam diameters 6 – 500 nm respectively.

3.7.2 Milling and deposition

Milling or sputtering of material with a FIB is achieved by the transfer of momentum, kinetic energy, from incident ions to atoms of the sample. Sputtering is a surface phenomenon resulting in the ejection of surface and near surface atoms if the kinetic energy is greater than the surface binding energy (~2 – 20 eV)[82]. Emissions of sputtered particles follow a cosine distribution and the particles possess energy on the order of 2 – 5 eV. The number of ejected particle per incident ion is termed the yield Y.

$$Y(E) = \left(\frac{4.2x10^{14}}{E_b}\right)\left(\frac{\alpha}{N}\right)\left(\frac{dE}{dX}\right) \qquad (3\text{-}3)$$

Where E_b is surface binding energy, α is the ratio ion to atomic mass and N is substrate density. Typical values range $10^{-1} < Y < 10^2$ and when multiplied by the beam current gives the sputter rate which is commonly reported in units of μm^3/nC. An example calculation of the sputtering rate for a GaN on SiC substrate sample is provided in Appendix A.1.

FIB systems can also be configured for deposition of materials. This involves the introduction of a precursor gas used to produce site specific deposition of metals or insulators. Applications include formation of a protective 'cap' to minimize damage due to the incident beam during a milling process and mask repair for lithographic processes. An inlet needle is brought to close proximity (~100 μm) of

the sample surface. Gas molecules from the needle adsorb on to the sample in vicinity of the inlet needle. The incident ion beam then 'cracks' the molecules which over repeated cycles of adsorption and decomposition leads to build-up of material in the scanned region. As this process is balance between sputtering and deposition a precursor must have sufficient sticking probability, low evaporation rate and decompose more rapidly than sputtered away. The most commonly used deposition gases that meet this requirement are tungsten hexacarbonyl $W(CO)_6$ and platinum carbonyl $C_7H_{17}Pt$. Here it should be noted that the resulting deposition is mix of the elements found in the precursor gas and of course Ga.

3.7.3 Artifacts

In addition to sputtering and deposition, ion-solid interactions produce unintended artifacts. Let us consider the types of energy loss experienced by an incident ion. Nuclear energy loss occurs between the nuclei of ion and substrate atom. The interaction causes the lattice atom to recoil from its equilibrium lattice position and leads to the formation of an amorphous layer. This is an elastic event as the energy lost by the ion is transferred to the atom. However, since sputtering occurs in energy ranges dominated by nuclear energy losses, formation of an amorphous layer is expected with FIB milled samples. Alternatively, electronic energy loss is an inelastic process whereby electrons of the incident ion interact with electrons of atoms in the sample. However, this effect does not begin to dominate until ion energies pass 100 keV, which is well beyond FIB energy ranges.

Implantation of gallium is another unintended FIB artifact. This is a function of the beam current, dwell time, scan area and incidence angle. In addition, low index crystals have open channels which ions can travel through. To characterize implantation the average depth ions come to rest is called the projected range, R_p. Over that distance the implant concentration is considered to be uniform. Extending beyond R_p the concentration follows a half Gaussian to the depth of $2R_p$. As gallium is a metal, implantation can affect the electrical properties of samples by forming a short or in some cases a rectifying junction.

Lastly, with any sputtering process redeposition is a possibility. It is a function of the kinetic energy of atoms leaving the surface, sticking coefficient of the sample material, geometry of feature milled and sputtering yield. In addition, the low vacuum environment of a FIB system produces few scattering events for sputtered particles. A line of sight process, redeposition is supported by the low vacuum environment. It is not surprising that redeposition increases noticeably with sputtering yield and beam current. Redeposition can be reduced by tilting the sample or the use of reactive gasses such as Cl_2, I_2 or XeF_2. The gas reacts with the sputtered material volatizing it for removal by the vacuum system. However, there are both operator and instrument safety concerns with the use of reactive gases.

4. Sample Preparation Methods and Results

4.1 Introduction

Sample preparation is a key step in order to do successful analytical work. The old adage that you get out what you put in is especially true when applied to sample preparation for electron microscopy and in particular high-resolution electron microscopy. To emphasize this point TEM classes devote several lectures to sample prep methods[83]. The particular challenge faced with preparing (S)TEM samples is one of size. In general these samples are small sections taken from the bulk material. If one is not careful, damage induced by sample prep can distort or mask the specific material properties being investigated. The end goal of any (S)TEM prep is to produce a sample that accurately represents the bulk properties of the material investigated. Thus, characterization of the preparation process is necessary to give confidence in the subsequent investigation.

Preparation of (S)TEM samples typically require several steps and the sample becomes more fragile with each subsequent step as its thickness is decreased. Hence, the risk of damage increases with the time spent per sample. In addition, some analysis techniques impose additional preparation requirements. EBIC requires the sample be functional with an active positive and negative contact. Consequently, there is a need for rapid sample prep methods that accurately represent the bulk material properties. It is to that end that the work in this chapter was undertaken. Two novel prep methods and an extension to an existing method were investigated. Based on results from each method one was selected for use in prep of MQW blue and green LEDs for STEM-EBIC/CL analysis.

4.2 Sample characterization

4.2.1 Current-voltage characterization

Both sample preparation and electron beam interaction may affect device performance. Current-voltage (I-V) curves can be used to qualify either damage to or repair of functional samples. I-V curves are fairly easy and fast to obtain and can be applied to in-situ characterization. The approach taken here is to use I-V curves

to gauge the 'quality' of prepped samples for STEM-EBIC and CL analysis. To this end an understanding of the I-V characteristics for an LED is required.

Current-voltage characteristics of a pn-junction are described by the Shockley equation[6, 84, 85].

$$I = qA\left[\sqrt{\frac{D_p}{\tau_p}}\frac{n_i^2}{N_D} + \sqrt{\frac{D_n}{\tau_n}}\frac{n_i^2}{\tau_n}\right]\left[\exp\left(\frac{qV}{kT}\right) - 1\right] \tag{4-1}$$

Where A is diode area, $D_{n,p}$ is diffusion constant, $\tau_{n,p}$ is minority carrier lifetime, $N_{A,D}$ doping concentration, and n_i intrinsic concentration. Rewriting equation (4-1) with the term preceding the exponential function defined as the saturation current (I_s) and for typical forward bias conditions where V > kT/q yields the following.

$$I = I_S \exp\left(\frac{qV}{kT}\right) \tag{4-2}$$

Equation (4-2) gives the theoretical I-V characteristic of a pn-junction. In order to describe experimentally measured results a fitting parameter termed the ideality factor (η) is included and yields the diode equation.

$$I = I_S \exp\left(\frac{qV}{\eta kT}\right) \tag{4-3}$$

For an ideal diode η=1 and current is dominated by minority carrier recombination in neutral (bulk) regions of the sample. However, recombination does occur in other ways and these recombinations produce ideality factors other than unity. For the case η=2 current is dominated by recombination in the space charge region. More will be said about ideality factors a later.

To interpret changes to the sample an equivalent circuit was defined. In addition to the pn-junction the circuit needs to account for parasitic resistances either present in the diode structure or introduced by sample prep and any subsequent electron beam damage. Figure 24 shows the equivalent LED circuit.

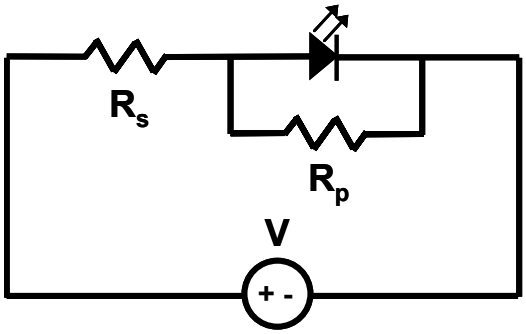


Figure 24: Equivalent LED circuit with parasitic resistances.

Regarding the parasitic resistances, a series resistance (R_s) is included to account for contact and bulk resistance. A parallel resistance, often termed shunt resistance, is included to account for any current bypass mechanisms around the pn-junction. Potential shunt paths can be caused by damaged regions of the pn-junction or surface imperfections.

The diode equation (4-3) needs to be modified to take into account resistances R_S and R_P. First, the voltage across the diode must be reduced by the series resistance $V \rightarrow V\text{-}IR_S$. Next, the shunt current around the diode needs to be included and is simply the voltage across R_P divided by the R_P. The current-voltage relation for a pn-junction can then be rewritten and is given by equation (4-4).

$$I = I_S \exp\left[\frac{q(V - IR_S)}{\eta kT}\right] + \frac{V - IR_S}{R_P} \qquad (4\text{-}4)$$

From this equation it is now possible to consider how changes to R_S and R_P affect current-voltage characteristics. Two cases observed with sample prep are considered; an increase to R_S and a decrease to R_P. First, consider a device with an increased series resistance. The result is less voltage drop across the diode and thus less overall current flow. This effect is reflected in Figure 25 as tilting of the I-V curve away from the zero-R_s case. The other condition is reduced parallel resistance, which enables current to flow around the rectifying junction of the diode. The effect of reduced R_P is observed in Figure 25, as a low-voltage shoulder to the I-V curve. Because R_P is not in the exponential term of equation (4-4) its effect on current flow is swamped out at higher voltages.

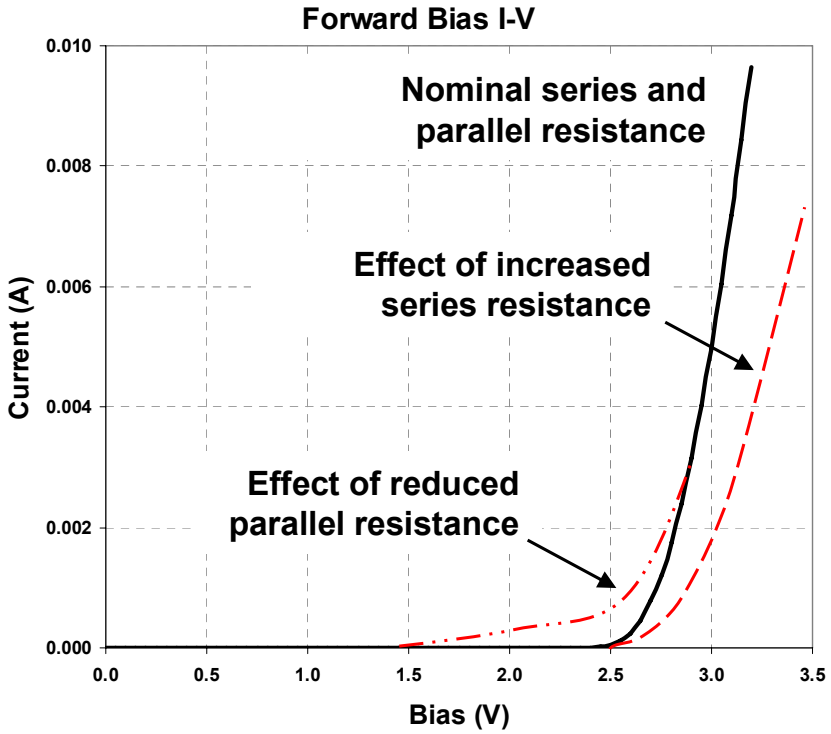


Figure 25: Effect of series and parallel resistance on pn-junction I-V curves.

At this point a discussion on the ideality factor is in order. Plotting the data in semi log as shown in Figure 26 reveals the ideality factors, n[86]. From this figure we can observe three distinct regions which are characterized by the dominant current mechanism in that region[87]. In region 1, current flow is dominated by leakage around the pn-junction. Referring to the equivalent circuit (Figure 24) this would be represented by current flowing through R_P. In region 2, the injection of carriers becomes sufficiently high that the charge transfer through the pn-junction dominates. This is also the region of interest for extracting the ideality factor as it is an indication of deviation from classical drift diffusion and generation-recombination models[87]. From Figure 26, the I-V curve for a blue LED indicates an ideality factor of ≈2.8. While this is higher than the expected values of 1.0 to 2.0, ideality factors ranging from 2.0 to 7.0 have been reported for GaN based pn-junctions[88-90].

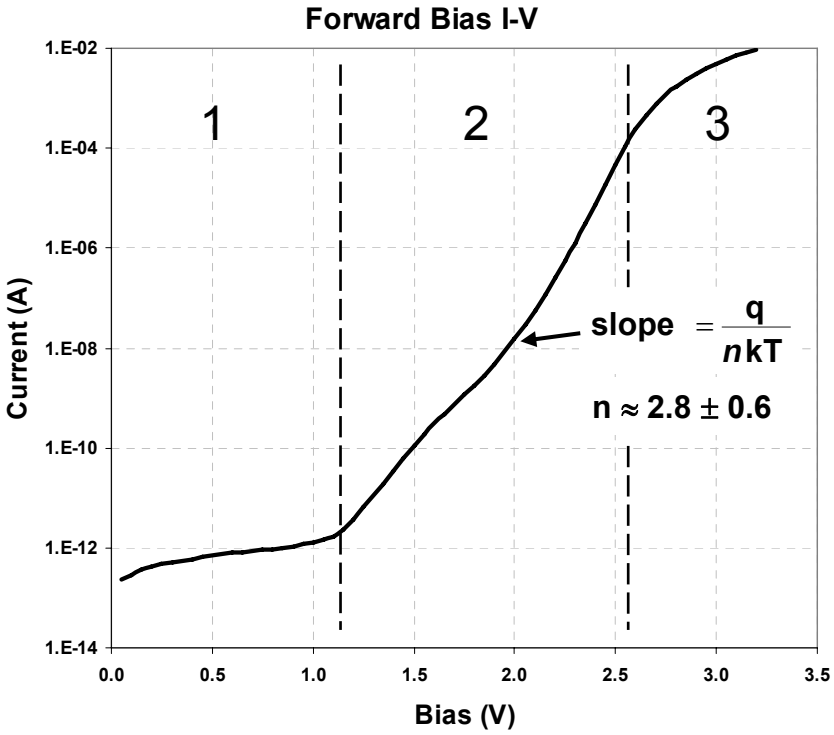


Figure 26: Semi log plot of I-V data for blue MQW InGaN LED.

The source of high ideality factors in GaN based LEDs is still unknown and the literature remains divided. Large ideality factors have been attributed to deep-level assisted tunneling by Dmitriev[91], Casey et al.[92], Perlin et al.[93]. Alternatively, Shah et al.[94] proposed an explanation based on the influence of additional rectifying heterojunctions and metal-semiconductor junctions of the diode. For work in this research, changes to the ideality factor due to sample prep or beam damage are of interest and the ideality factor will be used qualitatively to gauge changes due to FIB milling or STEM beam damage.

Returning to Figure 26, region 3 shows the I-V curve roll-off as the voltage increases. This is due to resistance from the bulk n- and p-regions as well as contact resistance. The combined resistance effect limiting current flow in region 3 is denoted as R_S in our discussion of the equivalent circuit.

4.2.2 In situ current-voltage characterization

It was recognized that close tracking of sample preparation would help characterize damage formation and identify potential problems. This lead to the development of a novel in situ focused ion beam characterization method. The Hitachi 2100 FIB was configured with a TEM stage as can be seen in Figure 27. The stage is designed to take a (S)TEM holder so that samples can go directly from the FIB to the (S)TEM for analysis. A STEM holder, configured for EBIC analysis, is shown is shown in Figure 28. This holder fit the TEM stage on the FIB, and along with automated test electronics enabled in situ I-V characterization.

The test cart consisted of custom developed LabView[95] software to control a Keithely 428 current amplifier. The current amplifier was capable of both applying a voltage and measuring current. The current reading at each voltage step was passed from the Keithley 428 through a 16-bit A/D converter and recorded by the LabView program. A complete description of the automated test cart and LabView program are provided in Appendix A.2. This configuration was also used for all I-V characterizations discussed in this work although; the sample holder was different as required by the particular experiment.

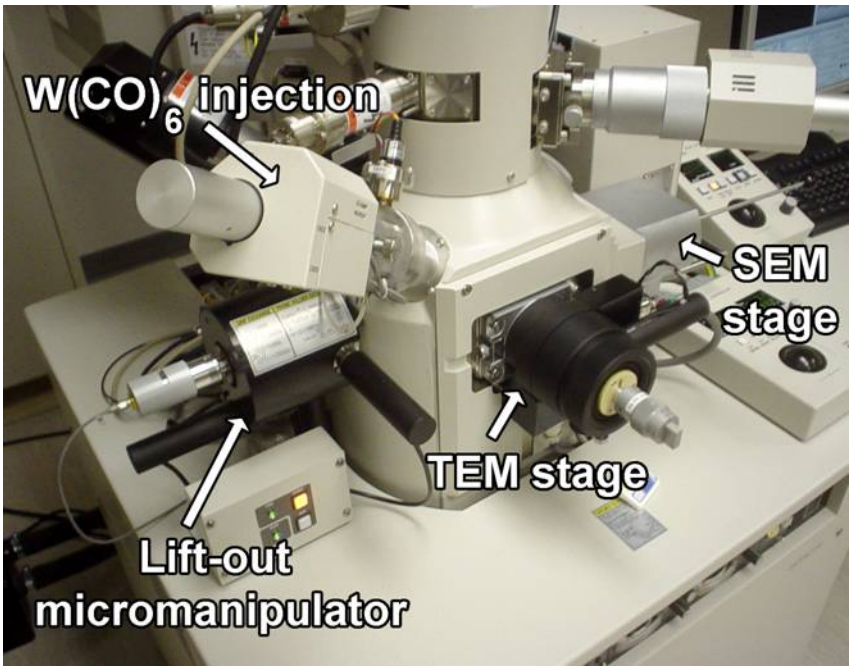


Figure 27: Detailed view of Hitachi 2100 FIB.



Figure 28: STEM-EBIC holder with sample.

4.2.3 Electroluminescence characterization

Electroluminescence is the emission of photons due to an applied electrical field and the operational mode for LEDs. Spectroscopy is the investigation of the spectral distribution of light. This yields information on the energies of different transitions in the sample. A number of transitions are possible that include but are not limited to; band-to-band, sub-band gap, excitonic and defect assisted. As discussed in the section 4.2.1, it is expected that sample prep will induce some amount of damage to the sample, which may introduce new or modify existing energy transitions. As spectroscopy yields information on different energy

transitions EL characterization will be used to monitor changes to bulk optical properties due to sample prep.

To implement EL characterization the STEM-CL lens system on the Hitachi HD 2000 was used. A sample was placed in the STEM-EBIC holder, loaded into the microscope and connected to an external source. A voltage was applied to produce electroluminescence and the spectral response measured. Light emitted from the sample was collected by the side mounted lens system developed by Bunker[75] and shown previously in Figure 23. This method was used for bulk characterization to qualify the effect of sample prep on optical properties of the sample. It is not a site specific method. EL leads to light emission from the entire sample including both damaged and undamaged regions. Spectral measurement from specific regions will be attempted with STEM-CL.

4.3 Lift-out prep method

4.3.1 Motivation

Sample preparation for STEM-EBIC can be time consuming, difficult and destroys most of the device. Ideally multiple samples from different locations are necessary to get a more complete characterization of a device. However, with existing sample prep methods, this is not possible. The lift-out method for (S)TEM sample prep is an established method, that has yet to be applied to the preparation of STEM-EBIC samples. The main barrier is the need to maintain contacts to both the cathode and anode sides of the device. In this section a novel approach for preparing STEM-EBIC samples using the lift-out method will be introduced. If the potential of this method can be realized it would greatly reduce sample handling while permitting site specific sample selection of multiple samples and rapid prep times compared to standard methods. As may be expected there are challenges to implementing this novel approach which will now be discussed.

4.3.2 Concept

To properly frame the obstacles faced preparing a STEM-EBIC lift-out sample an outline of the overall approach is useful. The basic concept can be seen in Figure 29 shown below.

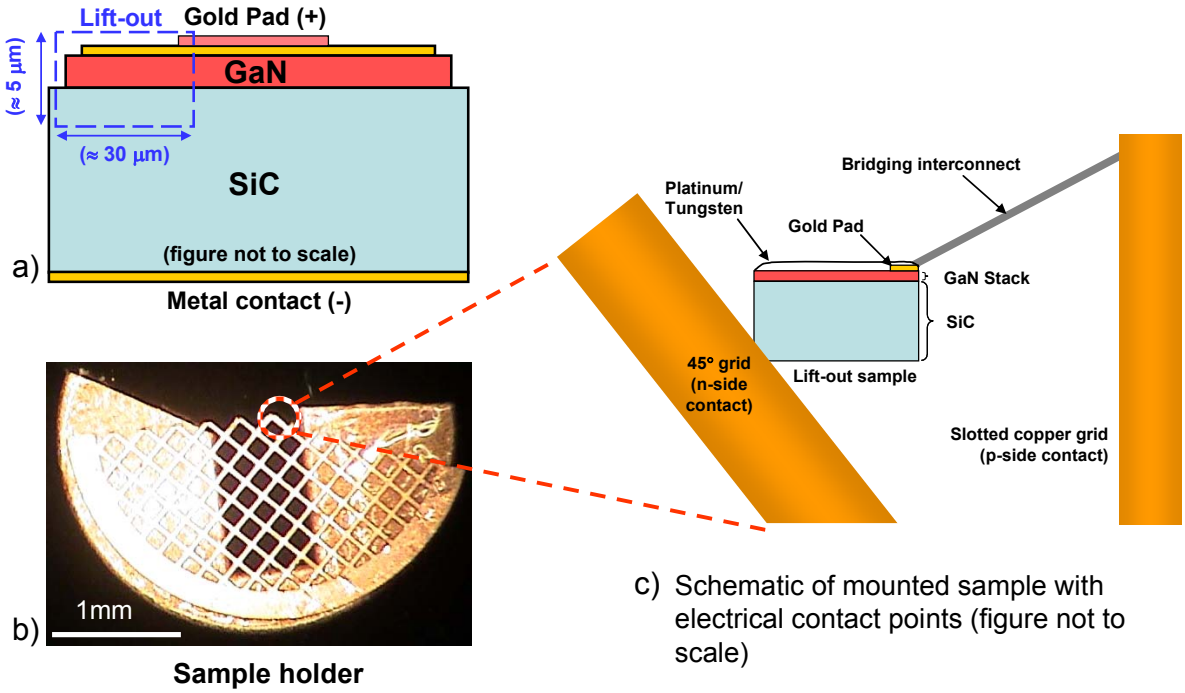


Figure 29: STEM-EBIC lift-out sample prep.

Consider Figure 29(a) which is a simplified cross-section of an LED. The idea is to use FIB based techniques to lift-out a thin section of the device. The lifted section would include the active area of interest around the pn-junction as well as part of the top contact and part of the SiC substrate. The process of removing a section of material breaks the positive (anode) and negative (cathode) contacts on the p- and n-sides respectively. As it is necessary to have a functional device in order to do EBIC, we will need to re-form those connections.

The first step is to provide a holder that the sample can be attached to, Figure 29(b). Not only does this provide a place to land the sample, but it also provides electrical contacts for extracting an EBIC signal. The two grids shown (slotted and cross hatched) in Figure 29(b) are insulted from each one another with M-bond 610

thermal epoxy. Referring now to Figure 29(c) if the SiC side of the lift-out sample is attached to the cross hatched grid it would be designate as the cathode (n-) contact. Likewise, if the gold pad side of the sample is attached to the slotted grid it would be designated as the anode (p-) contact. However, formation of neither contact will be straight forward. The p-side contact requires bridging an air gap between the sample and slotted grid and in both cases (n- and p-side) formation of an ohmic contact is a concern. The p-side contact may be less of an issue from an electrical stand point because the plan is to use the existing p-side contact (gold pad) of the device as the attach point for the bridging interconnect to the lift-out section. Thus, if the bridging interconnect can be formed it is expected to be an ohmic contact. On the other hand formation of an n-side ohmic contact is expected to be quite challenging. A discussion of ohmic contacts follows.

4.3.3 Ohmic contacts

Contacts on semiconductors are necessary to connect the device to the outside world. It is imperative that the contacts produce no adverse change to the device current-voltage characteristics and a minimal voltage drop. This is achieved through low-resistance ohmic contacts. An ideal ohmic contact is one where the current varies linearly with voltage and there are no barriers to current flow in either the positive or negative direction. Frequently this is not the case and trade-offs must be considered. Often it is acceptable to have ohmic behavior in one current direction but not the other as observed with a rectifying contact.

Formation of an ohmic contact occurs when the work functions (Φ) for the semiconductor and contact are about the same. However, work functions vary with doping and usually it is not possible to find the right combination. Typically there is mismatch between the work functions and depending on the semiconductor doping the resulting contact could be either ohmic or Schottky (rectifying). To understand the conditions that lead to formation of a particular contact it is helpful to look at energy band diagrams.

The energy band diagram for a metal work and n-type semiconductor are shown in Figure 30. The work function is the energy difference between the vacuum level and the Fermi level. The vacuum level defines the energy where the electron is free from that particular material. The electron affinity, denoted as X_n, is the energy distance from the bottom of the conduction band E_c to the vacuum level. It is not however, the minimum energy required to remove an electron from the semiconductor. Thermal equilibrium allows only a certain fraction of electrons in the conduction band at a given temperature. If an electron is removed from the conduction band then thermal equilibrium can be maintained only if an electron from the valence band is excited into the conduction band. This involves thermal excitation by absorbing heat from the environment thus resulting in more energy than solely X_n. Suffice it to say that in both the metal and semiconductor the work function represents the energy required to remove and electron from that material.

The energy band diagram for the case when the metal work function is less than the n-type semiconductor ($\Phi_m<\Phi_n$) is shown Figure 30(a). When the two solids are brought into contact, Figure 30(b), the requirement that the Fermi level be aligned is brought about more energetic electrons from the metal tunneling into the conduction band of the semiconductor in search of lower empty energy levels. The increase of electrons in the semiconductor generates an accumulation region near the metal-semiconductor junction. This condition is depicted by the energy bands bending down. The conduction electrons on either side of the junction have about the same energy and can easily move across the junction in either direction yielding an ohmic contact.

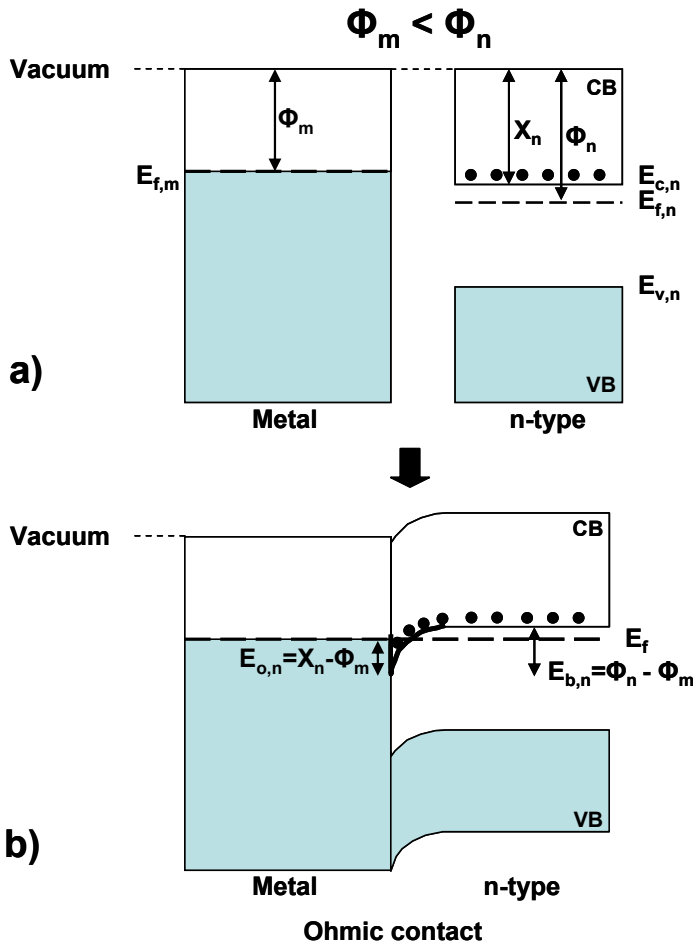


Figure 30: Metal to n-type semiconductor ohmic contact.

The energy band diagram for the alternate condition when the metal work function is greater than the n-type semiconductor ($\Phi_m > \Phi_n$) is shown Figure 31(a). When the two solids are brought into contact, Figure 31(b), the requirement that the Fermi level be aligned is brought about by more energetic electrons from the semiconductor tunneling into the metal in search of lower empty energy levels. Depletion of electrons in the semiconductor generates a space charge called the built-in potential denoted as $E_{b,n}$. The space charge region presents a potential energy barrier and for electrons moving from the metal to the semiconductor is called the Schottky barrier ($E_{o,n}$).

The rectifying nature of a Schottky contact is possible because the built-in

potential $E_{b,n}$ can be altered by biasing. Forward biasing reduces the potential barrier and allows electrons to flow from the semiconductor to the metal. On the other hand the Schottky barrier $E_{o,n}$ remains almost unchanged regardless of biasing polarity and presents a barrier electrons cannot easily overcome.

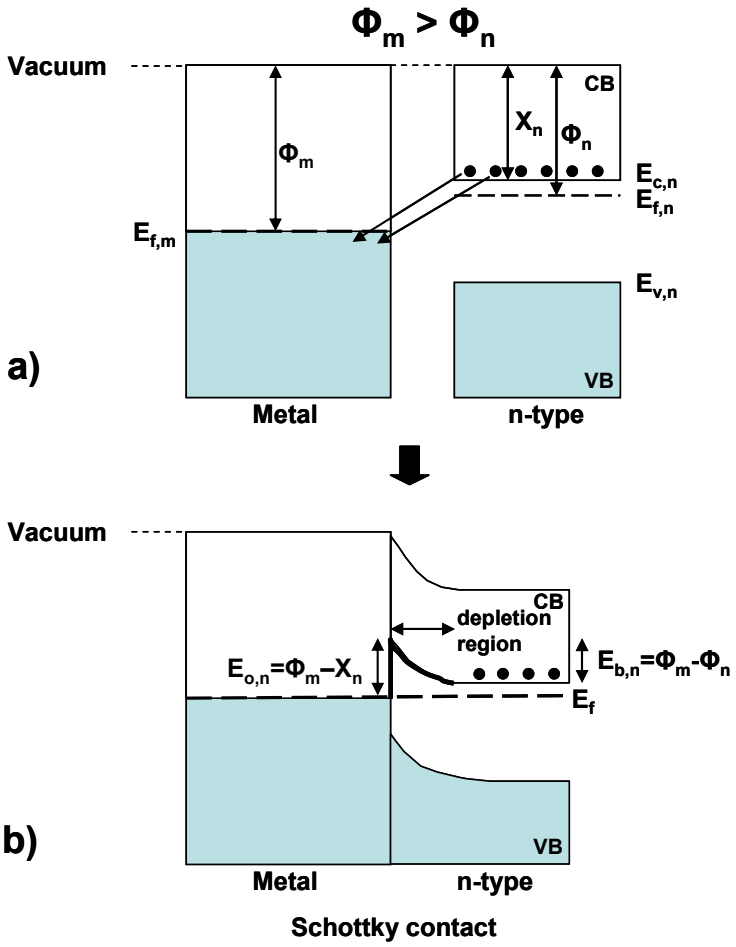


Figure 31: Metal to n-type semiconductor Schottky contact.

There are two primary mechanisms that govern the current flow across a metal-semiconductor junction. Thermionic emission refers to electrons that have gained sufficient thermal energy to surmount the potential barrier. This mechanism is typical for moderately doped semiconductors $N_d \approx 10^{17}$ cm^{-3} where the depletion region is too wide to tunnel through[8]. On the other hand if the depletion region is narrow direct electron tunneling is allowed in both directions. Narrowing of the

depletion region is achieved by heavily doping, $N_d \approx 10^{18}$ cm^{-3} the semiconductor[8].

The formation of a metal to p-type semiconductor contact is similar to that for the n-type case and for completeness is presented in Appendix A.3. However, as discussed at the end of section 4.3.2 the plan is to use the existing p-type contact of the device. While it is recognized that formation of an ohmic contact to the n-type SiC is a challenge it was decided to first pursue formation of a bridging interconnect to the p-side contact.

4.3.4 Bridging interconnect

4.3.4.1 Introduction

This section presents a review of different attempts made to form the p-side bridging interconnect shown schematically in Figure 29(c). The reader will need to recall that the process of removing a lift-out section from the device broke the electrical connections to the sample. Reforming the p-side connection requires spanning an air gap between the sample and sample grid. Given the fragile nature of the lift-out sample conventional methods of forming electrical connections across and air gap will not work. For example the amount of force used in a wire bonder is sufficient to dislodge the lift-out section from the TEM grid. In light of that the approach taken here is to use FIB based techniques and micro-manipulation to form the bridging interconnect. There is an additional benefit to following this approach and that is all sample preparation is done in the FIB with the net result being a sample ready for analysis. In other words handling of the sample is reduced.

Lastly, three different approaches to forming the bridging interconnect were considered. The decision to include each approach in this document is two fold. First, it shows the evolution from a concept to a final transferable method. Second, it highlights the capability of FIB based techniques for sample prep. In each case, the discussion picks up with the lift-out sample already removed from the device and attached to the cross hatched 45° grid as shown in Figure 32. As a reminder the cross hatched grid serves as the n-side (cathode) contact.

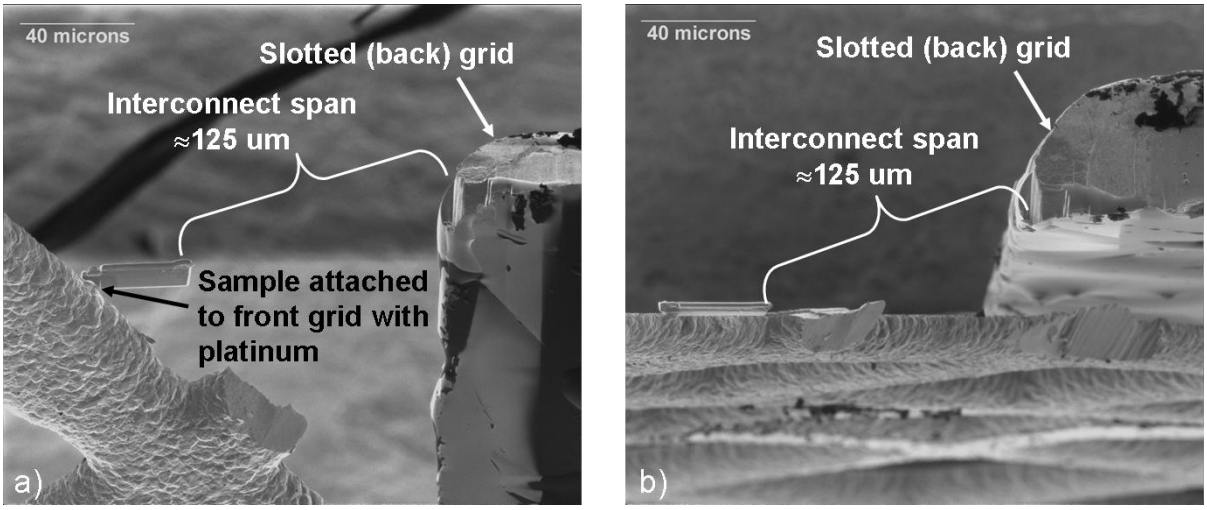


Figure 32: Lift-out sample attached to cross hatched grid.

4.3.4.2 Tungsten wire interconnect

The first attempt to form a bridging interconnect was with tungsten wire. Figure 33(a) shows the wire already thinned down and the lift-out probe attached. The probe was placed at midpoint to allow wire to 'pivot' during sample attach. In addition we can see a notched section termed the release bridge that sets the length of the wire interconnect as well as holds it in place. In Figure 33(b) the relief bridge has been cut through and the wire interconnect is free of the main section.

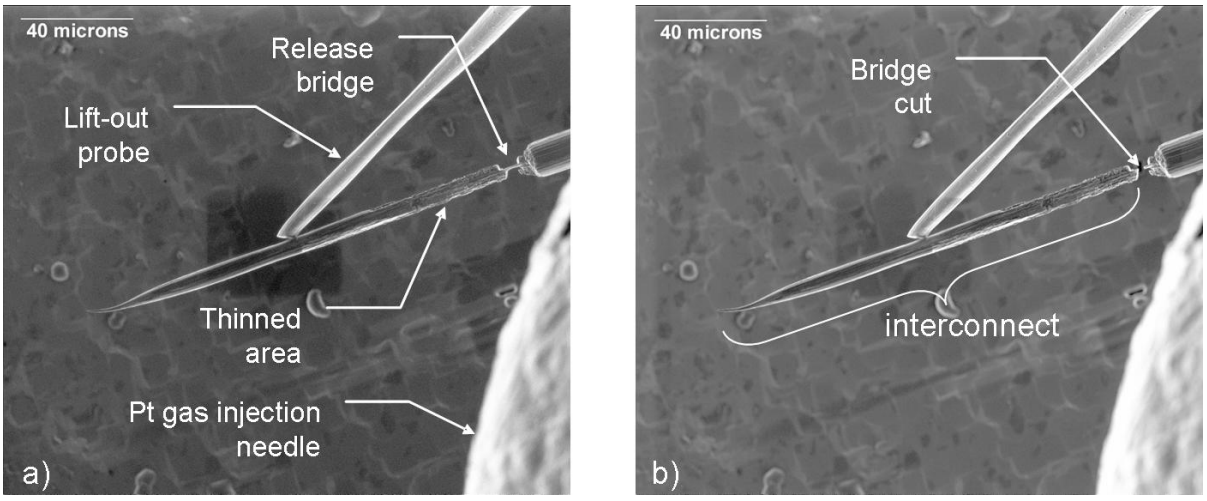


Figure 33: Preparation of tungsten needle for use as interconnect.

In Figure 34(a) the interconnect is shown attached to the lift-out probe and ready for transfer to the sample. In Figure 34(b) detail of the lift-out section can be seen. The bottom of the lift-out section includes part of the n-SiC substrate and is attached to the cross hatched grid with FIB deposited platinum. Also observable is the targeted attach point for the interconnect to the sample.

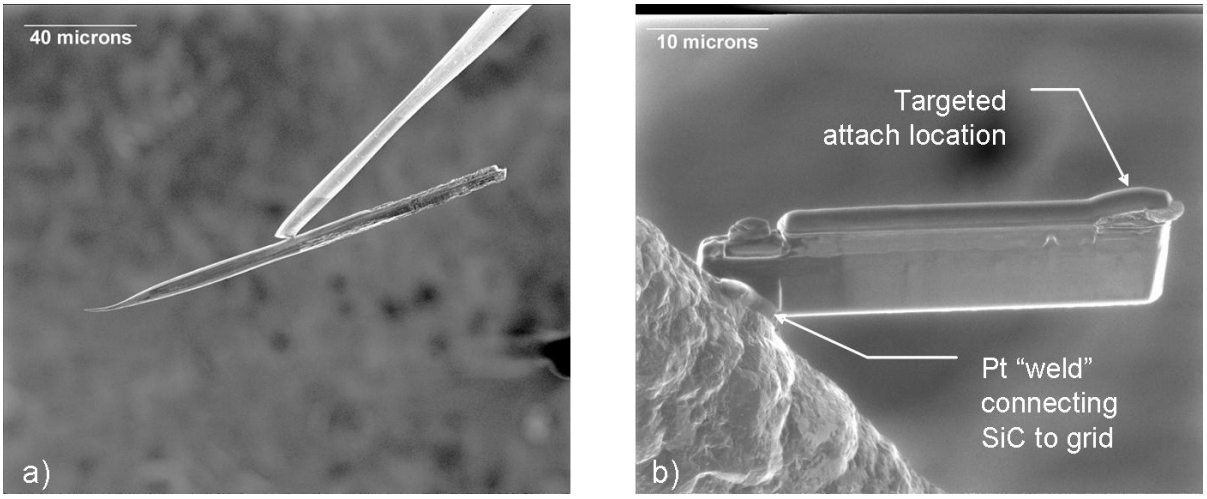


Figure 34: a) Tungsten wire interconnect. b) Attach points on lift-out sample.

In Figure 35(a) the sample holder has been brought into position and contact made to interconnect at top corner of slotted grid. FIB deposition of platinum forms electrical and mechanical contact of interconnect to slotted grid. Figure 35(b) shows the interconnect holding in place after disconnection from lift-out probe.

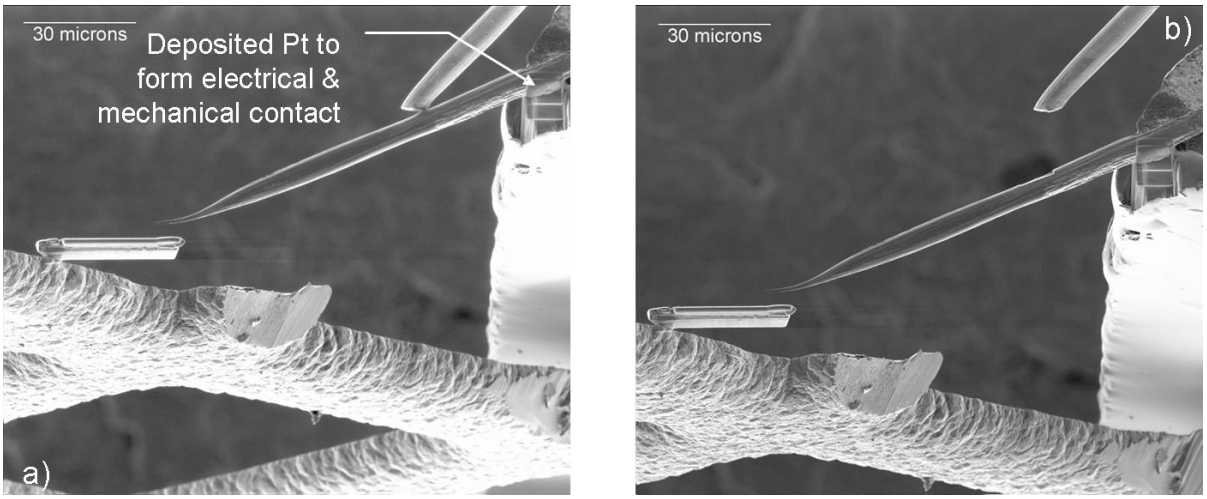


Figure 35: Placement and connection of tungsten wire interconnect to slotted grid.

At this point in the process it was recognized that the wire interconnect was too rigid. Therefore, notches were added as shown in Figure 36a) to increase flexibility prior to attach to the sample Figure 35(b) shows that proximity to the sample after initial placement was good, but the gap to the sample still needs to be closed. The lift-out probe was brought back in and used for maneuvering interconnect tip to the sample. Proper placement of the interconnect required the lift-out probe be attached to the tip of the interconnect with FIB deposited platinum. The sample stage was then maneuvered to bring the sample into contact with the wire and FIB deposited platinum formed the electrical and mechanical contact, Figure 36(b).

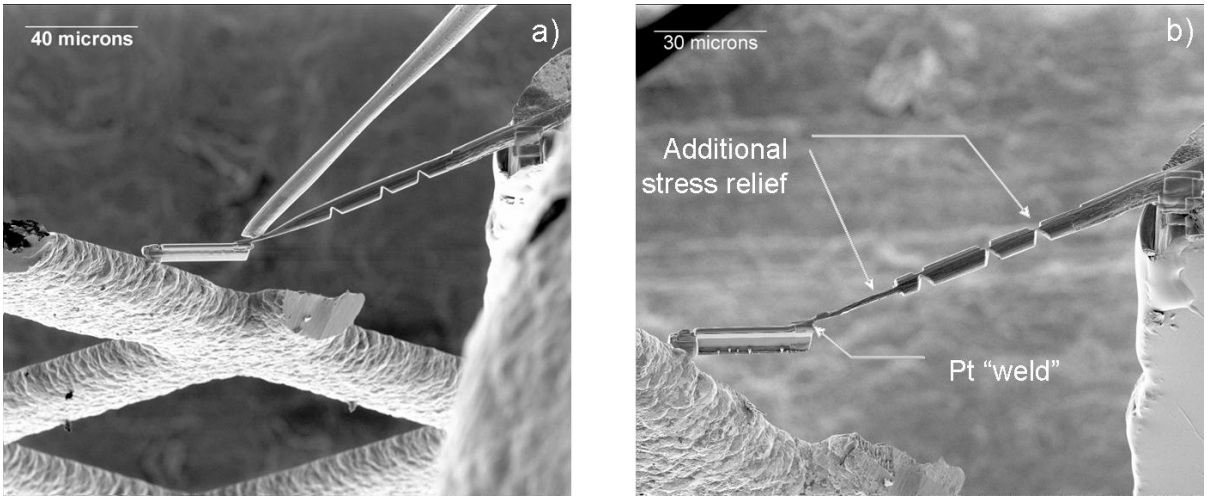


Figure 36: a) Lift-out probe holding interconnect to sample. b) Completed interconnect with additional stress relief.

With the mechanical aspects of forming the interconnect now complete we moved on to cleaning the surface of damage or potential shorts from previous steps. Figure 37(a) shows the cleaned sidewalls of the sample as well as a region near the cross hatched grid that will be cut back to remove any shorting potential. Some channeling artifacts can also be seen along the bottom edge of the sample, but these are away from the area of interest. Figure 37(b) shows the cleaned sample ready for FIB placement of electron transparent window.

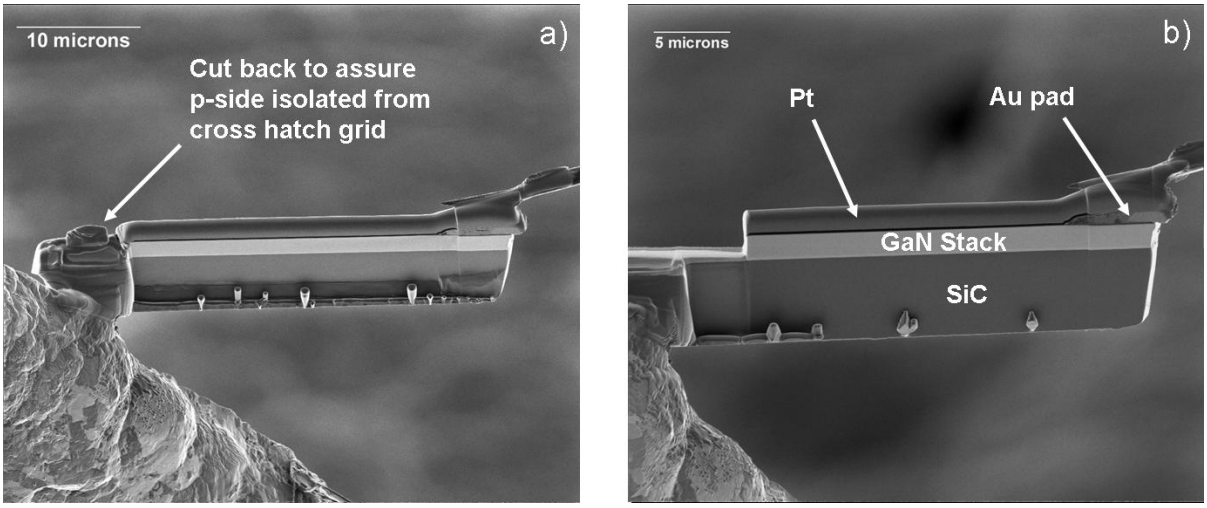


Figure 37: a) Cleaned lift-off sample showing completed contacts. b) Sample ready for formation of electron transparent section.

With completion of the electron transparent window, the sample was removed from the FIB. However, even with several stress reliefs added the interconnect was still too rigid and could not flex with the sample holder. Consequently post-FIB handling broke the interconnect free of the sample. Rather than a rigid wire type of interconnect a thinner, more flexible interconnect was required.

4.3.4.3 Copper micro-trace interconnect

A search for commercially available small gauge wire did not yield any viable options. The alternative solution was to extract Damascene micro-traces from a test wafer (Figure 38). Copper trace widths (0.2 – 0.6 μm) in the test wafer are on the size order needed for use as an interconnect and if extracted could be cut to length.

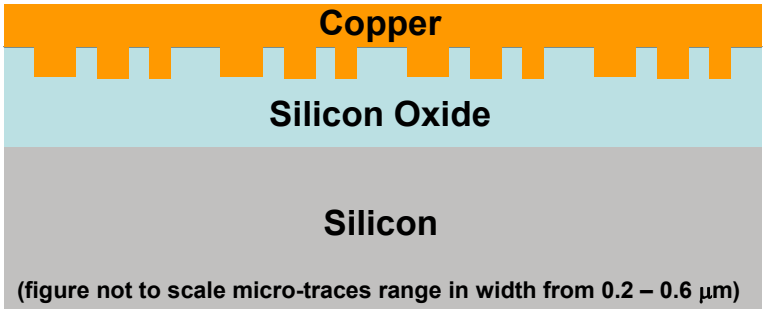


Figure 38: Cross-section schematic of Damascene micro-trace wafer.

The first step to extracting the traces was to remove the top layer of copper. A 0.5 μm diamond pad was used to polish to the top of copper trenches followed by a cleaning polish with 0.05 μm colloidal silica. Figure 39(a) shows the partially polished wafer with exposed traces. The polished wafer was broken into smaller sections and epoxy strips added to reduce potential tangling. The wafer was placed in a 7:1 water-HF buffered etch for 5 minutes to remove oxide from under the traces. Finally, the wafer was rinsed clean and dried before receiving a sputter coat (≈ 0.1 – 0.2 μm) of platinum to provide extra support to the traces. An optical image of the processed wafer is shown in Figure 39(b).

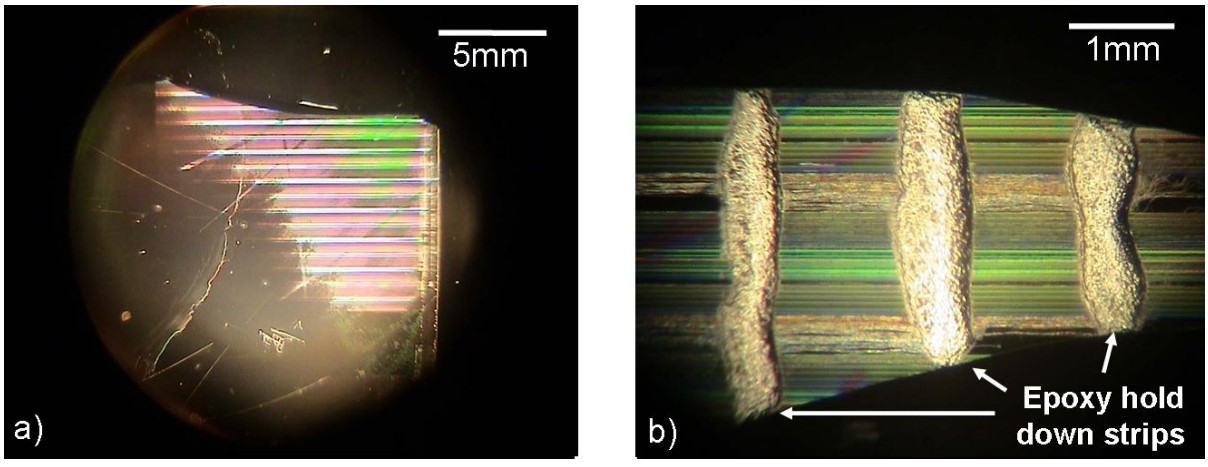


Figure 39: a) Planar view of partially polished wafer. b) Processed wafer ready for trace extraction.

The prepared wafer and lift-out sample, already mounted to the sample holder, were loaded into the FIB. Figure 40(a) shows that for the most part the epoxy hold down strips prevented significant tangling among undercut traces. The region between epoxy strips is the area available for selection of a suitable trace. It can be seen that some traces appear to be free from the surface as well as the hold down strips. At first these were considered ideal removal targets. However, free standing traces tended to tangle and were narrow as well which combined made them difficult to remove. It was therefore decided to target the widest trace possible in as open an area as possible. An example of just such a trace is shown in Figure 40(b).

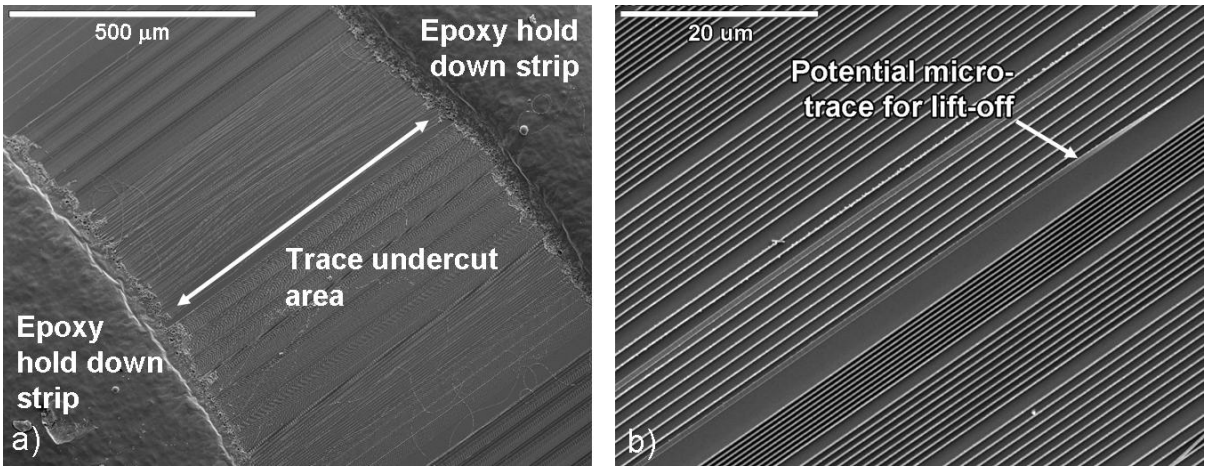


Figure 40: a) Area with undercut micro-traces. b) Targeted micro-trace for lift-off.

The trace removal process begins by placing fiducial cuts to set the trace length. Next the lift-out probe is brought in and attached to the trace with FIB deposited platinum at one end. The trace is cut at that end and the stage lowered to begin removal as seen in Figure 41(a). Lowering of the stage is continued and the removed portion of the trace approaches the end cut until eventually the trace is free of the wafer. Figure 41(b) shows the extracted trace and gives a good indication of its flexibility.

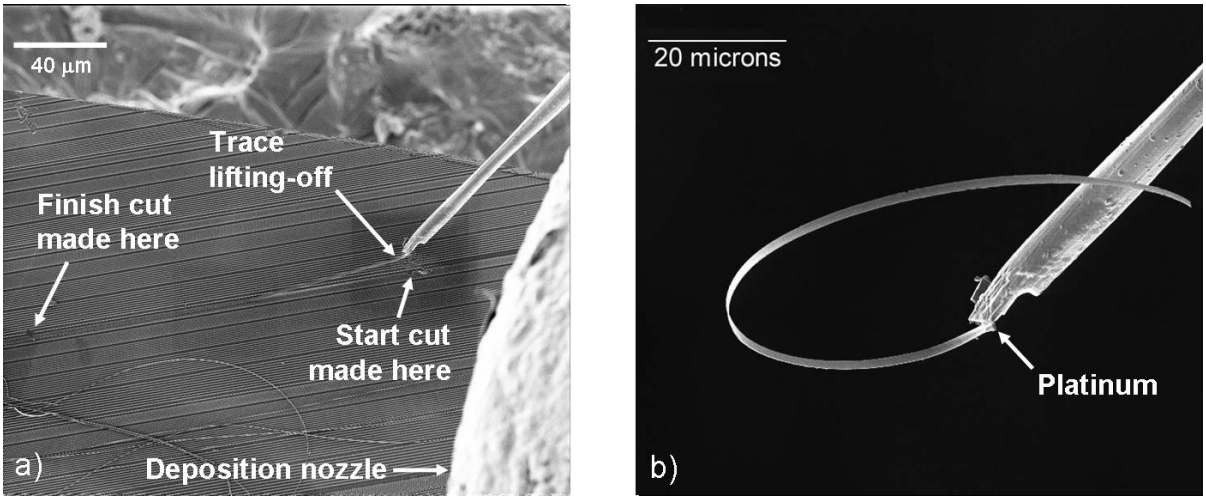


Figure 41: a) Initiation of trace removal. b) Extracted trace.

Figure 42(a) shows the extracted trace after transfer and attach to the slotted grid with FIB deposited platinum. As a reminder the slotted grid serves as the p-side (anode) contact. To complete the p-side contact the micro-trace needs to be extended to the sample. Maneuvering of the trace was done with the lift-out probe which held the trace by surface contact, Figure 42(b), FIB deposited platinum was not necessary.

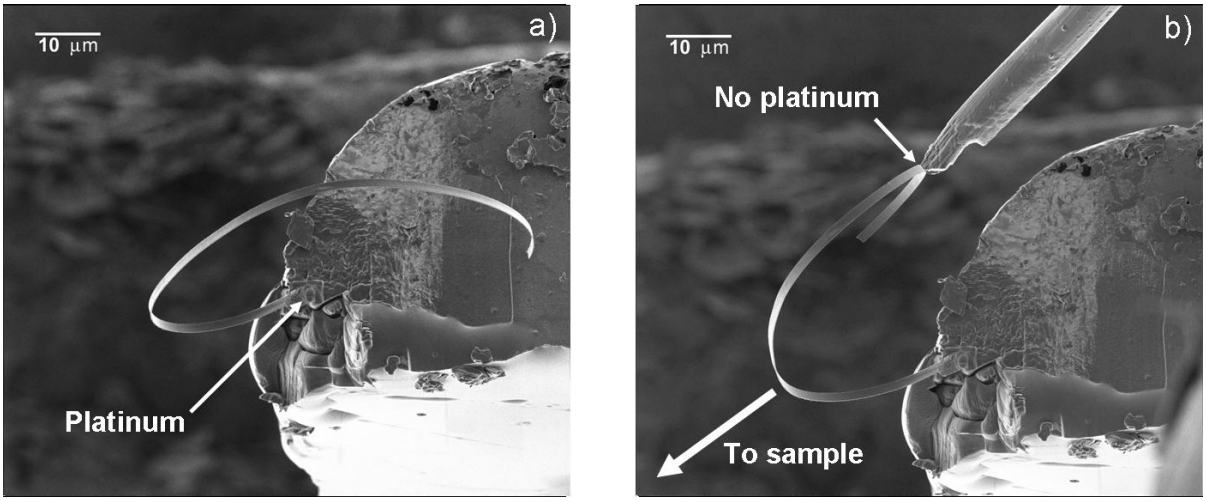


Figure 42: a) Grid side attach of micro-trace. b) Micro-trace held to lift-out probe by surface contact.

Careful maneuvering of the stage allowed the micro-trace to effectively slide across the tip of the lift-out probe. Figure 43(a) shows the micro-trace almost spanned across to the sample and the lift-out needle nearly to the end of the micro-trace. The sample was maneuvered into position to contact the micro-trace and FIB deposited platinum formed the mechanical and electrical contact. Figure 43(b) shows the completed interconnect with excess micro-trace cut free.

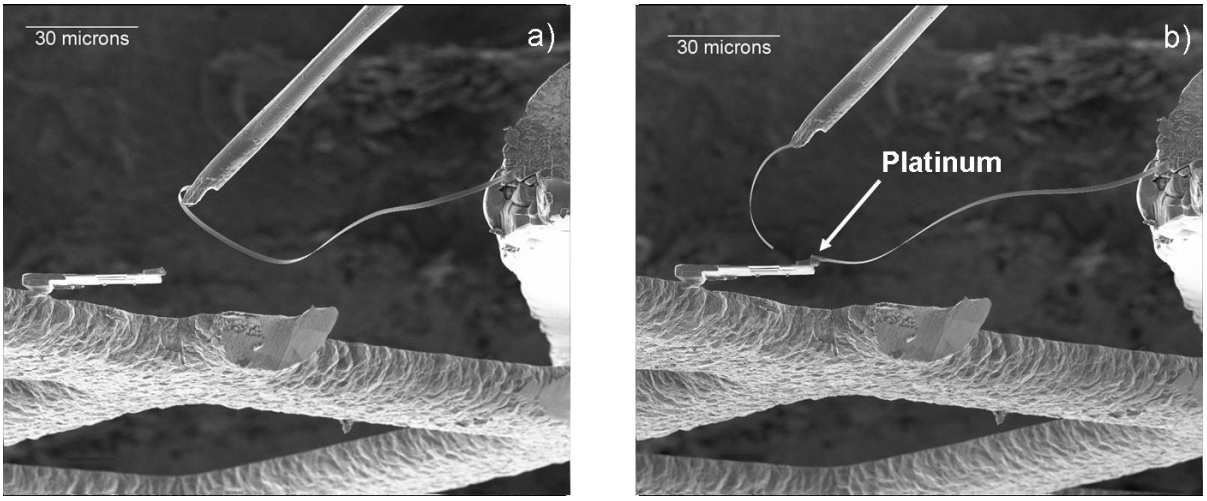


Figure 43: a) Extending micro-trace to sample. b) Micro-trace interconnect.

Using the micro-trace method it was possible to form a flexible, long range interconnect that bridged an approximately 125 µm wide gap. Furthermore, the resulting interconnect was robust enough to survive post FIB handling. However, it was recognized that wafers with micro-traces are not readily available. Also, use of Damascene micro-traces required prep work in order to extract those traces. Finally, a survey of the prepared wafer is necessary to identify suitable traces. In light of these drawbacks a possible improvement was investigated.

4.3.4.4 Thin foil interconnect

To address the drawbacks identified with the micro-trace method, formation of interconnects from a thin foil was attempted. The material selected was a gold foil 1 – 2 µm thick, which is thin enough to yield a flexible interconnect. To support the foil

and allow for easier handling and loading into the FIB a simple jig was constructed. A schematic of the jig is shown in Figure 44. Gold foil was stretched across two strips of carbon tape mounted to a silicon support. Raising the foil in this manner would make it easier to attach the lift-out probe to the milled interconnect.

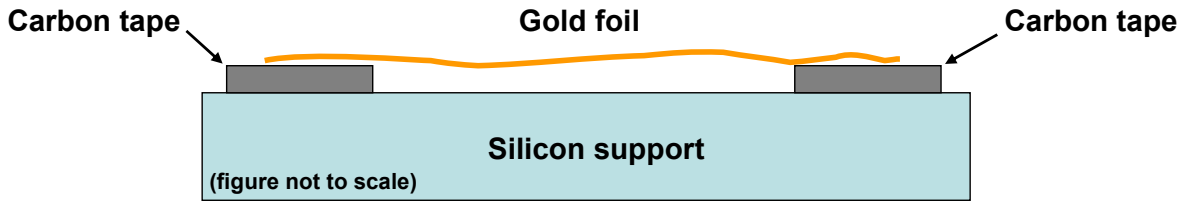


Figure 44: Cross section schematic of foil support jig.

The actual implementation of the jig with gold foil is shown in Figure 45(a). Also shown is the area where the interconnect will be formed. Figure 45(b) shows the jig in the FIB and a partially formed interconnect. First the foil edge was FIB milled to form a straight section. Then FIB milled cuts were placed to begin formation of the interconnect. To minimize curling of the interconnect as it was formed, foil ribs were left between large FIB cuts. The support ribs would be cut through later after connecting the lift-out probe to the interconnect.

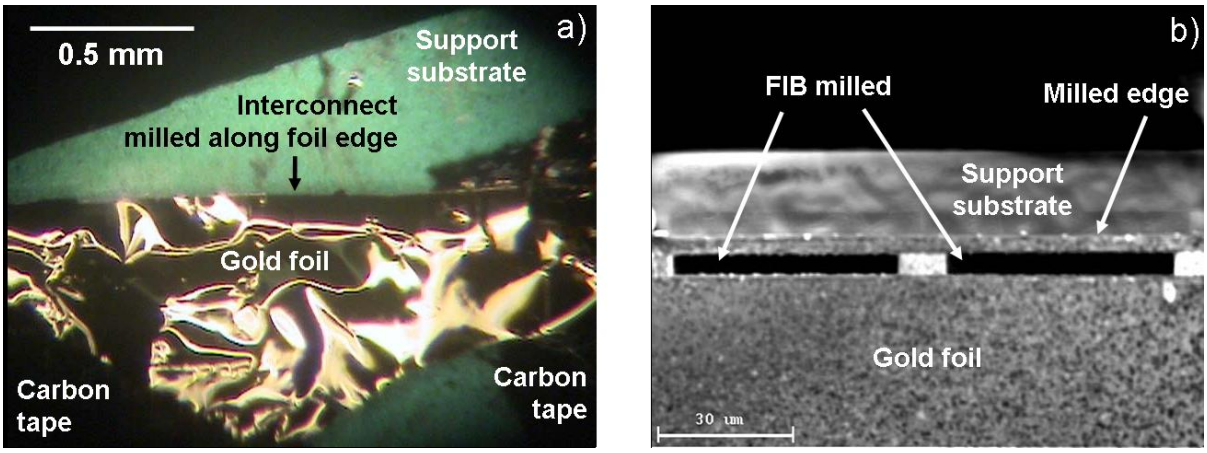


Figure 45: a) Foil and support jig. b) FIB processing to form foil interconnect.

Transfer of the gold foil interconnect to the sample is similar to that shown with the copper micro-trace interconnect and not shown again here. We pick-up with

the foil interconnect already attached to the slotted grid as shown in Figure 46. The next step then is to bridge the air gap and attach to the sample. However, unlike the micro-trace interconnect the foil interconnect would not hold in place on the lift-out probe by surface contact alone. Use of FIB deposited platinum was necessary to secure the end of the interconnect to the lift-out probe and maneuver it to the sample.

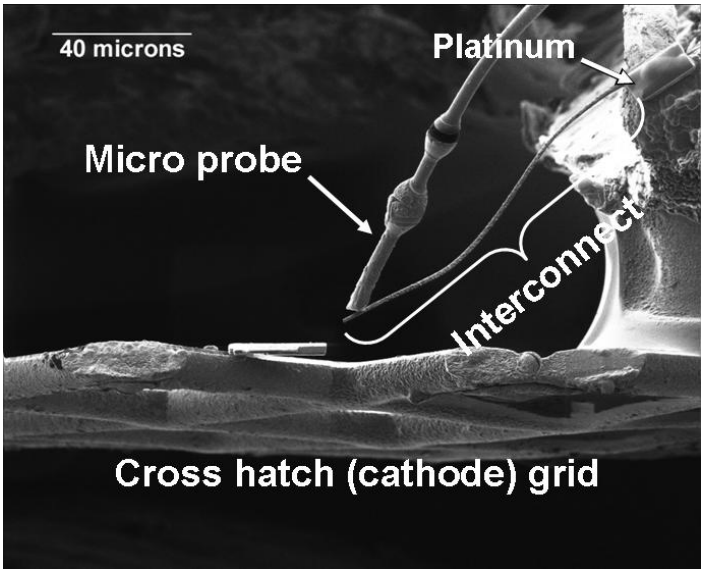


Figure 46: Placement of foil interconnect.

The completed gold foil interconnect is shown in Figure 47. As before attachment of the interconnect to the p-side metallization of the sample both electrically and mechanically used FIB deposited platinum. From the images in Figure 47 we also observe the flexibility of the foil interconnect.

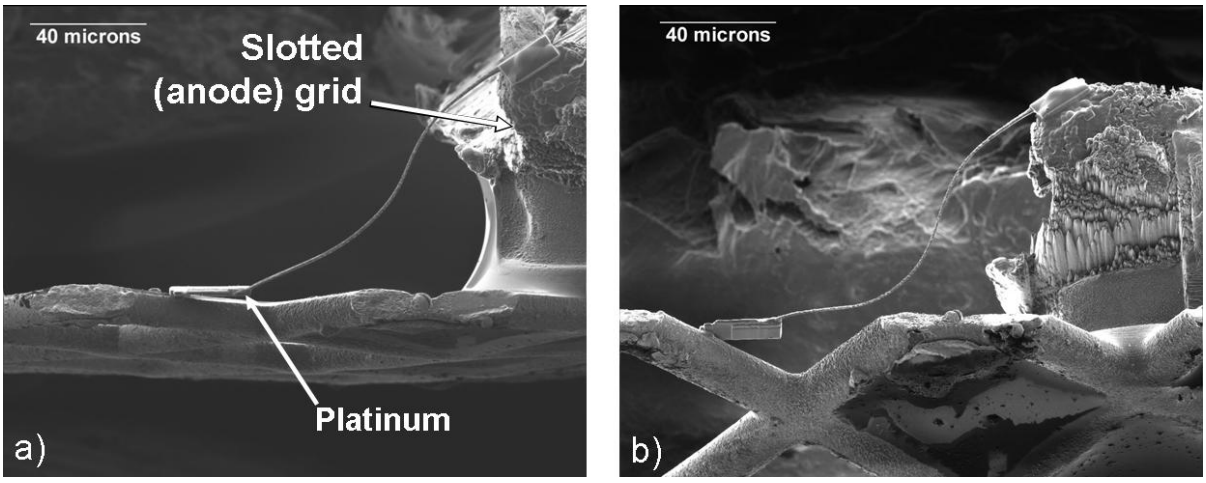


Figure 47: a) Top-view. b) Angled-view of completed interconnect.

The thin foil method enabled formation a flexible, long range interconnect. The attached interconnect was robust and survived post-FIB handling. Furthermore, forming interconnects from thin foil required less prep time compared to the micro-trace method. In addition, thin foil is commercially available from suppliers such as Alfa Aesar[96]. The thin foil method does not limit the interconnect shape. Any two dimensional pattern that can be realized with the FIB can be milled into the foil for use as an interconnect.

4.3.5 Contact characterization

4.3.5.1 Introduction

Recall that removal of the lift-out sample from the bulk device broke the external p- and n- side electrical contacts. In order to have a functioning EBIC sample re-formation of those contacts is necessary. As discussed earlier it was recognized that formation of an ohmic contact to the n-type SiC would be a challenge. However, as the n-side mechanical contact of the lift-out section to the sample holder is straight forward it was decided to first pursue formation of a bridging interconnect to the p-side contact. With the demonstration of a successful mechanical bridging interconnect method, described in the previous section, the focus now moves to contact characterization of the lift-out sample prep method.

4.3.5.2 I-V characterization of lift-out sample contacts

In light of the need to do I-V characterization of several STEM-EBIC samples over the course this work, a test jig was deemed necessary. While the STEM-EBIC holder could serve as a test fixture it was not designed or intended for this type of use. An alligator clip was modified to serve as a test jig. The end of an insulated wire was stripped and the exposed wire flattened. An insulator was glued to the inside flat of the alligator clip and the flattened wire glued to the insulator. This was repeated on the opposing side of the alligator clip. Testing of an appropriately mounted sample simply required placing it in the alligator clip where spring force from the clip assured good contact. Figure 48 shows the test clip with a blue LED emitting under forward bias.

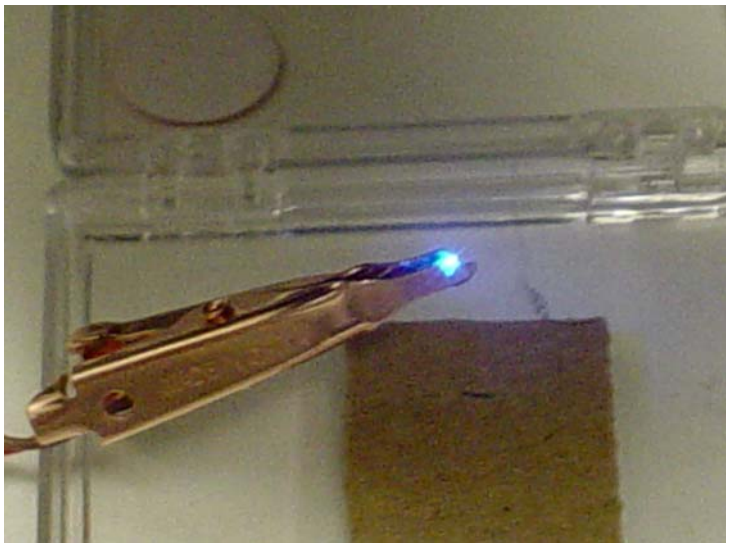


Figure 48: Modified alligator clip for electrical testing with LED emitting under bias.

The first electrical test performed was characterization of the metal-to-metal contact between sample grid and interconnect. FIB deposited platinum was used to mechanically secure the interconnect to sample grid and determine the quality of the resulting electrical contact. To investigate, a gold foil interconnect was placed between the cross hatch and slotted grids of an STEM-EBIC sample holder, which should effectively short the contacts. The sample was placed in the alligator test

clip and a quick check with a digital multi-meter indicated the assembly had a resistance of ~48Ω. To further characterize the interconnect-grid contact I-V data was taken.

Results are presented in Figure 49 below and confirm a linear current-voltage relation with a contact resistance of 51Ω. This is about two orders of magnitude higher than the contact or series resistance observed for packaged LEDs. However, from the discussion in the I-V characterization section of this document we do not expect the higher resistance to affect the junction properties.

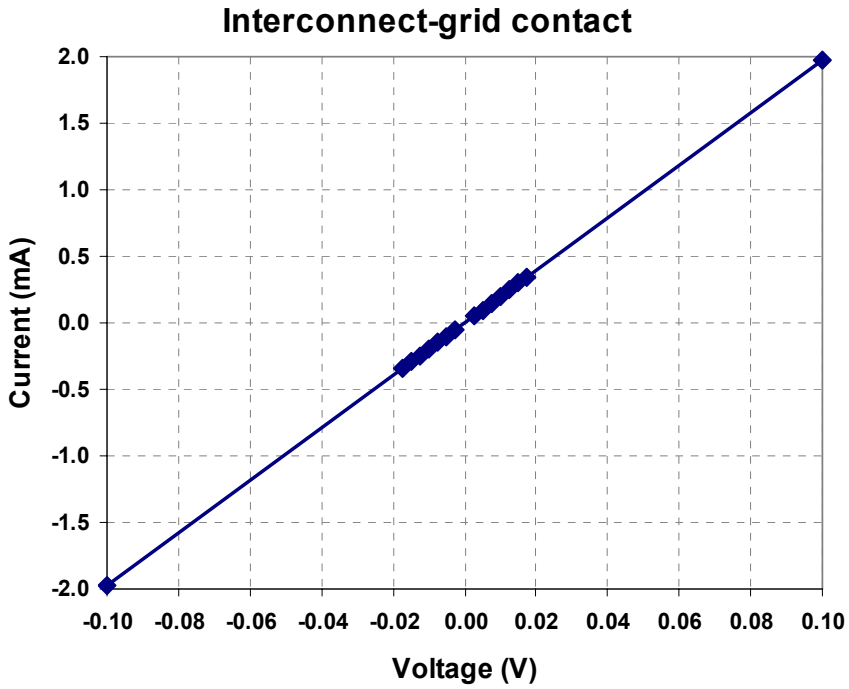


Figure 49: I-V curve interconnect to grid contact.

It was concluded that the FIB based method of attaching an interconnect to a metal yielded a quasi-ohmic electrical contact suitable for connecting to the lift-out sample. Let's now consider the interconnect to p-side contact. Recall that the lift-out section was prepared such that the internal p-side to metallization contact was retained. Therefore based on the interconnect to metal results, re-forming the anode contact should have been achieved by attaching the interconnect to p-side

metallization. The working hypothesis at this point is a re-formed electrical connection from p-side of the lift-out sample to the anode (slotted) sample grid is achievable.

The question now becomes what is the n-side contact characteristic. Ohmic contacts to n-SiC produced during LED manufacturing require high temperature, >800 C, processing[97]. Therefore, reproducing production quality contacts is not likely. On the other hand, FIB milling uses a gallium source which produces a damage layer of implanted gallium and damaged silicon carbide that may be conductive. As this layer was not removed prior to attaching the n-side of the lift-out sample to the cathode (cross hatch) grid, an electrical contact may exist. Proceeding under the premise that a p-side contact existed, I-V data of for the lift-out sample from Figure 43 is presented below.

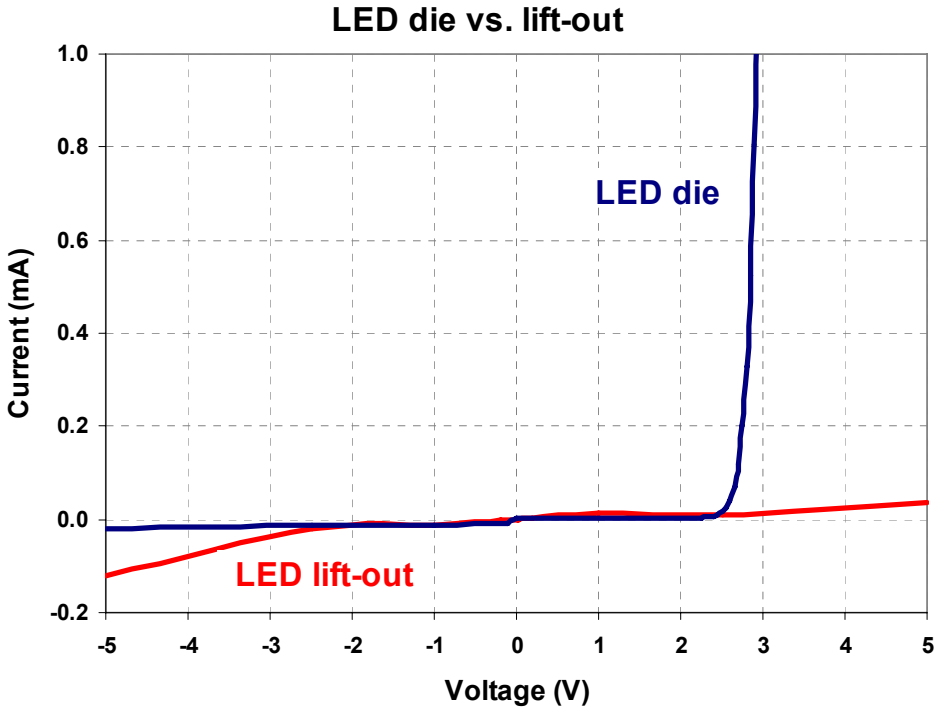


Figure 50: I-V curve LED die vs. lift-out.

Figure 50 indicates that the lift-out sample does not behave as pn-junction diode. Of interest is a current was measured and it is greater for the reverse bias

condition than forward bias. A possible explanation for this behavior is the n-SiC to grid contact is a Schottky contact. Note that FIB deposited platinum was used to attach the lift-out sample both mechanically and electrically to the cathode grid. Therefore, the contact formation between platinum and silicon carbide must be considered and this means looking at the work functions for the two materials. Doing so reveals that the work function for platinum (Φ_{Pt} = 5.65 eV) is greater than the work function for intrinsic SiC (Φ_{SiC} = 4.75 eV) with the work function for n-SiC being less than that. Hence, from the discussion in section 4.3.3 it is concluded that the n-side contact is Schottky. The updated equivalent circuit for the lift-out sample is shown below in Figure 51. Under reverse bias conditions the Schottky barrier would be lowered, which likely accounts for the increased current in that direction. Regardless, the I-V characteristic shown in Figure 50 indicates that the re-attached lift-out section does not behave as a diode. This means that some other method to form an Ohmic contact to n-SiC, other than FIB deposited platinum, is required.

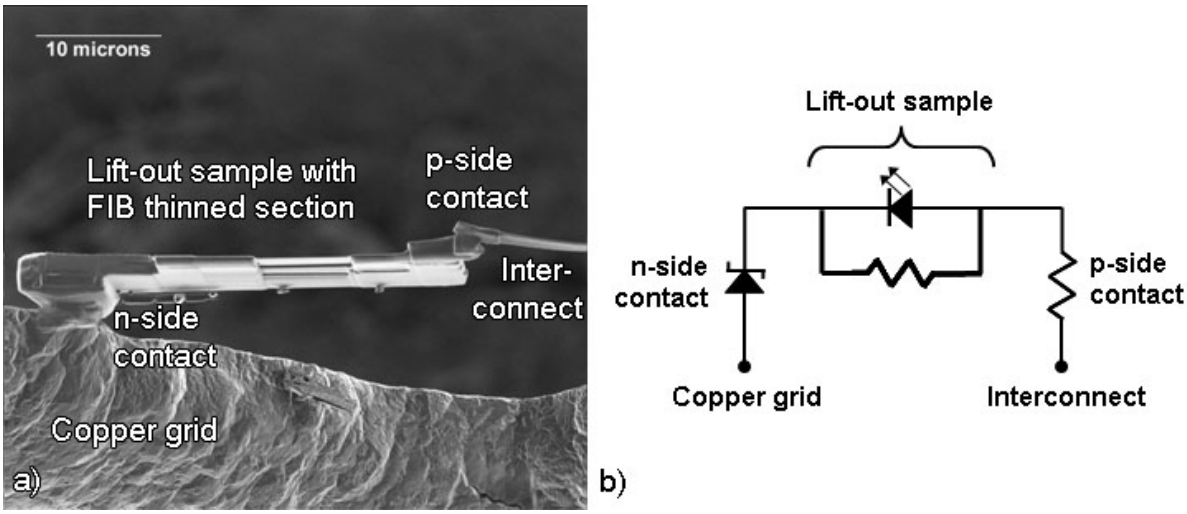


Figure 51: (a) Physical sample and (b) equivalent circuit schematic.

4.3.6 Contact options n-SiC

4.3.6.1 Introduction

As discussed in the previous section, formation of a low resistance contact to n-SiC on the lift-out sample has not yet been achieved. A literature search of contacts for silicon carbide was undertaken, but yielded few options. In part this was due to restrictions placed on potential formation process. First, it needed to be room temperature with no annealing requirement so as not to damage the sample or holder. Second, the process needed to be fairly rapid so as not to extend the prep process from hours to days. Given these requirements the literature[97, 98] reports sputtered titanium, molybdenum and titanium as the only room temperature metallization methods that do not require high temperature annealing for Ohmic contacts on n-SiC.

4.3.6.2 Metallization experiment

An experiment was needed to test different sputter coating metallizations to see if any would form an Ohmic contact to n-SiC. The approach taken was to use LED wafers as the test platform. These wafers contained pre-diced functional LEDs and were already mounted on a transistor outline (TO) header, Figure 52.

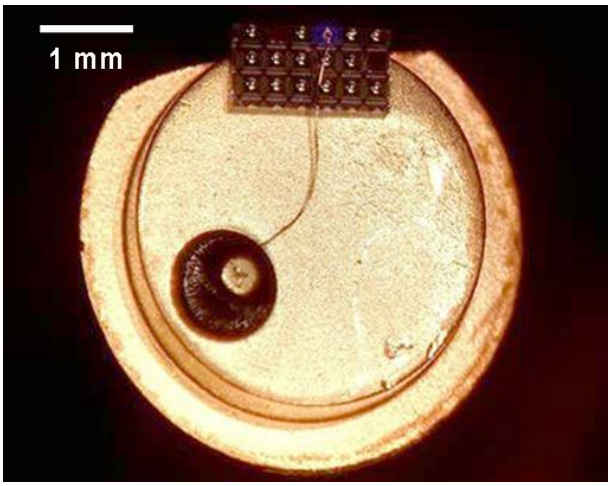


Figure 52: LED wafer mounted on TO-header.

First, I-V characterization of the initial wafer with the existing Ohmic contacts was recorded. Next, the wafer was removed from the TO-header and mounted n-side up in crystal bond. Mechanical polishing with a diamond lapping pad was used to remove the n-side metallization and expose the n-SiC substrate, Figure 53. Note that the p-side wire bond contact was maintained.

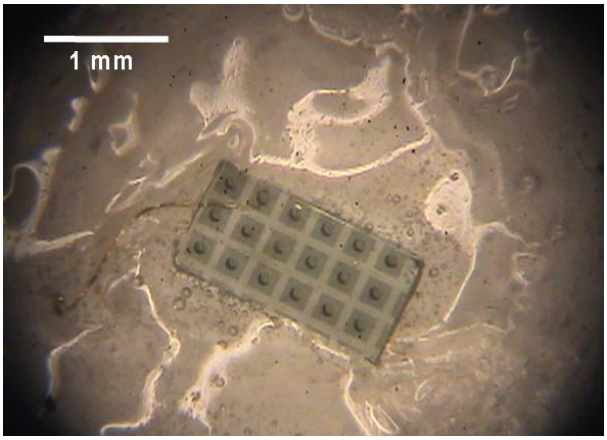


Figure 53: Wafer mounted in crystal bond with n-side metallization polished off.

The wafer was left in crystal bond which served as a crude mask to protect the sidewall and p-side during sputtering. The polished side of the wafer was then sputter coated first with metallization and then with gold to protect the metallization. Extracting the sputter coated sample from the crystal bond mask was achieved by placing it in acetone. This was followed by an ethanol then methanol rinse to clean the contact surface. Figure 54 shows a wafer with the n-side sputter coated metallization and gold cap.

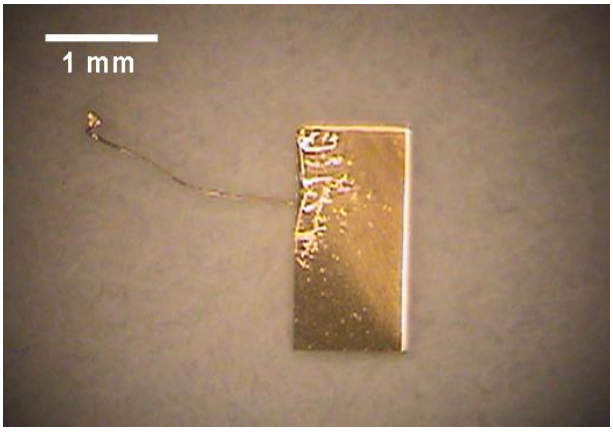


Figure 54: Sputter coated metallization.

Three wafers were prepared in this manner one for each metallization investigated (Mo, Ti, Ta). Each wafer was then reattached to a TO-header using silver epoxy and cured at 100 C for ten minutes. I-V data was then recorded to characterize the re-formed n-side contact and compare it to the initial Ohmic contact.

4.3.6.3 Metallization results

Results for the three test wafers are summarized in the next set of images. Not only was the I-V characteristic of the sputter coated wafers considered, but also how closely it matched the I-V curve for the initial wafer. Thus, the first curve presented is for the wafer before removal of the n-side Ohmic contact. The second curve is for the wafer after sputter coated metallization and reattach to TO-header. Lastly, as noted before but repeated here, the initial p-side wire bond was retained.

The discussion starts with wafer-1, which received a sputter coating of Mo/Au. Figure 55(a) shows the initial wafer yielded a typical diode I-V characteristic. Also the 'knee' of the curve is sharp and occurs at about 3.25V. Post sputter coating I-V results shown in Figure 55(b) indicate that the Mo/Au contact permits current flow. However, the current is significantly suppressed by four orders of magnitude. A 'knee' is still present, but the large radius indicates a large series resistance. As this was not observed in Figure 55(a) we concluded that the increase in resistance is due to poor contact formation between Mo and n-SiC.

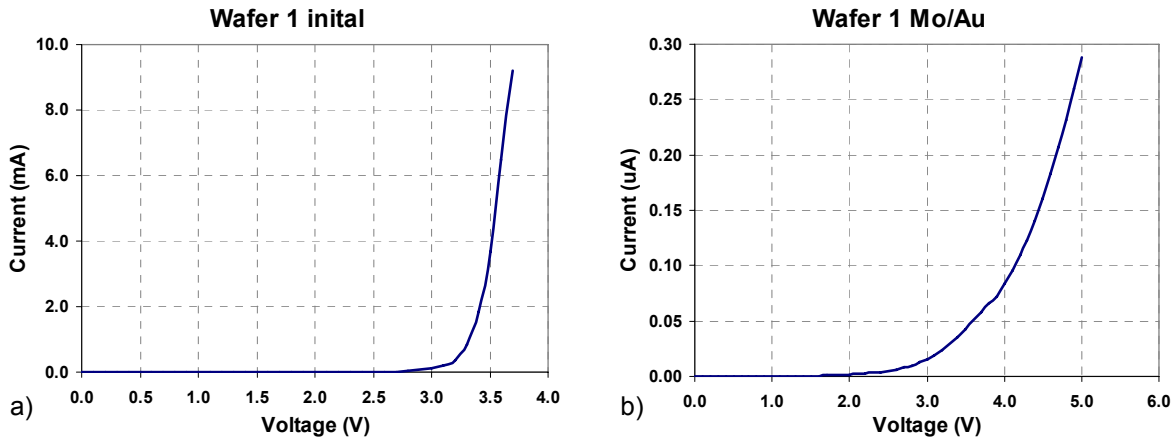


Figure 55: a) Wafer-1 initial I-V. b) Wafer-1 Mo/Au metallization I-V.

Next is wafer-2, which received a sputter coating of Ti/Au. Figure 56(a) shows the I-V relation for the initial wafer. The post sputter coating results presented in Figure 56(b) show that the Ti/Au contact permits current flow and the I-V relation exhibits diode characteristic behavior. The current flow is suppressed compared to the initial wafer, but only by an order of magnitude. Also an increase in the series resistance is observed reflected by the higher voltages necessary to drive similar currents.

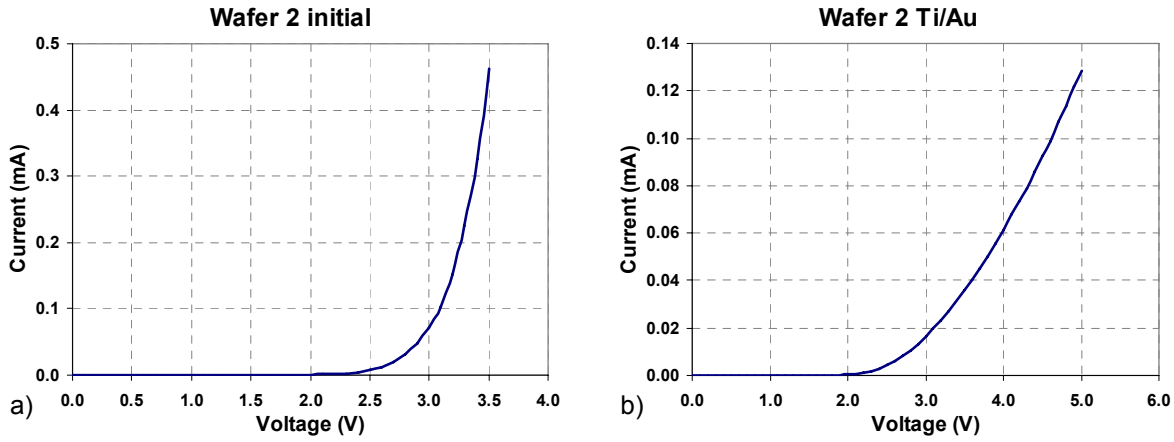


Figure 56: a) Wafer-2 initial I-V. b) Wafer-2 Ti/Au metallization I-V.

Lastly, wafer-3 received a sputter coating of Ta/Au. Figure 57(a) shows the I-V relation for the initial wafer. The post sputter coating results shown in Figure 57(b) indicate that the Ta/Au contact permits current flow and the I-V curve exhibits diode characteristic behavior. As with the previous two samples the current flow is suppressed, but the Ta/Au contact did yield the highest current flow observed for the three test wafers. An increased series resistance was also observed reflected by the higher voltages required to produce similar currents.

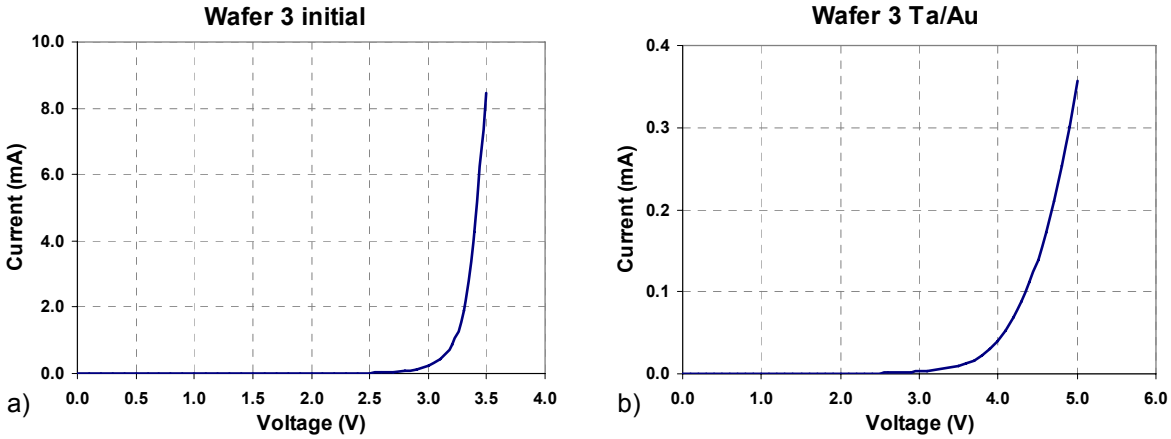


Figure 57: a) Wafer-3 initial I-V. b) Wafer-3 Ta/Au metallization I-V.

For completeness Figure 58 shows the three test wafers remounted on TO-headers. The current amplifier on the test cart had a max voltage of 5V. Only the sample with Ta/Au coating, shown in Figure 58(a), emitted sufficient light at that voltage to allow it to be visible for image capture by stereoscope. A 10V power supply was necessary to yield the emission observed for Ti/Au shown in Figure 58(b) while no emission was detected for Mo/Au shown in Figure 58(c).

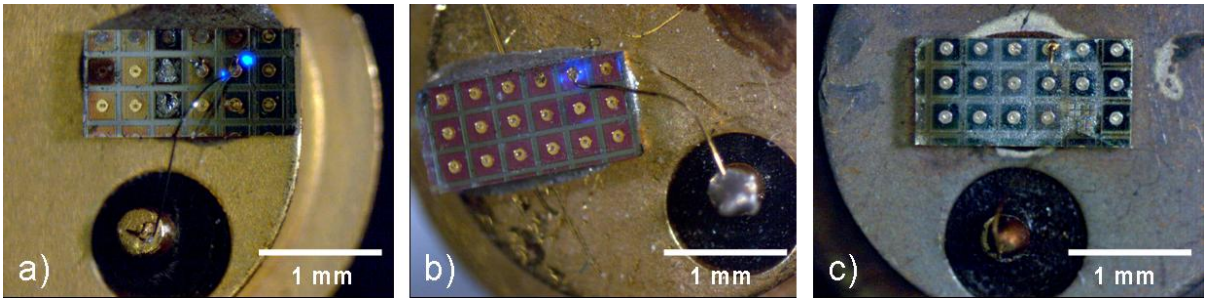


Figure 58: Sputter coated metallization a) Ta/Au. b) Ti/Au. c)Mo/Au.

In conclusion, results for the different sputter coated metallizations were mixed. While all of the metals investigated yielded electrical contacts the resulting current flow was suppressed compared to samples with factory formed n-side Ohmic contacts. The resulting I-V curves for the reattached wafers exhibited diode characteristics, but with increased series resistance. Based on these results it was concluded that the sputtering processes as tested are not capable of reforming a sufficiently low resistance contact to n-SiC. While some of the metallization results were encouraging, development into a working method would likely require significant time and effort. As such, a strategic decision was made to put-off further attempts at reforming the n-SiC Ohmic contact in favor of alternative sample preps.

4.3.7 Summary lift-out method

In this section a novel sample prep method for STEM-EBIC was presented. The approach taken was to use FIB based lift-out techniques and micromanipulation to reduce handling and increase sample through-put. Two challenges related to formation of electrical contacts to the lift-out sample needed to be overcome. The p-side metallization was kept intact, but a method for bridging between the sample and anode contact was required. The solution was to form bridging interconnects from thin gold foil and the functionality of this method demonstrated. In fact the method developed is robust enough that it can be applied to FIB based circuit repair if so inclined.

The last hurdle to implementing the STEM-EBIC lift-out method was forming an Ohmic contact to n-SiC. This was necessary because the lift-out did not reach the n-side metallization due to the depth (90 - 250 μm) of the SiC substrate. To simplify the STEM-EBIC lift-out method, specific requirements were placed on potential n-SiC Ohmic metallizations. These requirements were rapid turn around and no annealing. Three potential sputter coated metals were identified Mo, Ti and Ta. An experiment was set-up that compared I-V characteristics for three LED wafers that were tested with the n-side metallization and then re-worked with one of the sputter coat metallizations. Results from this experiment were mixed showing some promise, but not yet capable of forming the required Ohmic contact to n-SiC. Thus it was decided to forgo any further effort developing the STEM-EBIC method and pursue alternative sample preps that retained the n-side metallization. Lastly, reforming the n-side contact may be less of an issue with other material systems. In that case the STEM-EBIC lift-out method should be considered as a potential sample prep option.

4.4 Cross-rib prep method

4.4.1 Introduction

The goal with this method was to prep STEM-EBIC samples while retaining the existing p- and n- side LED Ohmic metallization. An additional requirement was no mechanical prep. This decision was based on the desire to eliminate the handling associated with mechanical prep which would increase prep time and the potential for sample damage. To meet these requirements the idea proposed was to develop a FIB based method for preparing STEM-EBIC cross rib sections in a full die. The basic concept of proposed method is shown in below in Figure 59. As can be seen both the p- and n- side contacts are retained eliminating the problem encountered trying to reform the n-side contact with the lift-out method.

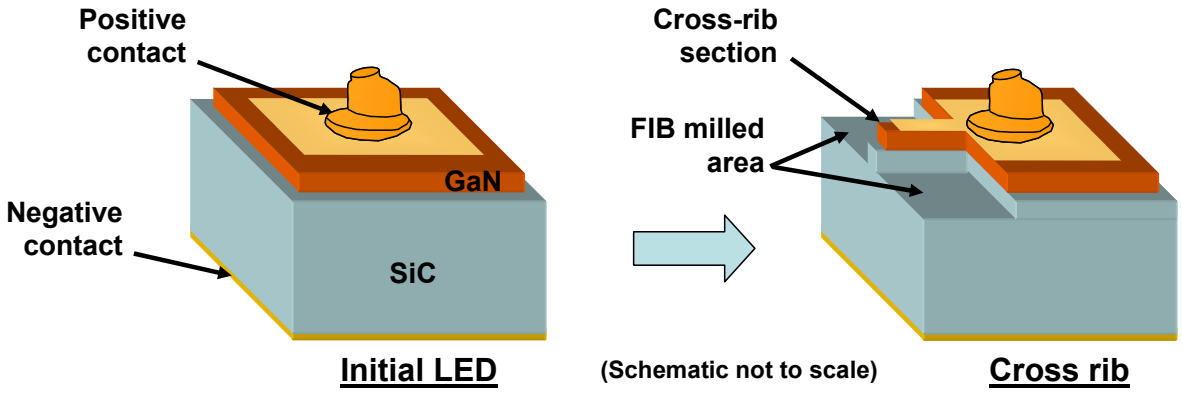


Figure 59: Schematic of Cross-rib sample prep.

The use of FIB based milling eliminates mechanical polishing and the sample can be completely prepped in the FIB. The only significant handling required is the initial mounting of the LED die to the sample holder. It is worth noting that this is effectively the first step in the prep process which provides the following benefits. First, little time has been invested in the sample prep so the opportunity cost for a damaged sample is low. Second, the LED is still a full die and relatively less susceptible to damage than at any other time during sample prep. While mounting of the LED die at the beginning of the prep process has advantages this does not mean that the sample holder and method for attaching to it can be overlooked. Thus the next section will described development of a holder for use with the cross-rib sample prep method.

4.4.2 Sample holder

When considering options for the sample holder it is imperative that the design does not limit the sample prep method. Furthermore attaching the LED to the holder needs to be repeatable so that there is consistency between samples. Also, the landed LED must remain secure on the holder through the prep process and subsequent analytical investigation. Bunker et. al.[99] developed FIB techniques and a holder for cross-sectional STEM-EBIC samples. However, their prep method required mechanical polishing with the resulting sample 'sandwiched' in the holder. Figure 60 shows the holder concept.

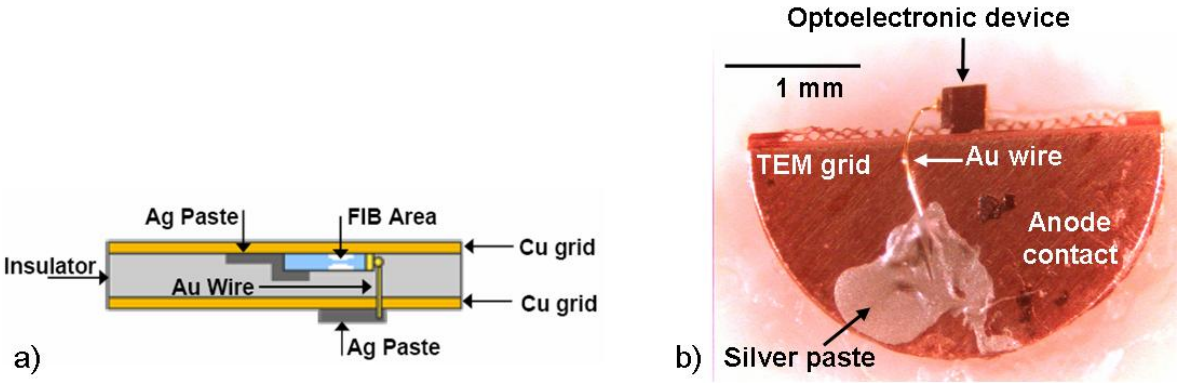


Figure 60: a) Cross-section schematic of sandwich style holder. b) Assembled holder with sample. (From Bunker[75]).

Two problems were identified with the holder design by Bunker et al. First, electrical contact was not made to the full base. This can be observed in Figure 60(a) where Ag paste is shown to contact only the portion the sample sandwiched between the Cu grids. The concern here is further increased series resistance resulting from reduced contact area as well as the consistency of this contact compared across several sample preps. Second, the sample must be long enough for the area of interest to extend beyond the Cu grids. While this is the case with the sample shown in Figure 60 it is not the case for LED devices considered in this investigation with a maximum height of 250 μm and width of 300 μm. Attempts were made to leverage the work by Bunker et al., but placing dies and contacting the n-side with Ag paste in a sandwich type holder was too problematic. A modified version of the holder was developed and shown below in Figure 61.

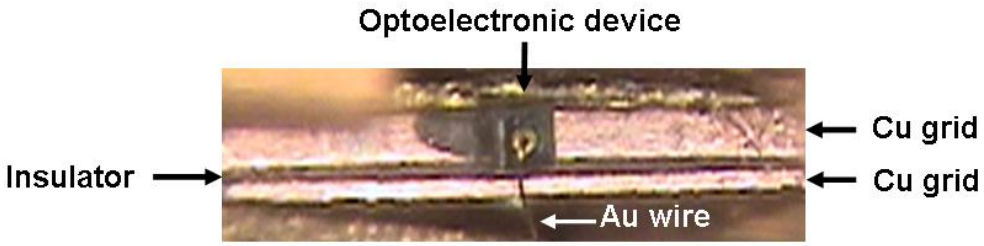


Figure 61: Top-view of modified holder with sample in place.

As with the previous method two copper grids are used and insulated from each other with epoxy. In this case the grids were formed from different thickness copper foils (0.25 and 0.1 mm). The thicker foil was sized to match the base of the LED and provide full contact along that surface. 3 mm discs were punched out for each foil thickness, cut in half and polished to form a smooth flat edge. Allied epoxy bond 110, a two part thermal epoxy, was used to form an insulating bond between the two copper grids. A process note, it was found that the epoxy was too runny after initial mixing. Under those conditions the epoxy thickness would not be uniform, but thick in the middle and thin along the edges requiring re-work to flatten. Waiting twenty-four hours after mixing allowed the epoxy to thicken. This greatly improved consistency and formation of the insulating bond. The mated grids were then cured at 100 C for ten minutes to complete the bond. The completed sample holders where then tested for shorts with a digital multi-meter.

The next step is to land an LED die onto the sample holder. This work needed to be carried out under a stereo microscope. A sample holder was loaded into a micromanipulator and positioned under the microscope. First a small amount of silver paste was applied to the cathode grid. Then a bare die with the p-side wire bond still attached was placed onto the silver paste. However, several attempts to attach the die in this manner were unsuccessful. The problem was that rapid dry-out of the silver paste produced enough of a surface affect so that the die did not wet sufficiently to form a contact. This was resolved by using a two part silver epoxy (Circuit Works Conductive Epoxy PN CW2400). The epoxy remained wet enough to allow seating and aligning of the LED on the cathode grid. To complete the n-side contact the holder with sample attached was cured at 100 C for ten minutes. A similar formation followed for the p-side contact to anode grid. Some care needed to be taken in manipulating the wire bond into contact with the anode grid so as not to break off. With the wire bond in place, silver epoxy was applied and to complete the contact the assembly was once again cured at 100 C for ten minutes.

Figure 62 below shows a side-view of the completed assembly. The top mounted approach for attaching the sample offers benefits over the sandwich style

sample holder. First, the full base of the LED is in contact with the cathode grid. Effectively this reproduces the intended electrical contact area for the n-side of the device. Second, the holder is not limited to samples of a minimum height. The LED shown in Figure 62 is 250 μm tall, but as will be seen later, low profile samples 85 μm tall can be attached with out any problem. Lastly, other than directly under the wire bond complete access to the GaN active layer possible. Thus the holder does not limit the sample prep method.

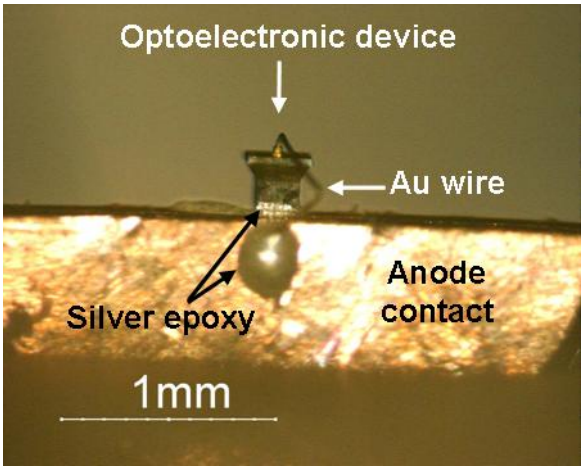


Figure 62: Side-view of sample holder.

By preparing several holders in advance, the landing and attach of samples can be completed at a rate of two per hour. With samples now mounted to the holder, the next step is to FIB mill in the cross-rib and electron transparent cross-section. Before proceeding to that step, a discussion on the expected I-V results due to processing a cross-rib sample is presented.

4.4.3 Expected I-V results

Sample prep to some extent will affect the device performance and thus it is important to understand how those changes theoretically impact the device I-V characteristic. To start the discussion we refer back to the equivalent circuit introduced in Figure 24 and consider how the cross-rib prep relates to the circuit

parameters. Figure 59 shows that FIB milling removes part of the GaN layer on both sides of the cross-rib. This results in a loss of planar area for the current to flow across. In the diode equation, (4-1), area is accounted for in the exponential pre-term that was defined as I_s. Thus it is expected the cross-rib prep method will reduce current flow. To observe the change in the I-V relation we evaluate the effect of a 'perfect' cut. For this purpose a perfect cut is defined as the removal of material without the introduction of any artifacts. The typical GaN area for the devices investigated is ~ 245 x 245 μm^2. Cross-rib prep is expected to remove ~ 65 x 120 μm^2 of material on both sides of the rib section. This process reduces the planar area by ~ 25%. Based on equation (4-1) the theoretical result to the I-V characteristic is shown below in Figure 63 which compares the before and after cut cases.

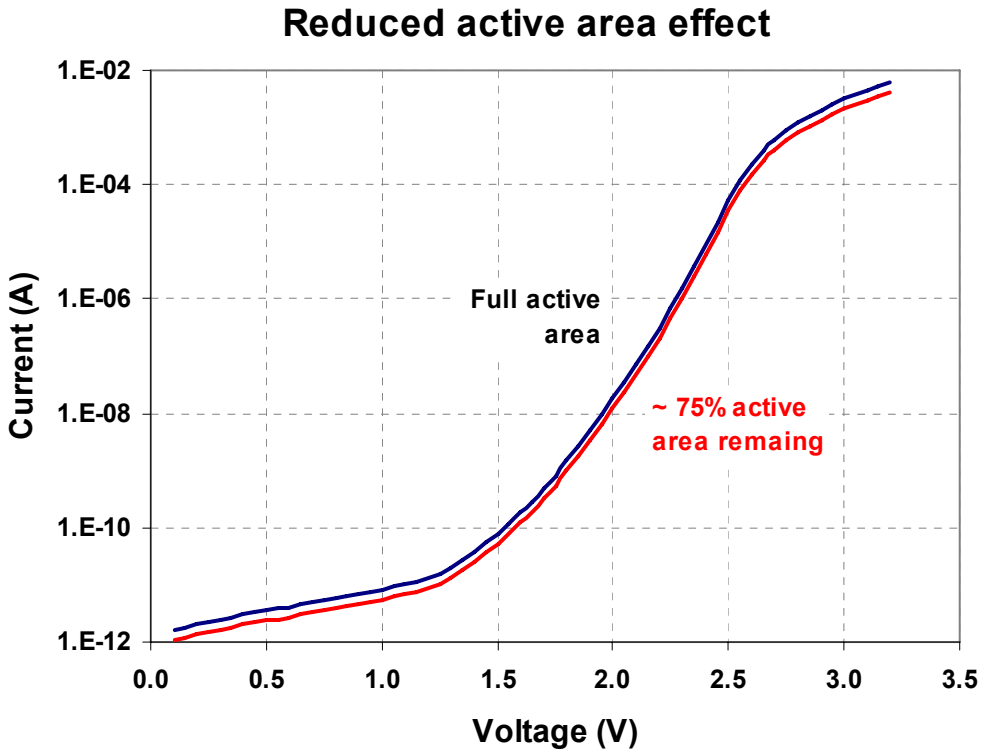


Figure 63: Expected effect of reduced planar area on I-V relation.

From Figure 63 it was concluded that for a perfect cut the cross-rib prep results in a reduction to current, but does not alter the current mechanism. However, the case of a non-perfect cut must now be considered.

FIB milling involves subjecting samples to energetic Ga^+ ions. This process inherently produces a damage layer along the sidewalls formed in the sample. The damage includes implanted gallium as well as amorphization of the surface. Now consider that forming the cross-rib exposes the pn-junction and the damage passes across it. Thus, FIB milling has the potential to produce a shunt current around the diode junction. This effect is modeled in the equivalent circuit by a placing a resistance in parallel, R_p, with the diode. To observe the expected result of a shunt current on the I-V characteristic of the device the following experiment was performed. Resistors with different resistances were placed in parallel with a packaged LED. The resistors model the damage enabled shunt current and the implied assumption is that the damage layer behaves as a thin conductor. This is similar to the perfect cut assumption from the previous discussion. Results of the I-V measurements are shown below in Figure 64.

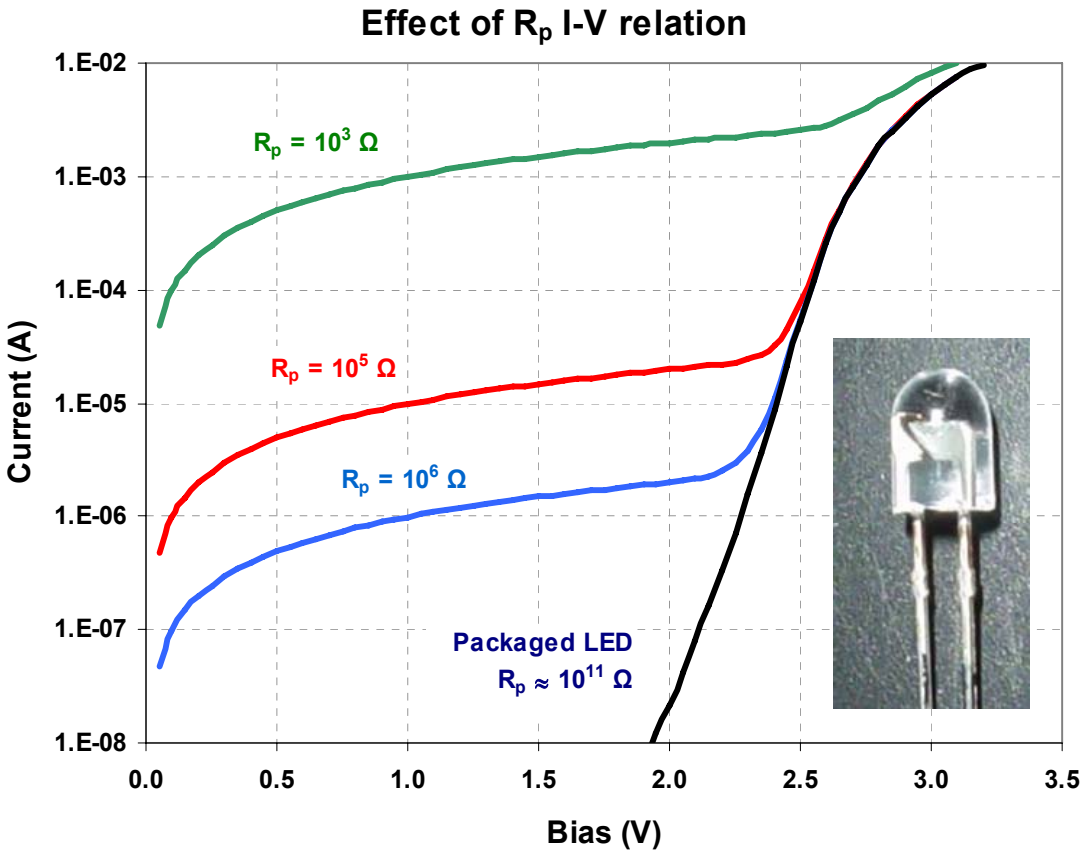


Figure 64: Expected effect of reduced parallel resistance on I-V relation.

The packaged LED is shown in the bottom right insert of Figure 64 and three different resistors 10^3, 10^5 and 10^6 Ω were tested. For the sake of discussion will define the black curve of the packaged LED as the diode threshold. Three observations can be made. First, for sub-diode, threshold voltages the current-voltage relation is linear. Second, the reduced parallel resistance results in increased current for voltages up to the diode threshold. At higher voltages the current follows the curve for the packaged LED. Third, it is apparent that the parallel resistance can be reduced sufficiently that the resulting current exceeds the packaged LED current across the voltage range (R_p=10^3 Ω in Figure 64). Under those conditions the current mechanism begins to deviate from that of the diode and the sample is no longer of interest analytically. Thus for the LED samples in this investigation the FIB induced parallel resistance needs to be greater than 10^3-10^4 Ω.

An additional requirement that needs to be considered is the instrumentation of the test cart. A Keithley 428 current amplifier is used to detect the EBIC signal from the sample. The manufacturer recommends minimum source resistances for each gain setting. If the parallel resistance is too low the highest gain settings on the current amplifier will not be available. Based on the manufacturer's recommendation, it was concluded that an acceptable cross-rib sample should have a parallel resistance no less than 10^6 Ω. This now concludes the discussion on expected I-V results due to processing of a cross-rib sample.

4.4.4 Prep results

The cross-rib prep is started by taking a mounted sample and loading it into the STEM-EBIC holder. Figure 65 shows the tip of the STEM-EBIC holder with a loaded sample emitting under bias. Electrical contact between the EBIC holder and sample is made via the cathode and anode pick-ups shown in Figure 65. The STEM holder was then loaded into the TEM port on the Hitachi FB2100 (Figure 27). An image of the sample in the FIB, prior to milling is shown Figure 66. In-situ I-V data of the initial sample is shown for both linear and semi-log scale in Figure 67.

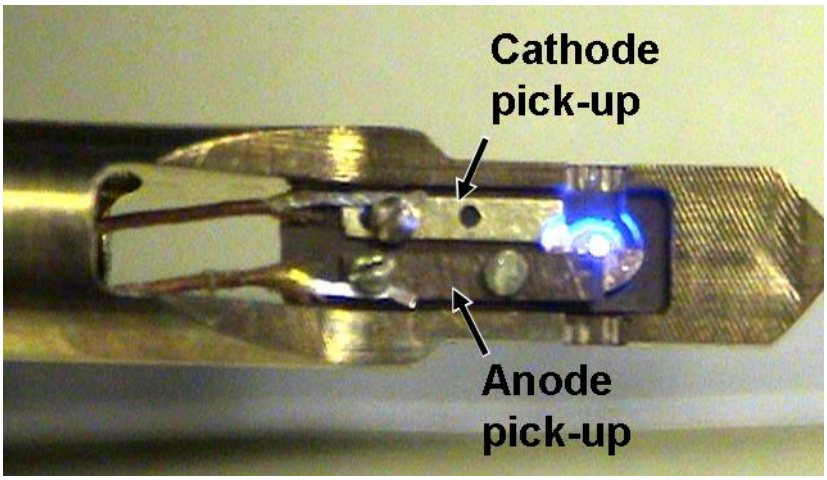


Figure 65: Sample in STEM-EBIC holder emitting under bias.

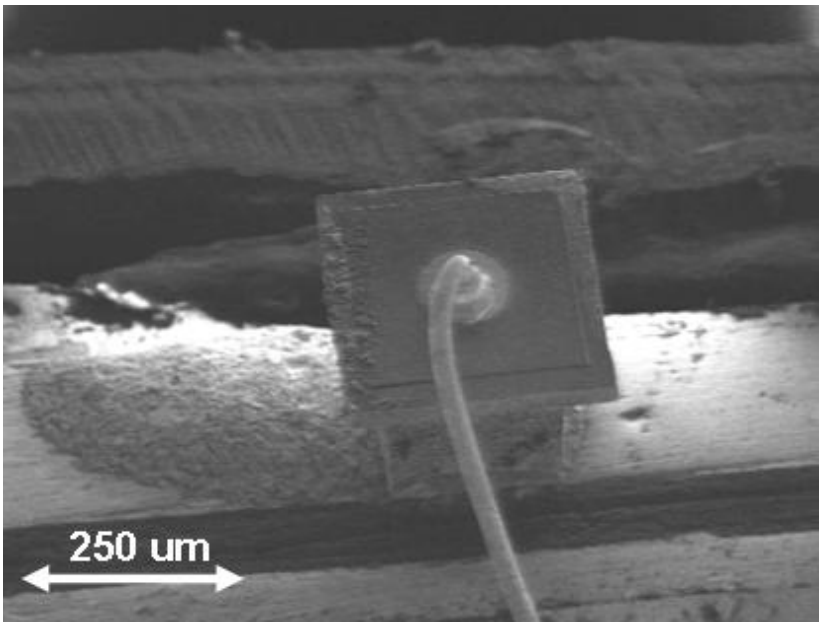
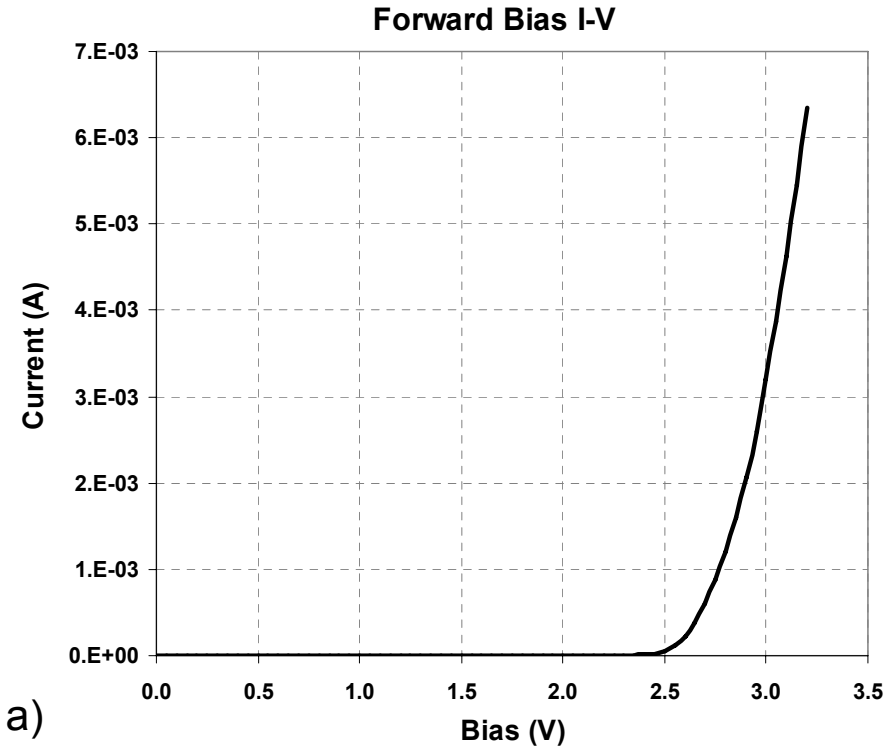
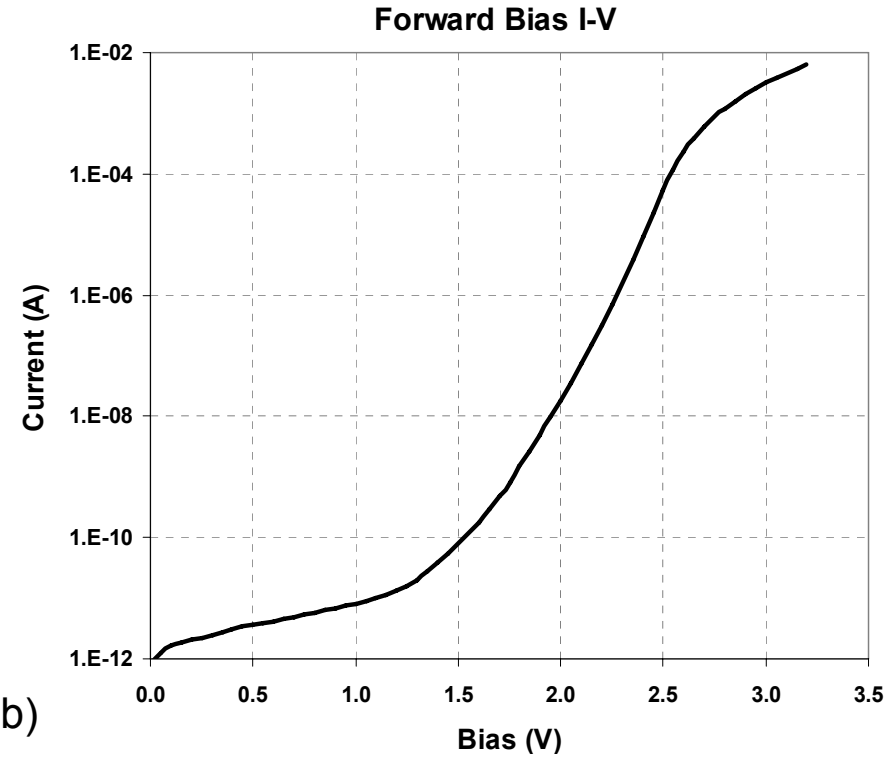


Figure 66: Sample in FIB prior to milling.



a)



b)

Figure 67: Initial sample in-situ FIB I-V. a) Linear plot. b) Semi-log plot.

A tungsten strip was then deposited to protect the top surface of the cross-rib section. This was followed by placing a 15x150x4 μm (WxLxD) cut (Figure 68). The depth dimension was selected to ensure an unobstructed view of the cross-section in the STEM. This was considered a potential problem in that the sample would need to be aligned on axis by tilting the holder. Recall that the sample is a full die and the cross-rib section is roughly at the midpoint. If the cut depth is too shallow the top edge of the die may block the beam when the sample is tilted on axis. Thus the 4 μm depth is precautionary as the junction is within the 1 μm of the surface for the samples investigated.

FIB parameters used for milling the cut were an accelerating voltage of 40 kV and beam current of 30 nA yielding a mill rate of ~ 6 $\mu m^3/s$. A 40 nA beam current was available, but practice cuts at that current yielded poor results. Beam tails, due to beam spreading, were too difficult to control and it was decided to go with the next highest beam current. Figure 68 shows a FIB image of the sample after milling of the first cut and Figure 69 shows the resulting I-V data.

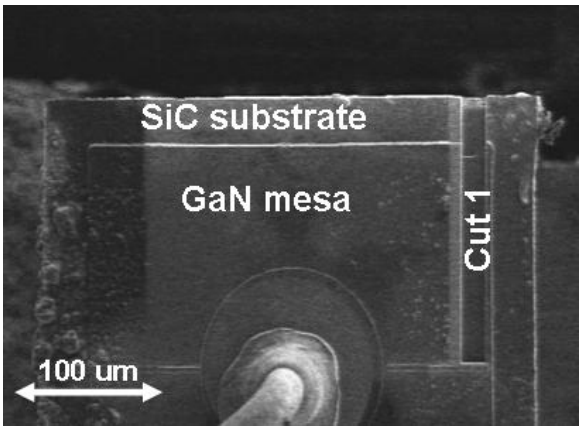
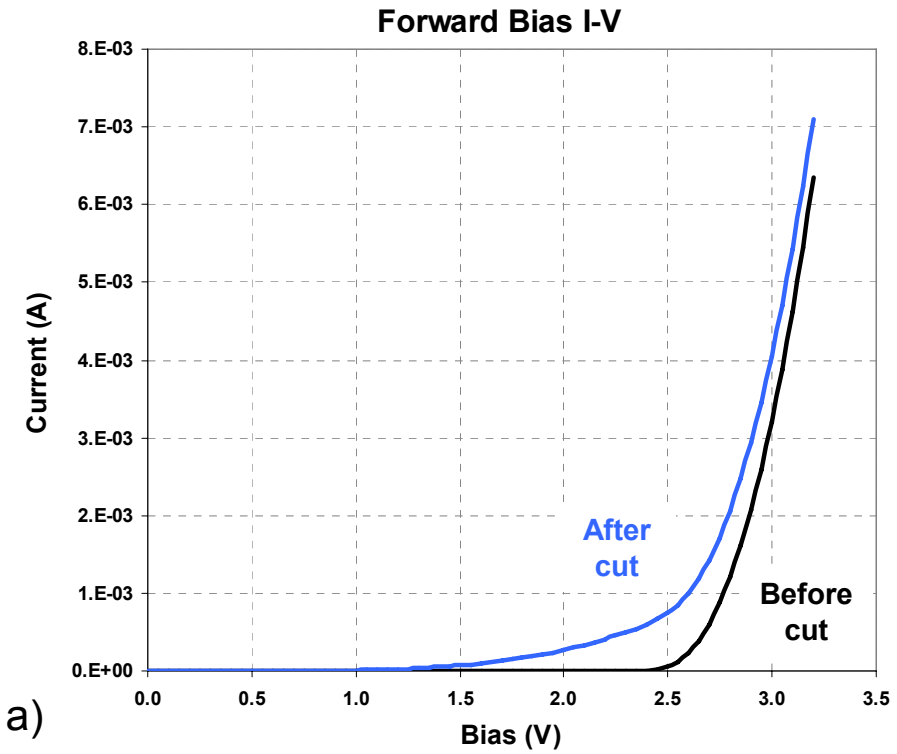
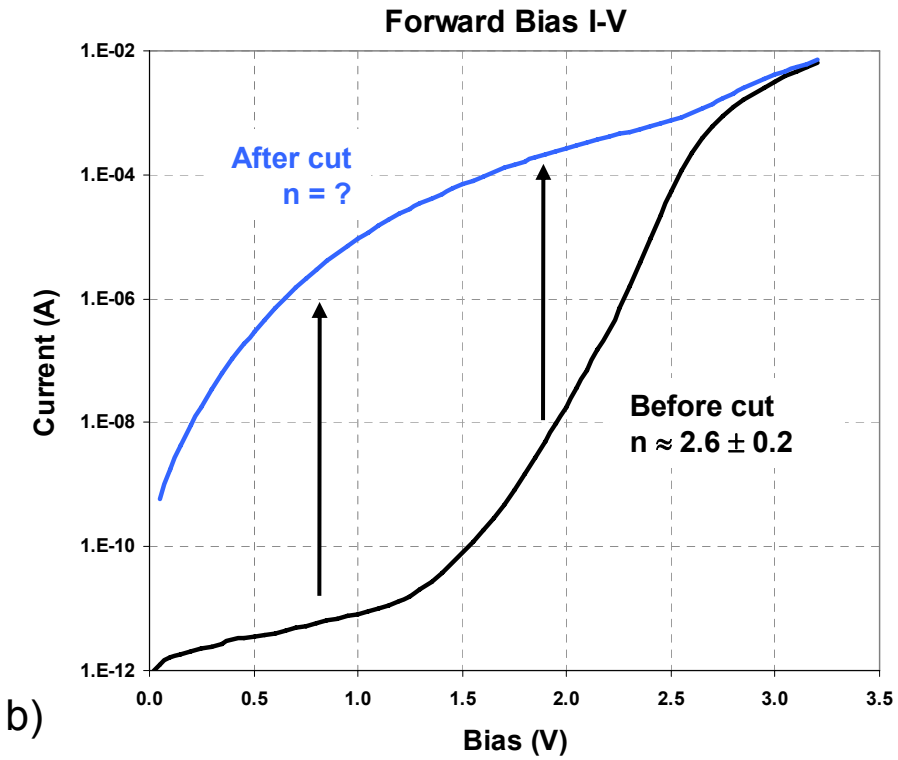


Figure 68: FIB image of sample after cut.



a)



b)

Figure 69: I-V results after initial cut. a) Linear plot. b) Semi-log plot.

The linear I-V plot shown in Figure 69(a) for the after-cut condition is similar to that predicted for a sample with reduced parallel resistance (Figure 25). This is in line with our expectation that FIB processing enables a shunt path around the junction as discussed in the previous section. If the behavior of the shunt is as predicted then the semi-log plot would confirm the sub-threshold relation. We therefore turn our attention to the I-V plots shown in Figure 69(b). It is immediately apparent the after-cut current-voltage relation is not at all similar to what was predicted by the conductive damage layer model in section 4.4.3.

Post-FIB current bowing is a dramatic deviation from the initial and expected post-FIB I-V results. An ideality factor of $n \approx 2.6$ was found for the initial sample, while for the post-FIB curve the ideality factor equation no longer fits the observed behavior. To further investigate device behavior, a second cut was made as shown in Figure 70 and the resulting I-V data shown in Figure 71.

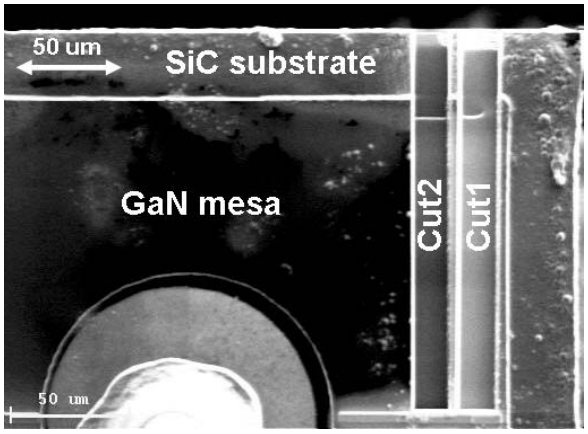
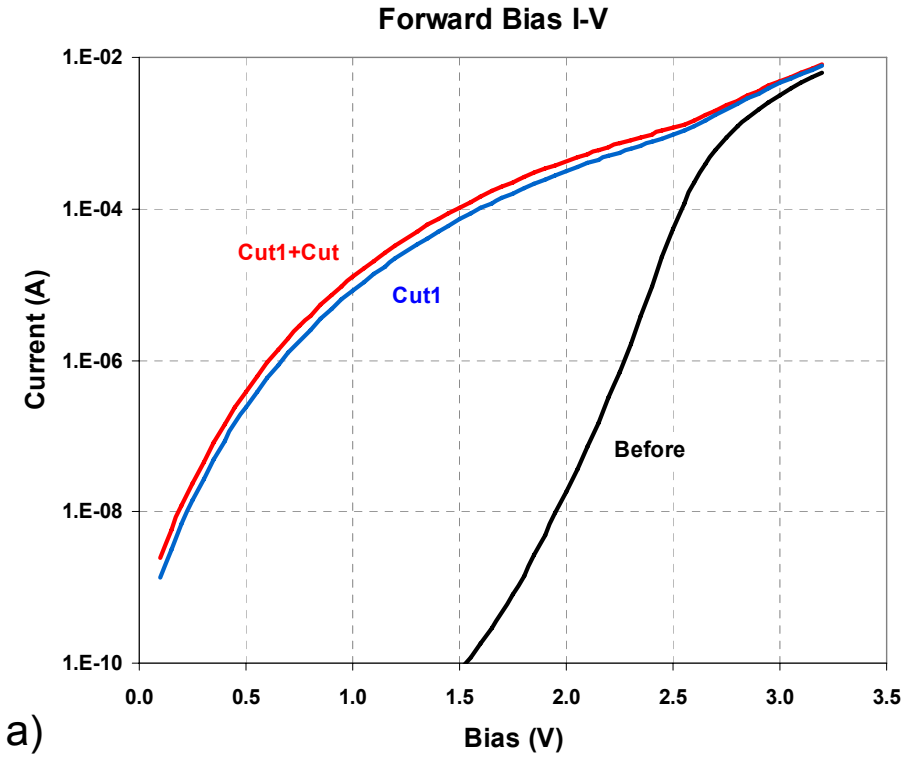
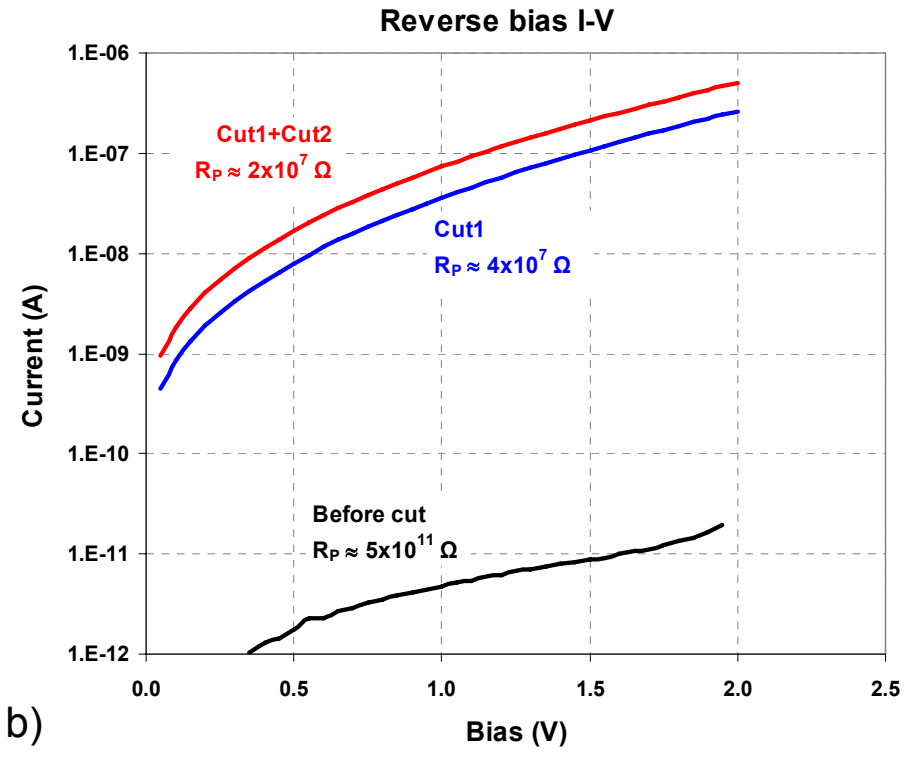


Figure 70: FIB image of sample after second cut.



a)



b)

Figure 71: I-V results after second cut. a) Forward bias. b) Reverse bias.

Figure 71(a) shows the forward bias result for the sample now with two cuts. The current increased slightly with the curve following the profile for that of the single cut case. To evaluate the change in parallel resistance it is useful to look at the reverse bias case, the results for which are shown in Figure 71(b). For the initial die a parallel resistance of $\approx 5x10^{11}$ Ω was measured. Formation of the first cut reduced the parallel resistance four orders of magnitude to $\approx 4x10^{7}$ Ω. Formation of the second cut reduced the parallel resistance to $\approx 2x10^{7}$ Ω. Of interest is the combined resistance from the two cuts followed the relation R/2. In other words, the two resistances add in parallel. This supports the case that the sidewall damage layer act as the shunt path. If it had behaved as a metal-like conductive layer the resulting I-V relation would look similar to that predict in Figure 64. However, the deviation from expected diode behavior indicates that a different current mechanism exists which requires a new model of damage layer behavior.

4.4.5 Etch damaged leakage current

A literature search was undertaken to understand the current mechanism observed in FIB damaged LED samples. The search yielded nothing specific to FIB induced leakage in GaN devices, but did turn-up studies on leakage currents due to plasma etch and reactive ion etching (RIE) applied to device fabrication. One of the earliest investigations was by Pernot et al. who reported on leakage current in GaN pn-junctions[100]. They looked at GaN mesas of different sizes formed by reactive ion etching. They concluded that surface leakage along the mesa sidewall was the primary source of leakage under low bias voltages. However, the authors did not speculate on the current transport mechanism other than linking it to the RIE-induced damages. Dang et al. reported on Ar plasma damage of GaN based diode rectifiers[101]. Their results, re-printed in Figure 72, for the forward I-V characteristic shows significant increase in low bias current. Interestingly these results are similar to the predicted I-V characteristic for the FIB damaged diode (Figure 64). In other words, the forward bias curves in Figure 72 correspond to a metal-like conductive layer in parallel with the junction. Measurement of the near-surface stoichiometry by

Auger spectroscopy indicated that plasma exposure created a nitrogen deficient region. The authors concluded that these regions are strongly n-type which would degrade the forward I-V characteristic by reducing the barrier to current conduction.

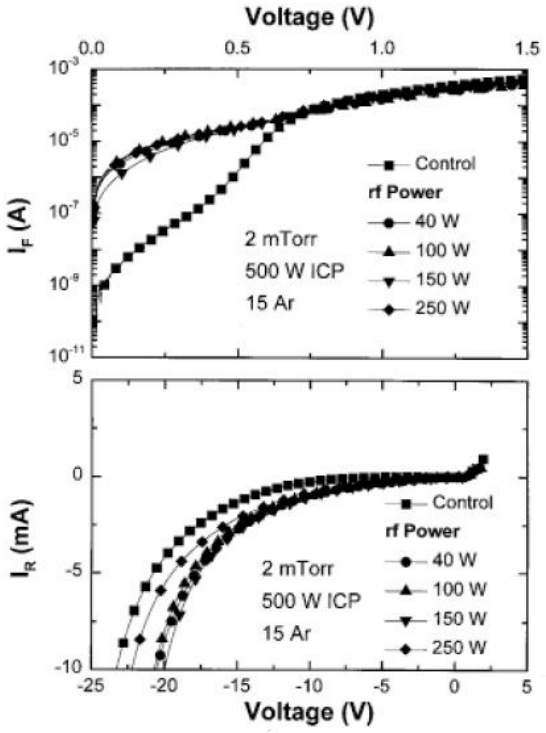


Figure 72: Forward (top) and reverse (bottom) I-V characteristics from GaN diodes exposed to Ar discharges (From Dang et. al.[101]).

Hirsch and Barriere[87] studied electrical behavior of GaN LEDs and described the charge carrier transport mechanism over different voltage regions. Of note to the FIB damage layer are results for what was defined as low bias conditions, $V \leq 1.5$ V. For this region Hirsch and Barriere characterized the leakage currents in parallel with the device junction. They hypothesized the presence of a shunt material that acted as a resistor R_{sh} connected in parallel with the junction. Based on measured currents Hirsch and Barriere surmised that the shunt was a semi-insulating material with a high density of electronic localized states. These states exist in the energy band gap due to the presence of defects. The leakage currents

could then occur at device sidewalls due to damage from reactive ion etching[100, 102]. The large density of defects yields a quasi-continuum of neutral or coulombic states in the band gap. Biasing then lowers the potential of the trap barrier making it easier for charge carries to escape by thermal emission or direct tunneling. Hirsch and Barriere went on to report for room temperature and above results indicate that leakage currents correspond to a field-enhanced thermal emission of charge carriers from coulombic states. Charge transport exhibiting this behavior corresponds to the Poole-Frenkel mechanism[103].

4.4.6 Poole-Frenkel effect

In an n-type semiconductor with no electric field the rate of change in electron concentration is given by;

$$\frac{\Delta n}{\Delta t} = \sigma v_{th} n \mathrm{N}_t \tag{4-4}$$

Where n is electron concentration, σ is trap cross-section, v_{th} is thermal velocity, and N_t is trap concentration. If an electric field is introduced the current produced is called Poole-Frenkel current[8, 103]. Similar to the Schottky effect, the electric field lowers the coulombic potential barrier making it easier for electrons to move into the conduction band. For both the Schottky and Poole-Frenkel, effect the barrier results from a coulombic interaction between the carrier and charge of the trap. To distinguish the Poole-Frenkel effect the trap, by definition, is positively charged when empty and neutral when an electron is captured. A trap that is neutral when empty and charged after capturing an electron or hole will not experience the Poole-Frenkel effect. Furthermore, with Poole-Frenkel emission the positive charge is fixed in the lattice, unlike Schottky emission where the positive charge is a mirrored image and moves away from the emission site. A schematic of the center resulting in Poole-Frenkel current is shown below in Figure 73.

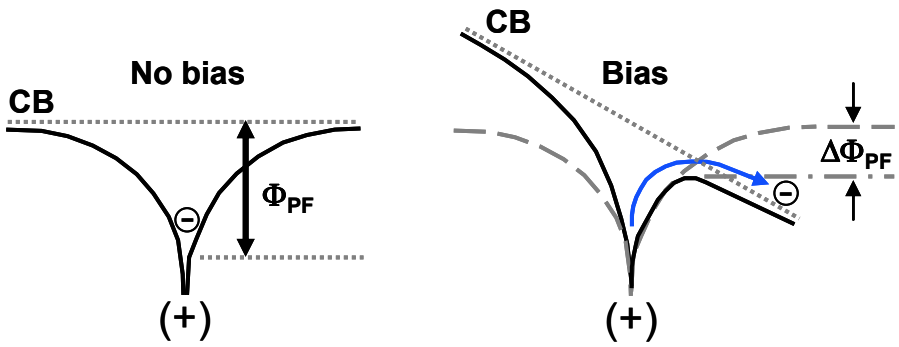


Figure 73: Energy diagram of trapping center with Poole-Frenkel emission (Adapted from Mitrofanov and Manfra[104]).

Electrons supplied to traps behaving as deep donors are emitted by thermal emission into the conduction band under an applied bias by thermal emission. The traps could be present in the as-grown material or introduced by processing.

For semiconductors the Poole-Frenkel effect manifests itself by a linear region in a log(I) versus $V^{1/2}$ at room temperature and above. Hirsch and Barriere observed this behavior observed for low bias leakage currents in GaN LEDs[87]. It has also been reported by Morkoc that the Poole-Frenkel effect has extensively been applied to conduction in amorphous materials[8].

Figure 74 is a Hirsch-Barriere log(I)-$V^{1/2}$ plot of the results shown in Figure 69(b). The dashed curves are for the initial die before FIB milling and the solid curves for the die after milling of Cut 1. Forward and reverse bias results are shown as well. The figure above shows log(I) is linearly dependent on $V^{1/2}$ for low forward bias conditions up to $\approx$ 1 V. Also observed, is similar dependence for the reverse bias condition (blue curves). This is expected as low forward bias and reverse bias conditions are both characterized by leakage currents. It is interesting to note that for the initial die absolute values of current for low forward and reverse bias are almost identical, as this regime is below the characteristic turn-on voltage of the diode and current flow is necessarily not via the junction itself. This is not the case for the post-FIB die where the forward bias I-V characteristic shows significant increase in low-bias current compared to absolute values from the similar reverse

bias range. Apparently, FIB damage degrades the forward I-V characteristic more so than the reverse. The exact nature of this behavior is unknown, but following Dang et al.[101] we speculate that the FIB induced damage layer results in an n-type region, which degrades the forward I-V characteristic. Alternatively, the reverse I-V characteristic is more dependent on bulk doping and less affected by the FIB damage. As such, the working hypothesis for the observed FIB damage I-V characteristic can be stated as: Leakage current from FIB milling damage to the device sidewalls occurs via Poole-Frenkel mechanism.

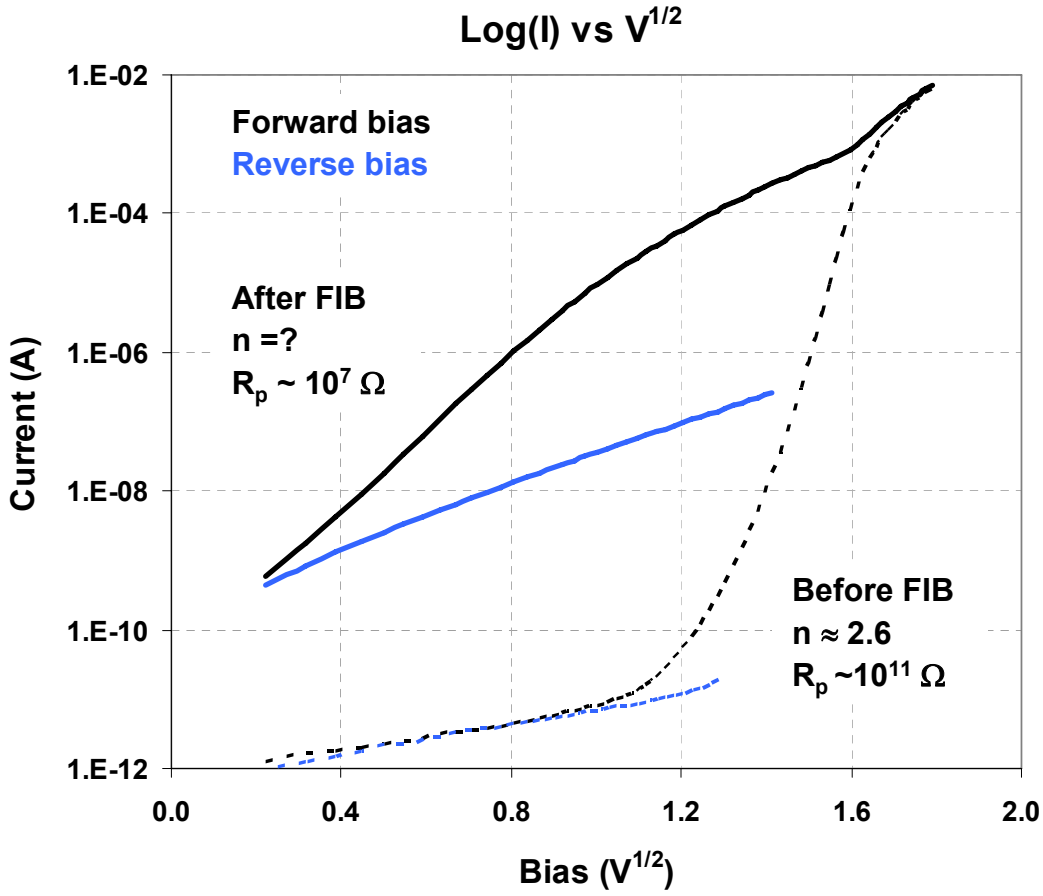


Figure 74: Low bias linear dependence of log(I) versus $V^{1/2}$.

4.4.7 Progressive mill

To investigate the sidewall effect a progressive mill study was set-up. The concept was to take an un-milled die and progressively FIB mill from one side taking I-V data after each cut was complete. The goal was to confirm that FIB induced leakage current is due to damage of the GaN sidewall. Recall the structure of the typical LED used in this work has a ~ 2 μm GaN mesa of slightly smaller area on top of a SiC substrate (Figure 10). The mesa contains the p- and n- GaN layers as well as the QWs.

The first cut then is into the SiC and up to but not into the GaN mesa. Figure 75(a) shows a schematic cross-section of the SiC cut and, (b) a top-view of the actual cut. Figure 76 shows the I-V characteristic for both the initial LED and post-SiC cut. As the I-V curves are effectively identical it is concluded that milling into the SiC did not enable a leakage current.

The second FIB cut was into the GaN mesa with Figure 77(a) showing the cross-section schematic and, (b) a top-view of the cut. In this case, the resulting I-V characteristics shown in Figure 78 indicate that milling into the GaN mesa did increase leakage current. This supports the picture thus far that FIB sidewall damage enables a shunt or leakage path around the pn-junction. The damage can result in a significant deviation of the I-V characteristic indicating that the diode behavior has changed. A deviation from expected diode behavior may mean the sample is no longer usable for STEM-EBIC analysis unless the damage can be removed and the diode behavior recovered.

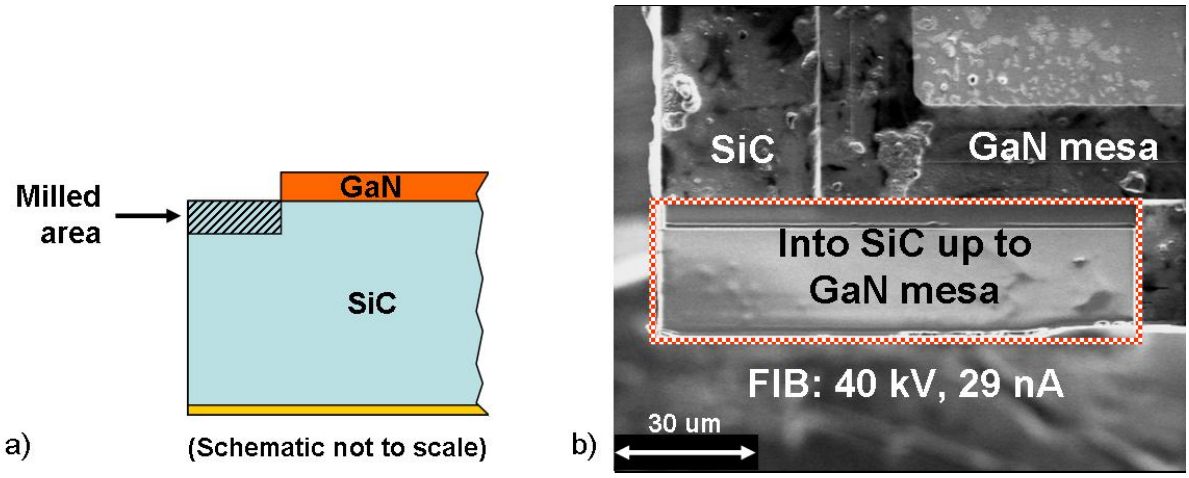


Figure 75: Progressive mill SiC cut. a) Schematic-cross section. b) Top-view of cut.

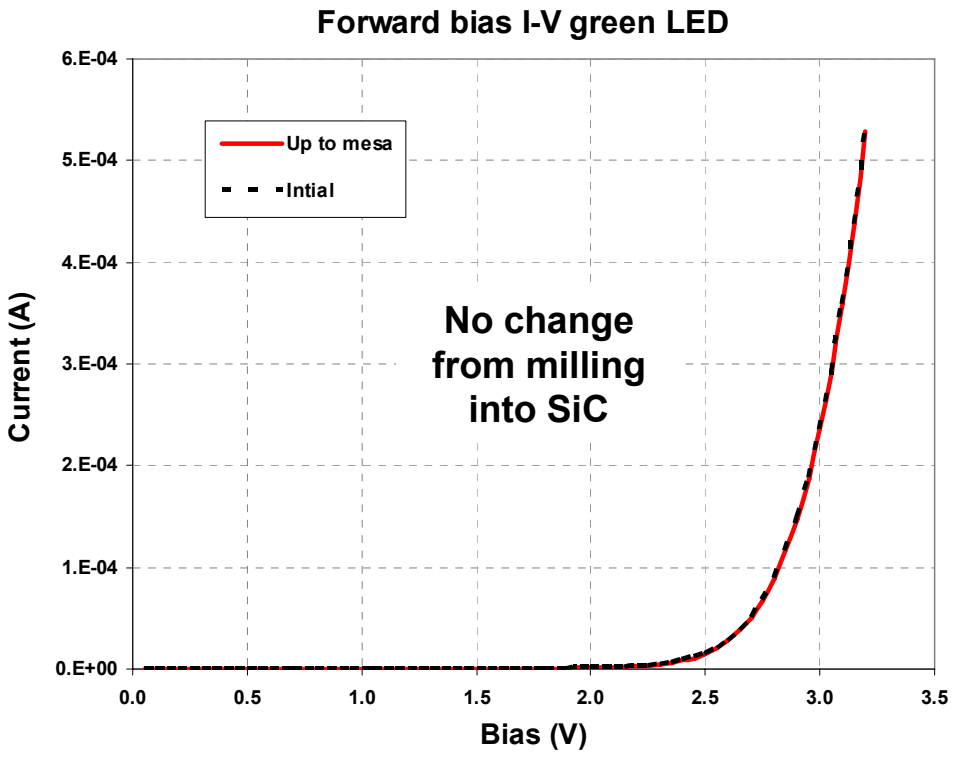


Figure 76: I-V characteristic after milling SiC.

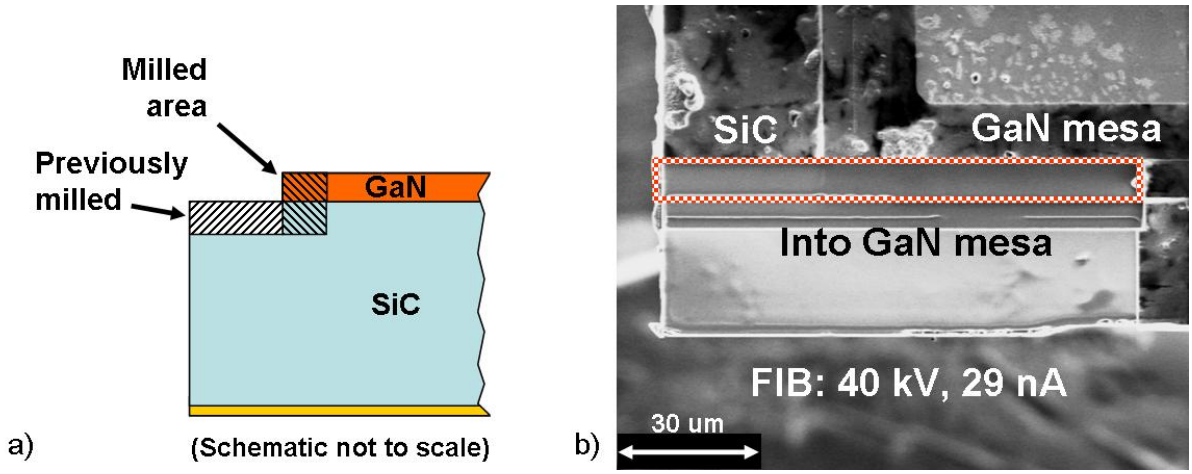


Figure 77: Progressive mill GaN cut. a) Schematic cross-section. b) Top-view cut.

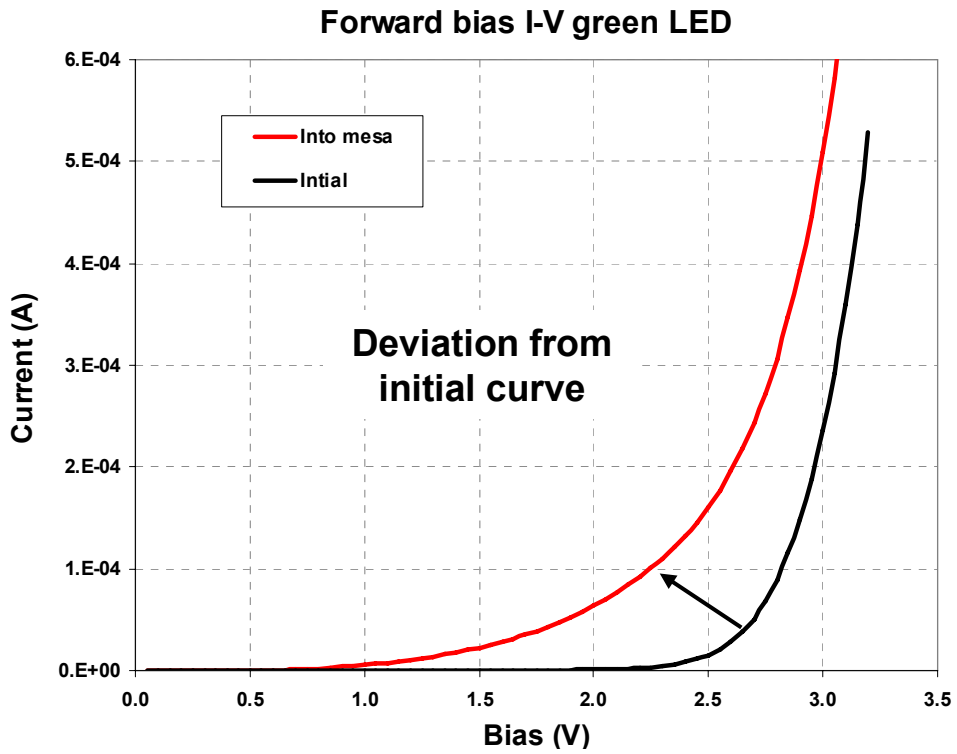


Figure 78: I-V characteristic after milling into GaN mesa.

4.4.8 FIB damage removal

4.4.8.1 Damage thickness

Before trying to remove any FIB induced damage it is worth estimating how much damage is present. SRIM[105] Monte Carlo simulations of the ion ranges of Ga^+ beams with GaN substrate for 10 and 40 keV are shown in Figure 79. From these results it was estimated that that a 40 keV Ga^+ beam can produce ~ 20nm of sidewall damage. If the beam energy is lowered less damage is induced. From the 10 keV simulation it was estimated that ~ 10 nm of sidewall damage was produced. The simulation results are in close agreement with experimental data for damage depths reported by several groups[106-108]. We now consider options for removing FIB damage from along the FIB formed sidewalls.

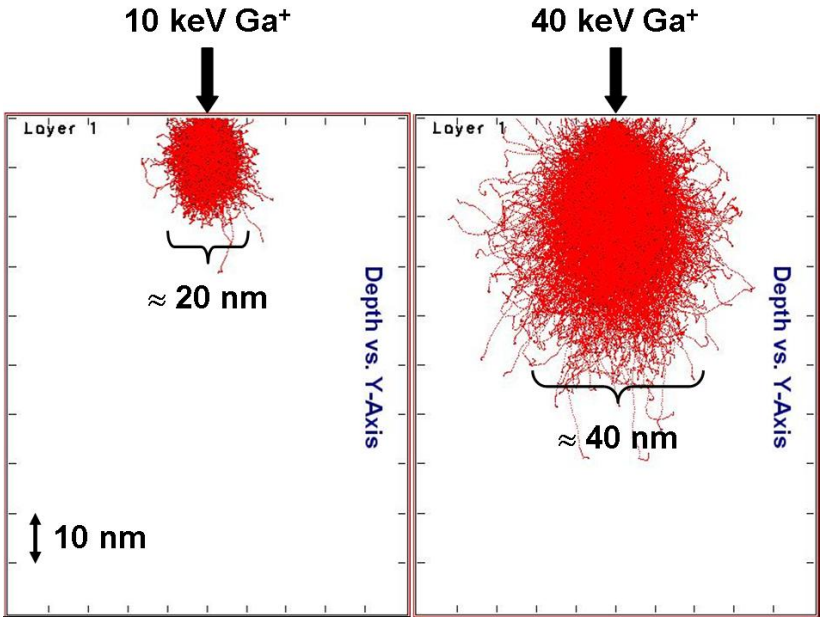


Figure 79: Simulations of ion ranges of Ga^+ beams with GaN substrate for 10 and 40 keV.

4.4.8.2 Low energy FIB polish

As shown in Figure 79 lowering the beam energy reduces the damage depth. However, lowering the beam energy also reduces the etch rate. The FIB used in this work can be operated at 10keV while other ion columns have been extended at the low range to beam energies 5 – 2 keV. FIB cuts made to LED samples in this work used a 40 keV Ga^+ beam with an expected 20 nm damage layer. The approach then is to use the smaller interaction of the lower energy 10 keV beam to remove damage from the 40 keV beam. This method was applied to the LED undergoing cross-rib prep. Figure 80 shows the I-V characteristic for the initial LED, after FIB milling of cross-rib section and after low energy polish.

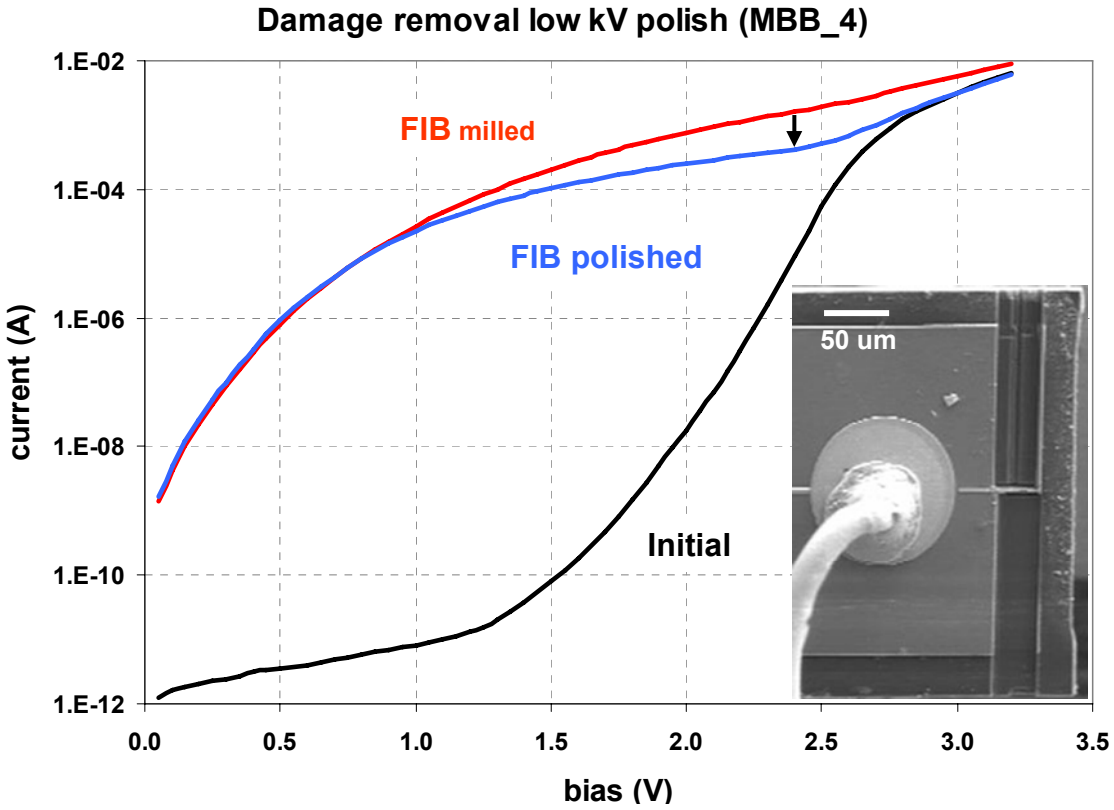


Figure 80: I-V characteristic of low energy FIB damage removal.

The 'FIB milled' curve reflects the I-V characteristic for the sample shown in the insert of Figure 80. To remove damage due to milling of the large cuts the FIB

was operated at 10 keV and the sidewalls polished. However, as seen in Figure 80 the I-V characteristic for the polished sample shows little recovery of the initial diode behavior. One problem resulted from managing the large exposed sidewall perimeter. Approximately 160 μm of sidewall on either side of the rib needed to be cleaned. To place the mill pattern with any accuracy required increased magnification. This in turn reduced the amount of sidewall that could be observed and cleaned at any given time. Thus the process was done piece meal rather than all at once. This likely lead to redeposition as milled material could reach cleaned surfaces by line of site. In all the trade-off between resolution and amount of perimeter cleaned made it difficult to successfully polish across a sidewall greater than 40 μm in length. Since by default long sidewall perimeters are produced by the cross-rib method we investigated an alternative damage removal option.

4.4.8.3 Wet etch

Literature reported that KOH wet etching has been used to remove surface damage in GaN[106]. Damaged regions were removed in hot solutions of KOH while the undamaged GaN does not etch at an appreciable rate[109]. To investigate, a 20% KOH solution heated to 60 C was prepared. For that concentration and temperature a 10 nm per minute etch rate was predicted. The sample at this point it had been through the cross-rib prep process and was expected to have a 20 nm damage layer along the side walls. Thus 1 and 2 min etch times were considered. I-V results for FIB damage removal using a KOH wet etch are shown in Figure 81.

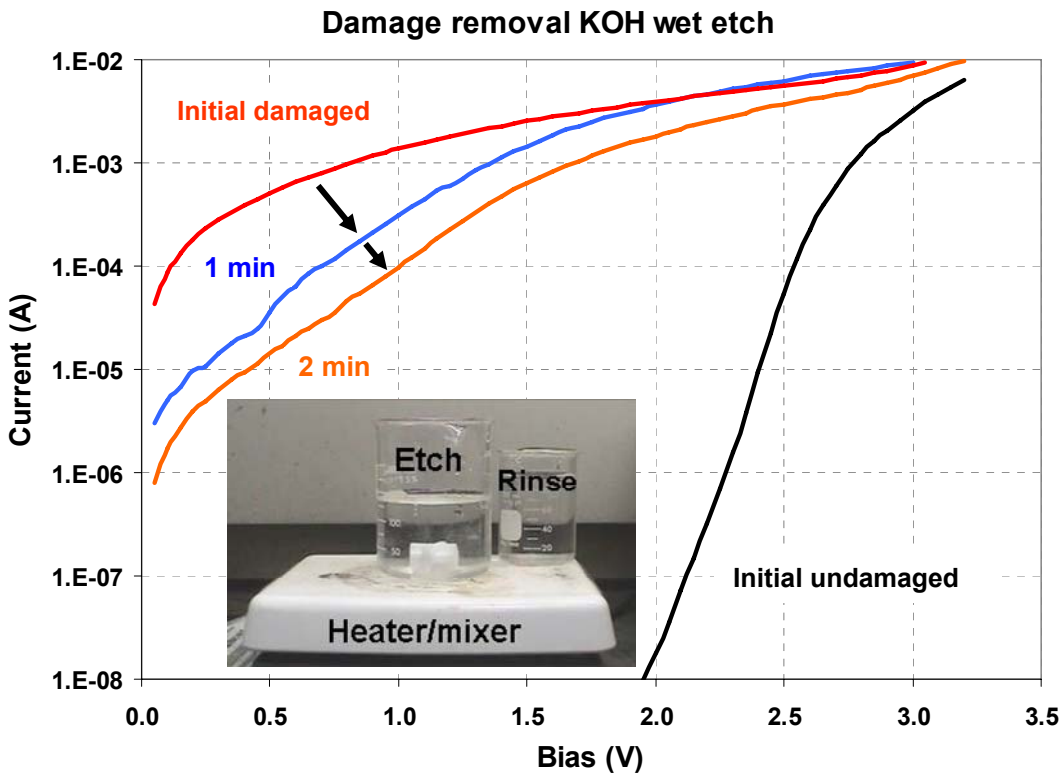


Figure 81: I-V characteristic of KOH wet etch FIB damage removal.

The initial damaged I-V characteristic is shown in red with the initial undamaged curve shown in black for reference. The wet etch set-up is shown in the insert. The mounted sample was dipped into the etch batch which was agitated by a magnetic mixer. When the desired etch time was reached, the sample was transferred to the rinse beaker to stop the etch process. The sample was then placed in a 40 C oven to dry before I-V data was recorded. From Figure 81 for the 1-minute etch a noticeable improvement in the I-V characteristic is observed for bias conditions below 2 V. This was encouraging and the sample was placed back in the etch bath for an additional minute. Results for the 2-minute etch showed continued improvement of the I-V characteristic over the entire bias range. Naturally the sample was once again placed into the etch batch for an additional minute. However, the previous two etch cycles weakened the silver epoxy bond holding the n-side of the sample to the holder. By completion of the third etch the sample

released from the holder. Attempts to reattach the sample were unsuccessful.

Never the less, some observations of the wet etch results can be put forth. First, if estimates for the etch rate were correct, then after 2 minutes the sidewall damage should have been removed. However, I-V results do not indicate that is the case. Second, while the I-V characteristics improved after each etch it was only marginal improvements. From these observations it was concluded that for the dip set-up used it was difficult to control etch and rinse conditions. The sidewall feature is ~ 4 μm and dipping the sample into a gently agitated bath is not sufficient to achieve the required etch rate. It is likely that some form of forced flow or impingement is necessary to properly remove sidewall damage with wet etching.

4.4.8.4 Additional damage removal options

Results for the damage removal options investigated were somewhat disappointing. While alternatives exist and should be considered, none were readily available for testing. However, for completeness and future consideration those methods will be introduced here.

Ideally damage removal methods are site specific such as low-keV polish. Otherwise as noted with wet etching unwanted side effects can result in loss of the sample. Two additional methods were identified that have this capability. The first is gas-assisted etching. This involves the simultaneous exposure of an area being etched by a FIB to a reactive gas. Thus, chemically-assisted low-keV FIB etching may be another possibility for removing the damaged surface layers while introducing minimal new damage. The second method is electron-beam chemically-assisted etching. This is similar to the method just discussed, but because an electron beam does not cause surface amorphization or implantation like an ion beam, e-beam etching would produce little damage. It should be noted that while both these methods should be considered, a significant development effort is likely necessary to realize their potential. Lastly, while not site specific low-energy ion milling with a broad Ar ion beam can be used to remove FIB induced damage

layers[110]. Specialized ion polishers are available from vendors such as Fiscione that enable controlled milling.

4.4.9 Cross-rib prep summary

In this section a novel sample prep method for STEM-EBIC was presented. The approach taken was to use FIB based milling techniques in lieu of mechanical polishing for initial thinning of the sample. Expected benefits were less damage from reduced handling and mechanically introduced stress, and rapid sample prep. Furthermore, the approach retained the n-side device contact which was problematic with the STEM-EBIC lift-out method.

The development of a full die, non-mechanical polish STEM-EBIC prep method first required a modification to the sample holder design. The successful redesign produced a holder that did not limit the sample height and provided access to the full active area of the sample for FIB milling. Next feasibility to form the cross-rib section was demonstrated as well as the potential for reduced sample handing. Novel implementation of in-situ I-V data collection was used to characterize the milling process and effect of FIB induced damage on the device behavior. It was concluded that FIB sidewall damage provides a shunt electrical path around the device junction. Results suggest that the electrical transport phenomenon in the damage layer corresponds to the Poole-Frenkel mechanism. It was observed that damage can be significant enough that the device deviates from diode behavior. As such two damage removal methods with the goal of recovering the diode I-V characteristics were evaluated. Results for both wet etching and low-energy polish were somewhat disappointing. For both methods it was concluded that the implementation as applied to the cross-rib sample was too difficult to control. In the case of wet etching the use of a bath did not provide sufficient fluid flow across the sidewall surface to satisfactorily enable the etching process. In the case of low-energy polish the long sidewall perimeter required piecemeal polishing resulting in redeposition on cleaned surfaces. Lastly, additional damage removal methods were

presented for consideration, but did require development efforts to realize their potential.

4.5 Mechanical pre-thin

4.5.1 Introduction

Results from the cross-rib prep method indicated that it was difficult to remove FIB damage from large sidewall perimeters. The primary factor that determines the resulting sidewall perimeter length is sample size. Recall that the cross-rib method was intended as a FIB only prep that started with a full sized die. Thus, to reduce the sidewall perimeter means reducing the starting sample size. This then is the basic premise of the pre-thin method shown schematically in Figure 82.

Lastly, a distinction between mechanical and FIB damage needs to be made. The pre-thin method effectively exposes the entire pn-junction along one direction while the cross-rib method exposed approximately half. How does the sample I-V characteristic change after polishing and how sensitive is the exposed junction to contamination will need to be determined.

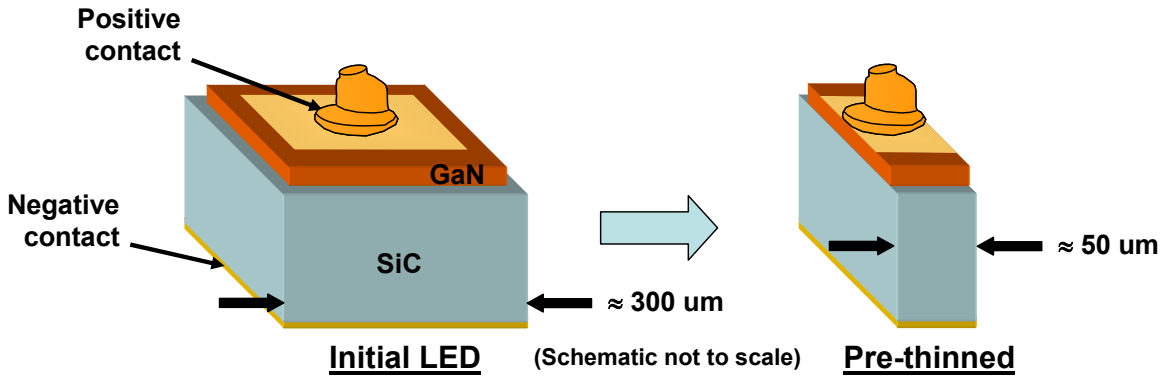


Figure 82: Schematic of pre-thin sample prep.

4.5.2 Pre-thin process

As with the cross-rib method the pre-thin method will need to retain the device side n- and p-contacts. Doing so for the n-side contact should be straight forward, but for the p-side contact it will be beneficial to retain the wire bond as well for

reasons explained later. Furthermore, the pre-thin method reduces the sample area and the impact on the I-V characteristic needs to be considered.

In order to reduce handling and preserve the p-side wire bond each sample that was to be pre-thinned was first mounted on a sacrificial jig. The jig base consisted of a 12 x 6 mm piece of silicon. A drop of super-glue gel was placed near the short edge of the silicon and a sample placed in the gel standing up. Before the gel had time to set the wire bond was used to position the sample parallel with the silicon edge. Pieces of a 0.2 mm cover side ~ 4 mm square where then super-glued and stacked close behind the mounted LED sample. The stack height was determined by the sample height and bend radius for the wire bond. An additional piece of cover slide that will serve as the cap window was cut to size ~ 4 x 6 mm. The window is critical not only for protecting the top of the die but also for allowing a top down view of the sample through out the polishing process. The jig assembly was then placed on a hot plate set at ~ 110 C and Crystalbond 509 melted to cover sample and fill gap between slide stack. The cap window was then applied and the assembly set aside to cool. The completed jig is now ready to be mounted to a polishing stub for mechanical thinning.

Bunker et al.[111] developed diamond lapping polishing techniques for optoelectronics devices to mechanically thin samples. While cross-section sample thicknesses of ≈ 50 μm were achieved, the method used a rather course 6 μm diamond pad. It has been reported that polishing damage can extend into the sample distances equal to the particle sizes on the diamond pad[112]. Here polishing was extended to finer grit sizes to minimize surface damage. The polishing sequence is detailed below were transition to the next finer pad was made at a distance from the target start of the next pad approximately equal to 3x the grit size of that pad.

1. 6 μm diamond pad to polish through excess glass and silicon. Stopped ~ 9 μm short of die.
2. 3 μm diamond pad to polish into die. Stopped ~ 5 μm from targeted final polish surface.

3. 1 μm diamond pad to polish ~ 3 μm. Stopped ~ 2 μm from targeted final polish surface.
4. 0.5 μm diamond pad to polish ~ 2 μm to targeted final polish surface.
5. 0.05 μm colloidal silica to produce final polished surface.

Following this sequence the first side of the sample was polished. Next the sample had to be removed from the jig and remounted to polish the opposite side. Both super-glue and Crytalbond 509 dissolve easily in acetone and the extracted sample dried. Retaining the p-side wire provided a 'handle' to manipulate the sample and remount it polished face down on the silicon base. The rebuilt jig was then attached with Crystalbond 509 to a polishing stub. As before a cap window was placed so that polishing progress can be observed. Once the desired thickness was achieved the sample was cleaned in an acetone bath. A final clean in ethanol then methanol followed. This completes the pre-thin process and the sample was ready for attach to the sample holder.

4.5.3 Attaching pre-thinned sample

Several approaches to landing a polished sample on the test holder were considered. Initially the method used to land a full die, which was successful with the cross-rib method, was attempted. This proved difficult as the sample would tend to flop to one side or the other due to its increased aspect ratio. Eventually a method was worked out whereby the sample was placed on a glass slide and secured in place with super glue.

Figure 83(a) shows a polished Cree UltraThin LED secured to a glass slide. The sample was received as a full bare die mounted on a TO header. That configuration allowed initial I-V measurements to be taken which then served as a base line results. The sample was removed from the TO header and polished following the process described in the previous section. A sample holder with silver epoxy applied to the cathode contact was placed on the glass slide and mated to the n-side of the polished sample. Figure 83(b) shows the assembly from the anode side. To cure the silver epoxy, the sample holder was placed in an oven at 100 C for

ten minutes. Figure 83(c) shows the cathode contact and silver epoxy bond after curing. Next the super-glue was removed with acetone and the p-side wire gently positioned into contact with the anode and secured with silver epoxy. This yields a functional sample as confirmed in Figure 83(d) which shows the sample emitting under forward bias.

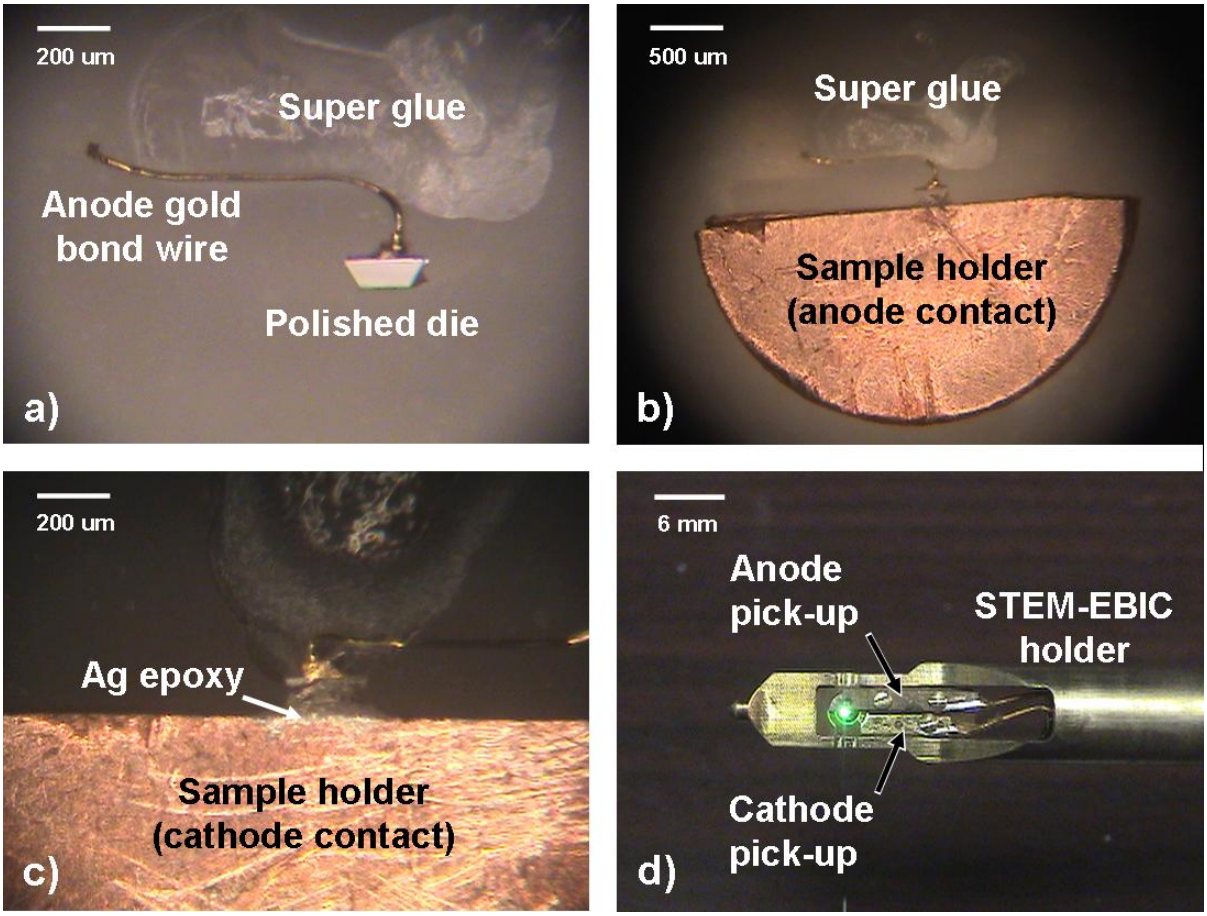


Figure 83: Mounting and test of pre-thinned sample. a) Mechanically polished die secured to glass slide. b) Sample holder attached to thinned sample. c) Cathode side of holder showing Ag epoxy attach. d) Sample in STEM-EBIC holder emitting under bias.

4.5.4 Characterization results

Figure 84 shows the current density (J) – voltage characteristic history for the pre-thin sample at various stages of sample preparation. Forward and reverse bias results for the initial sample reveal typical diode behavior with an estimated parallel resistance of ~ 10^{12} Ω with an ideality factor of 2.5. Mechanical polishing thinned the sample in cross-section to ~ 43% of its original size. By plotting current density the loss in sample size should be accounted for. This is almost the case as shown by the blue J-V plot for the mechanical polished sample. We observe a current increase for low bias conditions due to leakage across the exposed junction due to polishing damage. This is also reflected in the reduced parallel resistance of 10^{10} Ω. However, the resistance changed by only two orders of magnitude and overall the diode behavior was maintained. Indeed for roughly 2 V and above the J-V characteristic for the sample after polish essentially matches that for the unpolished initial condition. From this we conclude that mechanical polishing introduces negligible levels of sidewall damage.

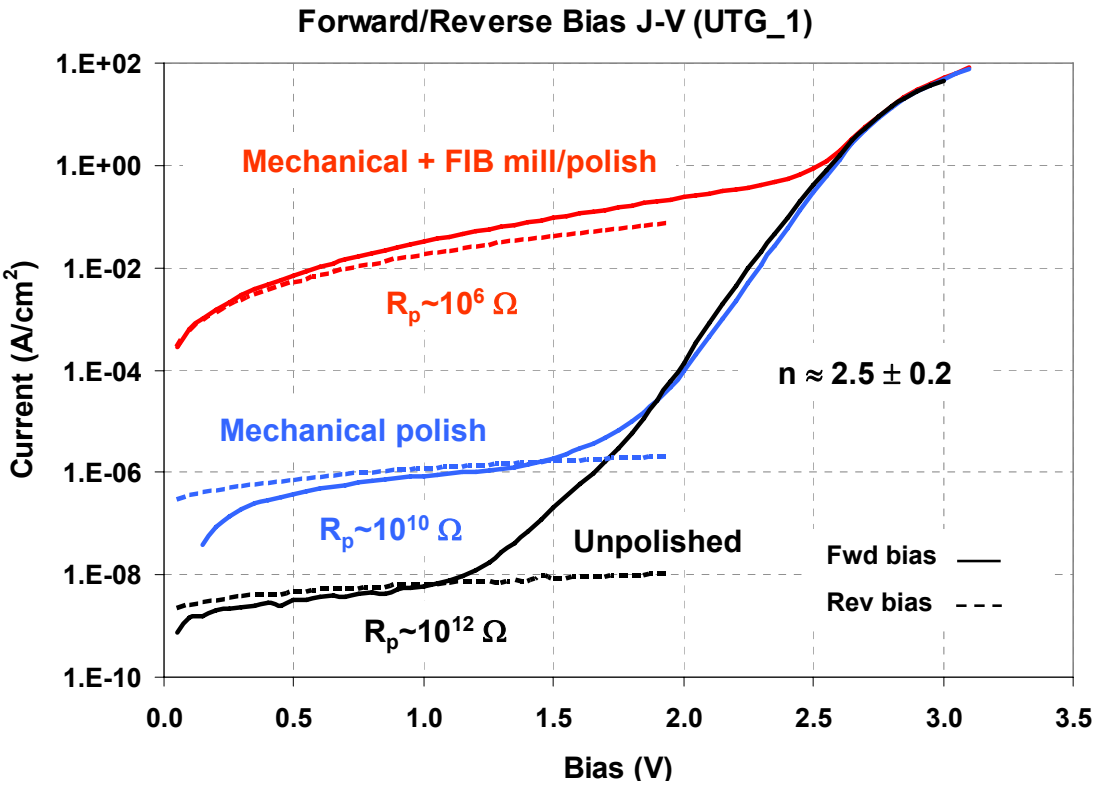


Figure 84: Current density versus voltage characteristics for pre-thin sample prep.

The sample was next placed into the FIB and processed following the cross-rib method from section 4.4. The sample had been pre-thinned to ~ 85 μm so the resulting sidewall perimeter with FIB damage was ~100 μm on each side of the rib. This is still fairly large, but ~⅓ less than with FIB prep of a full die. The pre-thinned sample with FIB milled cross-section is shown in Figure 85 below.

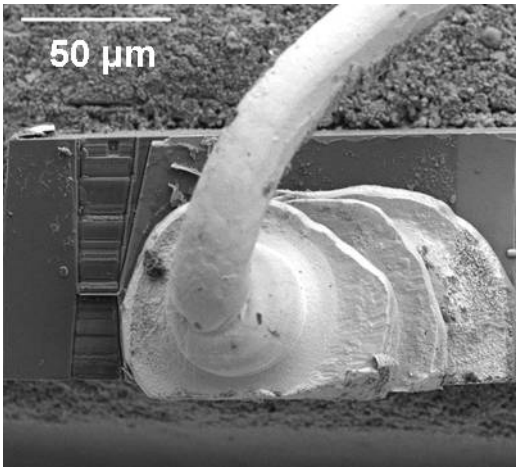


Figure 85: Mechanical pre-thinned sample with FIB formed cross-section.

The resulting J-V characteristic for pre-thinned sample after FIB shows a marked increase in current for biases up to 2.5 V. Parallel resistance decreased by four orders of magnitude to ~ 10^6 Ω reflecting increased leakage current due to the FIB damage layer. However, unlike the 'bowed' I-V characteristic observed in Figure 69(b), with the full die prep, the J-V profile for the pre-thinned sample is relatively flat. This was taken as an indication of better control of FIB induced damage. In addition, an after FIB parallel resistance of 10^8 – 10^6 Ω was set as the acceptable range target. As such, the pre-thin method was employed for sample prep of all STEM-EBIC samples discussed from here on.

4.5.5 Offset mounting jig

One last bit of sample processing specific to the attach method needs to be discussed. It was soon recognized that the approach used for mating a holder to

sample had limitations. The sample and holder were on the same plane of the glass slide. One problem would result from silver epoxy smearing as the holder with epoxy was slid into contact with the sample. After contact, the epoxy tended to wick across the sample surface and sometimes reach the exposed pn-junction. Another problem appeared as polishing improved and mounting of thinner samples was attempted. In this case the holder would tend to ride above the sample rather than mate to it. After several unsuccessful attempts to tweak the sample height by titling, the need for an off set mounting jig was acknowledged. Figure 86(a) shows a schematic cross-section of the jig and (b) shows the actual jig. As can be seen the (2) pedestal is offset from the (3) pedestal by 0.05 mm. By positioning the holder on (2) and the sample on (3) this aligns the sample to land near the middle of the bottom contact. A small gap ~ 0.15 mm was placed between (2) and (3) to prevent any smeared epoxy from wicking across to the sample junction. Furthermore, the assembly was made with thermal epoxy and can go directly into an acetone bath to remove the sample as well as cleaning for the next sample. Lastly, the jig helps position the sample parallel with the holder, which in turn helps with on axis alignment in the STEM.

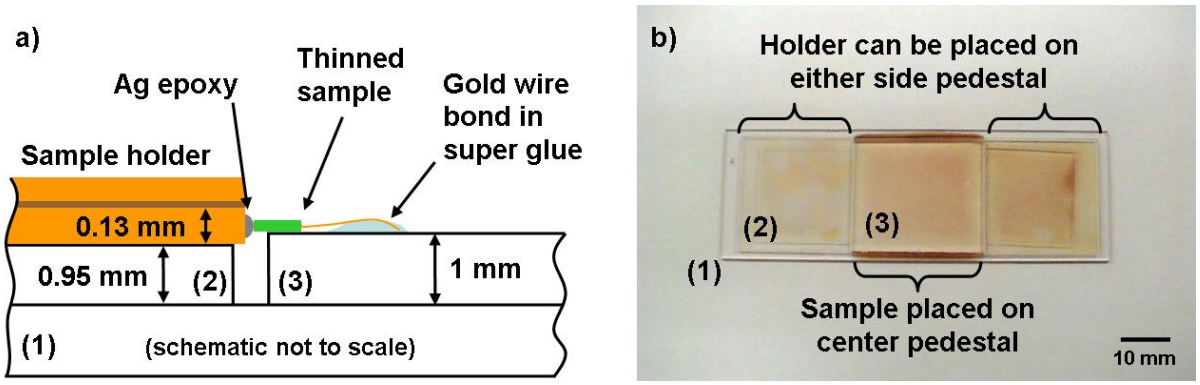


Figure 86: a) Schematic cross-section of mounting jig. b) Jig assembly.

4.6 Sample prep methods and results summary

Sample preparation is a key step in order to do successful analytical work. The old adage that you get out what you put in is especially true when applied to

sample preparation for electron microscopy and in particular high-resolution electron microscopy. The end goal of any (S)TEM prep is to produce a sample that accurately represents the bulk properties of the material investigated. Thus, characterization of the preparation process is necessary to give confidence in the subsequent investigation.

For STEM-EBIC samples, I-V curves were used to characterize alternative preparation methods and qualify samples for analysis. A novel in situ I-V measurement technique was applied to FIB and used to characterize and monitor processing damage to GaN based LEDs. With these tools three sample prep methods were investigated and the resulting device behavior discussed.

The first method presented was a novel application of FIB based lift-out techniques and micromanipulation to produce STEM-EBIC samples. First, a method for bridging between the sample and anode contact using an interconnect formed from gold foil was demonstrated. A FIB deposited Pt contact between the gold foil interconnect to sample grid yielded 25 Ω contact resistance. Methods to reform a low resistance contacts to n-SiC were also investigated. Three sputter coated metals Mo, Ti and Ta, were tested and showed some promise, but as yet not capable of yielding the required contact to n-SiC. Thus it was decided to forgo any further effort developing the STEM-EBIC method and pursue alternative sample preps that retained the n-side metallization. As a note, reforming the n-side contact may be less of an issue with other material systems. In that case the STEM-EBIC lift-out method should be considered as a potential sample prep option.

Next, a FIB based milling technique in lieu of mechanical polishing for initial thinning of the sample was investigated. Novel implementation of in situ I-V data collection was used to characterize the milling process and effect of FIB induced damage on the device behavior. It was concluded that FIB sidewall damage provides a shunt electrical path around the device junction. Results suggested that the electrical transport phenomenon in the damage layer corresponds to the Poole-Frenkel mechanism. Two damage removal methods with the goal of recovering the diode I-V characteristics were evaluated. Results for both wet etching and low-

energy polish were somewhat disappointing. For both methods it was concluded that the implementation as applied to the cross-rib sample was too difficult to control.

To reduce the resulting FIB damaged sidewall-perimeter meant reducing the starting sample size. Pre-thinning of the sample was achieved by mechanical polishing. To minimize damage a modified diamond lapping technique was employed. From J-V results of the thinned sample it was concluded that mechanical polishing as implemented introduced negligible levels of sidewall damage. The thinned sample was then milled in the FIB to produce the final cross-section. Test results then showed an increase in leakage current due to FIB sidewall damage. However, unlike the 'bowed' I-V characteristic observed with the full die prep the characteristic profile for the pre-thinned sample was relatively flat. This was taken as an indication of better control of FIB induced damage. As such, the pre-thin method was employed for sample prep of all STEM-EBIC samples discussed from here on.

5. STEM-EBIC Experiments and Results

5.1 Motivation

In this work motivation for STEM-EBIC came from the need to investigate the affect of LED device structure on EBIC inhomogeneity observed with SEM-EBIC. EBIC contrast variation similar to that shown in Figure 87 is observed in cross-sectional SEM-EBIC of MQW LEDs. The top half of the figure shows a secondary electron (SE) image of a polished LED cross-section. Half-way through the scan the input was switched from SE to EBIC. The bottom-half of Figure 87 is the resulting EBIC image where the vertical line indicates the pn-junction. From this image it is possible to determine the location of the junction and under appropriate electron-hole pair injection conditions minority carrier diffusion lengths. For a discussion on the latter, the reader is directed toward a review of various fitting models by Parish and Russell[113]. Of interest here, is the inhomogeneity of the EBIC signal present in Figure 87.

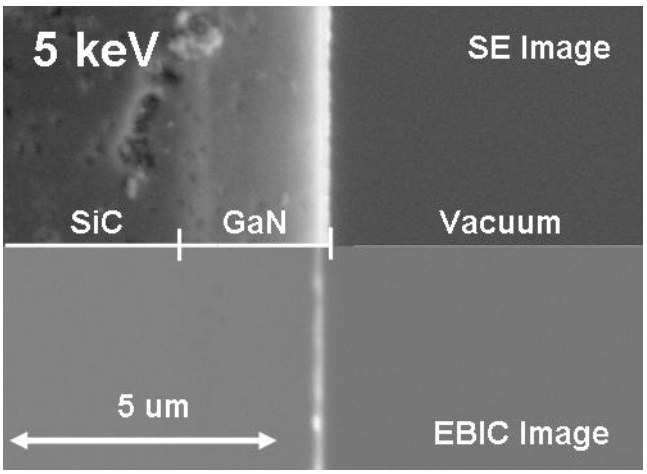


Figure 87: Cross-sectional view SEM-EBIC polished LED showing inhomogeneous EBIC signal.

A potential source of the observed EBIC contrast variation is electrically active defects. Recall that EBIC is a technique that allows the measurement of electrical properties of semiconductors in an SEM or STEM instrument. Defects

increase recombination rate, and reduce the recombination lifetime, of minority carriers. As such, areas near a recombination-enhancing defect are expected to have a high contrast and appear dark in an EBIC micrograph. Defects that are known to be present in GaN-based MQW LEDs were discussed in section 2.4 and include large threading dislocation densities, lattice mismatch stress and V-defects. On the other hand, the variation may result from some type of surface artifact altering the electron beam probe. In recognition of that possibility, it is necessary to first confirm that sample prep does not introduce the observed inhomogeneity.

Initially, the surface artifact hypothesis seems to be invalidated by results observed for plan-view EBIC. Unlike cross-sectional EBIC, plan-view EBIC does not require any sample prep of the top surface other than it be exposed to the electron beam. As a reminder, the reader is referred to Figure 14 for a schematic showing a plan-view EBIC experiment. Figure 88 shows plan-view EBIC results for the corner of an LED GaN mesa. The EBIC signal is observed to be inhomogeneous with clusters of dark spots spread across a bright background. In this case surface artifacts are in general not the cause of the observed contrast variation.

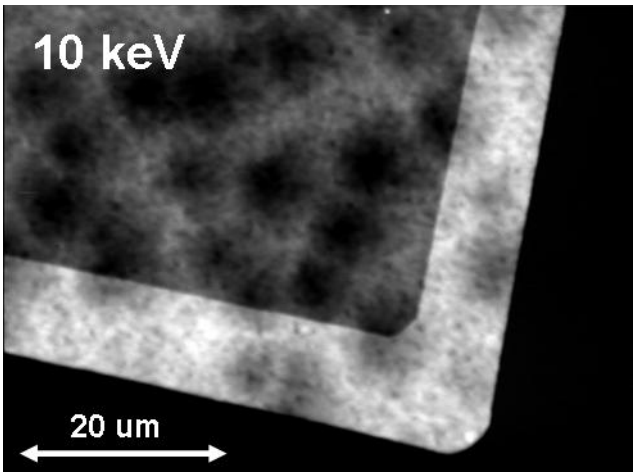


Figure 88: Plan view SEM-EBIC showing inhomogeneous EBIC signal (From Parish[114].

Of interest are both cross-sectional EBIC results in Figure 87 and plan-view EBIC results in Figure 88 show an inhomogeneous EBIC signal. A literature search on this artifact turned up nothing definitive related to combined plan-view and cross-sectional EBIC results. However, when the search was narrowed to a single technique two papers on cross-sectional EBIC stood out.

Kuroda et al.[115] investigated the control of pn-junction profiles. The authors looked at diffusion behavior of Mg impurities and the impact on pn-junction profile. The samples studied were InGaN/GaN based MQW laser diodes fabricated on sapphire and GaN substrates. Analytical methods used were secondary ion mass spectroscopy (SIMS) and EBIC measurements. SIMS was used to investigate Mg diffusion behavior while cross-sectional SEM-EBIC was used to evaluate the pn-junction. SIMS depth profile results indicated that Mg reached the n-side of the sapphire sample, but not the GaN sample. As the GaN sample should have a lower dislocation density because of better lattice matching, the authors suggested that unintentional Mg diffusion observed for the sapphire sample was enhanced by the presence of dislocations. Cross-sectional EBIC results for the sapphire and GaN substrates samples are reprinted below in Figure 89.

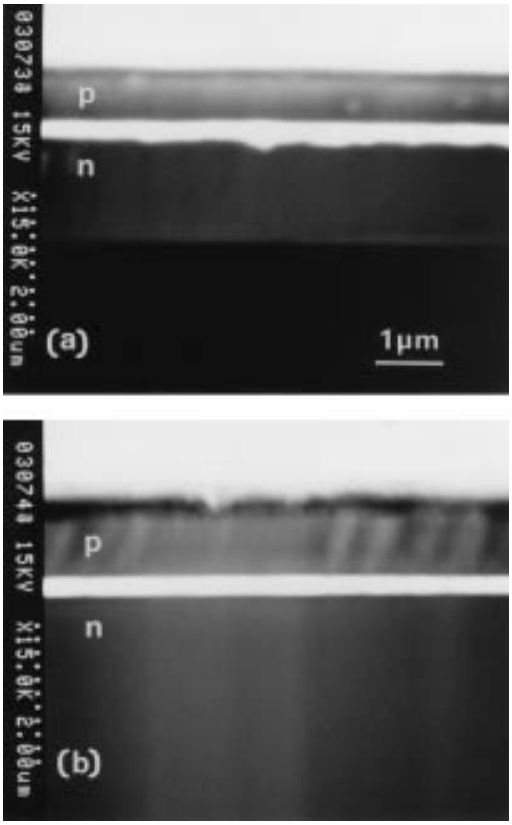


Figure 89: Cross-sectional EBIC images. a) Sapphire substrate. b) GaN substrate. (From Kuroda et. al.[115]).

The sapphire sample in Figure 89(a) shows an EBIC image that is wavy on the n-side and straight on the p-side, indicating the minority-carrier diffusion length within the n-side is inhomogeneous. The authors found that the spacing of the lateral inhomogeneity peaks roughly coincide with the expected spacing of the dislocation density. From that observation Kuroda et al. concluded that the minority-carrier diffusion length increased around dislocations with the inhomogeneous pn-junction profile due to unwanted Mg diffusion enabled by the presence of dislocations. This conclusion explains the wavy nature of the pn-junction, but not the contrast inhomogeneity observed in Figure 87.

More recently, pn-junction inhomogeneity was investigated by Moldovan et al.[116]. Low-voltage cross-sectional EBIC was used for characterization of GaN-based MQW LEDs. The samples studied were cross-sections of InGaN/GaN MQW

devices grown on sapphire. SEM-CL was used to investigate the optical activity and the reprinted results shown in Figure 90. A varying CL intensity is observed along the MQW layer in Figure 90(b). Areas of low CL emission indicate high non-radiative recombination, but correlation to the SE image could not directly confirm the presence a defect. However, based on the observed frequency of contrast variation and Moldovan et al. attributed the varying CL emission to threading dislocations.

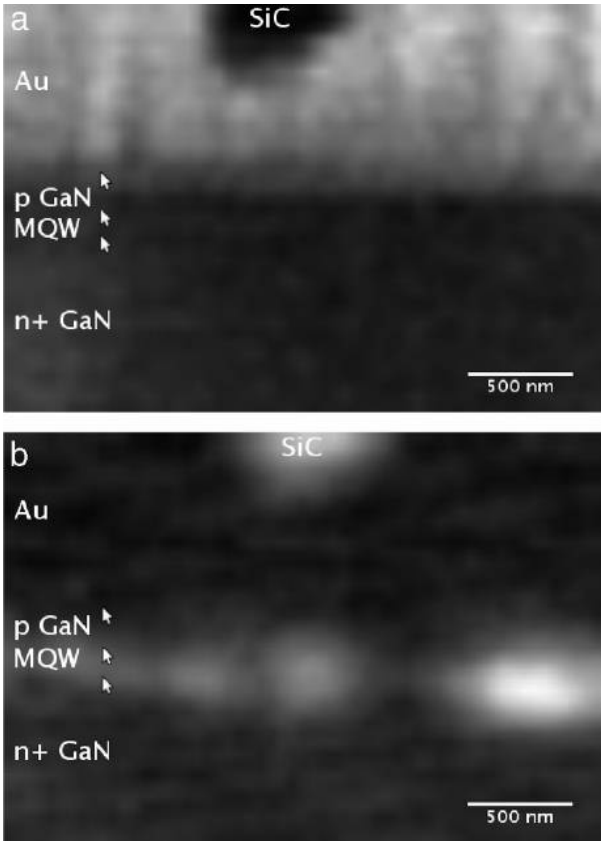


Figure 90: Low-voltage (7 keV) cross-sectional (a) SE and (b) CL images (From Moldovan et. al.[116]).

EBIC images were then taken of the same area and an inhomogeneous EBIC signal observed. Figure 91 is a reprint of the cross-sectional SE and EBIC results. The position of the bright extension identified in SE image, Figure 91(a), correlates with reduced EBIC signal identified in Figure 91(b). The authors went on to claim

that those artifacts correspond to the threading dislocations identified in the CL images from Figure 90. However, the methods used by Moldovan et al. did not directly correlate reduced CL or EBIC emission to dislocations. The correlation is based on comparable linear densities between threading dislocations and the varying CL/EBIC signals. Direct correlation of electro-optical properties to defects will require STEM-based analytical techniques.

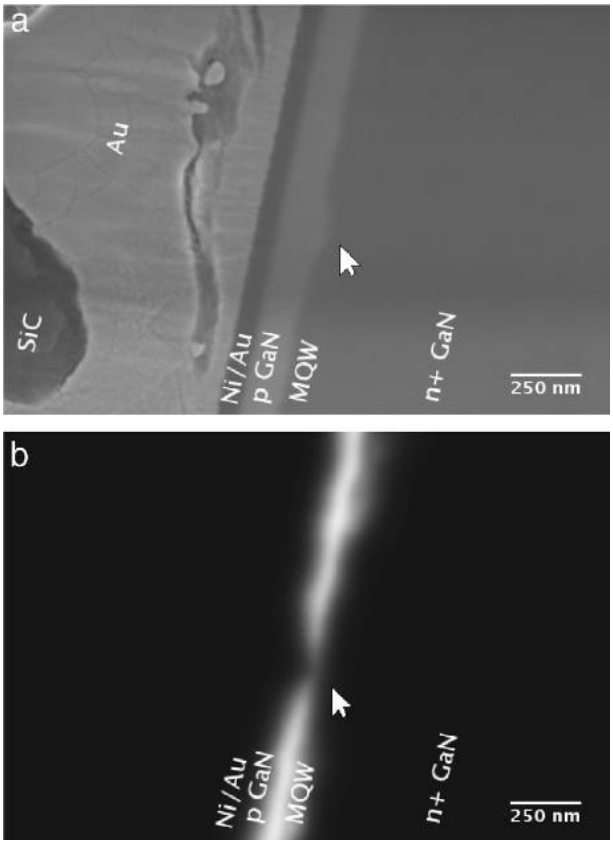


Figure 91: Low-voltage (4 keV) cross-sectional (a) SE and (b) EBIC images (From Moldovan et. al.[116]).

A search of STEM-EBIC investigations of GaN devices returned only the work by Bunker et al.[75] which was focused on precise location of the pn-junction in SQW GaN-based LEDs. While this goal was accomplished additional STEM-EBIC investigations were left for future efforts. The motivation then for work presented here is to extend STEM-EBIC capabilities to directly correlate defects to observed

EBIC behavior. The results could be passed on to device manufacturers and, used for process and subsequently device improvement.

5.2 Surface effect investigation

Before introducing the STEM-EBIC experimental plan, the earlier conclusion that inhomogeneity observed in the cross-sectional SEM-EBIC signal is not due to surface artifacts is revisited. To confirm this conclusion, the cross-sectional SEM-EBIC signal was first mapped to the sample. Figure 92(a) shows a SE image of a mechanically polished LED cross-section while Figure 92(b) shows the SE image repeated in the top-half before the input was switched to an EBIC signal. The images are aligned by comparing distinctive features in the top-half of both images. In this manner the EBIC signal from Figure 92(b) can be mapped to the SE image shown in Figure 92(a). Two emission levels are highlighted with arrows pointing to the location on the SE image for comparison. Doing so reveals that the contrast variation observed in the EBIC signal cannot be correlated to any visible surface features in the SE image.

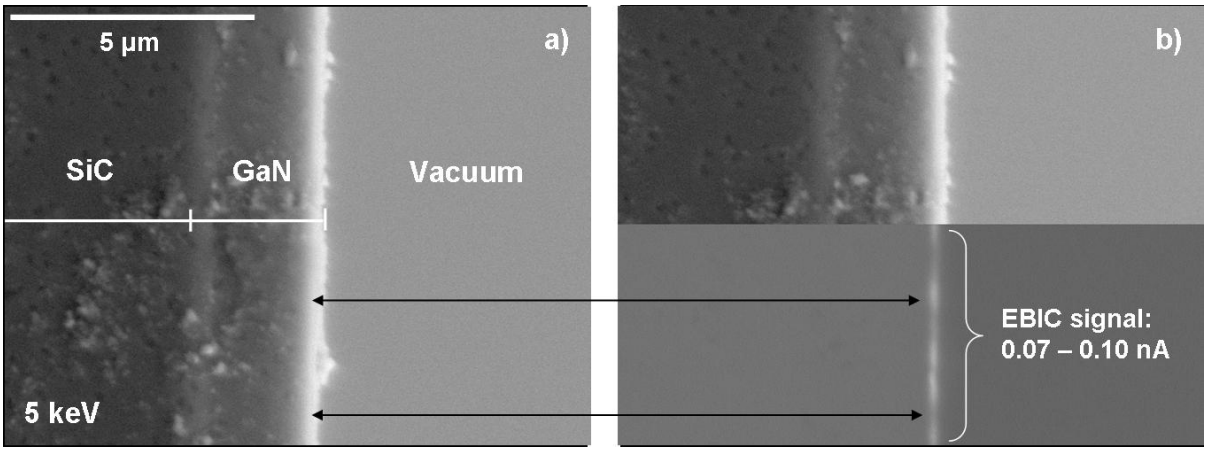


Figure 92: Cross-section SEM-EBIC mapped to SE image indicates that contrast variations in EBIC signal are not due to visible surface artifacts.

Continuing, the sensitivity of the exposed pn-junction was investigated. The sample was plasma cleaned and before/after cross-section EBIC results compared. Plasma cleaning was accomplished in situ with an Evactron® RF plasma system already mounted to the SEM chamber. The Evactron system uses low-powered RF plasma to produce oxygen radicals, which then oxidize and etch away hydrocarbons from the specimen surface. Figure 93 below shows an infra red (IR) image of the SEM chamber illuminated by the oxygen plasma during an Evactron clean cycle.

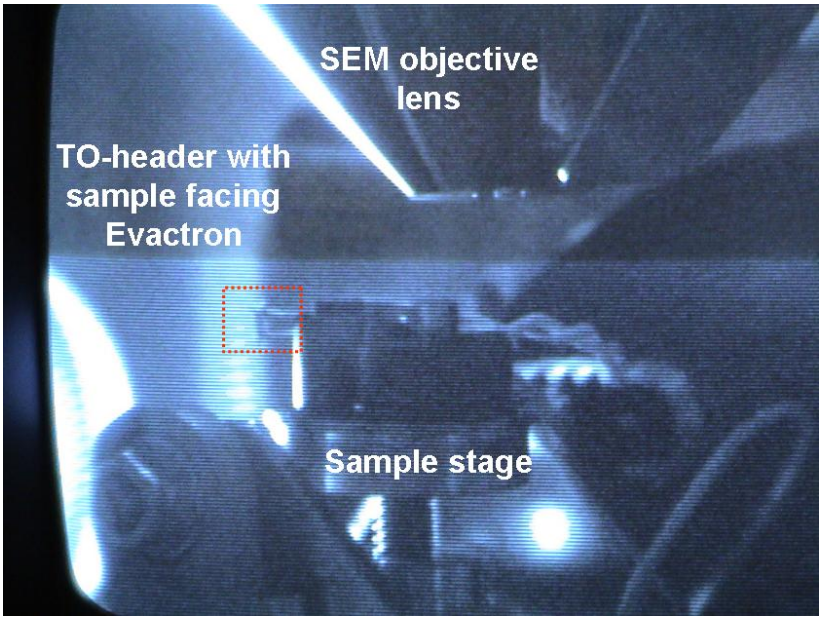


Figure 93: Oxygen plasma illuminated IR image of sample in SEM during Evactron clean. Sample is highlighted by dashed box.

The sample being cleaned is shown facing the Evactron port and is highlighted by a dashed box. After a 20 minute clean at an RF setting of 10 W the sample was repositioned under the objective lens. An EBIC image was then recorded from the same region prior to clean. To evaluate the surface before/after cleaning, EBIC intensity along the pn-junction was compared. Before and after plasma cleaning results, adjusted for brightness offset, are shown below in Figure 94. The insert at the bottom of the image is the pn-junction along which the before and after EBIC intensity measurements were taken.

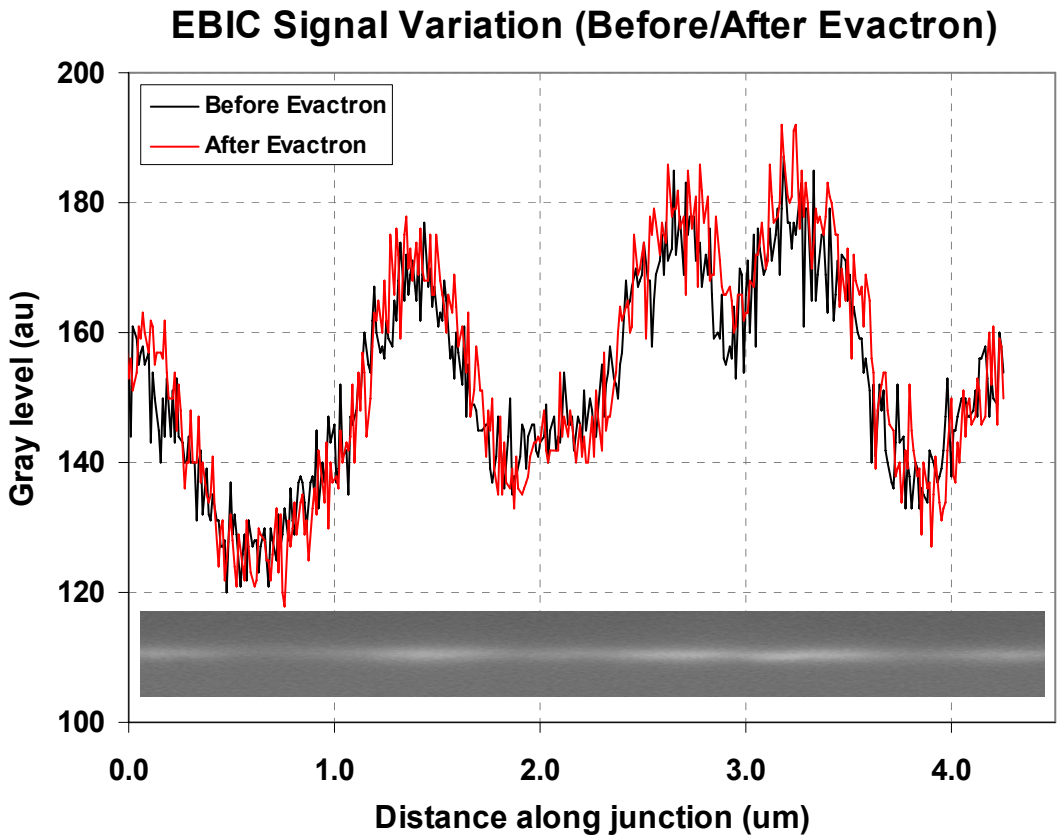


Figure 94: EBIC signal comparison along junction before and after plasma clean. Insert at bottom shows pn-junction along which intensity measurements taken.

From Figure 94 it is observed that the before and after intensity profiles are the same. This indicates that the spatial location of the source of signal variation did not change. Furthermore, relative intensities before/after plasma cleaning are the same, suggesting that the source of contrast variation was not affected by surface cleaning. Based on the results discussed in this section, surface artifacts were ruled out as the source of the observed EBIC signal inhomogeneity.

5.3 Experiment design

From the discussion in section 5.1, two explanations for the observed EBIC inhomogeneity were presented. Kuroda et al. reported that the inhomogeneous pn-

junction profile is due to unwanted Mg diffusion enabled by the presence of dislocations. While Moldovan et al. claimed that threading dislocations acting as non-radiative recombination sites produced the inhomogeneous pn-junction profile. However, neither group reported direct observation of individual defects on the EBIC signal. Furthermore, the results were for cross-sectional EBIC, and correlation to plan-view EBIC was not considered.

This presented an opportunity for extending STEM-EBIC capabilities to directly correlate defects to observed EBIC behavior and thereby investigate the hypothesis that threading dislocations produce the observed EBIC signal inhomogeneity. An experiment was designed that would first identify an area of interest in plan-view EBIC, then isolate that area for STEM-EBIC analysis. The individual steps for that process are now discussed.

1. Start with an LED sample that has been mechanically polished following the process detailed in section 4.5. In addition, the polished sample is already mounted to sample holder and functionally tested.
2. The sample is loaded into the Hitachi S3200 conventional SEM for plan-view SE imaging. This step allows the surface to be inspected for surface artifacts and identification of fiducials.
3. Plan-view EBIC is then used to identify regions of interest. Areas of dark contrast may indicate internal defects. Comparing the EBIC and SE images rules out any contrast effects due to surface artifacts. The selected area of interest is then mapped to the SE image. Figure 95 shows the outcome from the mapping steps 2 and 3.

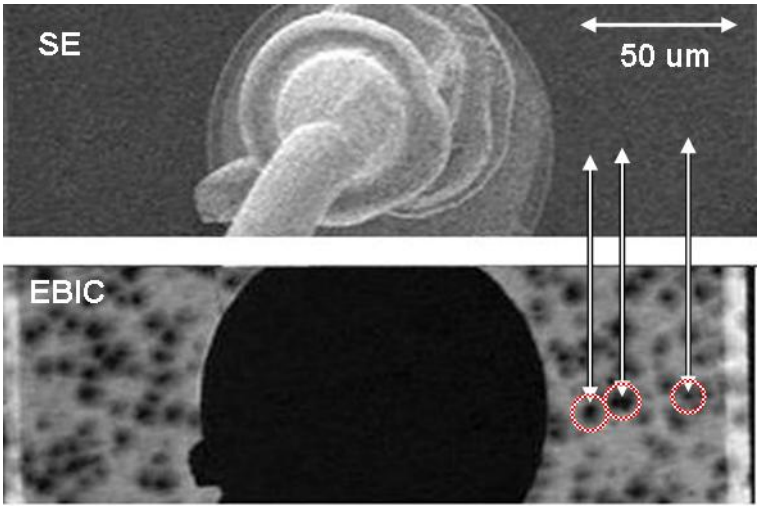


Figure 95: Mapping regions of interest identified by plan-view EBIC.

4. FIB based milling is then used to first isolate the regions of interest. This is followed by final thinning to form TEM cross-section at selected areas of interest. The anticipated outcome after the initial thin step is represented in Figure 96 shown below.

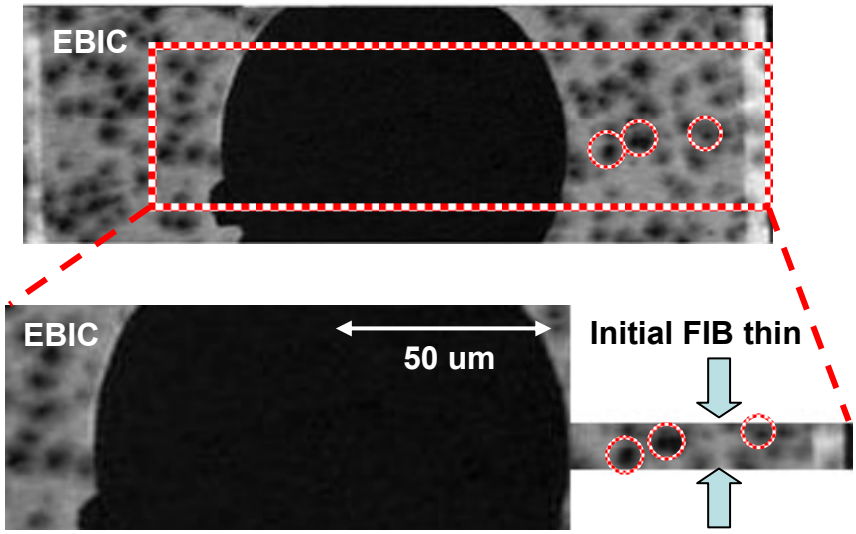


Figure 96: Initial FIB based milling isolates region of interest which is then followed by final thinning to form electron transparent cross-section at selected areas of interest.

5. The prepared sample is tested and I-V data collected to confirm that the damage reduced parallel resistance, R_p, is within the 10^8 - 10^6 Ω range and no indication of current bowing is observed (as discussed in chapter 4).
6. The prepared sample is now ready for analysis.

5.4 Samples

The devices used in the study were commercial Cree, Inc. InGaN based MQW UltraThin™ blue and green LEDs[117]. Blue LEDs consisted of eight $In_xGa_{1-x}N$ QWs while the green LEDs had three QWs. Indium composition in the quantum wells was controlled to obtain blue and green light emission. Size of the QWs and indium mole fraction is proprietary. The structures were grown by metal-organic chemical vapor deposition on a (0001) SiC substrate. The donor and acceptor concentrations were N_d = 3-4x10^{18} cm^{-3} and $N_a \leq 1x10^{19}$ cm^{-3}. Ohmic contacts were deposited on the n-SiC substrate and p-GaN layer. A schematic of the device structure reprinted from the Cree[117] web site is shown below in Figure 97

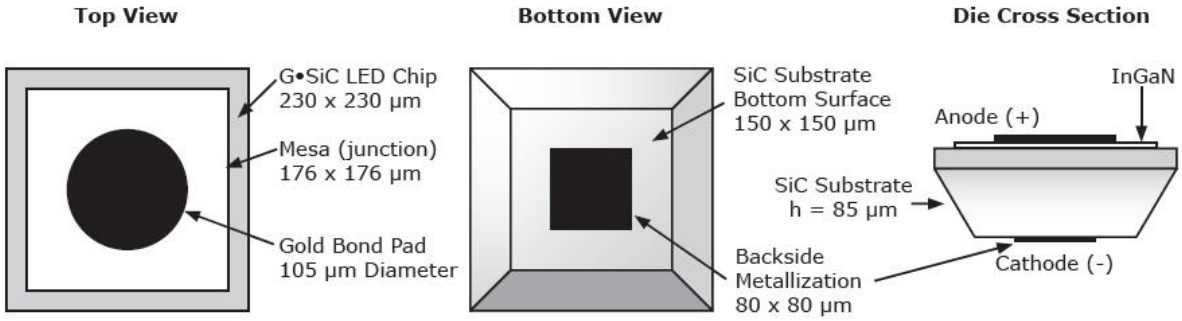


Figure 97: Schematic UltraThin LED (From Cree[117]).

The blue LED was specified for an output power of 5.5 mW operating at 20 mA, with a full width half maximum emission of approximately 22 nm centered at 470 nm. The green LED was specified for an output power of 2.5 mW operating at 20 mA, with a full width half maximum emission of approximately 35 nm centered at 527 nm. The as received samples were unpackaged LEDs supplied mounted on a TO-

header as shown below in Figure 98. The devices were removed from the TO-header and prepared for analysis following the process described in section 4.5.2.

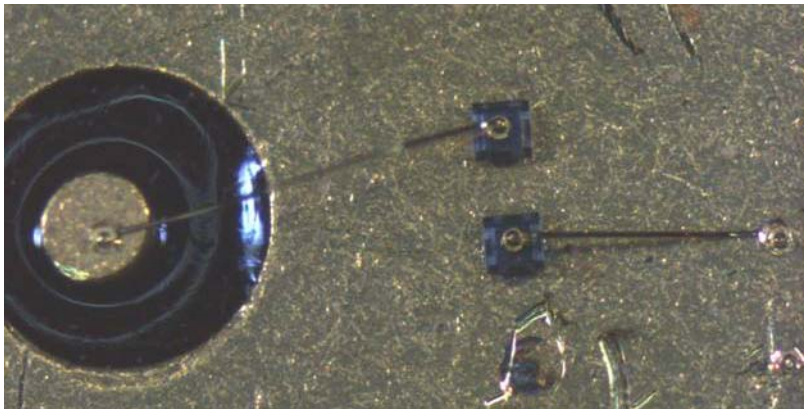


Figure 98: As received LED samples mounted on a TO-header with silver paste.

5.5 UltraThin Blue LED

5.5.1 Plan-view SEM-EBIC mapping

A blue UltraThin LED was mechanically polished in cross-section to 50±10 µm thickness and mounted to a custom EBIC sample holder. The sample was then loaded into a Hitachi S3200 conventional scanning electron microscope for plan-view SE and EBIC imaging. The top of the device is shown in Figure 99 and the top surface on either side of the wire bond is available for investigation. For this sample, the surface to the left of the top electrical contact was selected for mapping. Figure 100 is a higher magnification view of the device surface and was used to identify surface artifacts and eliminate those areas as potential EBIC regions of interest. Figure 101 shows a plan-view EBIC image where a region of interest was identified that contained an area of dark contrast indicating the potential presence of recombination-enhancing defects. The region was mapped to the SE image and its position located as shown in Figure 102.



Figure 99: SE plan-view image of mechanical polished blue LED mounted on sample holder.

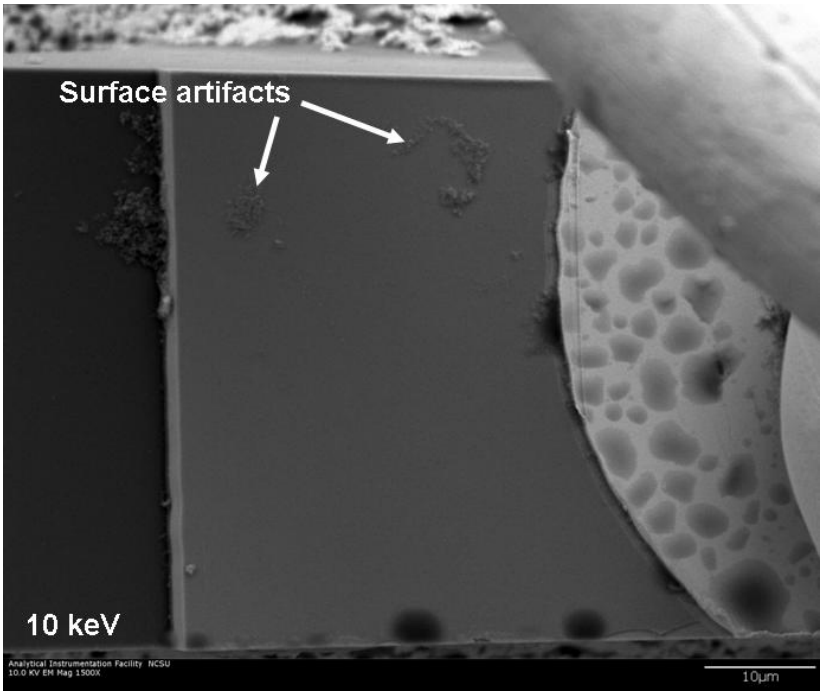


Figure 100: SE plan-view image of blue LED showing area to be mapped.

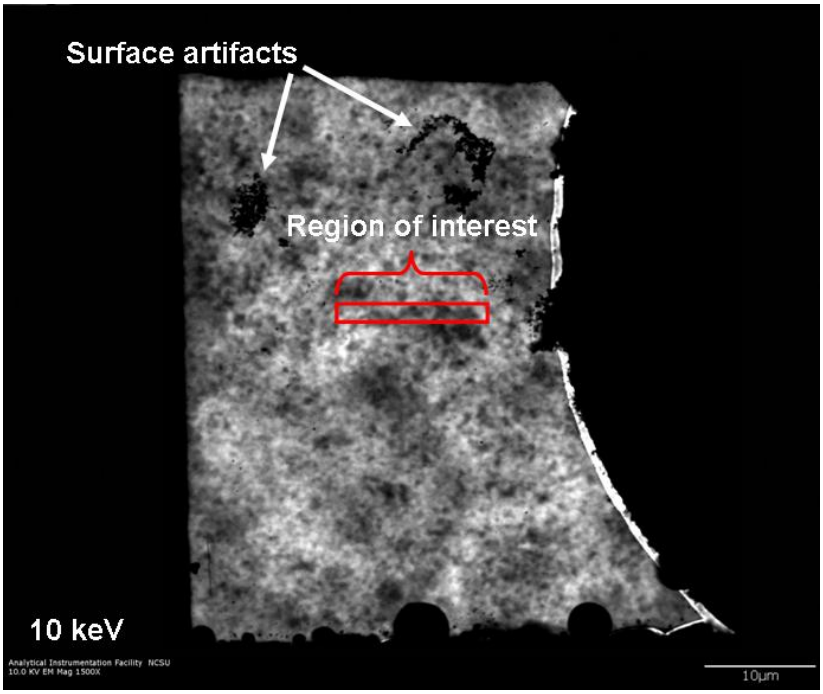


Figure 101: Plan-view EBIC to identify region of interest.

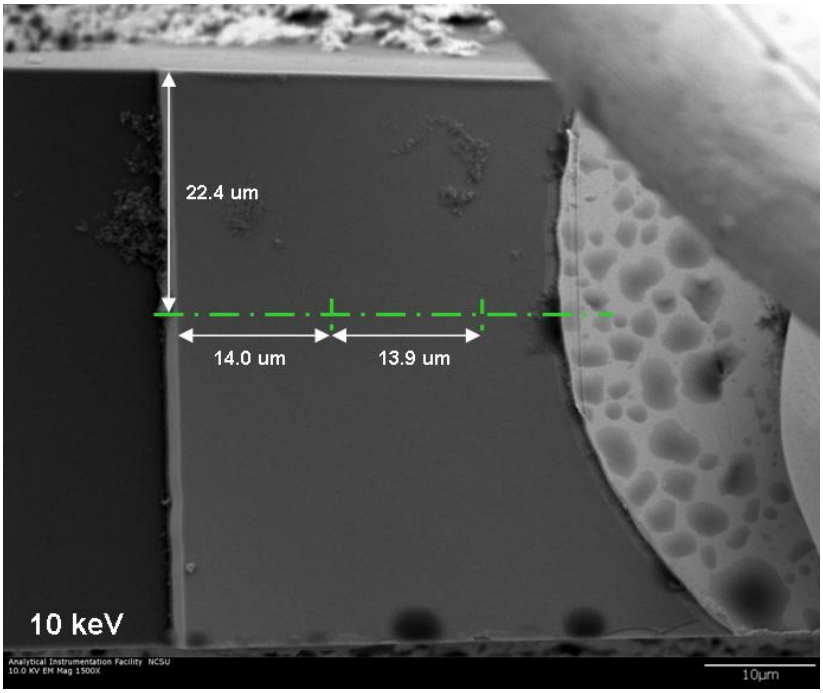


Figure 102: SE plan-view image blue LED with region of interest denoted.

5.5.2 FIB prep of cross-section

With the region of interest located, the sample was loaded into a FEI 210 FIB for site specific preparation of an H-bar TEM cross-section. First, a fiducial was placed to assist with locating the cross-section. Next a platinum protective strap 2 μm wide by 1 μm thick was deposited. The purpose of the strap is to serve as a sacrificial layer and protect the top of the cross-section during subsequent milling steps. The strap does not functionally affect the device. Figure 103 shows the sample after placement of the alignment fiducial and platinum strap. To define the cross-rib section, the FIB was operated at an accelerating voltage of 30 kV and beam current of 20 nA. These settings were used for bulk milling of material from both sides of the platinum strap. The result of this step is shown in Figure 104 where the region of interest is isolated within the ~ 2 μm wide cross-rib section. Still operating the FIB at 30 kV accelerating voltage, a series of lower beam current cuts were made to form the TEM cross-section shown in Figure 105. The beam current sequence used is summarized below.

1. 7 nA to thin window to ~ 1 μm.
2. 3 nA to thin window to ~ 0.5 μm.
3. 1 nA to thin window to ~ 0.25 μm.
4. 0.1 nA to remove sidewall taper.

Lastly, a 5 kV, 0.15 nA polish was used to reduce sidewall damage and complete the sample preparation process.

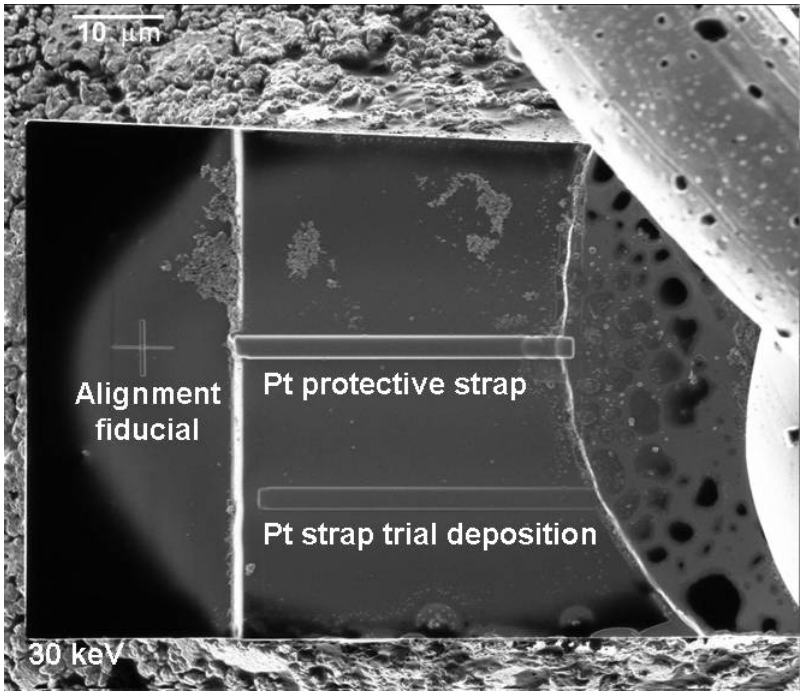


Figure 103: Placement of alignment fiducial and Pt protective strap.

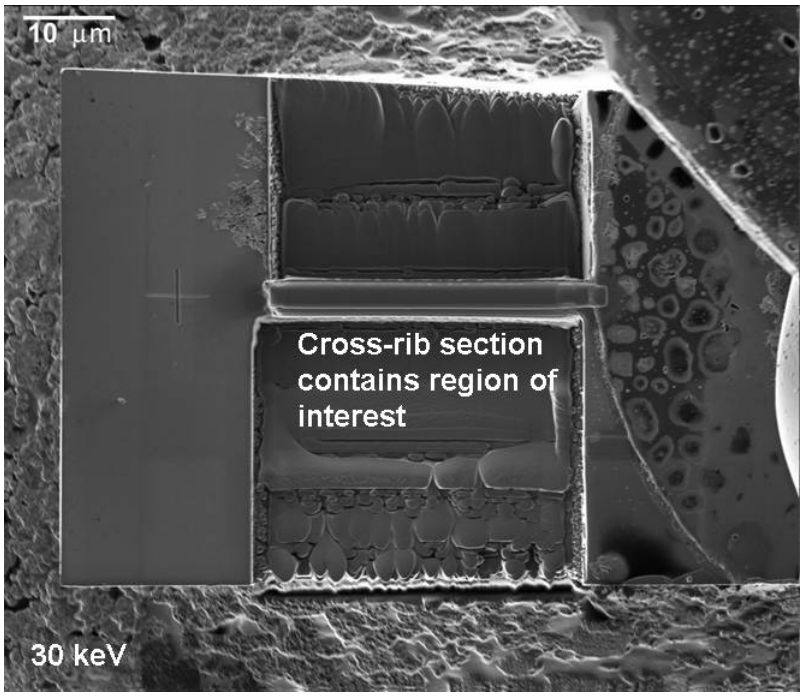


Figure 104: Formation of cross-rib isolating region of interest.

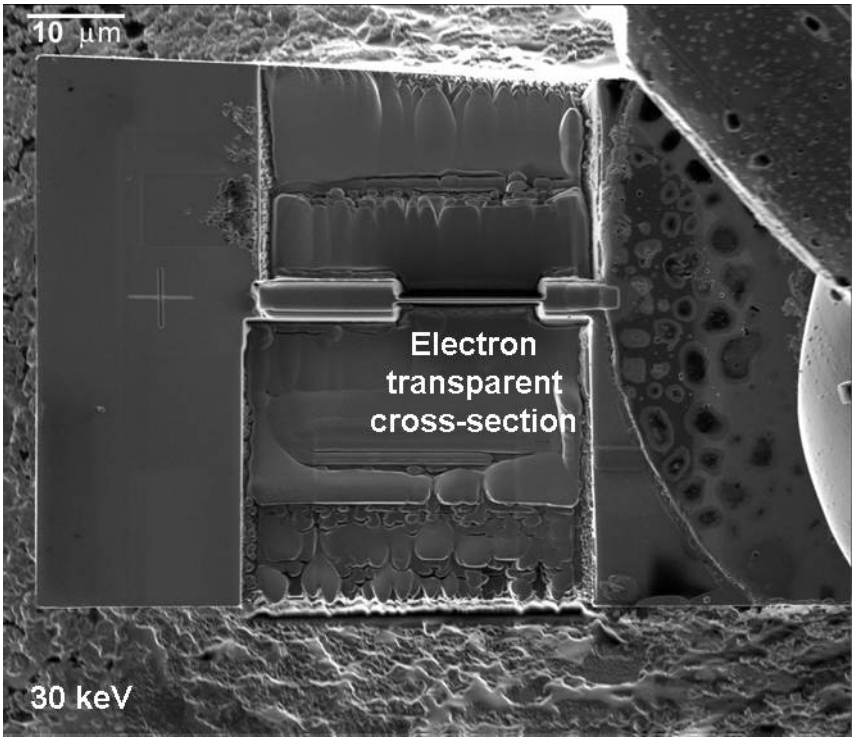
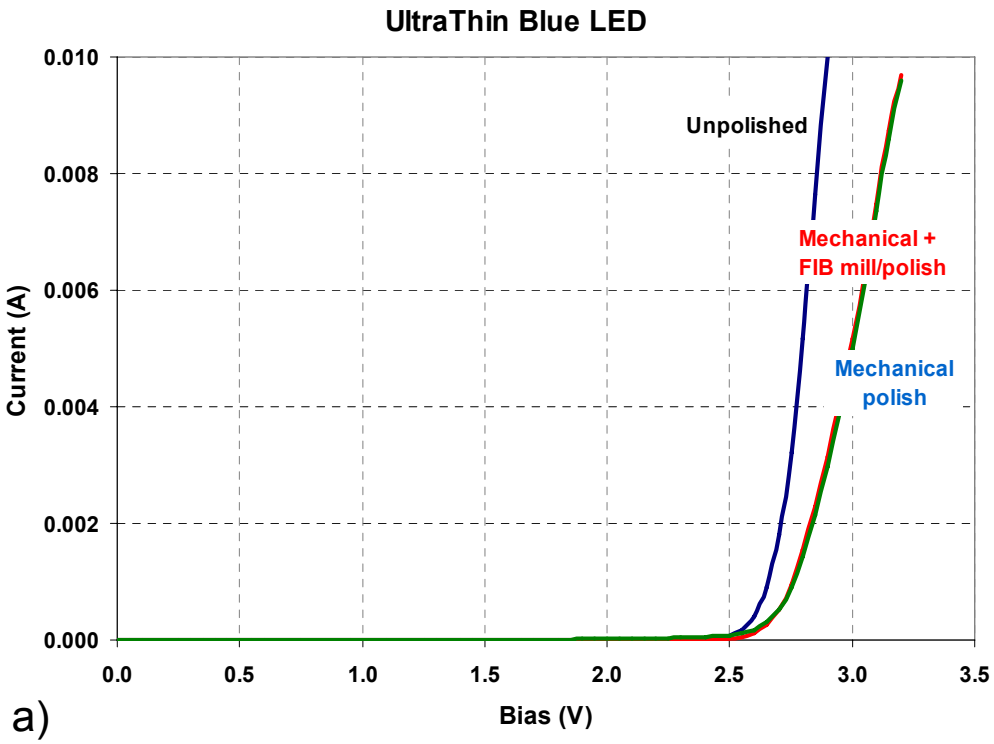


Figure 105: Electron transparent cross-section ~ 0.2 µm thick.

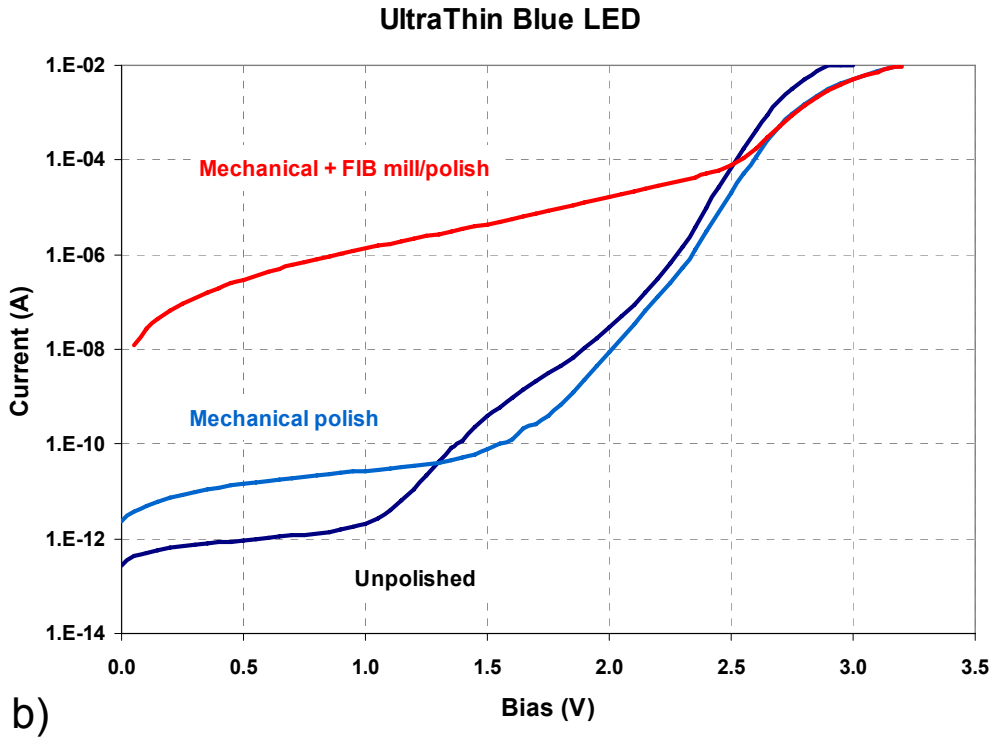
5.5.3 Electro-optical characterization

Forward bias I-V results are shown in Figure 106 for the device at various stages of sample preparation: unpolished, mechanical polish, and mechanical + FIB/mill polish. For completeness both (a) linear-scale and (b) semi-log scale plots are shown. The mechanical polish curve shows a current increase for low bias conditions, < 1.25 V. Increased leakage current is due to polishing damage to the exposed junction. As the bias is increased current flow through the junction dominates, but is limited by reduced cross-section area. The result is lower current than observed with the unpolished die for voltages ≥ 1.25 V.

For the FIB mill/polish sample the I-V characteristic shows increased leakage current due to FIB damage along the exposed junction sidewall that has not been removed or repaired. Overall, the FIB polished I-V characteristic displays a well behaved profile with a reduced parallel resistance, $R_p \approx 10^6\ \Omega$, and no indication of Poole-Frenkel current bowing. Based on these results the sample was electrically qualified for STEM-EBIC analysis.



a)



b)

Figure 106: I-V data taken at various stages of sample preparation for STEM-EBIC a) Linear scale b) Semi-log scale.

The ability to do electroluminescence (EL) characterization of samples in the STEM was discussed earlier in section 4.2.3. Here EL is used to look for any changes to the LED emission characteristics due to sample preparation. Figure 107 shows EL spectra for the blue LED sample taken after mechanical polish (Figure 99) and FIB prep (Figure 105). Results are normalized to the sample after mechanical polish. A forward bias of 2.4 V was selected as a compromise between sample time and resolution as determined by set-up of the Acton spectrometer. Settings used for the spectrometer were; 250 μm input slit, 0.5 nm step, 50 ms integration time and 3 samples per step. The range of the PMT was 350 – 650 nm. From Figure 107 we observe that the peak remained at 475 nm and the full width half max (FWHM) showed little change after FIB prep. While no change was expected EL characterization was performed to confirm. The drop in EL intensity however was expected as part of the polished sample was milled away during FIB preparation.

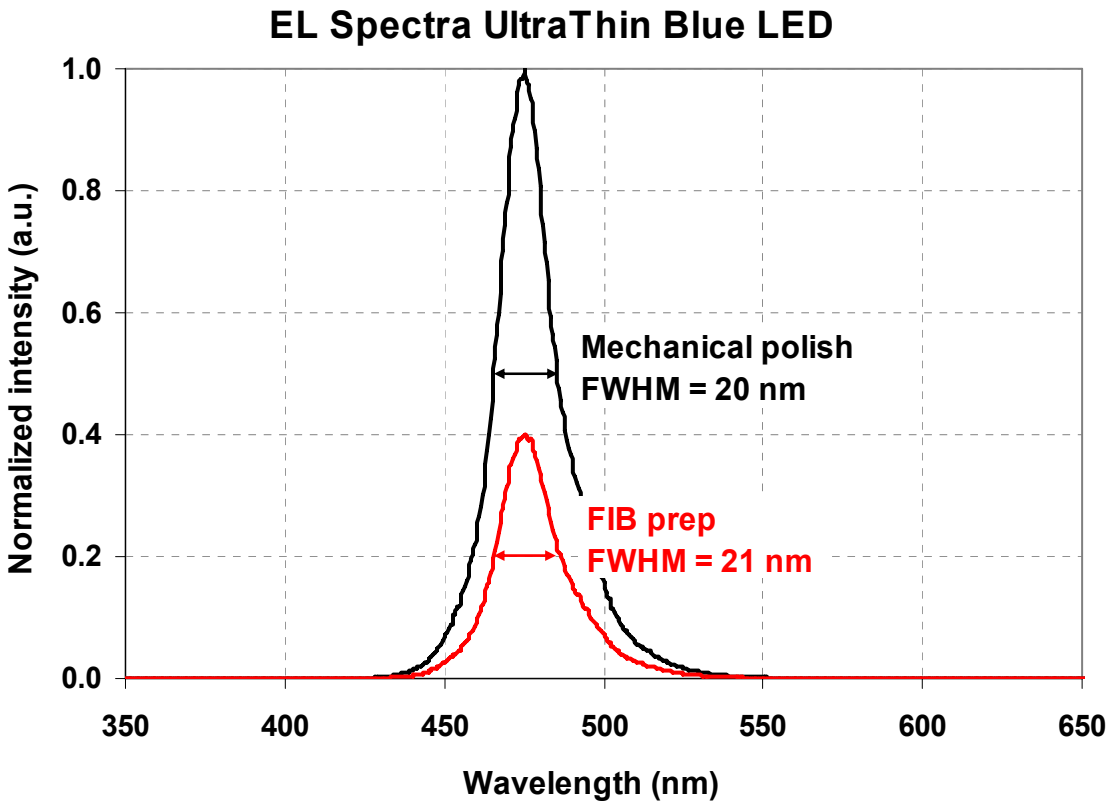


Figure 107: EL spectra normalized to the mechanical polished UltraThin blue LED under 2.4 V forward bias in STEM shows little change to FWHM after FIB prep.

To further investigate the effect of sample preparation on optical behavior, the EL spectrum was re-plotted with the intensity scaled to reveal emission detail over the shorter wavelength range from 350 – 430 nm. The re-plot is shown below in Figure 108 and an emission around the 370 nm wavelength associated with GaN is observed.

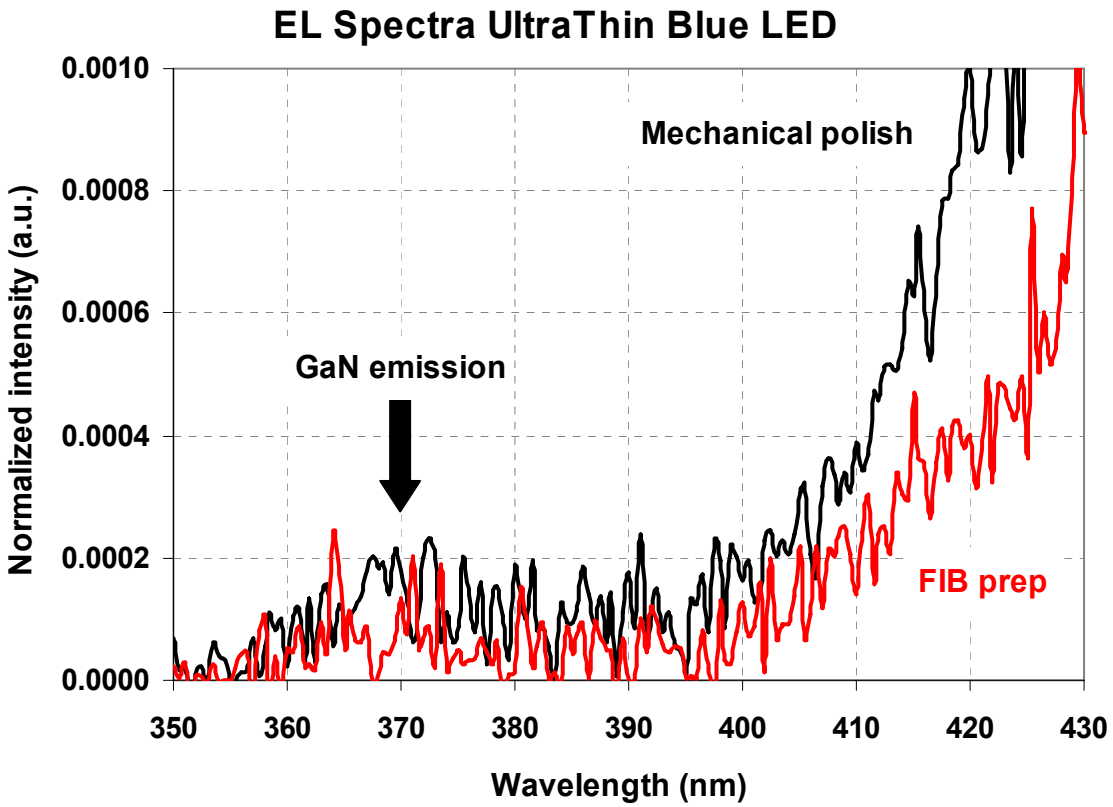


Figure 108: Short wavelength detail of UltraThin blue LED EL spectra under 2.4 V forward bias in STEM reveals GaN emission.

The EL spectrum was also re-plotted with the intensity scaled to reveal emission detail over the longer wavelength range from 525 – 650 nm. This range is of interest as it includes the yellow defect-band emission range 520 – 620 nm. Yellow band (YB) emission is associated with Ga-vacancies in the n-GaN layer[118]. As sample preparation may increase Ga-vacancies, it was necessary to look at changes to YB emission. The re-plot for longer wavelength range is shown below in Figure 109. No indication of YB emission is present; however, it should be noted that EL emission comes from the entire active area of the sample and may mask increased YB emission from the TEM cross-section.

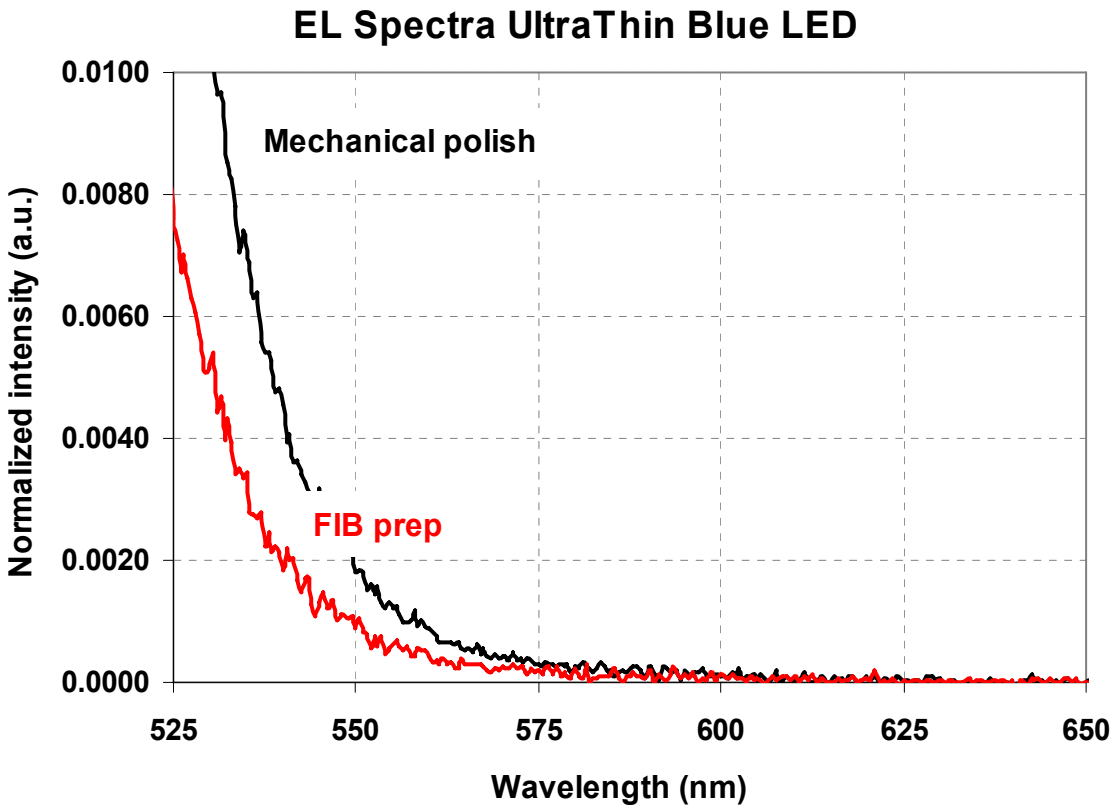


Figure 109: Long wavelength detail of UltraThin blue LED EL spectra under 2.4 V forward bias in STEM.

5.5.4 STEM-EBIC setup

All STEM-EBIC experiments were done at room temperature in a Hitachi HD-2000 Field Emission 200 kV dedicated STEM[119]. The microscope has high-annular dark field (Z-contrast), bright field and secondary electron imaging capabilities. A Thermo Noran Vantage[120] EDS acquisition system was used to simultaneously obtain Z-contrast and EBIC data from the HD-2000 STEM. Capturing the EBIC signal required an intermediate circuit. Collection and amplification of the EBIC signal utilized a Keithley 428 current amplifier in series with a custom designed imaging circuit for gain and level control. Output from the imaging box was passed to a Thermo Noran voltage to frequency converter (VFC). Auxiliary input ports on the EDS system require a frequency signal thus necessitating the signal conversion. The VFC has an adjustable input voltage of 0 - 3 V and a 16-bit output (~ 65 kHz

max). The setup on the HD-2000 STEM used for STEM-EBIC is shown below in Figure 110 without the Noran system.

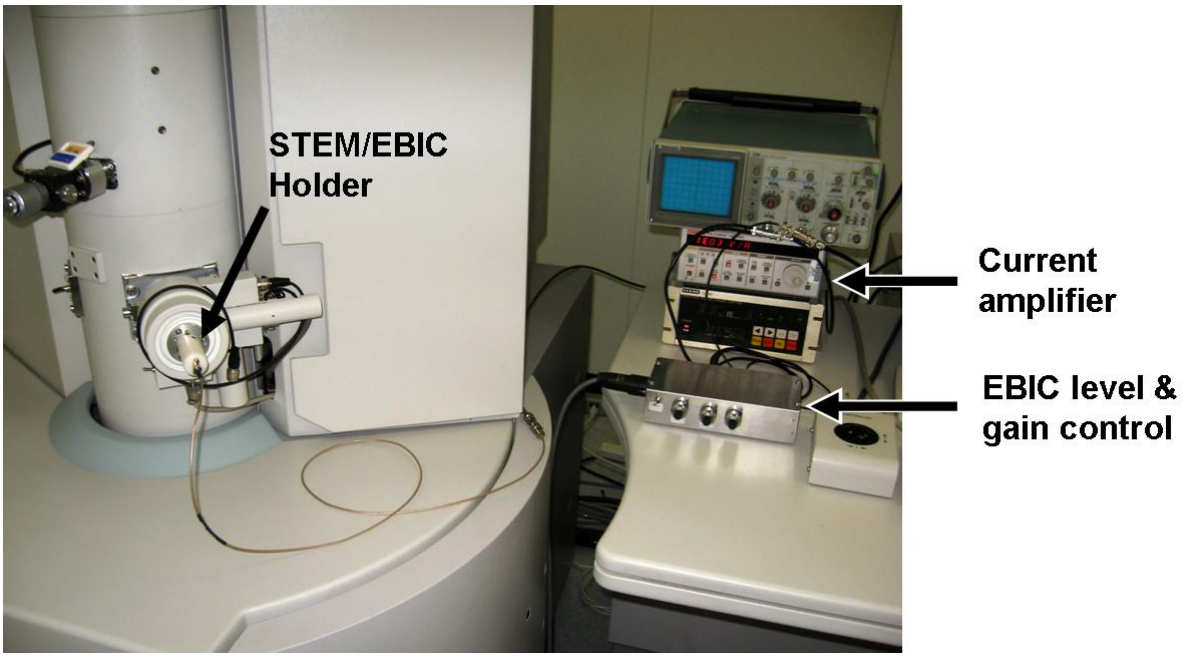


Figure 110: STEM-EBIC setup for Hitachi HD-2000 dedicated STEM.

Figure 111 shows a cross-section SE image taken in the HD-2000 STEM of the blue UltraThin sample from Figure 105. Key features are identified to help the reader visualize the sample orientation. The center region is the TEM cross-section and contains the area of interest identified from plan-view SEM-EBIC. To the top and bottom of the TEM cross-section is the unthinned cross-rib. To the right of the thinned section is the bulk sample substrate. To the left of the Pt layer is chamber vacuum. Between the Pt layer and SiC is the GaN mesa which is made up of n-GaN, InGaN/GaN MQWs and p-GaN. Direction toward the bond pad and device edge is also noted. This orientation was selected so that the beam raster is perpendicular to the pn-junction and used for all STEM-EBIC experiments.

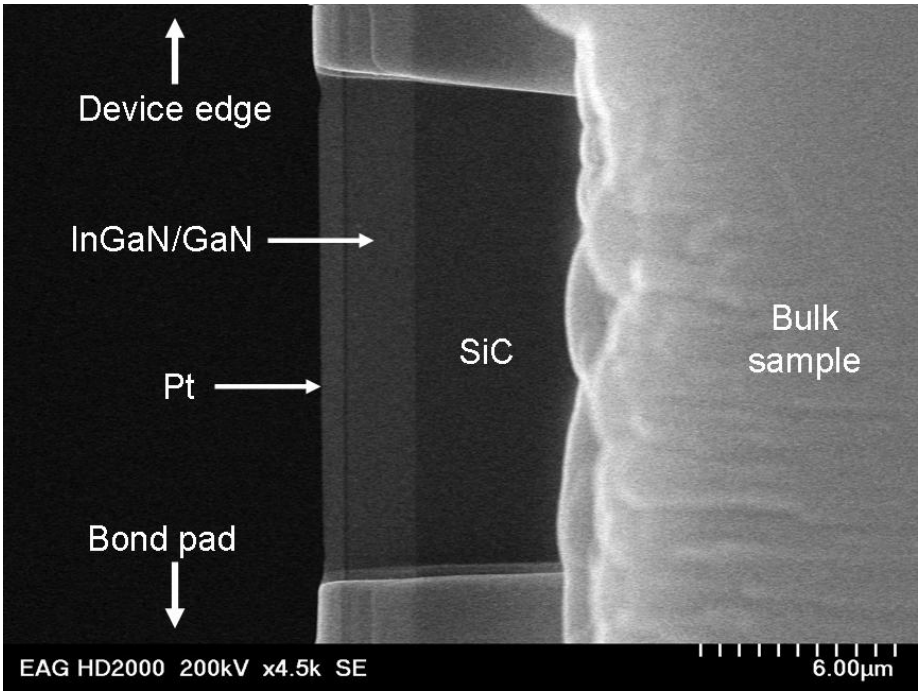


Figure 111: SE image of blue UltraThin sample in STEM.

5.5.5 STEM-EBIC mapping

The Hitachi HD-2000 was operated at 200 kV with a beam current of 275 pA and a spot size approximately 0.5 nm. After alignment of the sample, EBIC maps were taken to identify areas of interest and look for signal-defect correlation. STEM-ZC and EBIC maps shown in Figure 112 through Figure 118 were acquired simultaneously using the Thermo Noran EDS system. Map resolution and pixel dwell time are reported in the figure caption. The resulting composite image created by offline post-processing allows correlation of the EBIC signal to device structure. For reference, Figure 112 includes labels identifying key regions on the cross-section. As the orientation of the sample in the HD-2000 did not change over the course of mapping, labels are not shown on subsequent ZC images. Results show V-defects rather than threading dislocations interacting with the QWs.

STEM-ZC imaging revealed two types of V-defects both of which are shown in Figure 112(a) and classified by location within the cross-section. An embedded defect, upper region Figure 112(a), is thought to be below the cross-section surface

as only minor disruption to the QW structure is observed. On the other hand, sectioned defects intersect the surface of the cross-section, and significant disruption of the QWs is visible. EBIC mapping shown in Figure 112(c) indicates that both types of V-defects suppress the EBIC signal, but sectioned defects have a greater effect than embedded defects. The position of the peak intensity indicates the pn-junction is located within the QWs and offset toward the n-GaN layer. Defect associated signal suppression can be seen more clearly in Figure 113(c), which is a higher magnification image of Figure 112. From this image the defect capture range was extracted by plotting the local induced current along the junction as shown in Figure 114. From Figure 114, the induced current falls of less steeply towards the embedded defect than the sectioned defect determined by the slope. A capture range of 53 nm was measured for the embedded defect while the sectioned defect had a measured capture range of 64 nm. This difference suggests that the embedded defect is further away from the sample surface than the sectioned defect.

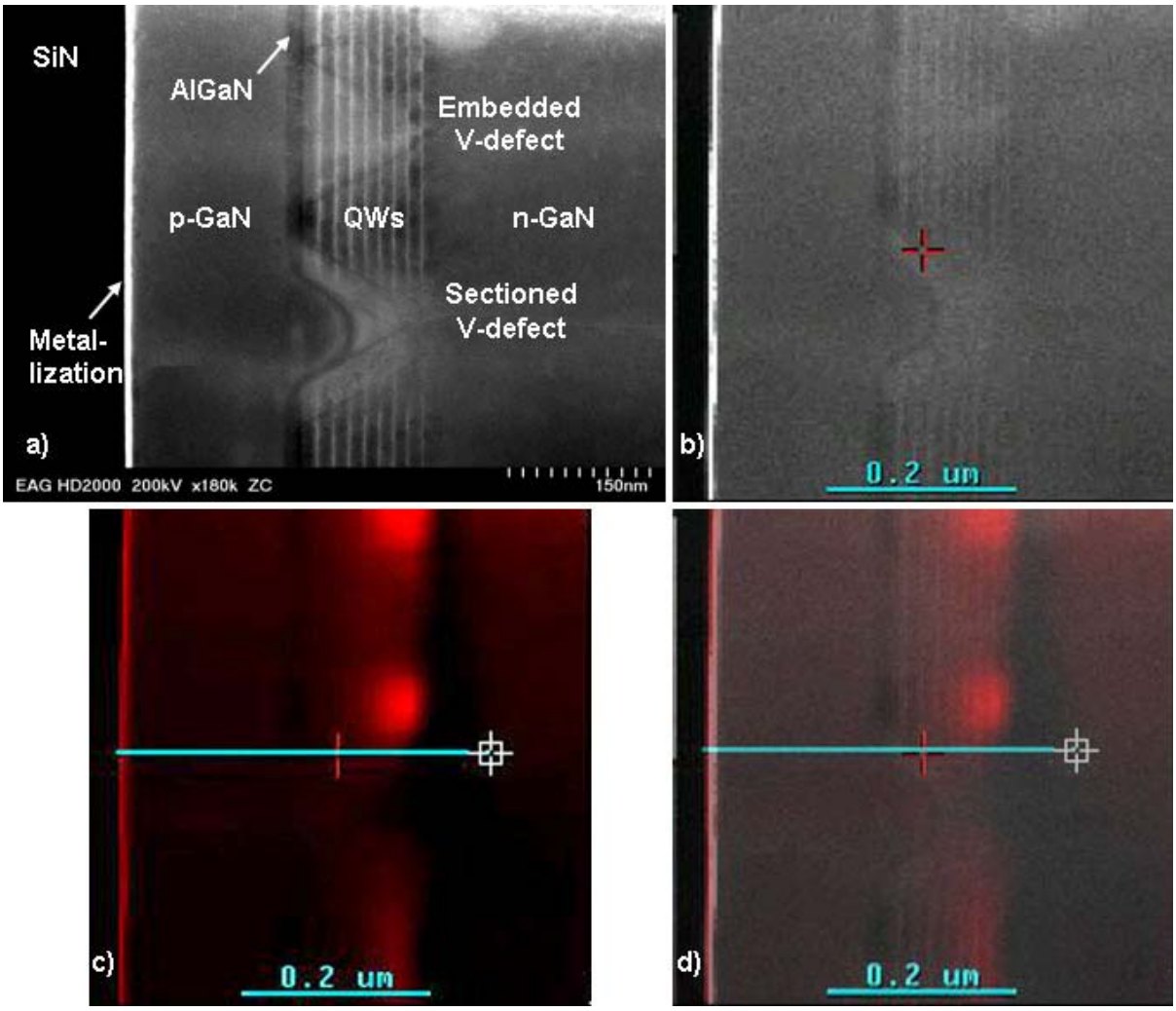


Figure 112: a) ZC image acquired with HD-2000 STEM b) ZC map & c) EBIC map acquired simultaneously using Noran with 128x128 pixels and 0.03 sec dwell time per pixel. d) Composite image of EBIC map overlaid on ZC map.

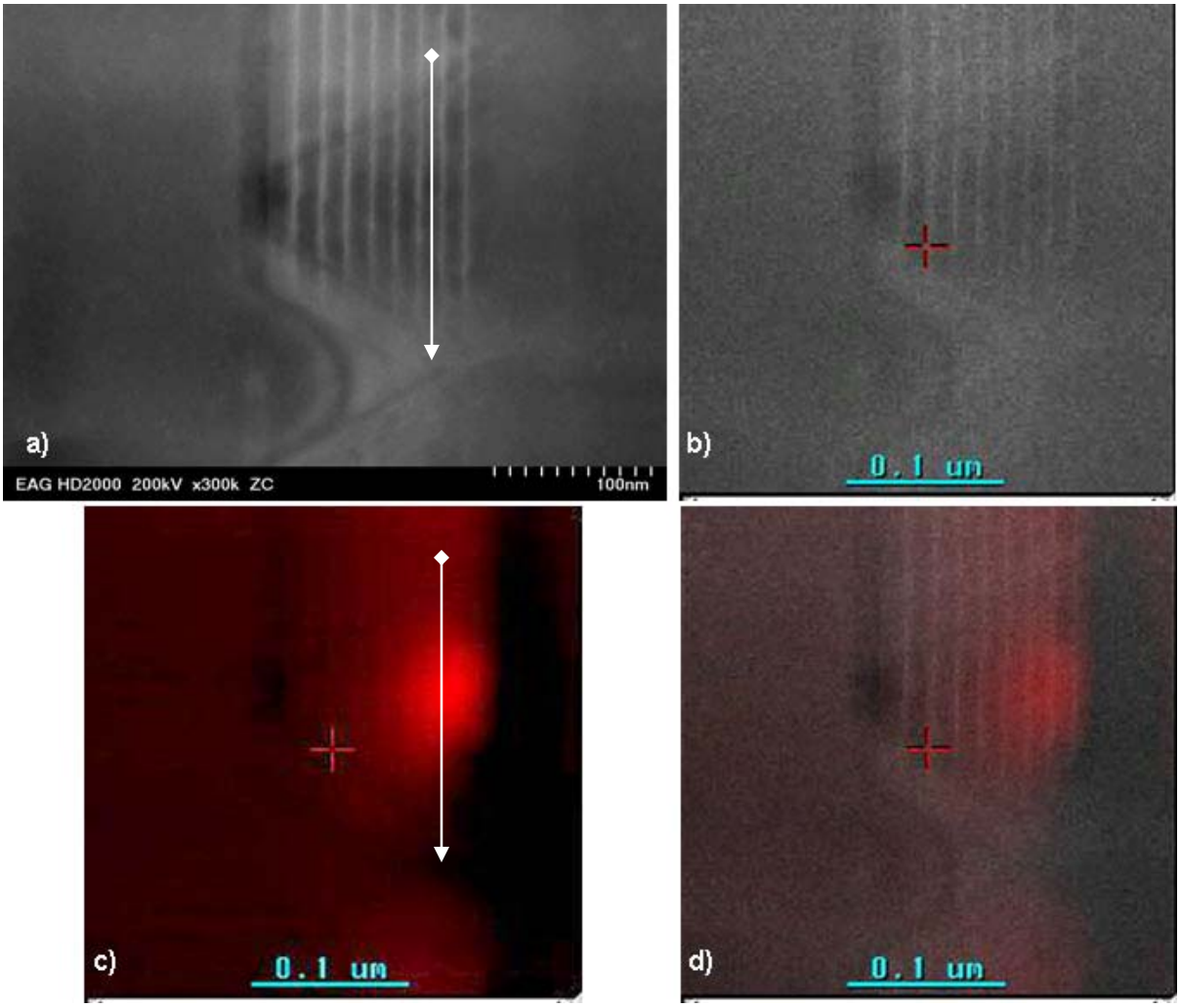


Figure 113: a) ZC image acquired with HD-2000 STEM b) ZC map & c) EBIC map acquired simultaneously using Noran with 128x128 pixels and 0.03 sec dwell time per pixel. d) Composite image of EBIC map overlaid on ZC map. White line in a) and c) shows location local induced peak current measured for defect capture range.

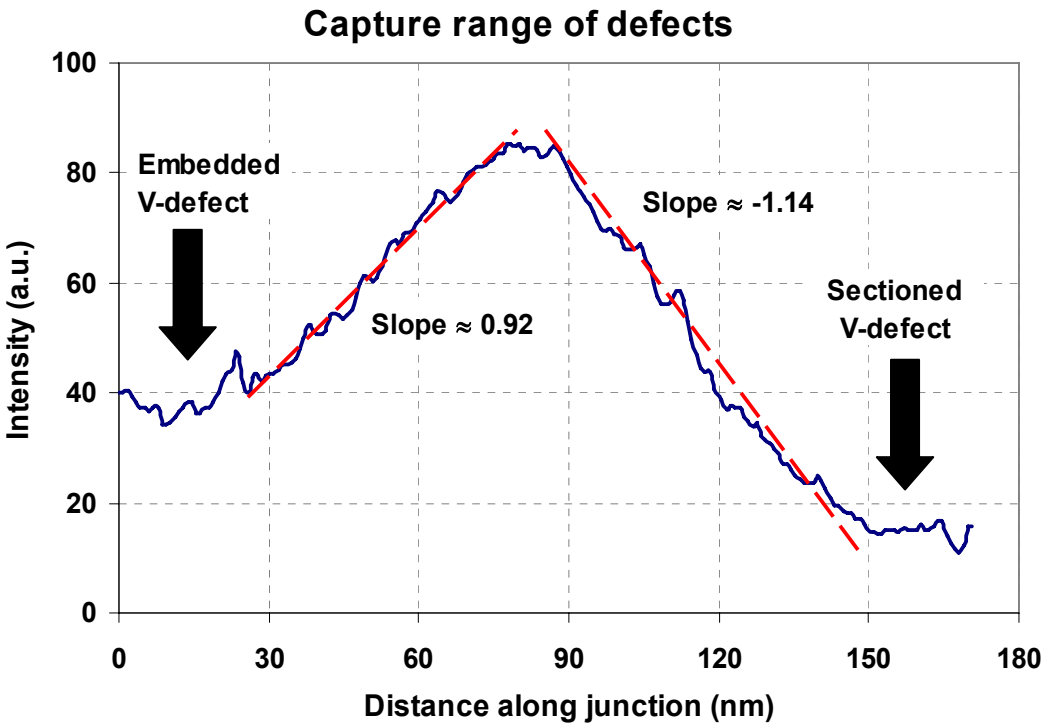


Figure 114: Changes in peak induced current along junction.

Figure 115(a) shows a larger region between defects than previously presented. The EBIC map shown in Figure 115(c) indicates that increased defect separation results in a sustained EBIC signal across that region. Location of the pn-junction is placed within the MQWs shifted toward the n-GaN layer.

Figure 116(a) shows a region containing multiple V-defects. The EBIC map in Figure 116(c) appears disrupted by the V-defects and identification of the pn-junction is difficult. In Figure 117(a) a region with multiple defects was located that also included a small defect free section. Figure 117(c) presents the EBIC map and in this case the distance between defects was sufficient to allow the EBIC signal to recover. Lastly, multiple sectioned V-defects were investigated and are shown in Figure 118(a). The EBIC map is presented in Figure 118(c) and effectively shows that multiple sectioned V-defects effectively eliminated the EBIC signal.

The STEM-EBIC mapping results presented in Figure 112 through Figure 118 represents the first direct correlation of EBIC contrast variation to V-defects. While EBIC mapping was useful for identifying areas of interest, EBIC line scans are necessary to probe specific locations and improve signal to noise.

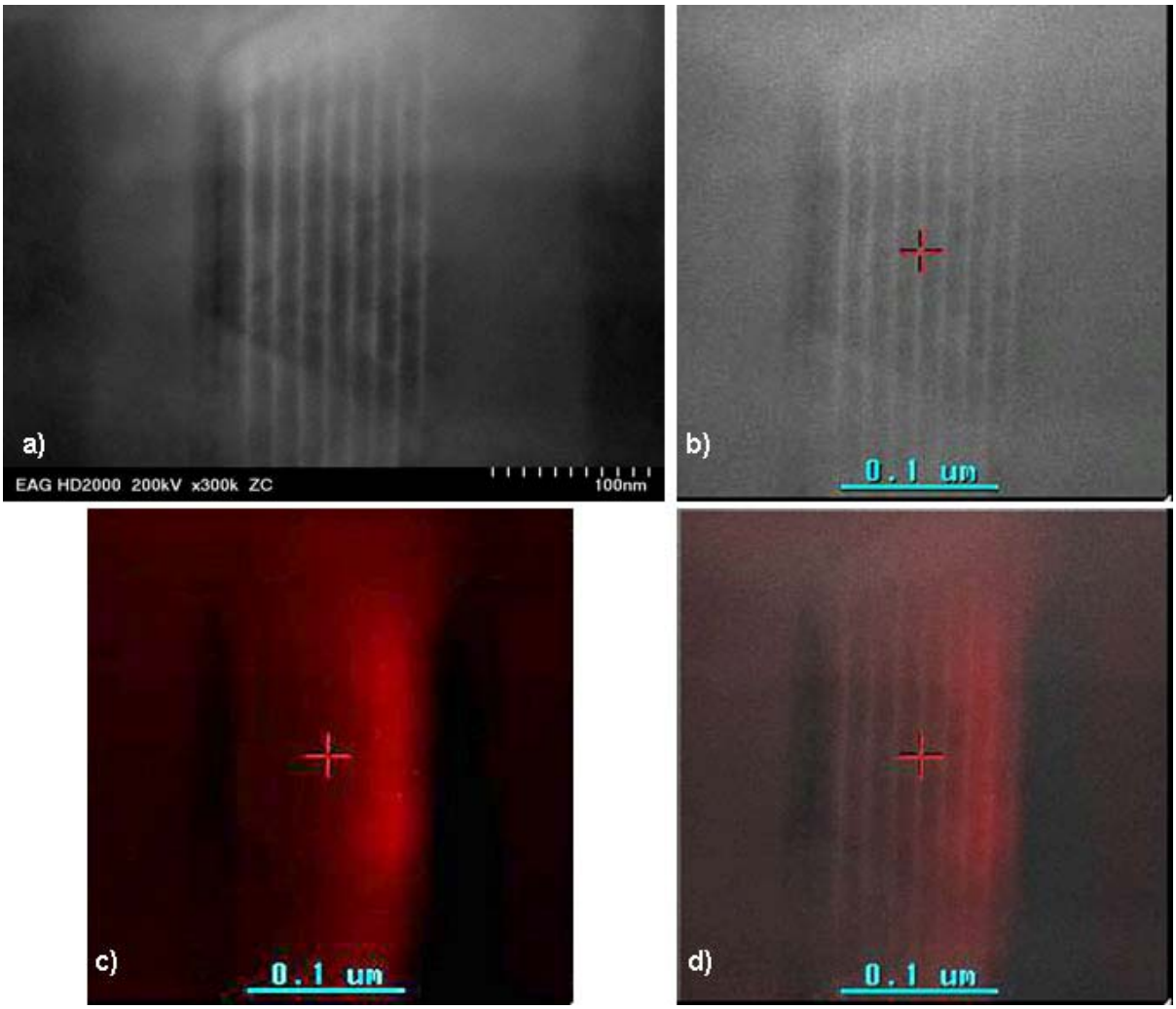


Figure 115: a) ZC image acquired with HD-2000 STEM b) ZC map & c) EBIC map acquired simultaneously using Noran with 256x256 pixels and 0.01 sec dwell time per pixel. d) Composite image of EBIC map overlaid on ZC map.

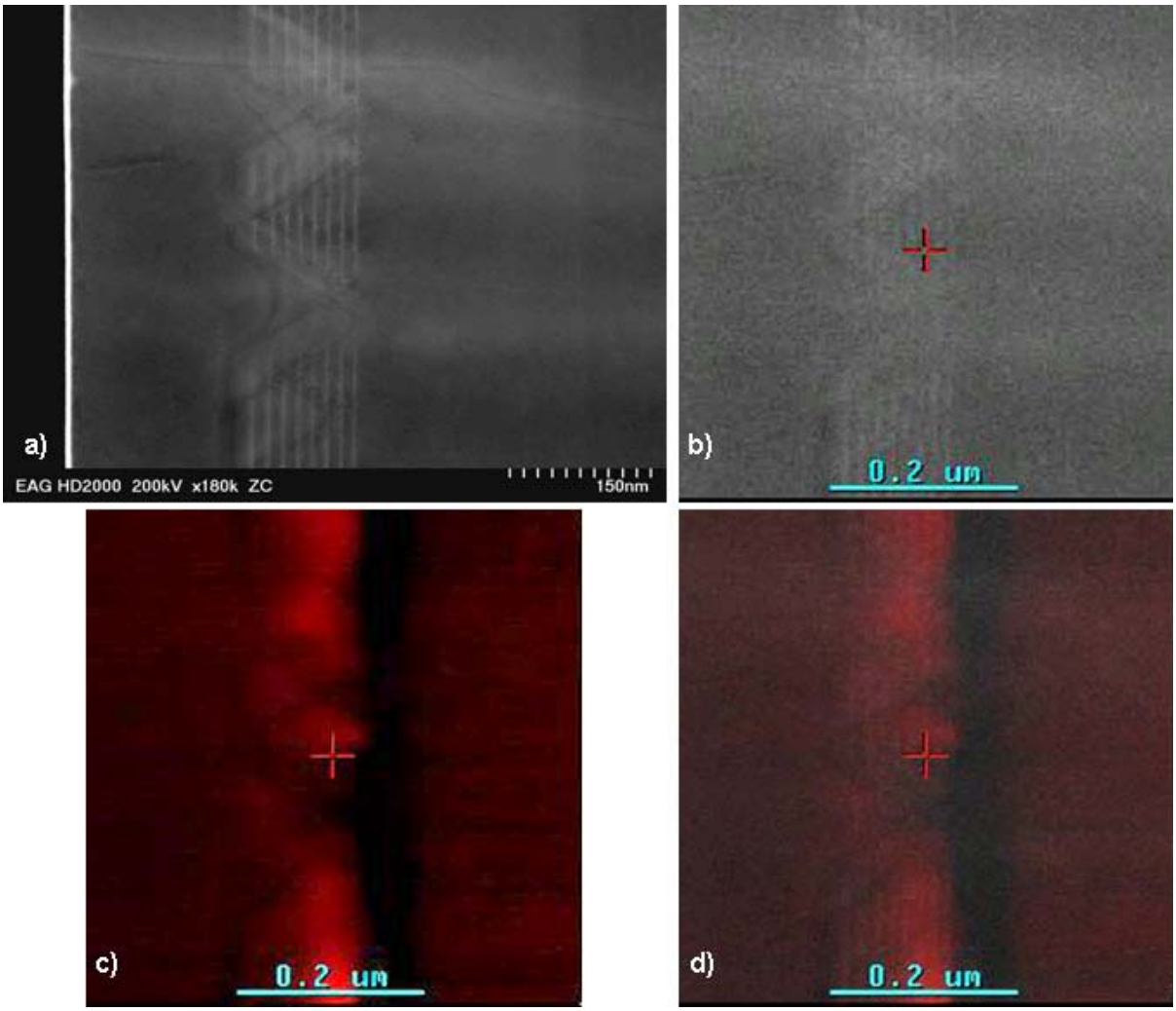


Figure 116: a) ZC image acquired with HD-2000 STEM b) ZC map & c) EBIC map acquired simultaneously using Noran with 128x128 pixels and 0.03 sec dwell time per pixel. d) Composite image of EBIC map overlaid on ZC map.

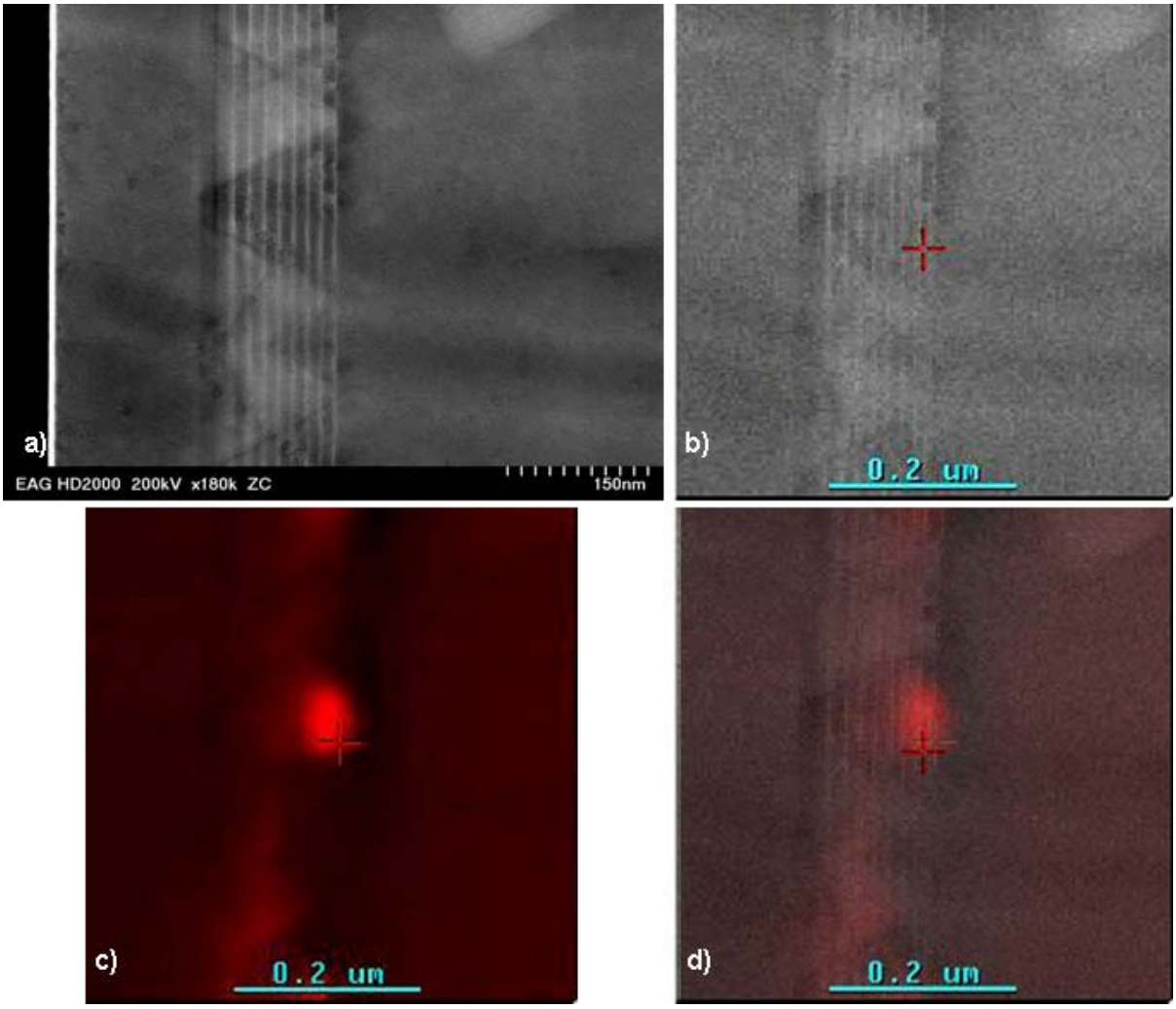


Figure 117: a) ZC image acquired with HD-2000 STEM b) ZC map & c) EBIC map acquired simultaneously using Noran with 128x128 pixels and 0.03 sec dwell time per pixel. d) Composite image of EBIC map overlaid on ZC map.

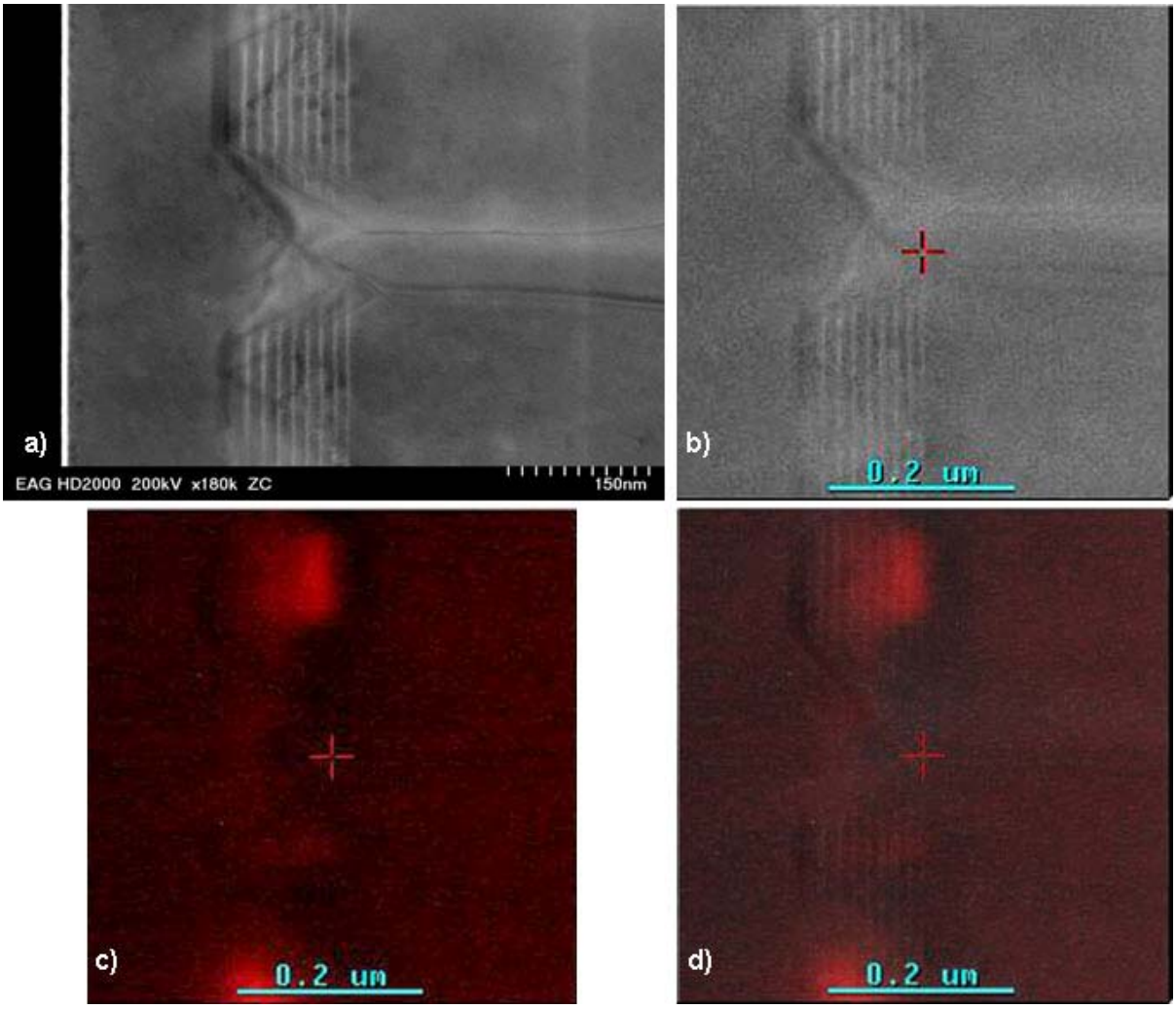


Figure 118: a) ZC image acquired with HD-2000 STEM b) ZC map & c) EBIC map acquired simultaneously using Noran with 256x256 pixels and 0.02 sec dwell time per pixel. d) Composite image of EBIC map overlaid on ZC map.

.

5.5.6 STEM-EBIC line scans

5.5.6.1 Results

The Hitachi HD-2000 was operated at 200 kV with a beam current of 275 pA and a spot size approximately 0.5 nm. EBIC line scans were acquired using the Thermo Noran EDS system. The scan length was set at ~ 200 nm to include a region on either side of the QWs and a dwell time of 0.5 sec per point, 100 points per line scan were utilized. Figure 119 through Figure 122 present EBIC line scan results mapped by post-processing to the associated region on the structure shown in a ZC image. In this manner the location of the pn-junction is identified and the affect of device structure on the EBIC signal is a direct correlation. EBIC line scans were taken at different locations from the core of both sectioned and embedded defects, and from V-defect free regions.

Figure 119 shows EBIC line scans taken traversing into a sectioned V-defect. Signal suppression is observed as scans are traversed into a sectioned V-defect. A defect contrast of 0.84 was measured from the change in peak to trough spread between line scans at (a) the fringe and (d) the core of the sectioned defect. From Figure 119 the peak induced current and hence pn-junction is initially located from line scan (a) at 22± 2 nm from QW-1. As the line scan interacts with more of the defect, the pn-junction shifted 77 nm toward the p-GaN layer and the signal profile broader and less defined. At the core of the defect the resulting EBIC profile (d) barely indicates presence of a pn-junction. Also, the presence of a sectioned V-defect disrupts the AlGaN confinement layer and the drop in current observed in profile Figure 119(a) is no longer present in profile (d).

A similar set of line scans was recorded traversing out of the same sectioned defect. Figure 120 shows recovery of the EBIC signal and a shift in pn-junction location as lines scans are located further from the core of a sectioned V-defect. A defect contrast of 0.73 was measured from the change in peak to trough spread between line scans at (c) the edge and (a) the center of the sectioned defect. Location of the pn-junction was observed to shift 67 nm between profiles (a) and (c) towards the n-GaN layer where it was located at 30± 2 nm from QW-1. Along with

recovery of the pn-junction, the drop in current due to the AlGaN confinement layer is observed to recover, as observed in profile (c).

Figure 121 shows a consistent EBIC signal and little shift in location of the pn-junction for a section of QWs between V-defects. The EBIC signal strength is observed to build, but only slightly as the scan location moves further away from the sectioned defect. A contrast of 0.19 was measured between EBIC profiles (c) and (a). From line scans (a) through (c) the pn-junction location shifted 8 nm toward the n-GaN layer and from profile (c) is located 22± 2 nm from QW-1.

Figure 122 shows EBIC signal suppression and pn-junction shift as lines scans are traversed into an embedded V-defect. EBIC signal suppression is observed as the line scan is located closer to the defect core. A defect contrast of 0.50 was measured from the change in peak to trough spread between line scans at (a) the fringe and (d) the core of the embedded defect. The peak induced current and hence pn-junction is initially located from line scan (a) at 20± 2 nm from QW-1. As the line scan interacts with more of the defect, the pn-junction shifted 12 nm toward the p-GaN layer and the signal profile broadened, but is still well defined. Both EBIC signal suppression and junction shift are reduced compared to similar results for sectioned defects indicating embedded defects are not as disruptive.

A review of the line scans results in Figure 119 through Figure 122 reveals that in regions free of V-defects, the peak induced current shows little spatial variation. To place the pn-junction, its location was measured for each line scan taken from a defect free region. The result located the pn-junction at 21 ± 2 nm from QW-1.

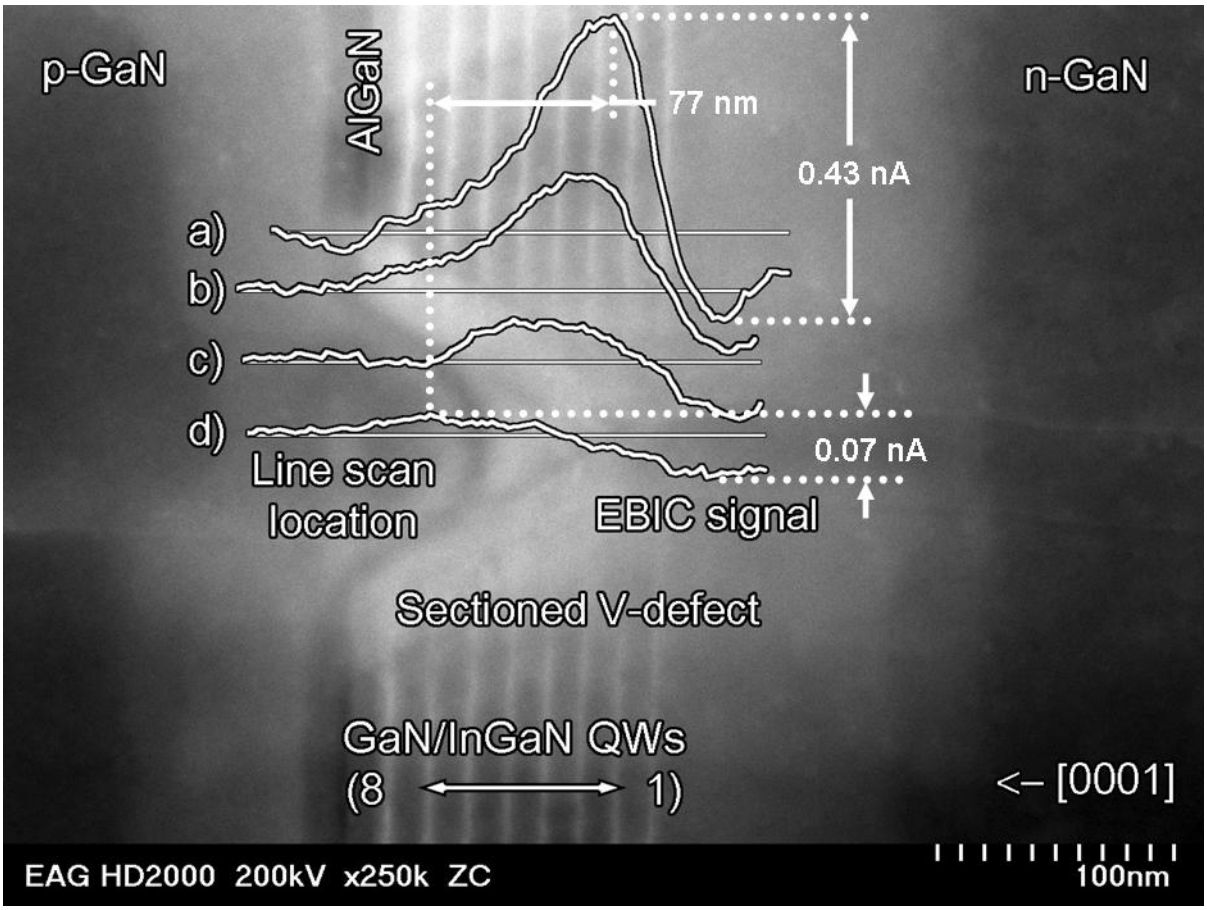


Figure 119: EBIC line scans taken traversing into a sectioned V-defect. Signal suppression observed as line scan cuts across more of the defect. A defect contrast of 0.84 was measured from the change in peak to trough spread between line scans (a) and (d). A defect related shift in pn-junction location is also observed. From line scan (a) with junction located 22± 2 nm from QW-1 to line scan (d), junction shifted 77 nm toward p-GaN.

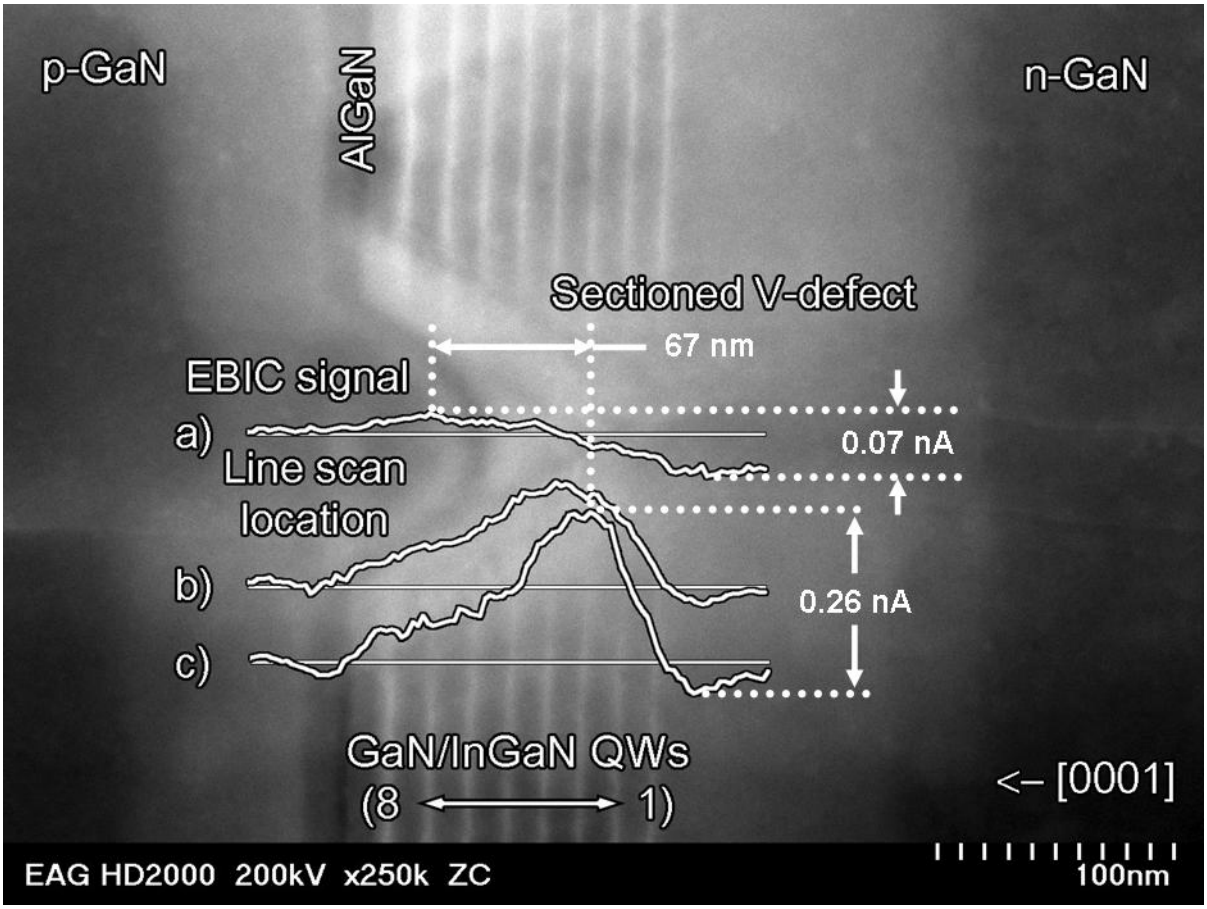


Figure 120: EBIC line scans taken traversing out of a sectioned V-defect. Signal suppression decreases as line scan cuts across less of the defect. A defect contrast of 0.73 was measured from the change in peak to trough spread between line scan (c) and (a). A defect related shift in pn-junction location is also observed. From line scan (a) to (c) the junction shifted 67 nm toward n-GaN layer and was located 30± 2 nm left of QW-1.

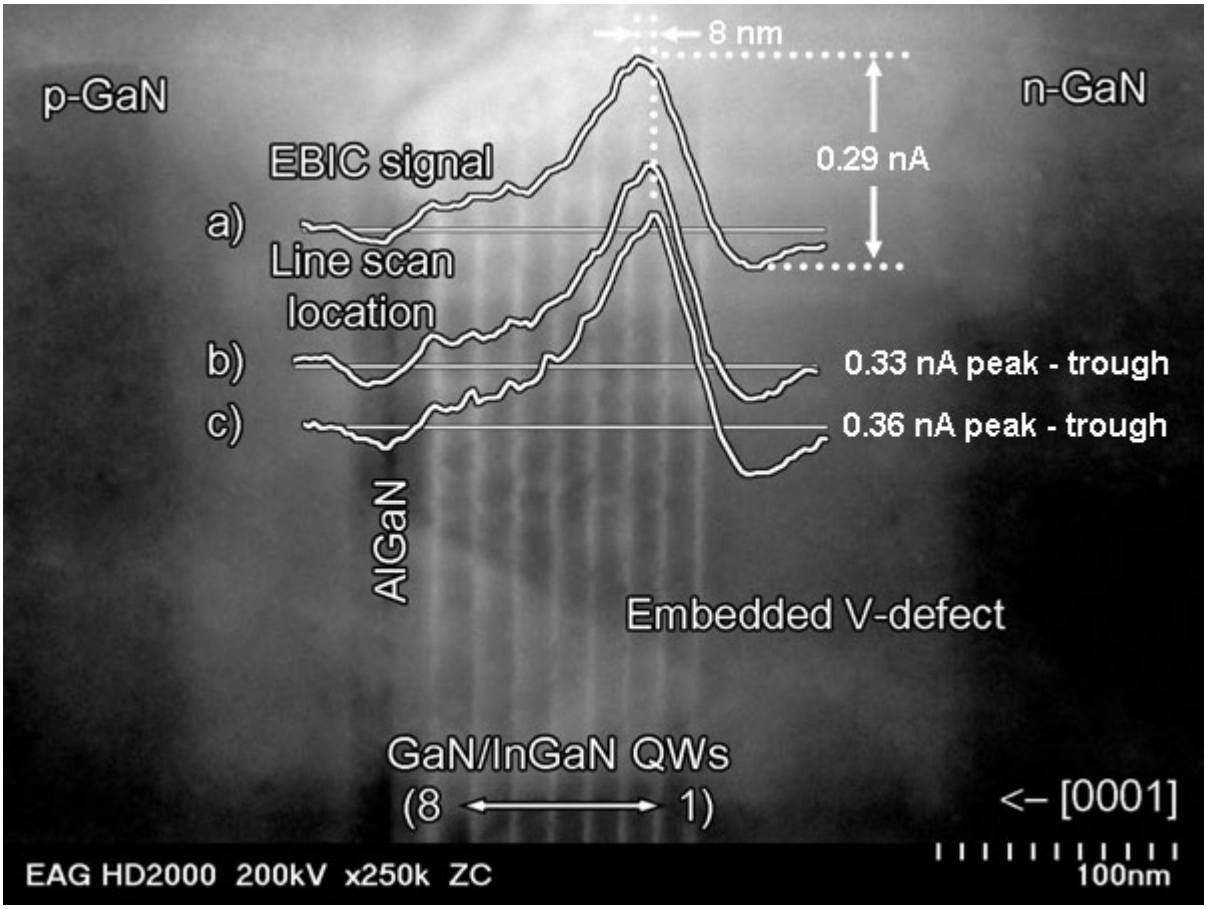


Figure 121: EBIC line scans taken traversing region between V-defects. Signal strength measured from the change in peak to trough spread increased as scan location moved away from sectioned V-defect. A slight shift in pn-junction is observed as line scan location is moved further away from sectioned V-defect. From line scan (a) to (c) the junction shifted 8 nm toward n-GaN layer and was located from (c) 22± 2 nm left of QW-1.

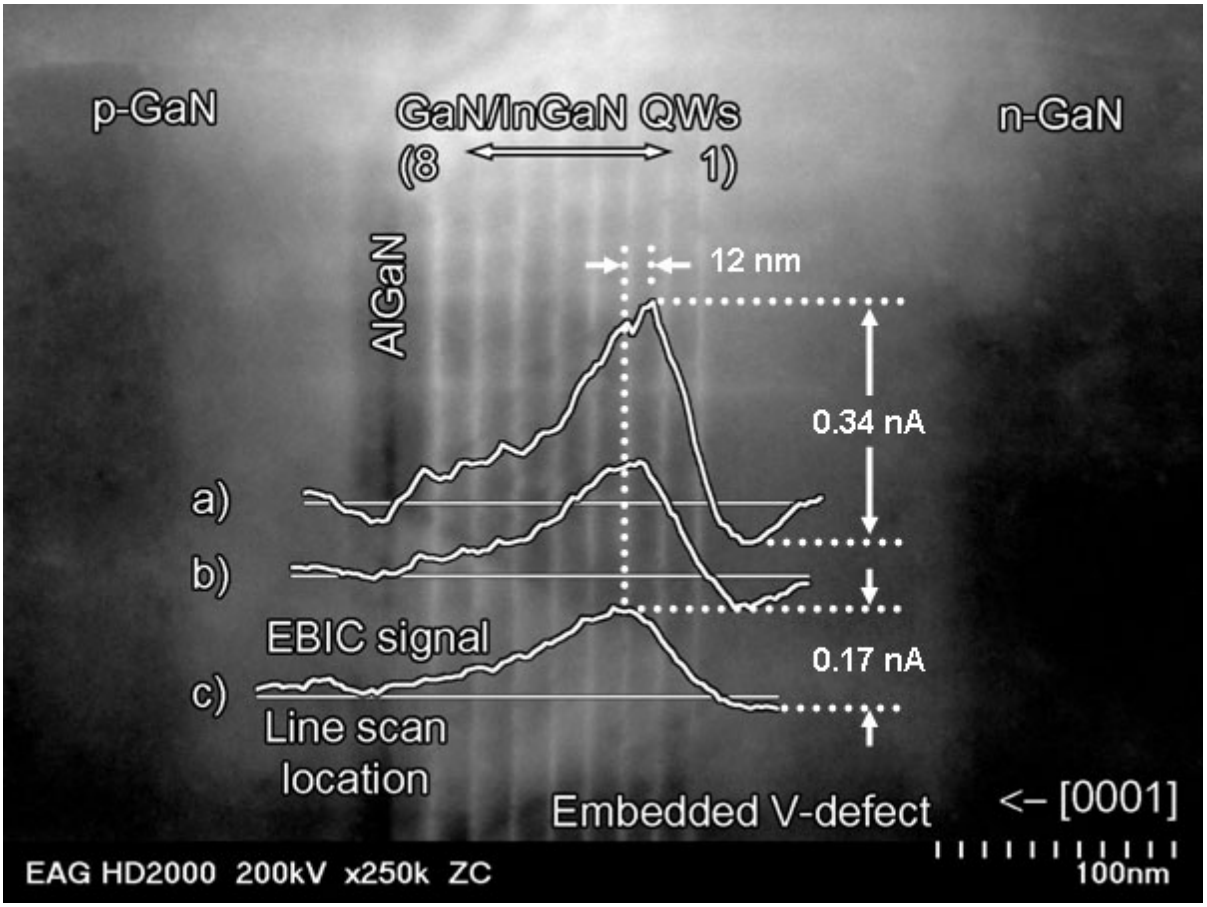


Figure 122: EBIC line scans taken traversing into an embedded V-defect. Signal suppression observed as line scan cuts across more of the defect. A defect contrast of 0.50 was measured from the change in peak to trough spread between line scan (a) and (d). A defect related shift in pn-junction location is also observed. From line scan (a) with junction located 20± 2 nm left of QW-1 to line scan (c), the junction shifted 12 nm toward the p-GaN layer.

5.5.6.2 Discussion

A drop in induced current may occur for several reasons. Voids can reduce the generation of carriers. But based on the trend observed for line scans and the lack of any visible evidence of voids, carrier generation is eliminated as the cause of reduced EBIC. On the other hand, recombination of carriers at defects can reduce the EBIC signal. Disruption of the built-in electric field can also produce a drop in induced current. Using a linear assumption based on the signal suppression observed in Figure 119 and Figure 122, an estimate of the drop in filed strength can be made. Accounting for partial dopant ionization yielded initial dopant concentrations of $N_d = 10^{18}$ cm^{-3} and $N_a = 5x10^{17}$ cm^{-3} per input from Cree. Based on those values an initial field strength of -0.066 V/nm was calculated. The field strength was then scaled by a defect contrast, 0.84, observed at the core of the sectioned V-defect in Figure 119. This equates to reduced field strength for the sectioned V-defect of -0.011 V/nm. Similarly the initial field strength was scaled by a defect contrast, 0.5, observed at the core of the embedded V-defect in Figure 122. This equates to reduced field strength for the embedded V-defect of -0.033 V/nm.

Next the reduced field strengths were used to back calculate estimates of doping concentrations. Results indicated that the reduced field strengths are possible with approximately one-to-two order drop in localized doping concentrations. The sectioned V-defect field strength can be achieved with reduced doping concentrations of $N_d = 5x10^{16}$ cm^{-3} and $N_a = 10^{16}$ cm^{-3}, while the embedded V-defect field strength can be realized with $N_d = 6x10^{17}$ cm^{-3} and $N_a = 10^{17}$ cm^{-3}. The mechanism for reduced doping levels may be V-defect enhanced diffusion. While these estimates are based on a linear assumption for what is likely a sub-linear behavior, it does provide an outer limit for what is happening numerically.

Defects can provide strong recombination sites, and carrier lifetimes are often reduced resulting in shorter minority carrier diffusion lengths and decreased EBIC. As EBIC can provide information on minority carrier diffusion lengths, this information can be used to characterize the affect defects have on carriers in their proximity. However, while models exist for extracting this information from an SEM-

type sample[121-123], no such model exists for extracting minority carrier diffusion lengths from EBIC line scans for a region with two free surfaces, and the sample is almost all surface (i.e. TEM cross-section). As such, the first and most widely used theoretical expression for the solution of the diffusion problem in a semi-infinite sample is applied to interpret the observed EBIC line scan profiles[121].

$$Intensity(EBIC) \propto e^{-\frac{x}{L_{n,p}}} \quad (5\text{-}1)$$

Where x is the position of the incident electron beam with respect to the pn-junction and $L_{n,p}$ is the electron, hole minority carrier diffusion length. The model was developed for semi-infinite (bulk) samples and assumes the generation of electron-hole pairs in the sample is from a point source. This requires x and L to be much larger than the electron range. Furthermore, the model assumes zero surface recombination. For a (S)TEM sample with two free surfaces both the point source and zero surface recombination assumption are unlikely to hold. Also, in this case extraction of the minority carrier diffusion lengths will be taken from within the depletion region. This was justified based on the accepted assumption that all EHPs generated within the depletion region are separated by the built-in electric field. For spot sizes smaller than the depletion region this would suggest that the EBIC signal plateau inside the depletion region. However, based on EBIC line scan results this is not the case. Instead a strong peak is observed with an exponential-like falloff to either side. Lastly, low-injection is an assumption for quantitative EBIC analysis models. The high-injection limit was taken to be the ionized doping level in the active region of the device 0.5 – 1.0x10^{18} carriers/cm^3. The current experimental conditions are estimated to be near 0.3x10^{18} carriers/cm^3, but not past the high-injection limit (Appendix A.4).

Equation (5-1) was used to extract estimates of the minority carrier diffusion lengths for the line scans shown in Figure 119 through Figure 122. However, given the limitations of applying this extraction model to a (S)TEM type sample, the diffusion lengths should be considered estimates. Table 3 shows a summary of the minority carrier diffusion lengths found. L_{n1} was extracted from left of the EBIC peak,

but in some cases a change in slope on the left hand side was present indicating a different value in electron diffusion length. In those cases a second diffusion length, L_{n2}, was also extracted.

Table 3: Extracted minority carrier diffusion lengths using VanRoosbroeck model[121].

	Line scan	L_{n2} (nm)	L_{n1} (nm)	L_p (nm)
Figure 119 Into sectioned V-defect	a)	164	75	23
	b)	294	120	43
	c)	135		119
Figure 120 Out of sectioned V-defect	b)	213	144	52
	c)	179	68	30
Figure 121 Between V-defects	a)	217	66	29
	b)	192	68	28
	c)	185	68	25
Figure 122 Into embedded V-defect	a)	189	70	25
	b)	227	102	39
	c)	244	139	59

In all cases the results presented in Table 3 suggest that hole minority carrier diffusion length is less than electron minority carrier diffusion length, $L_p < L_n$. This observation seems to agree with calculated results for minority carrier diffusion lengths based on reported electrical properties for GaN although the scales are dissimilar.

$$L_{n,p} = \sqrt{D_{n,p}\tau_{n,p}} \tag{5-2}$$

Where $D_{n,p}$ is the diffusion constant and $\tau_{n,p}$ the electron, hole minority carrier lifetime. From Chow and Ghezzo[124], D_n = 25 cm^2/s, D_p = 5 cm^2/s and assuming $\tau_{n,p} \approx 10^{-9}$ s yields $L_n \approx 1.6$ μm > $L_p \approx 0.7$ μm. Furthermore, Chichibu et al. recently

reported that random statistical fluctuations form localizing valence states that preferentially capture holes. This leads to the formation of localized excitons that emit light. As such, this results in shorter diffusion lengths for holes[39].

However, these results contradict those observed by Kuroda et al. and Moldovan et al., where both groups reported the minority carrier diffusion lengths for holes were slightly longer than electrons. Device structure is discounted as a potential source of difference in results, as Kuroda at al. and Moldovan et al. each had different devices. However, sample preparation for STEM-EBIC was FIB based and low-levels of surface doping from Ga-implantation might be influencing carrier behaviour. Post Ar-milling was not attempted to remove unwanted gallium because of the need to maintain metal contacts and the necessity of a higher Ar-dose to make up for the shadowing of the H-bar by the FIB-milled trench. To properly address the observed differences will require further investigation and an improved model for extracting minority carrier diffusion lengths from EBIC line scans of TEM cross-sections.

Reviewing EBIC profiles from Figure 119 through Figure 122 it is also observed that the EBIC profile flattens as the line scan position moves further into the V-defect. This trend indicates that minority carrier diffusion lengths become larger at the V-defect than in the defect free region as indicated by the results in Table 3. This behavior was also reported for MQW GaN devices by Moldovan et al. and Kuroda et al. both using SEM-EBIC. However, explanations for the observed behavior are still a subject of discussion and as of yet no consensus exists. Kuroda et al. state that the increase in L is due to increased minority carrier lifetime rather than mobility, which would typically be expected to decrease around defects. They argue that dislocations enhance diffusion resulting in larger donor compensation than the surrounding regions. This produces a local decrease of the majority carrier density. As radiative recombination is inversely proportional to majority carrier density, the radiative recombination time increases accounting for the larger minority carrier diffusion lengths. On the other hand, Moldovan et al. postulate that threading dislocations increase the escape rate of charge carriers from QWs. Consequently,

recombination efficiency is decreased due to the loss of carrier confinement and results in longer minority carrier diffusion lengths for carriers crossing the QWs.

The increase in $L_{n,p}$ suggests that the defect related decrease in EBIC is not due to increased recombination, which is associated with shorter minority carrier diffusion lengths. Alternatively, increased $L_{n,p}$ supports either reduced field strength or loss of carrier confinement as the cause of lower EBIC. However, the observed location of the pn-junction near the n-GaN layer suggests Mg diffusion deep into the QWs. The source of Mg diffusion could be V-defects which 'spike' the active layer with p-GaN and enable diffusion into the QWs from along the defect sidewall. Thus reduced field strength and location of the pn-junction suggest V-defects enhance unwanted diffusion of Mg.

5.5.7 Blue UltraThin LED summary

A Cree blue UltraThin LED was prepped and qualified for STEM-EBIC in accordance with methods developed and presented in this work. First, STEM-EBIC maps were taken to survey the sample, investigate trends in pn-junction location and influence of structure on charge carrier behavior. Results show V-defects rather than threading dislocations interacting with the QWs. By plotting the peak induced current it was possible to measure a capture range of 53 nm for an embedded V-defect and 64 nm for a sectioned V-defect. Mapping results indicated little spatial variation of the pn-junction location. STEM-EBIC mapping correlated EBIC contrast variation to V-defects present in the MQWs of GaN based LEDs. EBIC maps of regions with almost complete signal suppression were correlated to sectioned V-defects. These results presented the first direct correlation of EBIC contrast variation to V-defects in the QWs of GaN based LEDs.

While mapping was useful for correlating defects to EBIC contrast and identifying regions of interest, EBIC line scans were necessary to probe specific regions across V-defects and improve signal to noise. A series of experiments were performed that recorded STEM-EBIC line scan results from different locations from the core of V-defects. These results confirmed V-defects suppress the induced

current. Defect contrast values measured for sectioned V-defects ranged between 0.7 – 0.8 while defect contrasts for embedded V-defects measured 0.5. Larger contrast values suggest sectioned V-defects are more disruptive to the active layer than embedded V-defects and supports EBIC mapping results. For undamaged sections, the pn-junction was located 21 ± 2 nm measured from QW-1 near the n-GaN layer. Analysis of the EBIC signal profile indicated that minority carrier diffusion lengths for holes were less than electrons. Flattening of the EBIC signal suggests longer minority carrier diffusion lengths inside the defect. Reduced field strength and location of the pn-junction near the n-GaN layer suggest V-defects enhance unwanted diffusion of Mg.

5.6 UltraThin Green LED

5.6.1 Plan-view SEM-EBIC mapping

A green UltraThin LED was mechanically polished in cross-section to 50±10 μm thickness and mounted to a custom EBIC holder. The sample was then loaded into a Hitachi S3200 conventional SEM for plan-view SE and EBIC imaging. Figure 123 shows a SE plan-view image of the polished device. The top of the device on both sides of the wire bond pad is available for investigation. For this sample the surface to the left of the top electrical contact was selected for mapping. Figure 124 shows a plan-view EBIC image of the device left of the pad. A region of interest was identified which included a transition area from dark to light contrast. The region was mapped to the SE image and its position located as shown in Figure 125.

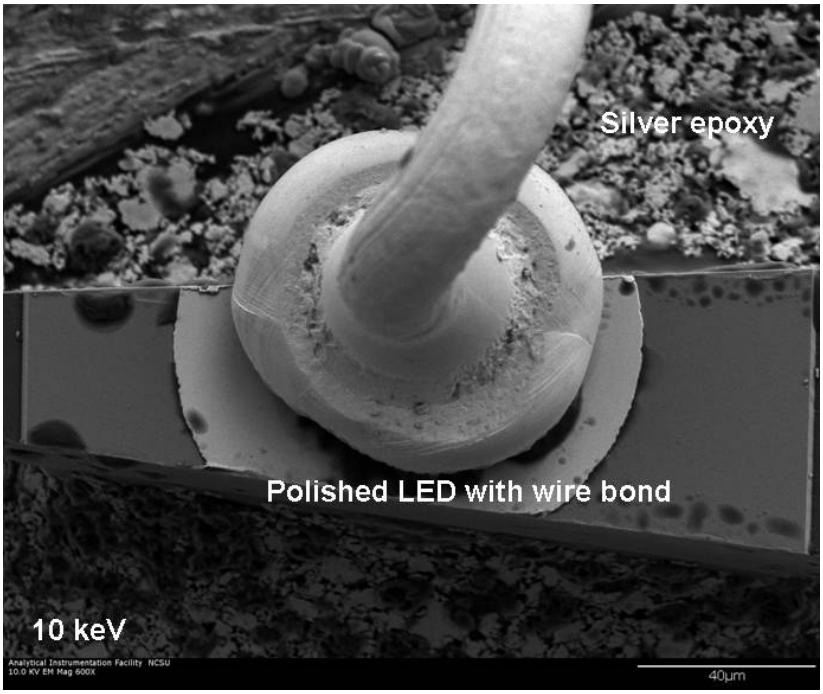


Figure 123: SE plan-view image of mechanical polished green LED mounted on sample holder.

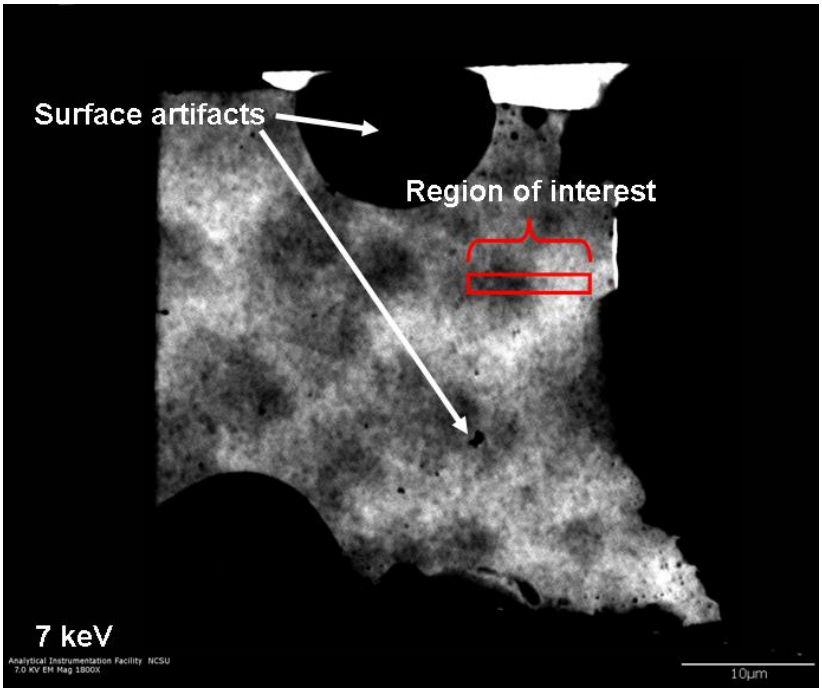


Figure 124: Plan-view EBIC to identify region of interest.

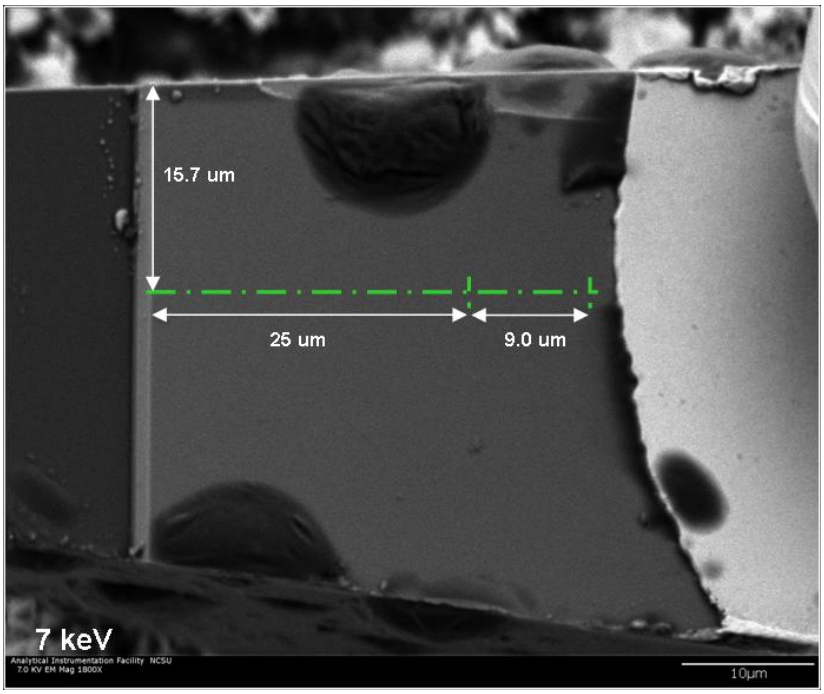


Figure 125: SE plan-view image green LED with region of interest denoted.

5.6.2 FIB prep of cross-section

The FIB milling/polish steps out lined in section 5.5.2 was followed here to prepare the UltraThin green LED. Figure 126 shows the sample in process up to formation of the cross-rib isolating the region of interest. Formation of the TEM cross-section followed and the sample was then ready for I-V and EL characterization.

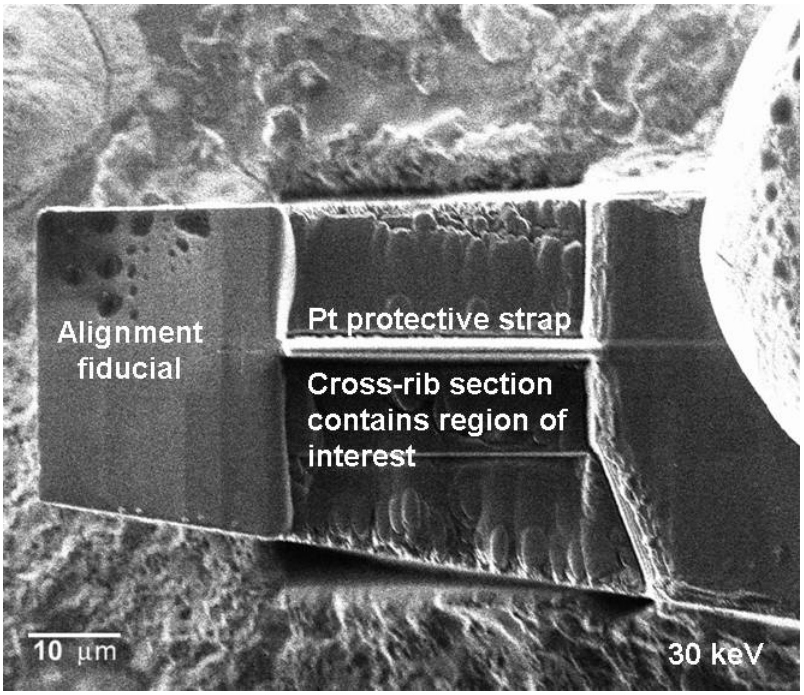
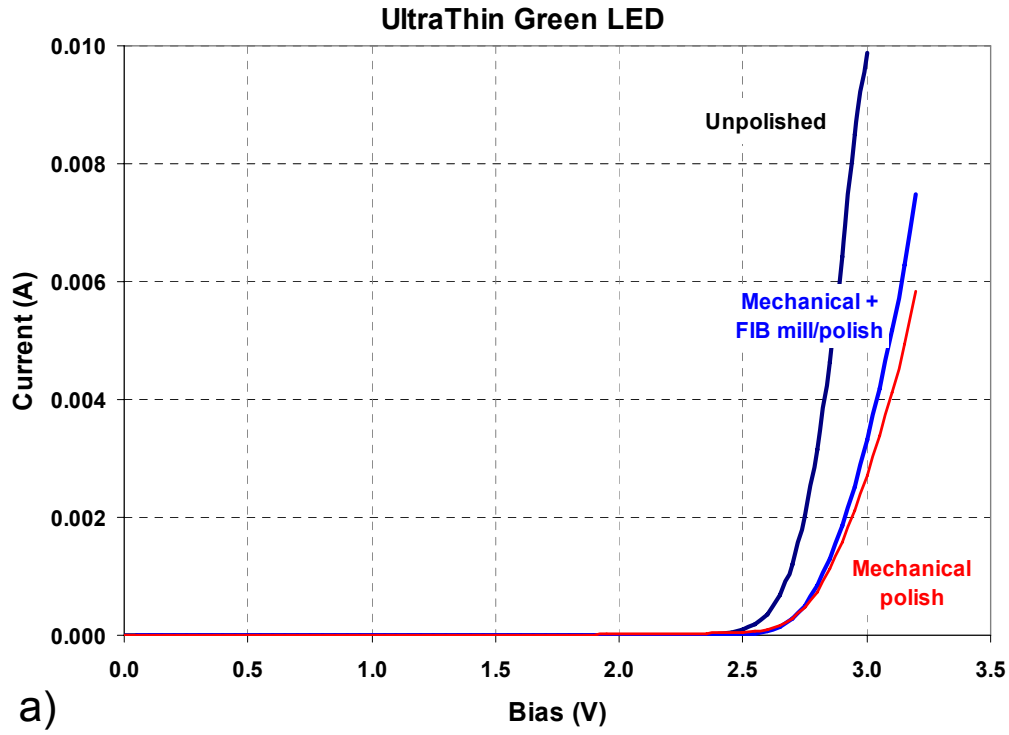


Figure 126: Formation of cross-rib isolating region of interest.

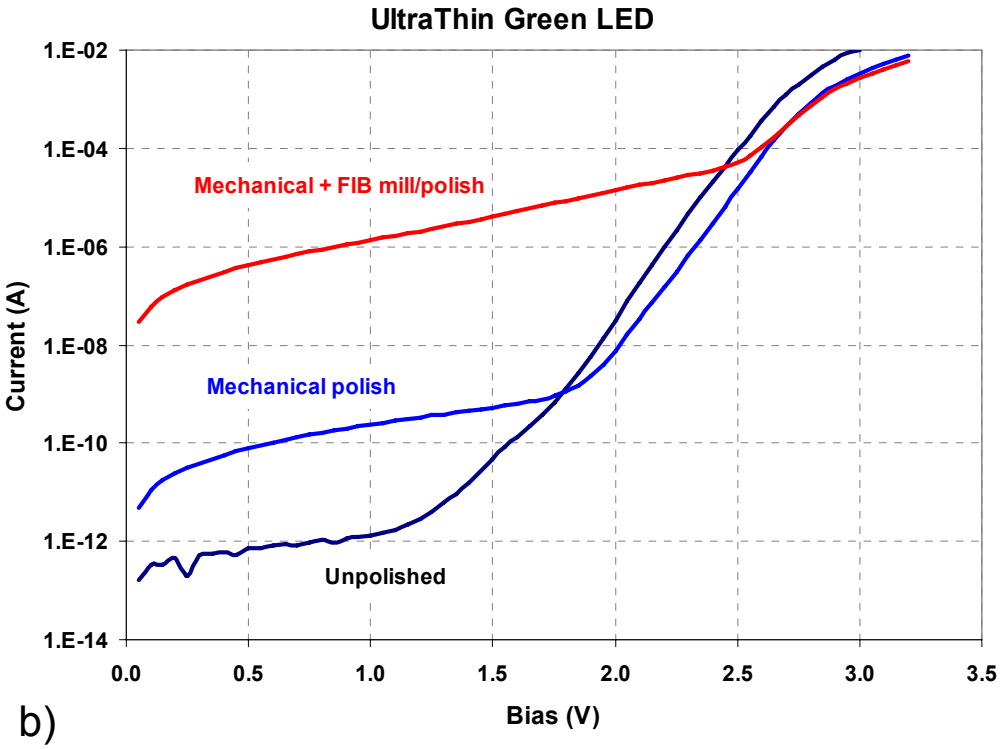
5.6.3 Electro-optical characterization

Characterization results for prep of the green UltraThin LED through formation of the electron transparent window are now discussed. Figure 127 shows forward bias I-V results for the device at various stages of sample prep; unpolished, mechanical polish and mechanical + FIB/mill polish. For completeness both (a) linear-scale and (b) semi-log scale plots are shown. The mechanical polish curve shows a current increase for low bias conditions due to leakage across the exposed polish damaged junction. As the bias is increased, current flow through the junction dominates, but is limited by reduced sample cross-section area. The result is lower current than observed with the unpolished die for voltages ≥ 1.75 V.

For the FIB mill/polish sample the I-V characteristic shows increased leakage current due to FIB damage along the exposed junction sidewall that has not been removed or repaired. Overall, the FIB polished I-V characteristic displays a well behaved profile with a reduced parallel resistance, $R_p \approx 10^6$ Ω, and no indication of Poole-Frenkel current bowing. Based on these results the sample was electrically qualified for STEM-EBIC analysis.



a)



b)

Figure 127: I-V data taken at various stages of sample preparation for STEM-EBIC a) Linear scale b) Semi-log scale.

The ability to do electroluminescence (EL) characterization of samples in the STEM was discussed earlier in section 4.2.3. Here EL is used to look for any changes to the LED emission characteristics due to sample preparation. Figure 128 shows EL spectra for the green LED sample taken after mechanical polish (Figure 123) and FIB prep (Figure 126). Results are normalized to the sample after mechanical polish. A forward bias of 2.4 V was selected as a compromise between sample time and resolution as determined by set-up of the Acton spectrometer. Settings used for the spectrometer were; 250 μm input slit, 0.5 nm step, 50 ms integration time and 3 samples per step. The range of the PMT was 350 – 650 nm. From Figure 128 we observe that the peak remained at 527 nm and the full width half max (FWHM) showed little change after FIB prep. While no change was expected, EL characterization was performed to confirm this. The drop in EL intensity however was expected as part of the polished sample was milled away during FIB preparation.

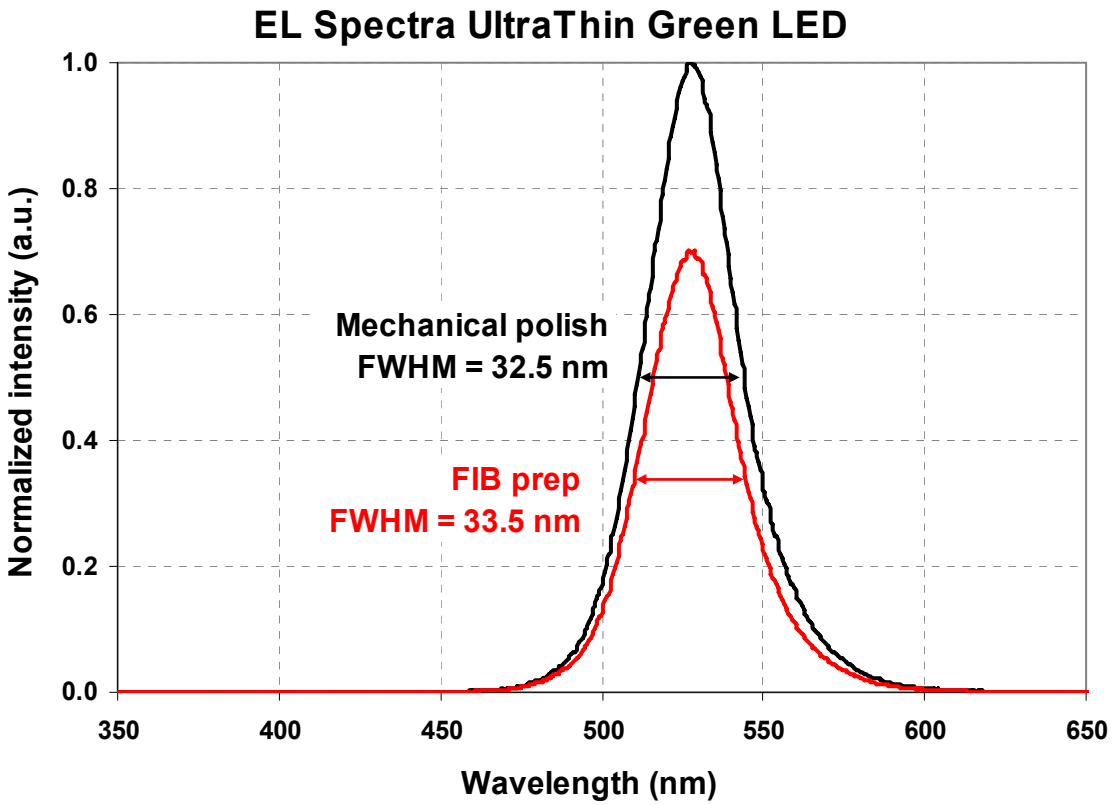


Figure 128: EL spectra normalized to mechanically polished UltraThin green LED under 2.4 V forward bias in STEM shows little change to FWHM after FIB prep.

To further investigate the effect of sample preparation on optical behavior, the EL spectrum was re-plotted with the intensity scaled to reveal emission detail over the shorter wavelength range from 350 – 460 nm. The re-plot is shown below in Figure 129 and a weak emission from 400 - 430 nm is observed. Morkoc[8] reported that p-GaN exhibits emission in this range due to deep states caused by Mg doping.

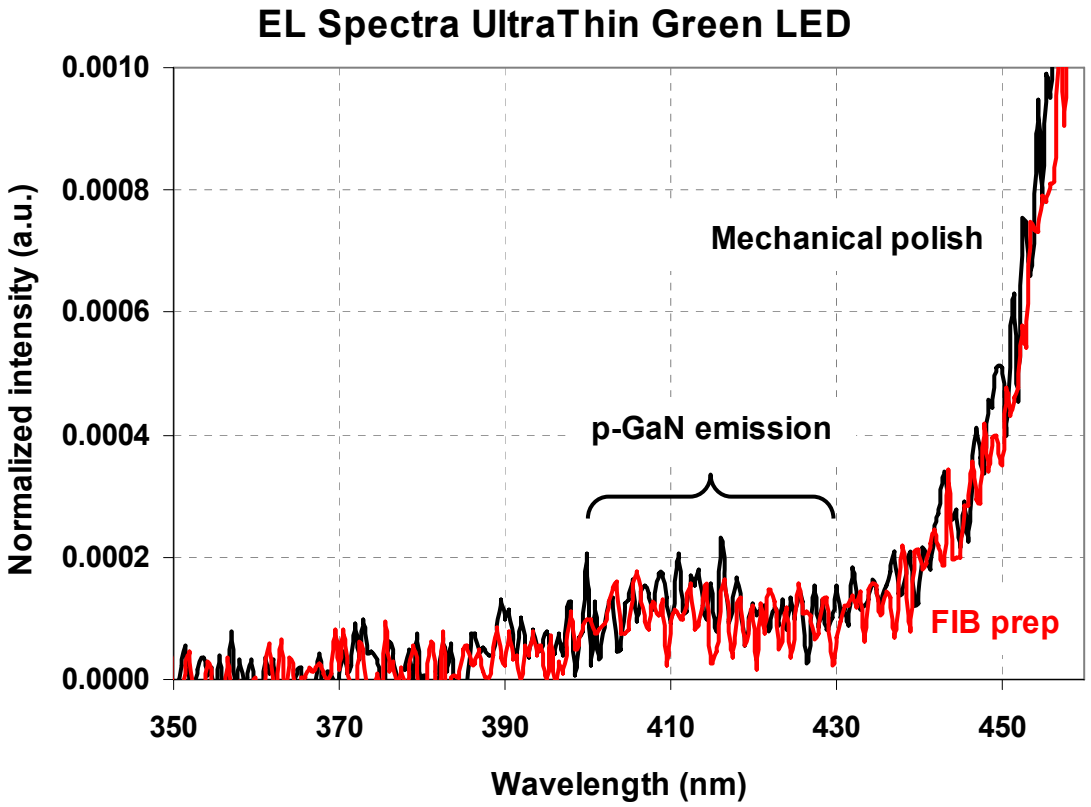


Figure 129: Short wavelength detail of UltraThin green LED EL spectra under 2.4 V forward bias in STEM reveals GaN emission.

The EL spectrum was also re-plotted with the intensity scaled to reveal emission detail over the longer wavelength range from 550 – 650 nm. This range is of interest as it includes the yellow defect-band emission range 520 – 620 nm. Yellow band emission is associated with Ga-vacancies in the n-GaN layer[118]. The re-plot for longer wavelength range is shown below in Figure 130. No indication of defect-band emission is present. However, it should be noted that EL emission

comes from the entire sample and may mask increased YB emission from the TEM cross-section.

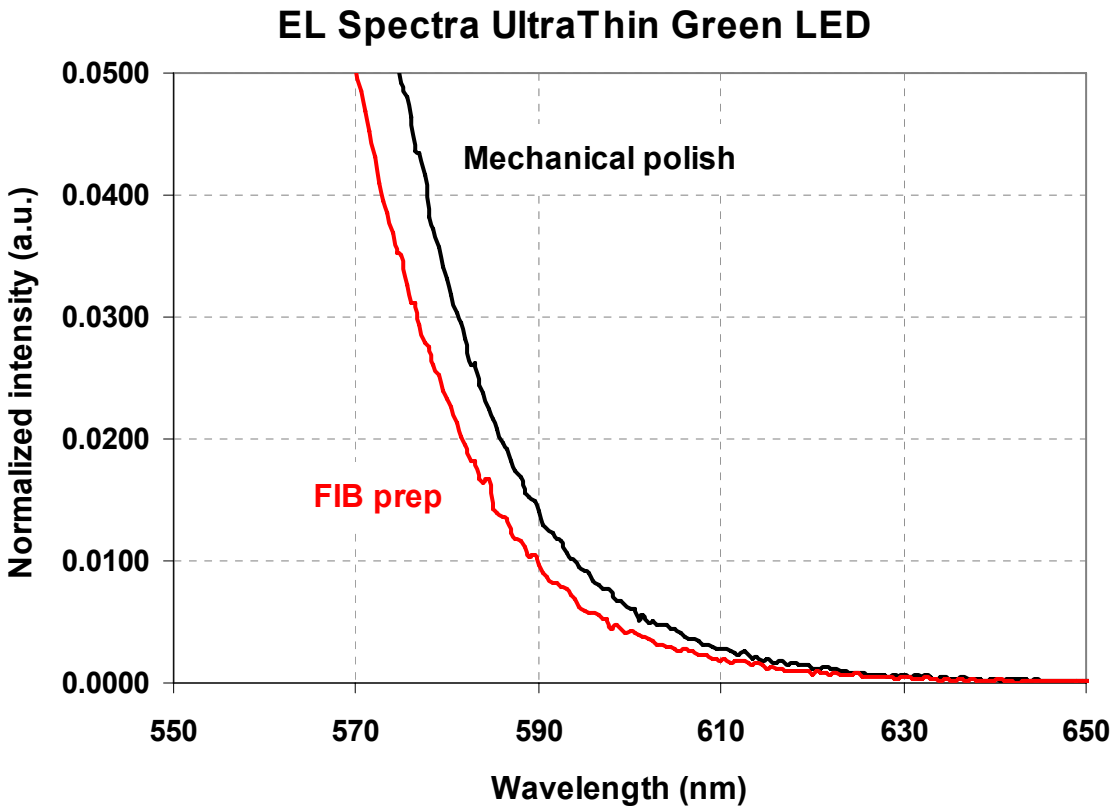


Figure 130: Long wavelength detail of UltraThin green LED EL spectra under 2.4 V forward bias in STEM.

5.6.4 STEM-ZC

The area of bright to dark contrast in the region of interest from Figure 124 makes up a ratio of approximately 1:3. Good delineation between the dark and bright contrast regions enabled an investigation comparing the two regions in cross-section. A series of ZC images were taken across the entire cross-section and used to create a continuous montage, which was then divided into bright and dark contrast sections based on the ratio of 1:3. Figure 131 shows the continuous bright contrast region. Ten V-defects were identified and labeled over the region's 3.58 µm length, which converts to an area defect density of 0.8×10^9 per cm^2. Figure 132

shows the continuous dark contrast region. Here, thirty-two V-defects were identified and over a distance of 6.26 µm, which converts to an area defect density of 2.6×10^9 per cm^2.

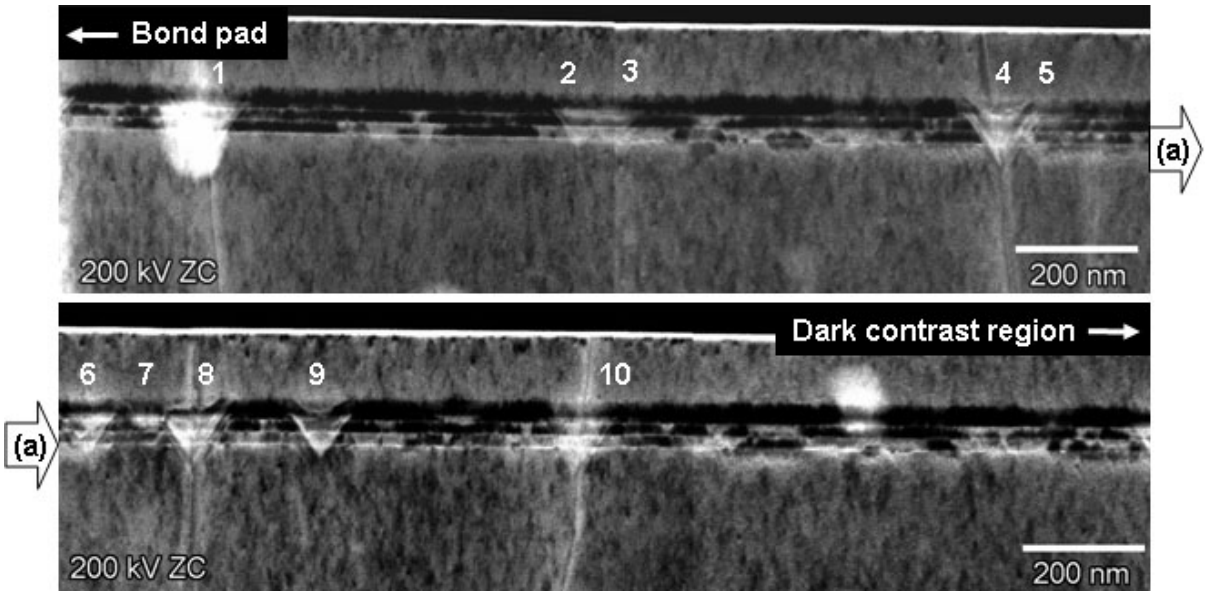


Figure 131: Composite image of continuous bright contrast region in cross-section.

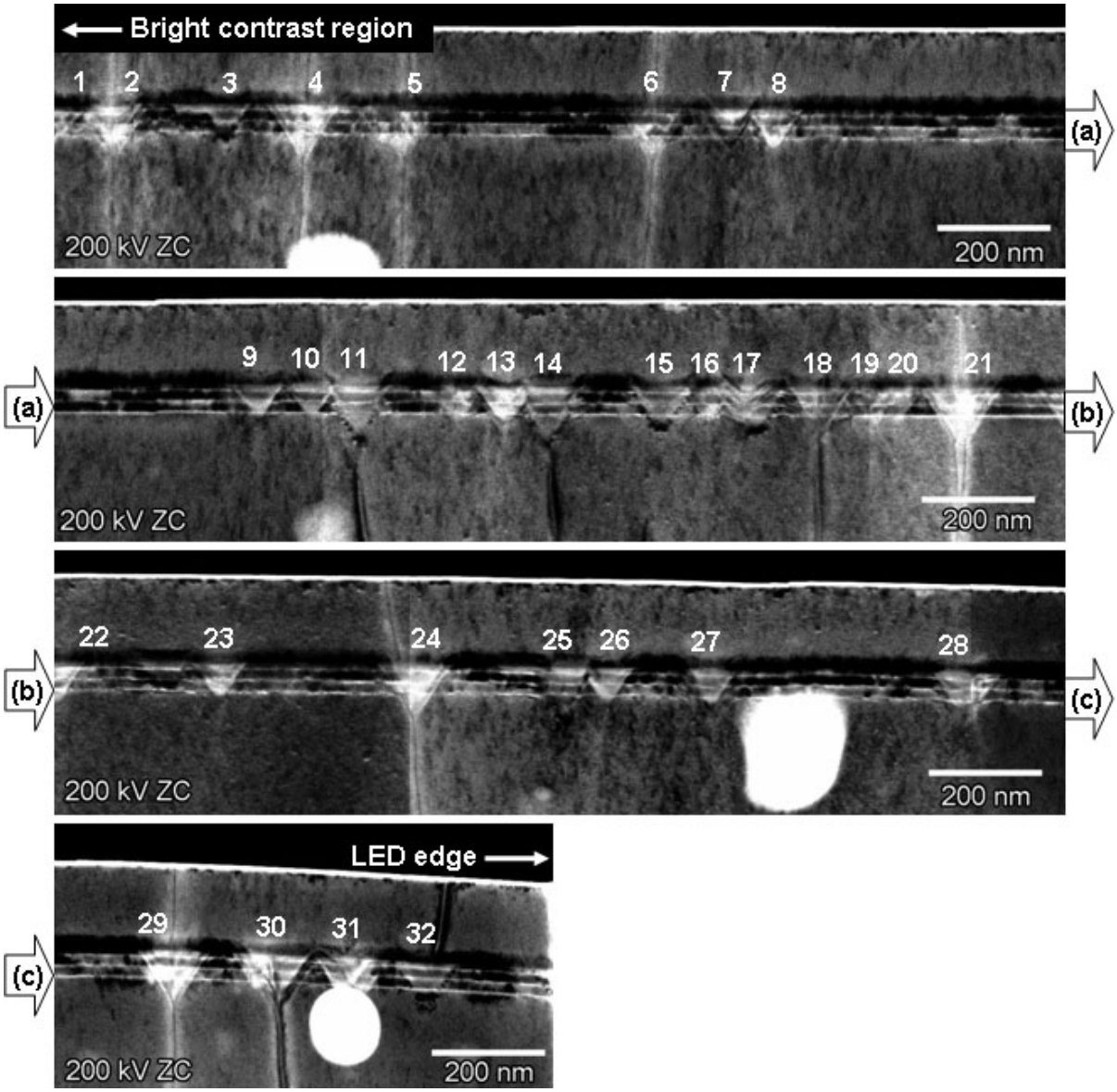


Figure 132: Composite image of continuous dark contrast region in cross-section.

The defect densities determined for the bright and dark contrast regions bracket the typical GaN dislocation density of 10^9 per cm^2. The results also agree with expected threading dislocation densities reported by Kuroda et al.[115] and Moldovan et al.[116] The GaN on sapphire sample used by Kuroda et al. had an estimated dislocation density of ~10^9 cm^{-2}. However, no value was given for the measured EBIC spatial inhomogeneity used to correlate to the dislocation density. Only that the spacing of inhomogeneity peaks coincides roughly with the expected

spacing of dislocation density. The samples used by Moldovan et al. had an estimated threading dislocation density in the mid-10^8 cm^{-2}. By measuring the dark defects present in SEM-CL and SEM-EBIC, a dislocation density in the low-10^8 cm^{-2} was calculated. This value compared well with the expected threading dislocation density and allowed correlation with contrast variation.

The results presented here support the work by Kuroda et al. and Moldovan et al. by correlating EBIC contrast variation directly to V-defects rather than expected threading dislocation density. Furthermore, it extends their work be correlating EBIC contrast variation to different dislocation densities. In the bright region, the defect density was 20% lower, while in the dark contrast region, the defect density was 160% higher than the typical dislocation density. From this 3x difference in defect densities, it was concluded that dark contrast regions observed in plan-view EBIC are due to a higher density of V-defects than present in bright contrast regions. In addition, V-defects rather than threading dislocations are the primary defect interacting with the MQWs.

5.6.5 STEM-EBIC mapping

The Hitachi HD-2000 was operated at 200 kV with a beam current of 275 pA and a spot size approximately 0.5 nm. After alignment of the sample, EBIC maps were taken to identify areas of interest. STEM-ZC and EBIC maps shown in Figure 133 through Figure 135 were acquired simultaneously using the Thermo Noran EDS system. Map resolution and pixel dwell time are reported in the figure caption. The resulting composite image created by offline post-processing allows correlation of the EBIC signal to device structure. Lastly, for reference Figure 133 includes labels identifying key regions of the observable cross-section. As the orientation of the sample in the HD-2000 did not change over the course of mapping, labels are not shown on subsequent ZC images.

Figure 133(a) shows a region containing multiple embedded V-defects some with threading dislocations passing through. The EBIC map in Figure 133(c) shows almost complete suppression of the EBIC signal. Identification of the pn-junction is

not possible, but a faint signal is present near the p-GaN/AlGaN interface. This indicates the presence of a rectifying interface, which will be discussed later.

Figure 134(a) shows an isolated embedded V-defect. The EBIC map is shown in Figure 134(c) and indicates that the presence of the defect suppresses the EBIC signal, which then recovers on either side of the defect. In the region above the defect, the pn-junction appears to be located near the center QW. However, below the defect the pn-junction appears shifted to the left or towards the p-GaN layer. As it turns out spatial variation of the pn-junction in defect free regions was observed quite often for the green LED sample.

Another example is shown in Figure 135(a) where multiple V-defects at the top of the image give way to a defect region at the bottom. Figure 135(c) shows the EBIC signal suppressed in the defect region and recovering in the defect free region. As the EBIC signal recovers, the pn-junction initially located near the far right QW progresses toward the left QW. Spatial variation of the pn-junction has been reported in SEM-EBIC results for GaN devices, but not directly mapped to the QW structure. This behavior was not observed with the blue LED sample. Other than the number of QWs, the most obvious difference between samples is indium concentration. As discussed earlier, the indium composition in the quantum wells was controlled to obtain blue and green light emission. The higher indium concentration necessary for green emission results in increased strain in the QWs. This may contribute to the observed spatial variation of the pn-junction, but would need additional investigation to confirm. Another difference between blue and green LED samples was the region of interest. For the green sample, a region was selected that included both bright and dark plan-view EBIC contrast. As such it is possible that the variation in pn-junction location is associated with the contrast variation. This possibility will be considered further in the section.

The STEM-EBIC mapping results presented in Figure 133 through Figure 135 represent the first direct correlation of EBIC contrast variation to V-defects in MQWs of GaN based LEDs. While EBIC mapping was useful for identifying areas of

interest, EBIC line scans are necessary to probe specific locations and improve signal to noise.

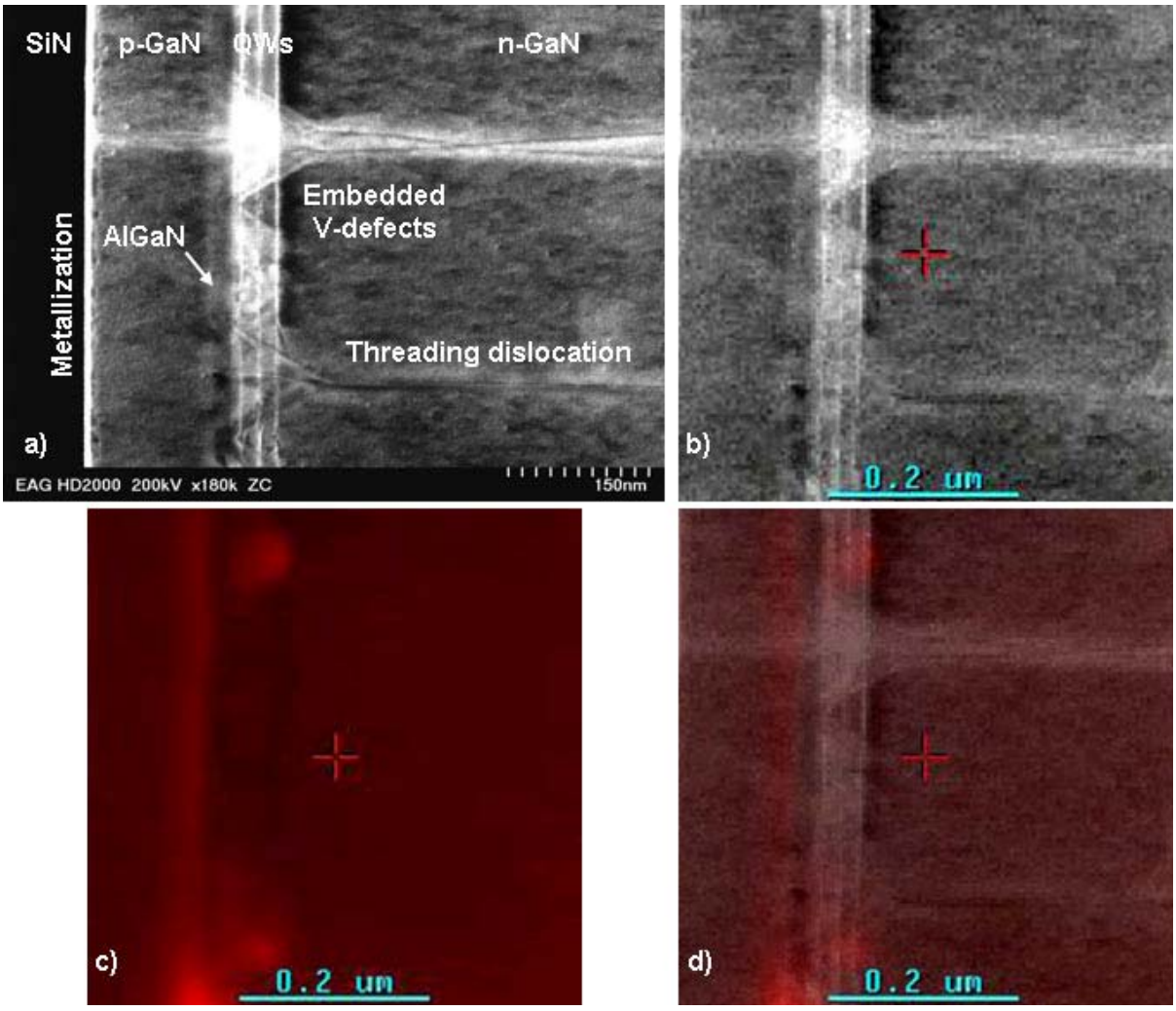


Figure 133: a) ZC image acquired with HD-2000 STEM b) ZC map & c) EBIC map acquired simultaneously using Noran with 128x128 pixels and 0.03 sec dwell time per pixel. d) Composite image of EBIC map overlaid on ZC map.

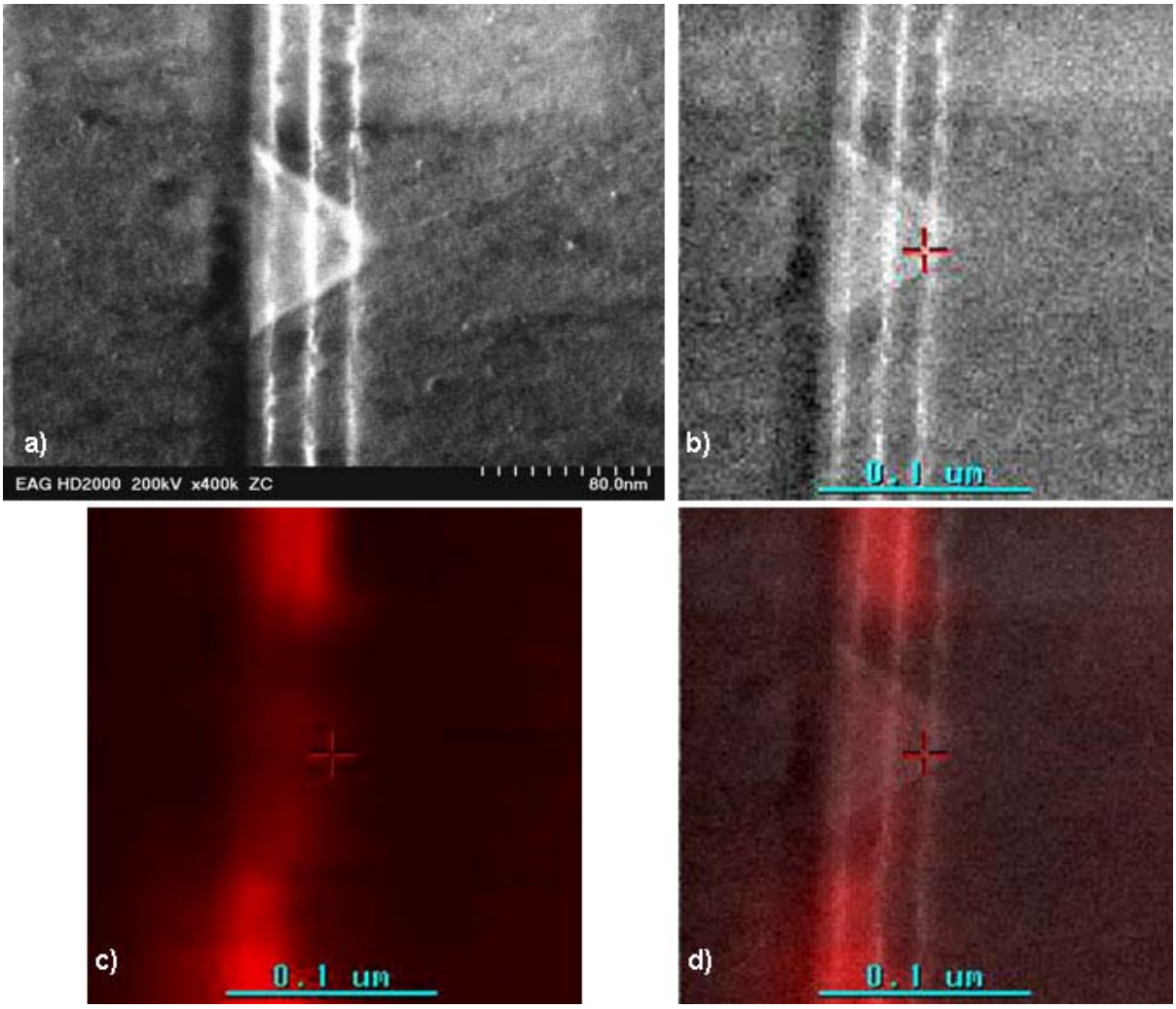


Figure 134: a) ZC image acquired with HD-2000 STEM b) ZC map & c) EBIC map acquired simultaneously using Noran with 128x128 pixels and 0.02 sec dwell time per pixel. d) Composite image of EBIC map overlaid on ZC map.

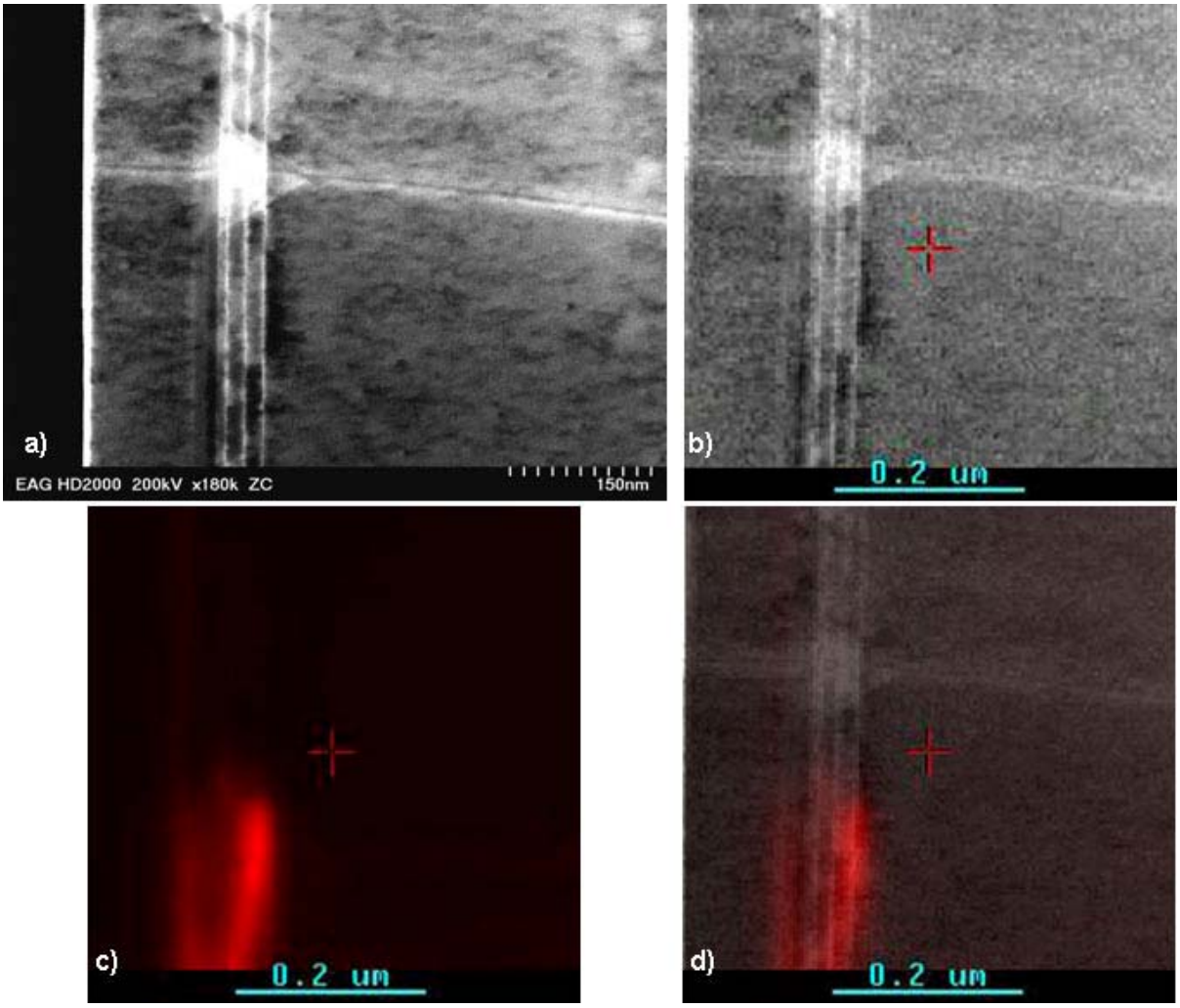


Figure 135: a) ZC image acquired with HD-2000 STEM b) ZC map & c) EBIC map acquired simultaneously using Noran with 128x128 pixels and 0.02 sec dwell time per pixel. d) Composite image of EBIC map overlaid on ZC map.

5.6.6 STEM-EBIC line scans

5.6.6.1 Results

The Hitachi HD-2000 was operated at 200 kV with a beam current of 275 pA and a spot size approximately 0.5 nm. EBIC line scans were acquired using the Thermo Noran EDS system. The scan length was set at ~ 150 nm to include a region on either side of the QWs and a dwell time of 0.5 sec per point, 100 points per line scan were utilized. Figure 136 through Figure 138 present EBIC line scan results mapped by post-processing to the associated region shown in a ZC image. In this manner the location of the pn-junction is identified and the effect of device structure on the EBIC signal is a direct correlation.

Figure 136 shows EBIC line scans taken from two locations across a region in the bright EBIC contrast area. The location of the line scans is to the far right of V-defect #10 in Figure 131. Recall that this region has a lower V-defect density than the dark contrast region. From line scans (a) and (b), the pn-junction is located 49± 2 nm from QW-1 placing it on the p-side of QW-3. Also noticeable in Figure 136, is a slight increase in current near the p-GaN/AlGaN interface indicating the presence of a rectifying junction, which is discussed below.

Figure 137 shows EBIC line scans taken from a region with an embedded defect with a threading dislocation passing through it. This is V-defect #24 from Figure 132 and is located in the dark EBIC contrast region. The pn-junction was determined from line scans (a) and (c) and located 20± 2 nm from QW-1 placing it near QW-2. The presence of the V-defect reduces the induced current within the V-defect. A defect contrast of 0.70 is measured between EBIC profiles (a)-(b) and 0.80 measured between profiles (c)-(b). Larger contrast values for a defects with a threading dislocation supports EBIC mapping results that showed similar behavior. For line scan (b) the EBIC profile taken at the defect core shows little presence of a pn-junction. However, there is a localized peak just inside the p-GaN region near the p-GaN/AlGaN interface. The increase in current indicates the existence of an additional rectifying junction, which are known to exist in GaN based diodes. Shah et al.[94] developed a theoretical model for anomalously high ideality factors that

modeled the p-GaN/AlGaN interface as a rectifying heterostructure. It would appear then that the line scan picked up the presence of this additional junction.

Lastly, Figure 138 shows EBIC line scan results taken from a defect free region and an embedded V-defect. From Figure 138(a), the pn-junction is located 7± 2 nm from QW-1. From Figure 138(b), the presence of the V-defect reduces the peak induced current with a defect contrast of 0.69 measured between EBIC profiles in Figure 138(a) and (b). The measured contrast is on the high-end for an embedded defect without a threading dislocation. However, unlike line scan (b) taken at the defect core in Figure 137 , the EBIC profile from Figure 138(b) still shows a defined peak that allows identification of the pn-junction. The defect related shift between profiles in Figure 138(a) and (b) measured 6 nm toward the p-GaN layer.

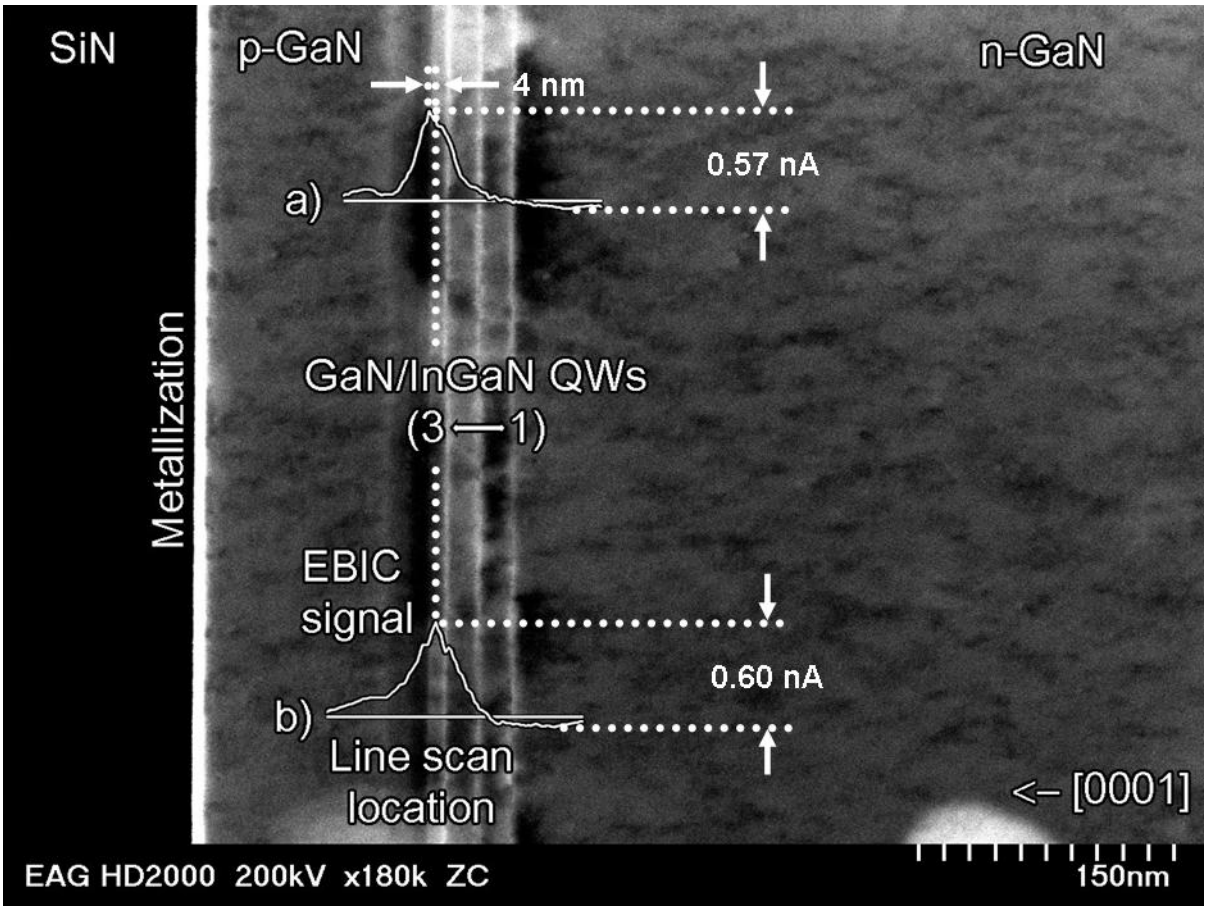


Figure 136: EBIC line scans taken from bright contrast region. Location is far right of V-defect #10 in Figure 131. From line scan (a) with junction located 49± 2 nm left of QW-1 and shows little variation in location between (a) and (b).

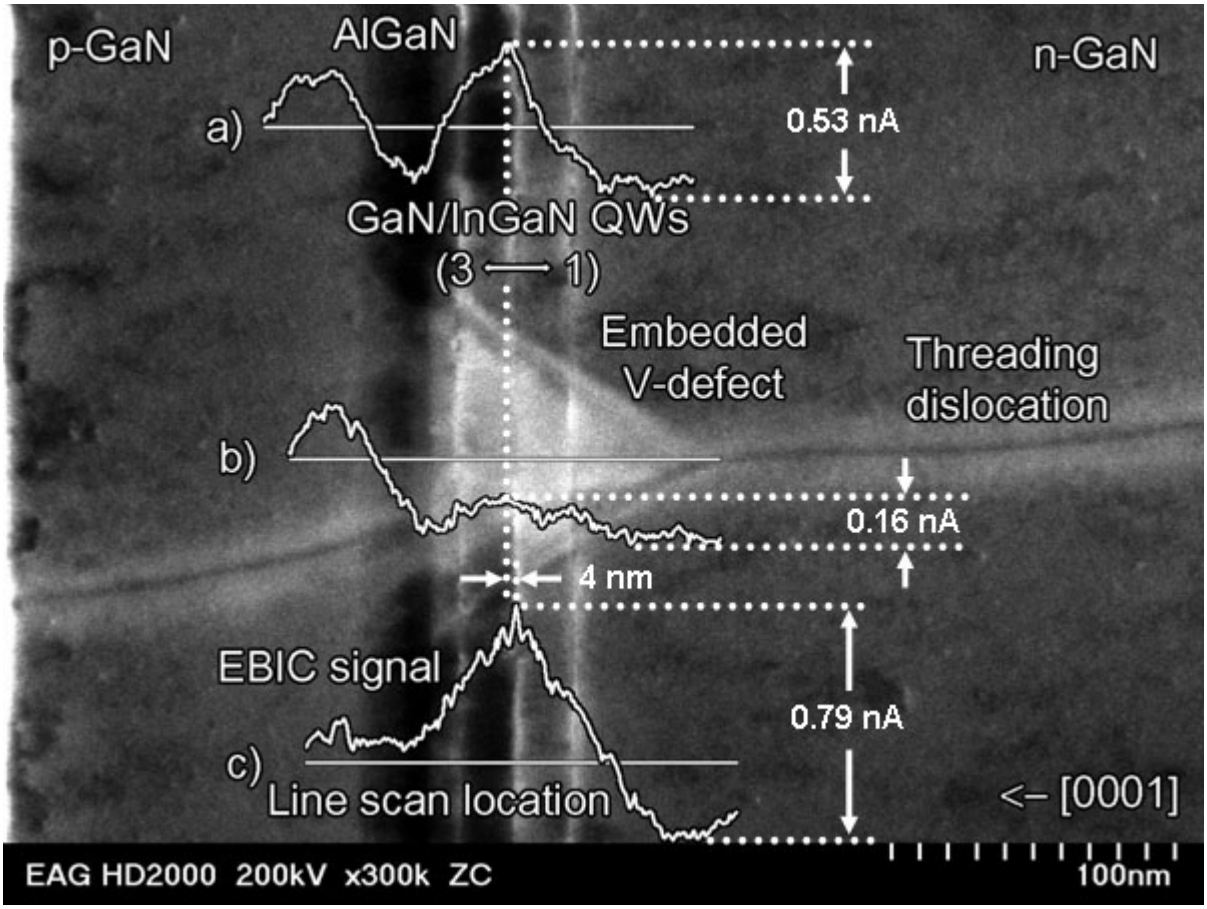


Figure 137: EBIC line scans taken from V-defect #24 in dark EBIC contrast region shown in Figure 132. A defect contrast of 0.70 to 0.80 was measured from the change in peak to trough spread between line scans (a)-(b) and (c)-(b). Little defect related shift in pn-junction location is observed. From line scan (c) the junction is junction located 20± 2 nm left of QW-1. Increase in EBIC signal in p-GaN layer indicates presence of additional rectifying peak.

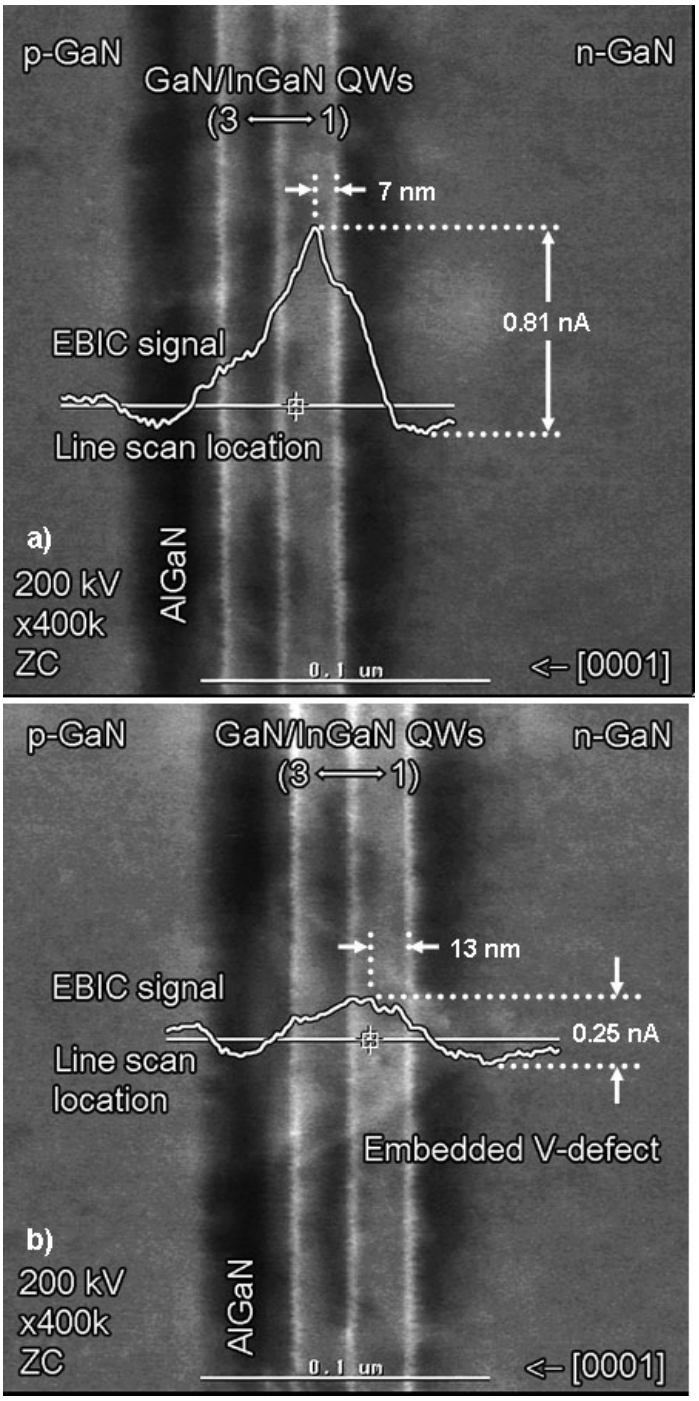


Figure 138: EBIC line scans taken from embedded V-defect. A defect contrast of 0.70 was measured from the change in peak to trough spread between line scans (a) and (b). At the defect core the pn-junction was located 13± 2 nm left of QW-1. From line scan (a) the junction is junction located 7± 2 nm left of QW-1.

5.6.6.2 Discussion

A review of the line scans shown in Figure 136 through Figure 138 confirms the spatial variation of the pn-junction location observed in EBIC mapping results. The cause of the variation appears due to different junction locations obtained from bright/dark contrast areas in the region of interest. In the bright contrast region the pn-junction is near the p-GaN layer (Figure 136), while for the dark contrast region the junction is located toward the n-GaN layer (Figure 136 and Figure 137). For the bright and dark contrast region the pn-junction was placed at 49 ± 2 nm and 15 ± 7 nm respectively from QW-1 near the n-GaN layer. It is interesting to note that this variation was not observed for the blue LED. Then again, the region of interest for the blue LED contained little to no bright contrast area. This suggests, as discussed in section 5.5.6.2, that V-defect enhanced Mg diffusion results in the location of the pn-junction near the n-GaN layer in the dark contrast region.

From the discussion in section 5.5.6.2, no model exists for extracting minority carrier diffusion lengths from EBIC line scans for a TEM type cross-section. As such, the same approach used in section 5.5.6.2 is followed and the shape of the EBIC profile was evaluated based on equation (5-1) with results shown in Table 4.

Table 4: Extracted minority carrier diffusion lengths using VanRoosbroeck model[121]

	Line scan	L_n (nm)	L_p (nm)
Figure 136 Bright contrast area	a)	38	40
	b)	56	44
Figure 137 Dark contrast area	a)	69	22
	c)	50	36
Figure 138 Dark contrast area	a)	25	17
	b)	48	35

The results presented in Table 4 suggest that hole minority carrier diffusion lengths, L_p are less than electron minority carrier diffusion lengths, L_n. A similar

result was observed for the blue LED. Furthermore, reviewing EBIC line scans taken through the cores of V-defects, in Figure 137 and Figure 138, flattening of the signal profile can be observed. This suggests that minority carrier diffusion lengths are larger inside the V-defects than in the defect free region. This trend is quantified in the last two rows of Table 4 where L_n and L_p increased from 25 nm to 48 nm and 17 nm to 35 nm respectively inside the V-defect. Defect related increases in minority carrier diffusion lengths were also observed with the blue LED sample and possible explanations were discussed in section 5.5.6.2.

5.6.7 Green LED summary

A Cree green UltraThin LED was prepped and qualified for STEM-EBIC in accordance with methods developed and presented in this work. First, bright/dark contrast regions observed with plan-view SEM-EBIC were correlated to defect structure observed across the electron transparent cross-section. Results indicated that the dark contrast region observed in plan-view was due to a higher density of V-defects, 2.6×10^9 per cm^2, than the bright contrast region, 0.8×10^9 per cm^2.

STEM-EBIC maps were used to survey the sample, investigate trends in pn-junction location and influence of structure on charged carrier behavior. Results indicated that the pn-junction varied spatially across an active region made up of three QWs. STEM-EBIC mapping also directly correlated EBIC contrast variation to V-defects in the MQWs of GaN-based LEDs. EBIC maps of regions with almost complete signal suppression were correlated to V-defects that contained threading dislocations.

While mapping was useful for correlating defects to EBIC contrast and identifying regions of interest, EBIC line scans were necessary to probe specific regions across V-defects and improve signal to noise. A series of experiments were performed that recorded STEM-EBIC line scan results from different locations at selected regions of interest. These results confirmed the signal suppression effect of V-defects. Defect contrast values measured for V-defects with threading dislocations ranged between 0.7 – 0.8 while defect contrasts for embedded V-

defects without threading dislocation measured 0.7. Larger contrast values suggest that defects with a threading dislocation are more disruptive to the active layer than embedded V-defects without threading dislocations and supports EBIC mapping that showed similar results. In addition, a defect related shift in the pn-junction toward the center QW (QW-2) was observed.

Line scans taken from bright contrast region placed the pn-junction 49 ± 2 nm measured from QW-1. This located the junction toward the p-GaN layer. Line scans taken from the dark contrast region placed the pn-junction 15 ± 7 nm measured from QW-1. This located the junction toward the n-GaN layer. Variation of the pn-junction appears to be due to V-defect enhanced Mg diffusion and the higher density of V-defects present in the dark contrast region. Analysis of the signal profile indicated that minority carrier diffusion lengths for holes were less than electrons. Flattening of the EBIC profile suggests longer minority carrier diffusion lengths inside the defect.

5.7 STEM-EBIC summary

In this chapter sample prep and qualification methods developed and documented in earlier chapters were applied to study the active region in GaN based LEDs. The motivation was to extend STEM-EBIC capabilities to directly correlate defects to observed EBIC behavior. STEM-EBIC characterization was performed on blue and green Cree UltraThin LEDs and the influence of device structure and defects on charged carrier behavior observed. EBIC mapping and line scan results for a Cree blue UltraThin LED are summarized below.

1. V-defects observed interacting with the QWs.
2. Measured defect capture range of 53 nm for an embedded V-defect and 64 nm for a sectioned V-defect.
3. Direct correlation of EBIC contrast variation to V-defects present in the QWs of GaN based LEDs. Regions with almost complete signal suppression were correlated to sectioned V-defects.

4. Defect contrast measured for sectioned V-defects ranged between 0.7 – 0.8 while defect contrast for embedded V-defects measured 0.5.
5. PN-junction in dark contrast region of interest was located 21 ± 2 nm from QW-1. Location possible due to V-defect enhanced diffusion of Mg.
6. Analysis of the EBIC signal profile indicated that minority carrier diffusion lengths for holes were less than electrons.
7. Flattening of EBIC profile by V-defects suggests longer minority carrier diffusion lengths inside the defect and was proposed due to reduced field strength.

EBIC mapping and line scan results for a Cree green UltraThin LED are summarized below.

1. The dark contrast region that was observed in plan-view EBIC was due to a higher density of V-defects, 2.6×10^9 per cm^2, than present in the bright contrast region, 0.8×10^9 per cm^2.
2. A direct correlation was established between EBIC contrast variation and V-defects in the QWs of GaN based LEDs.
3. Defect contrast measurements for V-defects with threading dislocations ranged between 0.7 – 0.8 while defect contrast values for embedded V-defects without threading dislocation measured 0.7.
4. PN-junction in bright/dark contrast region was located 49 ± 2 nm and 15 ± 7 nm respectively measured from QW-1. Difference in junction location possible associated with lower density of V-defects in bright contrast region and thereby less unwanted Mg diffusion.
5. Analysis of the EBIC signal profile indicated that minority carrier diffusion lengths for holes were less than electrons.
6. Flattening of EBIC profile by V-defects suggests longer minority carrier diffusion lengths inside the defect.

6. STEM-CL Experiments and Results

6.1 Motivation

The driving force behind this work is the need for correlated nano-characterization techniques to study electrical and optical properties related to the complex microstructure of $In_xGa_{1-x}N$ quantum wells. The STEM-EBIC methods demonstrated in the previous chapter enable the study of electrical properties. Here the emphasis is on obtaining optical information from the same site of the specimen. This can be achieved by observing the optical response that a specimen gives under electron irradiation, the process of cathodoluminescence. The potential of combining CL with EBIC is desirable in view of the growing interest in the analysis of defect structures that affect the optoelectronic quality in devices such as LEDs.

STEM-CL is a powerful technique that offers the potential to correlate crystallographic information directly to luminescence. However, as discussed in section 3.6 the low signal strength deriving from the thin samples used in STEM, and the difficulty of building instrumentation for STEM-CL, has significantly reduced its application. Previous in-house efforts by Bunker[2, 75] resulted in the development of a lens based CL-system for a Hitachi HD-2000 STEM. The system did not include a collecting mirror due to limited available space between pole pieces, 5 mm, on the HD-2000 STEM. Preliminary results, reproduced in Figure 139, show poor spectral resolution, but did indicate that signal detection was possible as indicated by the peak around 560 nm associated with yellow band emission. The goal in this work is to advance capability of the lens based STEM-CL system and improve spectroscopic capability.

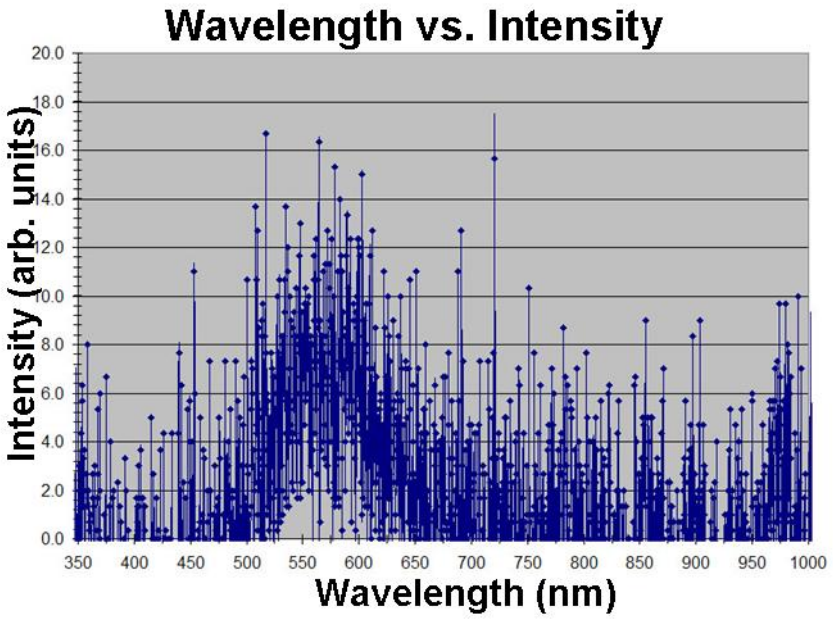


Figure 139: STEM-CL spectra for 10000 ms integration time with average of three in 300 nm region cross-section. (From Bunker[75]).

6.2 STEM-CL set-up

Limitations due to sample prep methods, holder design and detector sensitivity were all thought to contribute to the poor spectral results shown in Figure 139. Sample preparation improvements and qualification were discussed in chapter 4; attention is now turned to detector sensitivity and improvements. The spectrometer used by Bunker was an Ocean Optics USB2000 mini-spectrometer. However, its UV sensitivity was poor and its noise level very high, and was best used for large SEM beam currents, ≈ 10 nA, that excite significant CL signal. Alternatively an Acton SpectraPro 2150i monochromator/spectrometer shown below in Figure 140 was used. This was a 150mm nominal-focal-length Czerny-Turner

grating monochromator, equipped with a 1200 lines/mm 500nm-blaze grating. Slit widths are continuously variable from 10 to 3000μm, which gave quoted spectral resolutions of 0.04nm to ~12nm. The detector was a R1527P PMT, in an Acton PD471 housing. For spectroscopy the signal was processed by an Acton SpectraHub, coupled to the SpectraPro and a laptop computer. The controller is shown below in Figure 141. A schematic of the system set-up is shown in Figure 142 and the actual system set-up on the HD-2000 STEM is shown in Figure 143.

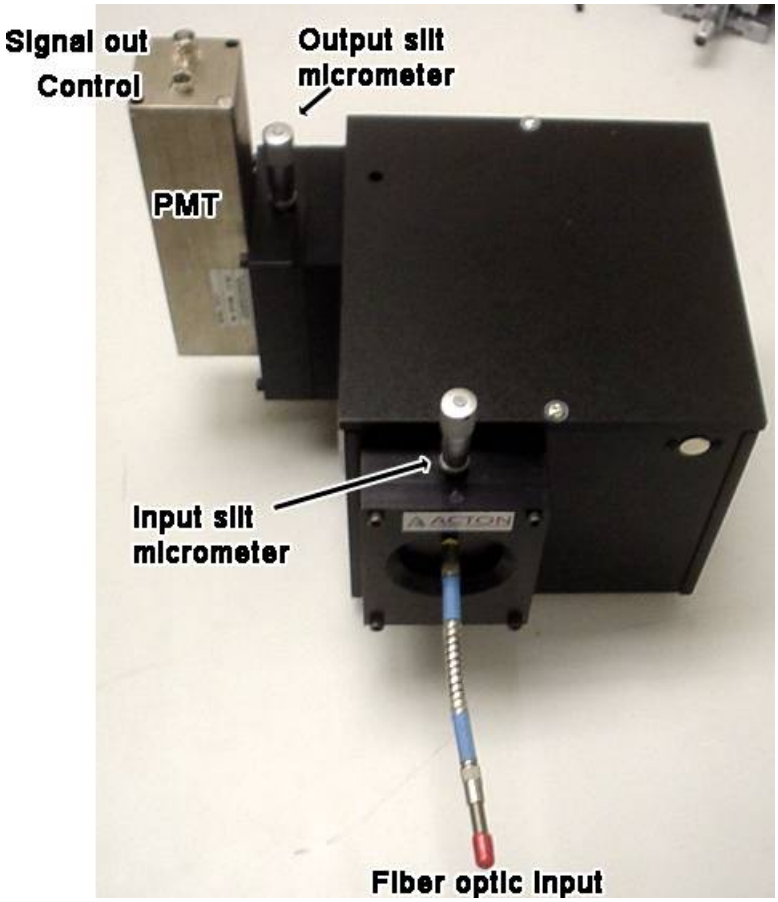


Figure 140: an Acton SpectraPro 2150i monochromator/spectrometer.

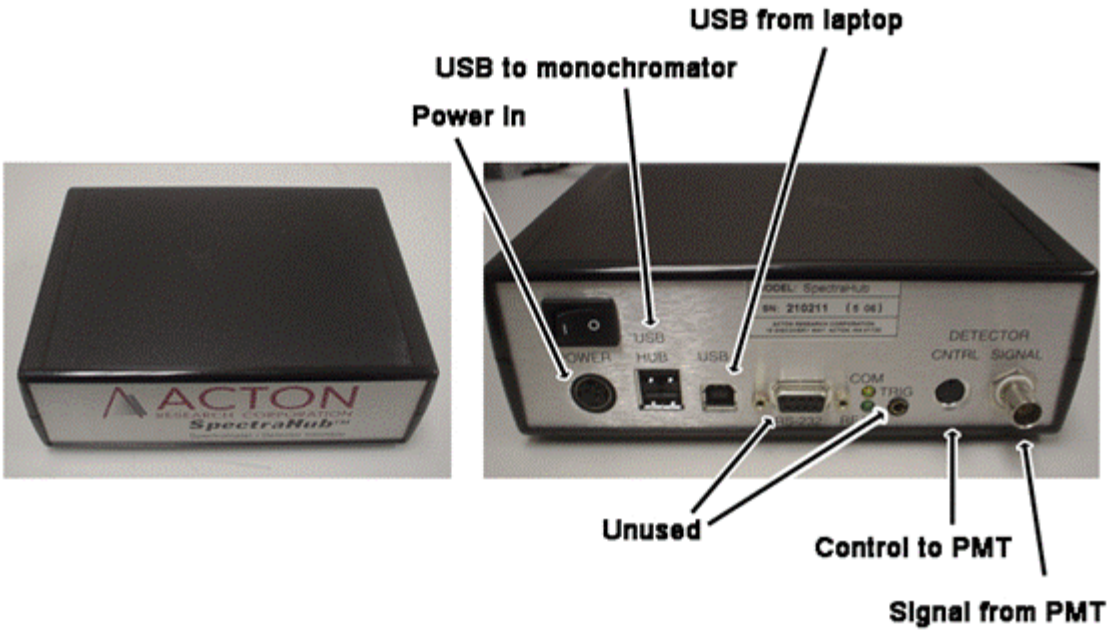


Figure 141: Acton SpectraHub monochromator/spectrometer controller.

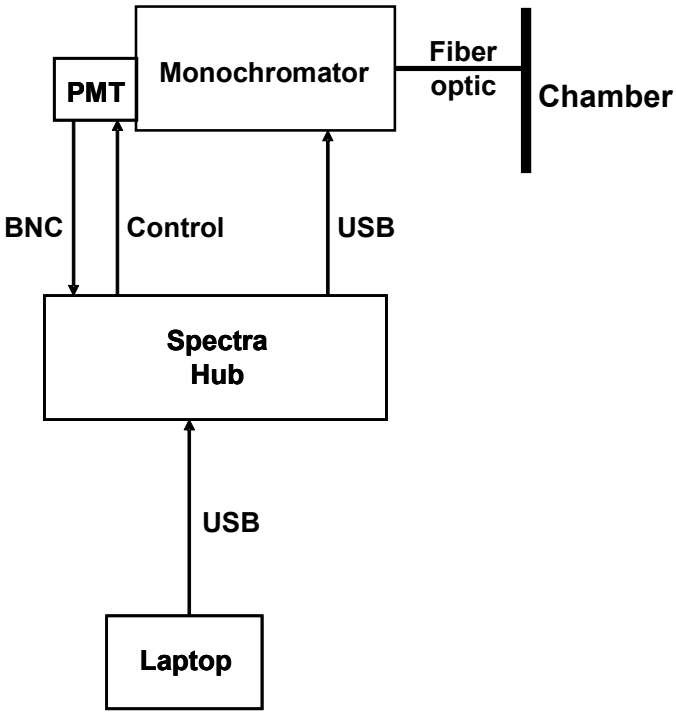


Figure 142: Schematic of STEM-CL spectroscopy system set-up.

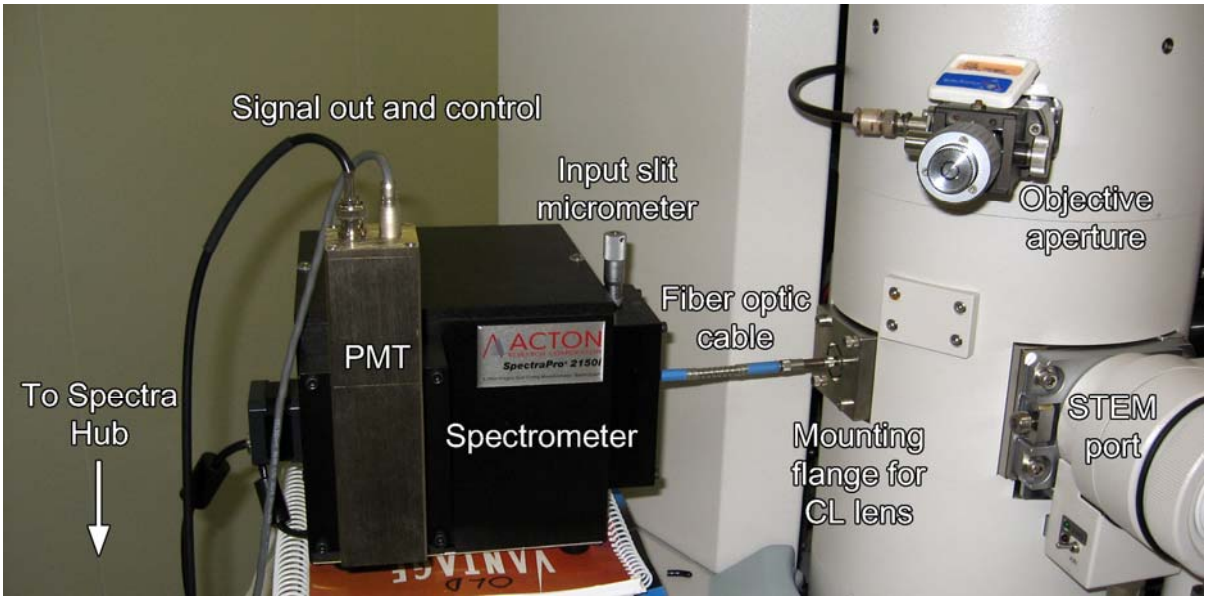


Figure 143: STEM-CL set-up for Hitachi HD-2000 dedicated STEM.

6.3 Samples

The device used in the study was a commercial Cree, Inc. InGaN based MQW UltraThin^{TM} blue LEDs[117]. The LEDs consisted of eight $In_xGa_{1-x}N$ QWs and the indium composition in the quantum wells was controlled to obtain blue light emission. Size of the QWs and indium mole fraction is proprietary. The structures were grown by metal-organic chemical vapor deposition on a (0001) SiC substrate. The donor and acceptor concentrations were N_d = 3-4x10^{18} cm^{-3} and $N_a \leq 10^{19}$ cm^{-3}. Ohmic contacts were deposited on the n-SiC substrate and p-GaN layer. The blue LED was specified for an output power of 5.5 mW operating at 20 mA, with a full width half maximum emission of approximately 22 nm centered at 470 nm. The as received samples were unpackaged LEDs supplied mounted on a TO-header and included the p-side wire bond contact. The devices were removed from the TO-header and prepped for analysis following the process described in section 4.5.2.

6.4 UltraThin Blue LED results and discussion

The blue UltraThin LED sample was loaded in the STEM-EBIC holder. In anticipation of STEM-CL the holder was designed with a notch toward the side of the

CL collection lens, Figure 144. The notch combined with the sample facing the lens helped to increase the CL collection solid angle. All images were collected at room temperature using a 200 kV electron beam. First, the sample was tilted to align on axis. Then ZC imaging was used to identify a region of interest along the active layer. Figure 145 shows the targeted region contained within the dashed box. Next the HD-2000 was operated in scan-box mode to confine the beam to the area of interest. A spectrum was then acquired using a monochromator slit width of 1500 um with an integration time of 500 ms and averaged over three scans.

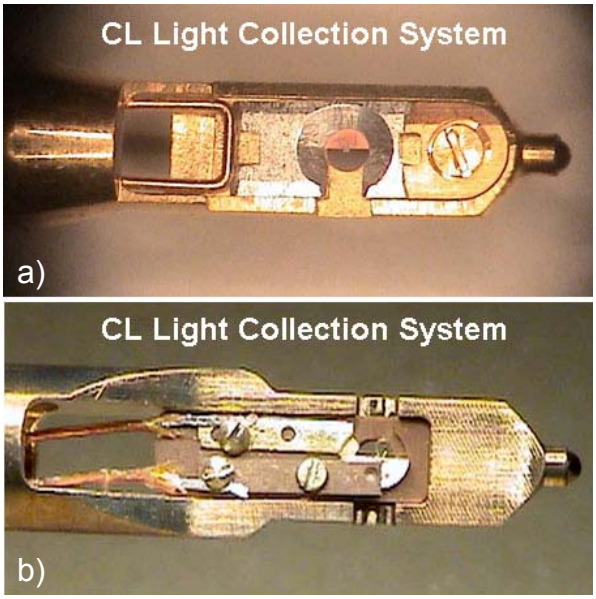


Figure 144: a) Previous STEM-CL holder. b) Modified STEM-EBIC/CL holder.

The resulting CL spectrum versus wavelength and energy is shown in Figure 146(a) and (b) respectively. The tails of the spectrum, 300 – 350 nm and 600 – 650 nm are outside the range of the PMT and were used for background correction. Compared to previous results shown in Figure 139, improvements to sample preparation, holder design and detector reduced integration time 95% while improving signal-to-noise. Inspection of Figure 146 indicates that detection of more than just yellow-band (YB) emission in the 550 - 600 nm wavelengths was achieved.

A broad peak is observed in the 370 – 440 nm range and a peak at the 490 nm wavelength is present as well. The short wavelength peak, 370 – 390 nm, corresponds to GaN emission; likely coming from the GaN barriers sandwiching each of the eight InGaN QWs. Another peak is observed in the 400 – 440 nm range. This is thought to be due to a combination of emission due to p-GaN (400 – 420 nm) and amorphous GaN (~440 nm). The amorphous GaN emission is probably due to FIB induced damage that remained after low energy cleaning. The next noticeable peak is around 490 nm and thought to be QW emission. However, the wavelength is greater than the 475 nm the device is specified for. This red-shift may be partially explained by the QCSE. Recall from section 2.4.3 that band bending due to the QCSE reduces the band gap resulting in longer wavelength. Charge carriers injected under bias partially screen the QCSE and increase the band gap. As the STEM-CL experiments were preformed under zero bias we would expect to see longer wavelength emission from the QWs.

Lastly, the broad peak from 510 – 570 nm corresponds to yellow-band emission associated with Ga-vacancies in n-GaN. It is not surprising that YB emission has the highest intensity. The barrier layers between QWs are n-GaN and preparation damage likely increased the number of vacancies. As charge carriers fill low energy states first, the result is higher measured intensity from YB emission.

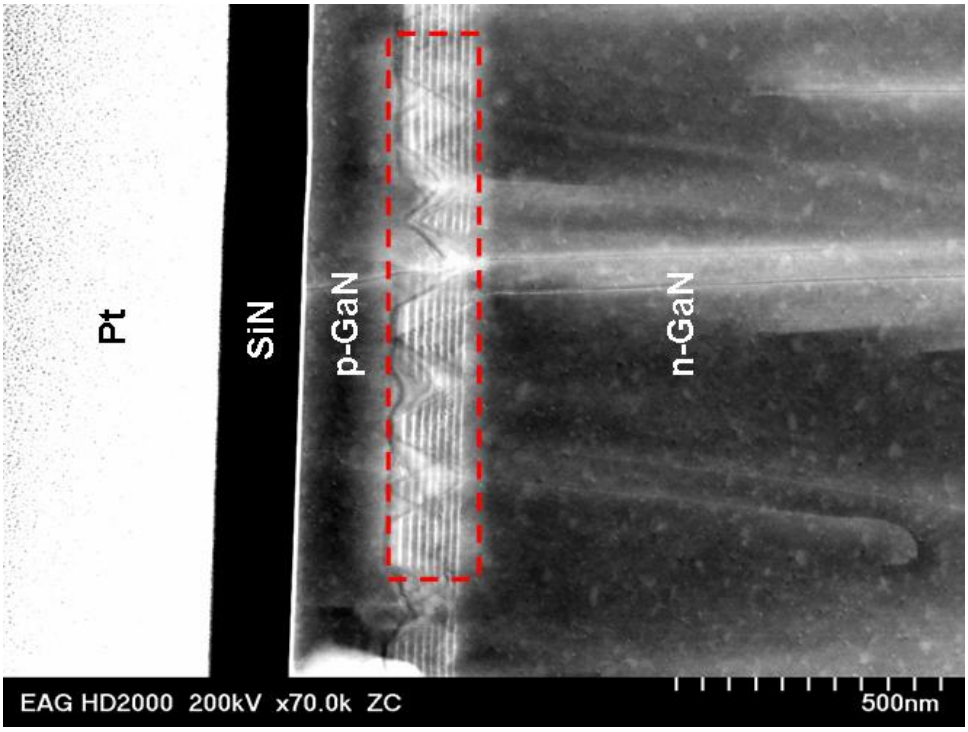


Figure 145: ZC image showing location of scan box used for STEM-CL.

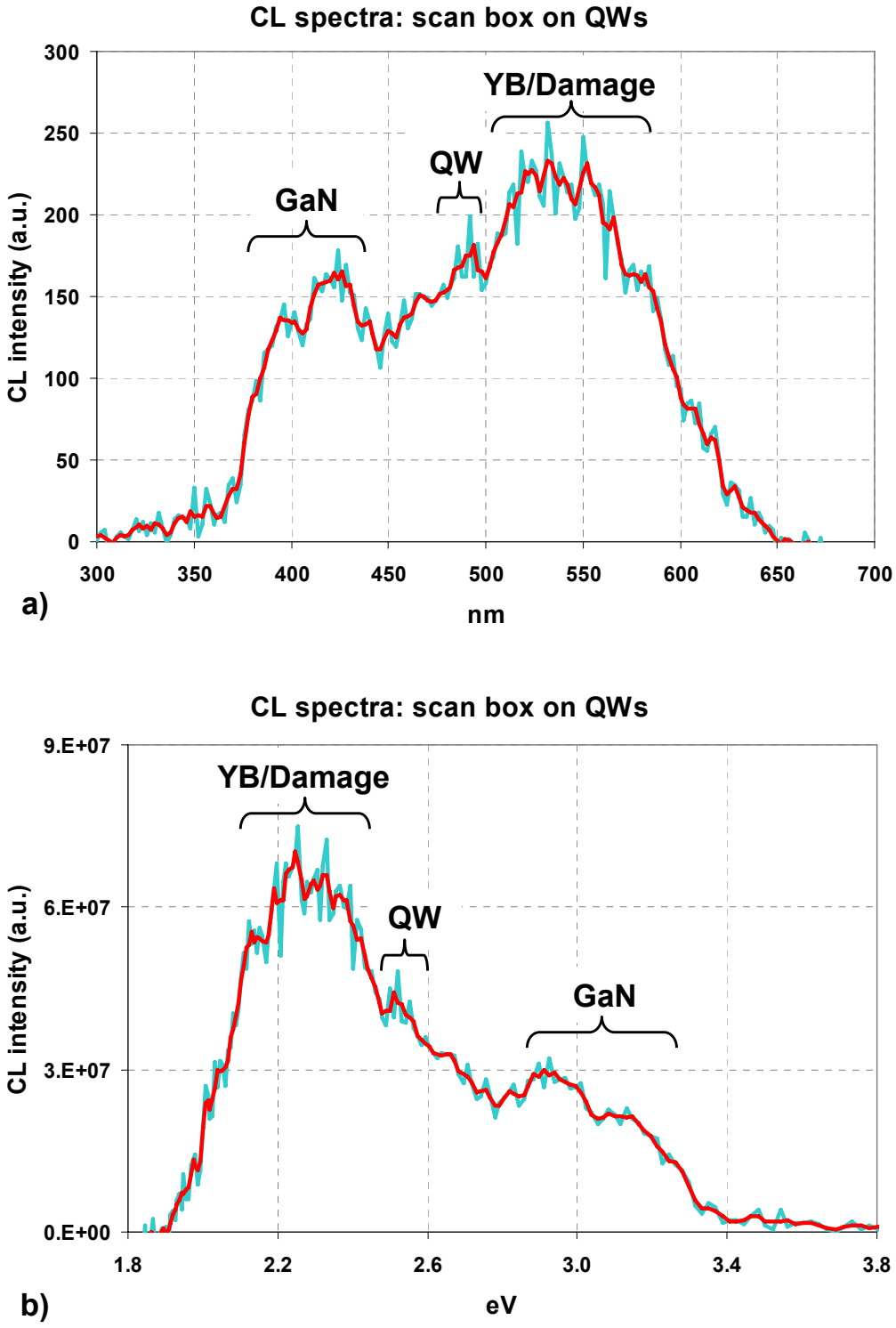


Figure 146: STEM-CL spectra results versus (a) wavelength and (b) energy for 500 ms integration time averaged over three scans (red line is moving average of 3).

The CL spectrum shown in Figure 146 represents the best achieved resolution resulting from a trade-off between slit width and intensity. Increasing the slit width increased the measured intensity, but also reduced resolution. Decreasing the slit width would improve resolution between peaks, but the reduced intensity made it difficult to resolve those peaks. The problem of low measured intensity is primarily due to poor collection efficiency resulting from no collection mirror. Recall from section 3.6.2 that collection efficiency for the in-lens system was estimated at ~5%. However, integration of a mirror into the CL system was considered not practical given the 5 mm gap between poles in the HD-2000 STEM.

Given these limitations it was decided to operate the HD-2000 in x-ray mode which provides a higher beam current, but also a larger spot size. Once again ZC imaging was performed to find an area of interest. In this case it was decided to look at different regions of the sample. CL spectra were compared from a section of undamaged QWs, damaged QWs and n-GaN. Figure 147 shows the region selected and the three dashed boxes show the locations for the scan boxes. The size of the scan box was fixed at 120 μm x 120 μm for the three locations shown. A spectrum was then acquired at each location using a monochromator slit width of 1000 um with an integration time of 1000 ms and an averaged over three line scans.

The resulting CL spectrum from each location versus wavelength is shown in Figure 148(a) and (b). The tails of the spectrum 300 – 350 nm and 600 – 650 nm are outside the range of the PMT and were used for background correction. The color coding of the CL spectra in Figure 148 match the color of the dashed scan box locations shown in Figure 147. It is observed that the higher beam current available with the EDX mode of the HD-2000 resulted in higher measured CL intensity than achieved with Normal mode (Figure 146). Also observed is a broad band characteristic present in all three spectrums.

The difference in spectra obtained from different regions of the sample is now discussed. The spectrum for the V-defect region has a broad peak centered on the 500 nm wavelength. No distinct QW peak emission can be identified, but the spectrum is somewhat level between 450 – 550 nm. This is unlike the spectrum

obtained for n-GaN, which drops off on either side of a peak around 540 nm. Also of note is that the measured CL intensity for the V-defect region is lower than the intensity obtained from either of the other two regions. Such behavior would be expected if the V-defect did indeed suppress luminescence, but it is interesting to observe that the spectrum for the V-defect region still exhibits strong emission. The V-defect has an intensity ~ 70% of that for the undamaged QW region measured at the QW emission wavelengths 480 - 490 nm. Recall that EBIC results for sectioned V-defects yielded signal intensities less than 20% compared to undamaged regions.

Results from Figure 148(a) seem to support the observation of strong luminescence from GaN-alloy LEDs despite the presence of large defect densities. Strong emission is also consistent with the discussion in section 5.5.6.2, that the defect related decrease in EBIC is due to reduction of the built-in electric field. If that were not the case, the defect related decrease in CL intensity would likely be greater. Consider that STEM-EBIC related defect contrast was approximately 0.7 – 0.8 depending on defect type. If the reduced EBIC signal was due to increased non-radiative recombination a similar drop in intensity would be expected from STEM-CL measurements, which is not the case. Alternatively, if the reduced EBIC signal is due to increased radiative recombination, an increase in CL intensity would be expected, which is also not the case. Instead increased recombination time due to reduced carrier concentration produces less emission resulting in the decreased CL intensity. Increased recombination time also leads to increased minority carrier diffusion lengths observed inside V-defects.

It is also interesting to note that between 450 – 550 nm wavelengths, the spectrum for the V-defect region exhibits a similar broad-flat profile as the spectrum for the undamaged QW region. Close inspection of Figure 147 reveals that the V-defect region did contain portions of undamaged QWs. It has also been reported that sidewall QWs form on the facets of the V-defects and exhibit a band gap larger than that of the regular c-plane QWs[28]. However, it is not clear if this is the source of the observed emission for the wavelength range mentioned above and requires further study.

Comparing the spectra for the undamaged QW and n-GaN regions shown in Figure 148(b), a separation is observed in measured intensity in the wavelength range from 400 – 525 nm. It is concluded, the difference is due to the QW emission that is not present in the n-GaN region. From 535 – 650 nm the spectra essentially match, which is attributed to the presence of n-GaN in both regions.

The observation of broad band emission from the three regions identified in Figure 147 is somewhat unexpected. Certainly there are distinctions between the spectra, but the broad band nature makes it difficult to fully resolve much more than general trends. The source of the broad band characteristic is unclear. (S)TEM-CL is typically done using a cold stage to improve signal strength. This was not the case here and it may be possible that injected EHPs first fill low energy defect states. Consequently, as the number of injected carriers is limited, fewer high energy states get filled. Radiative recombination from the defect states results in the long wavelength emission and broadening observed in all three spectrums.
The lack of both a cold stage and collecting mirror limit the resolution and measured CL signal strength. As such, until improvements can be made neither panchromatic nor spectrally resolved imaging will be able to provide any spatially related luminescence information. However, the cost of a cold stage at ≈ $40k was prohibitive and space between pole pieces (~ 5 mm) in the HD-2000 limits mirror options. Furthermore, access to the microscope has decreased making it unlikely that any modifications will be allowed in the near term.

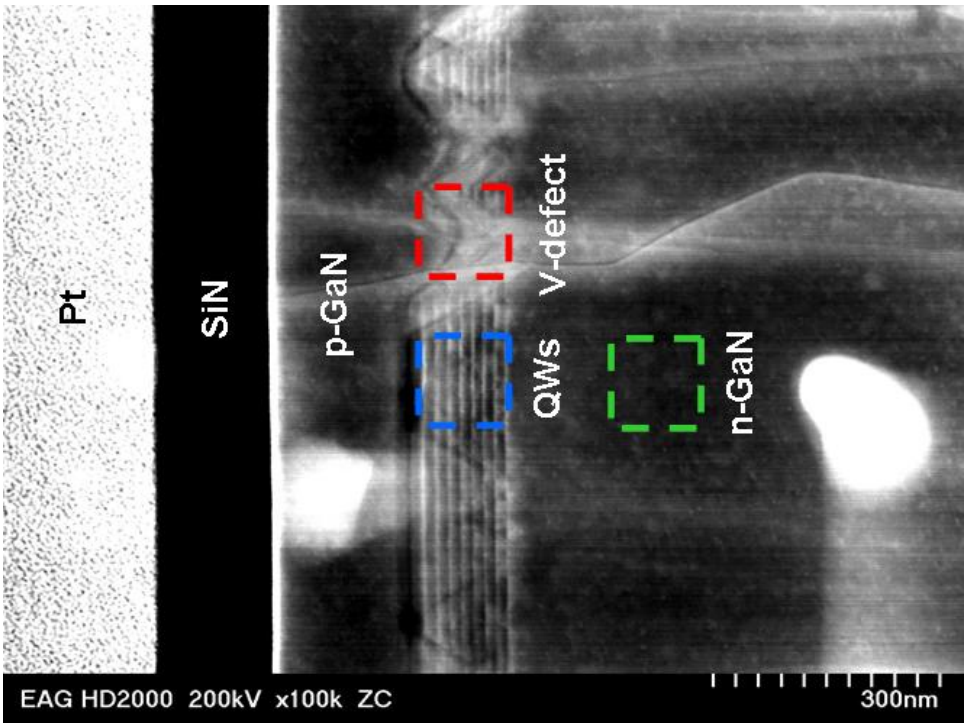


Figure 147: ZC image showing location of various scan boxes on different regions of blue LED sample.

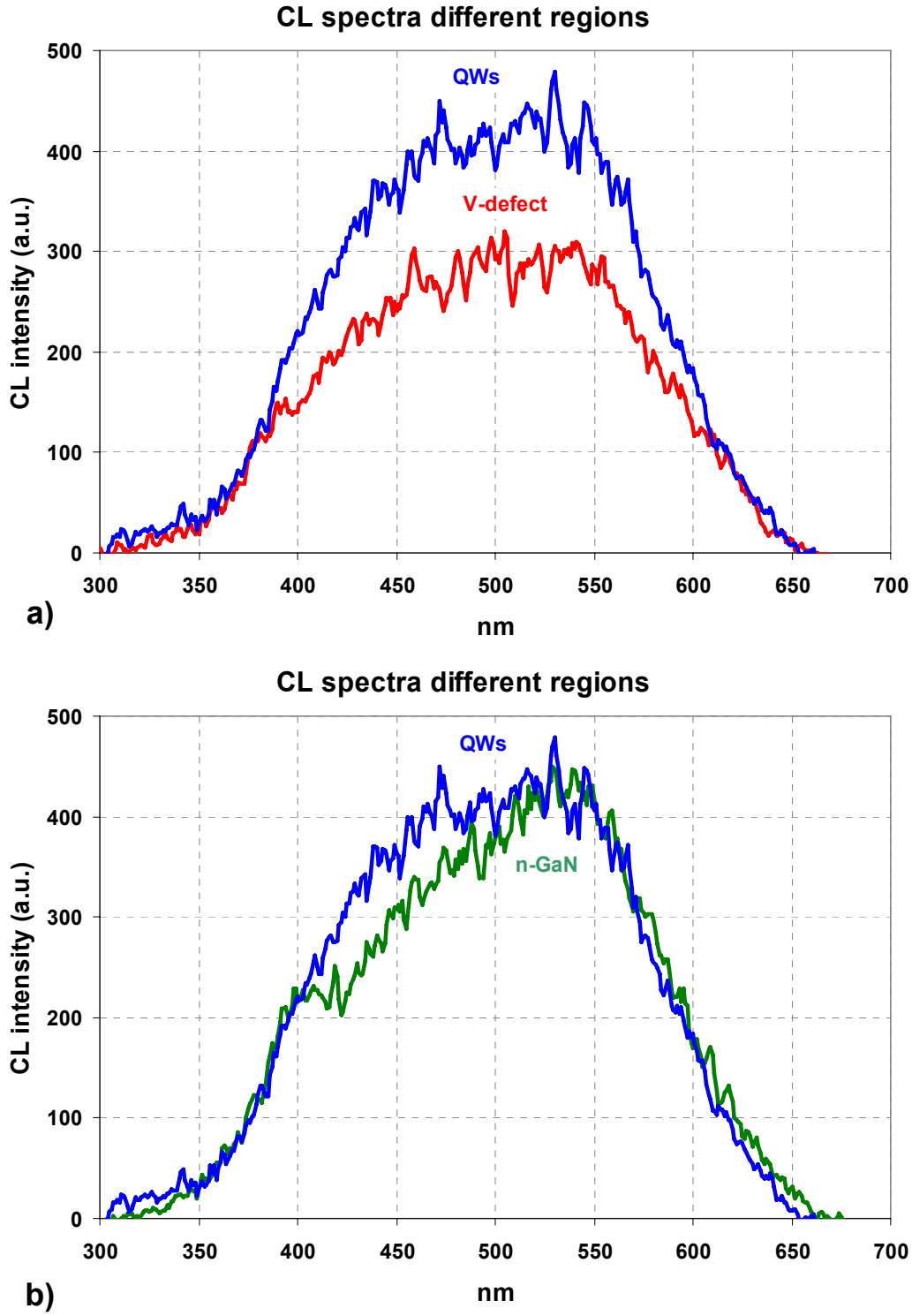


Figure 148: STEM-CL spectra results (a) QW, V-defect and (b) QW, n-GaN taken from scan box regions shown in Figure 147 (moving average of 3 applied).

6.6 STEM-CL summary

This chapter focused on improvements to an in-lens CL system for a dedicated Hitachi HD-2000 STEM. Previous results indicated that detection of a CL signal from a STEM sample with the in-lens design was possible. However, the signal was noisy and resolution poor. Improvements were required, but identification and implementation of those improvements was left for future work. Three improvements were implemented none of which required modification of the instrument. This was critical as the HD-2000 used for these experiments was a commercial STEM and could not be taken off-line for extended periods. The improvements addressed detector sensitivity, holder design and sample preparation resulting in better signal resolution and lower noise at 5-10% of the integration times used by Bunker. CL spectra were observed for different regions of the sample and results support increased recombination time due to reduced carrier concentration as the cause of decreased CL intensity. Increased recombination time also leads to increased minority carrier diffusion lengths observed inside V-defects. CL spectra obtained indicated the ability to detect both QW and GaN emission, which had not been achieved previously. However, the large slit width settings used on the spectrometer to let in more light also reduced resolution. To extend capability and enable panchromatic and spectroscopic imaging will require additional improvements; specifically a cold stage and some way to improve the collection efficiency. Never the less, the improvements implemented to the STEM-CL system have provided a new level of STEM-CL capability for future advances to build on.

7. Conclusions

7.1 Contribution

7.1.1 Summary

The motivation for work undertaken in this research was two fold. First, it attempted to address questions related to luminescence from GaN based Light Emitting Diodes. Second, it attempted to advance optoelectronic characterization techniques in a Scanning Transmission Electron Microscope. In the past, direct correlation between structural and electrical properties in complex multi-quantum well GaN based LEDs has been difficult[116]. In part from challenges associated with both sample prep and instrumentation. Cross-sectional analysis is necessary to provide access to the multi-layered structures of LEDs. While this is somewhat straight forward for bulk investigations, (S)TEM analysis requires electron transparent samples. This requirement complicates both the sample prep and instrumentation set-up.

Consequently, the first goal of this research was to develop sample prep and experimental methods for STEM based EBIC and CL analysis. Sample prep methods need to be repeatable without minimum alteration to sample properties. For this reason qualification of the sample prior to analysis was necessary. This was achieved using current-voltage characterization. The sample prep and experimental methods were then applied to directly correlate electrical to structural properties for the first time in GaN based blue and green UltraThin MQW LEDs.

Finally, the potential of combining CL with EBIC was desired in view of the growing interest in the analysis of defect structures that affect the optoelectronic quality in devices such as LEDs. The emphasis here was on obtaining optical information with STEM-CL from the same site of the specimen probed with STEM-EBIC. Improvements to an existing in-lens collection system for the HD-2000 STEM were implemented. Spectroscopic results showed the detection of QW and GaN emission in addition to YB/damage emission and indicated that the capability of the CL-system had been extended beyond previous efforts. CL spectroscopy was also performed on different regions of the sample and the results correlated to structure.

The contributions from this work improved both sample prep and high-resolution STEM-EBIC/CL analytical methods. Results were obtained that for the first time directly correlate electrical to structural properties in GaN LEDs. A brief review of each of the contributions related to sample prep and analytical results is presented below.

7.1.2 Contribution: Methods and techniques

1. FIB based bridging interconnects: A method was developed for forming electrical interconnects across air gaps or uneven surfaces using FIB micromanipulation and deposition. Intended for forming electrical contacts for lift-out STEM-EBIC samples, the method is robust and can be applied to other electrical interconnects requirements that can not be met with standard wire bond techniques. Current-voltage investigation revealed a contact resistance of ~ 50 Ω.
2. In situ FIB I-V method: In situ current-voltage characterization of FIB processed samples was performed for the first time. Results showed an increase in both forward and reverse current at low voltages. Further investigations confirmed that the increased current is associated with a sidewall damage of the exposed pn-junction. The increased current profile corresponds to the Poole-Frenkel mechanism and not a simple shunt current equivalent to a resistor connected in parallel with the LED.
3. Improved STEM-EBIC sample preparation: Developed a detailed and repeatable method for preparing and qualifying STEM-EBIC samples. A re-design of the sample holder was presented to improve sample positioning for STEM analysis while still providing electrical contacts for extracting an EBIC signal. Lastly, results from in-situ current-voltage characterization were used to establish qualification requirements for STEM-EBIC. The resulting parallel resistance after sample prep was limited to no less than 10^6 Ω and no indication of current bowing.

7.1.3 Contribution: GaN-alloy LED characterization

1. Direct correlation between electrical and structural properties: Cross-sectional STEM-EBIC mapping and line scans of UltraThin blue and green LEDs enabled for the first time direct correlation between electrical and structural properties in GaN based LEDs. V-defects were observed interacting with the QWs. Two types of V-defects were identified and characterized according to the observed structural damage to the QWs. Back filled V-defects disrupted the QW structure and had the largest measured defect contrast ranging from 0.7 – 0.8. Embedded V-defects did not produce significant disruption of the QWs and a defect contrast of 0.5 – 0.6 was measured. A capture range of 64 nm was measured for a back filled V-defect and 53 nm for an embedded V-defect. These results suggest that embedded V-defects are less disruptive to the active layer than sectioned V-defects.
2. Minority carrier diffusion lengths: Analysis of the signal profile suggests longer minority carrier diffusion lengths inside the defect. Increase may be due to by reduced carrier confinement resulting from disruption of the QWs by V-defects or reduced field strength resulting from V-defect enhanced diffusion.
3. PN-junction location in MQW LEDs: Location of the pn-junction in both blue and green MQW LEDs was determined. In the dark EBIC contrast region of a UltraThin blue LED the pn-junction was located at 21 ± 2 nm measured from the first QW on the n-GaN side. For an UltraThin green LED the pn-junction was less stable and the location varied around 28 ± 21 nm. The large variation is due to different junction locations measured from bright and dark EBIC contrast regions and suggests less unwanted diffusion is present in bright EBIC contrast regions.
4. Dark contrast correlation: Plan-view SEM-EBIC was used to identify potential regions of interest for cross-sectional STEM-EBIC revealed bright/dark contrast regions. By selecting an area of interest that contained a well defined delineation between dark and bright contrast, it was possible to

correlate V-defect densities to each region. The V-defect density measured in the bright region was $0.8x10^9$ per cm^2 while the dark region had a measured V-defect density of $2.6x10^9$ per cm^2. The dark region had more than 3x the number of V-defects measured in the bright region. Combined with STEM-EBIC results this supports defect clustering as the source of dark contrast observed in plan-view EBIC.

5. STEM-CL: Implementation of a spectrometer with improved optical resolution, a modified sample holder and improved sample prep methods resulted in a 95% reduction in integration time while improving signal-to-noise. For the first time QW and GaN emission in addition to YB emission were measured with an in-lens STEM-CL system designed for the HD-2000. CL spectroscopy was also performed on different regions of the sample and the results correlated to device structure. Diffusion from V-defects reduces carrier concentration and results in longer minority carrier diffusion lengths which produce less CL emission.

7.2 Future work

The methods developed and capabilities demonstrated show considerable promise for the use of high-resolution STEM-EBIC/CL characterization of electrical and optical properties in GaN based devices and LEDs in general. Below is a list of future investigations that would yield valuable results.

1. EBIC model for (S)TEM samples: An EBIC model for evaluation minority carrier properties in thin samples with two free surfaces does not exist. Development of such a model will require STEM-EBIC to test and confirm theoretical results. The result will be the ability to measure minority carrier properties near defects.
2. Electron beam damage: The potential effect of electron beam damage on STEM-EBIC and STEM-CL was not investigated. A study to characterize the impact of extended electron beam probing on EBIC and CL results will help determine if limits need to be established.

3. PN-junction variation: The variation of the pn-junction observed for the green UltraThin LED needs to be understood. Higher indium concentration in the QWs increases lattice mismatch and strain. A study to determine if the EBIC signal can be used to correlate structure to stress would be novel.
4. V-defect sidewall characterization: Emission characteristics for the sidewall structure of V-defects need to be investigated.
5. Defect capture range: This study would leverage the sidewall characterization investigation. Here STEM-EBIC would be used to measure the capture range of different defects and correlate the results to sidewall structure.

8. References

1. LaPedus, M. Device makers rush into GaN market. http://www.eetimes.com/news/semi/showArticle.jhtml?articleID=190300189&pgno=2
2. Edmond, J.; Abare, A.; Bergman, M.; Bharathan, J.; Bunker, K. L.; Emerson, D.; Haberern, K.; Ibbetson, J.; Leung, M.; Russel, P.; Slater, D., High efficiency GaN-based LEDs and lasers on SiC. *Journal Of Crystal Growth* **2004,** 272, (1-4), 242-250.
3. Worldwise Fluorescent lights. http://www.worldwise.com/recflourlig.html
4. Registry, A. f. T. S. a. D., Toxicological Profile: Mercury. In Service, D. o. H. a. H., Ed. 1999; pp 509 - 524.
5. Kung, P.; Razeghi, M., III-Nitride wide bandgap semiconductors: a survey of the current status and future trends of the material and device technology. *Opto-Electronics Review* **2000,** 8, (3), 201-239.
6. Schubert, E. F., *Light-Emitting Diodes*. Cambridge university press: Cambridge, 2005.
7. Zuo, J. M.; Mabon, J. C. *WebEMAPS Software*, Univsersity of Illinoise Urbana-Champaign.
8. Morkoc, H., *Nitride Semiconductors and Devices*. 1st ed.; Springer: Berlin, 1999.
9. Johnson, W. C.; Parson, J. B.; Crew, M. C., *J. Phys. Chem* **1932,** 36.
10. Maruska, H. P.; Tietjen, J., J., *Applied Physics Letters* **1969,** 15, (327).
11. Amano, H.; Sawaki, N.; Akasaki, I.; Toyoda, Y., Metalorganic Vapor-Phase Epitaxial-Growth Of A High-Quality Gan Film Using An Ain Buffer Layer. *Applied Physics Letters* **1986,** 48, (5), 353-355.
12. Amano, H.; Kito, M.; Hiramatsu, K.; Akasaki, I., P-Type Conduction In Mg-Doped Gan Treated With Low-Energy Electron-Beam Irradiation (Leebi). *Japanese Journal Of Applied Physics Part 2-Letters* **1989,** 28, (12), L2112-L2114.

13. Nakamura, S.; Harada, Y.; Seno, M., Novel Metalorganic Chemical Vapor-Deposition System For Gan Growth. *Applied Physics Letters* **1991,** 58, (18), 2021-2023.
14. Steigerwald, D.; Rudaz, S.; Liu, H.; Kern, R. S.; Gotz, W.; Fletcher, R., III-V nitride semiconductors for high performance blue and green light-emitting devices. *Jom-Journal Of The Minerals Metals & Materials Society* **1997,** 49, (9), 18-23.
15. Liu, L.; Edgar, J. H., Substrates for gallium nitride epitaxy. *Materials Science & Engineering R-Reports* **2002,** 37, (3), 61-127.
16. Akasaki, I.; Amano, H.; Itoh, H.; Koide, N.; Manabe, K. In *GaN based UV/blue light-emitting devices*, GaAs and Related Compounds conference, 1992; 1992.
17. Nakamura, S.; Senoh, M.; Mukai, T., p-GaN/n-InGaN/n-GaN Double-Heterostructure Blue-Light-Emitting Diodes. *Japanese Journal Of Applied Physics Part 2-Letters* **1993,** 32, (1A-B), L8-L11.
18. Nakamura, S.; Fasol, G., *The Blue Laser Diode: GaN Based Light Emitters and Lasers*. Springer: Berlin, 1997.
19. Jain, S. C.; Willander, M.; Narayan, J.; Van Overstraeten, R., III-nitrides: Growth, characterization, and properties. *Journal Of Applied Physics* **2000,** 87, (3), 965-1006.
20. Liliental-Weber, Z.; Chen, Y.; Ruvimov, S.; Washburn, J., Formation mechanism of nanotubes in GaN. *Physical Review Letters* **1997,** 79, (15), 2835-2838.
21. Chen, Y.; Takeuchi, T.; Amano, H.; Akasaki, I.; Yamano, N.; Kaneko, Y.; Wang, S. Y., Pit formation in GaInN quantum wells. *Applied Physics Letters* **1998,** 72, (6), 710-712.
22. Wu, X. H.; Elsass, C. R.; Abare, A.; Mack, M.; Keller, S.; Petroff, P. M.; DenBaars, S. P.; Speck, J. S.; Rosner, S. J., Structural origin of V-defects and correlation with localized excitonic centers in InGaN/GaN multiple quantum wells. *Applied Physics Letters* **1998,** 72, (6), 692-694.

23. Cho, H. K.; Lee, J. Y.; Yang, G. M.; Kim, C. S., Formation mechanism of V defects in the InGaN/GaN multiple quantum wells grown on GaN layers with low threading dislocation density. *Applied Physics Letters* **2001,** 79, (2), 215-217.
24. Sanchez, A. M.; Gass, M.; Papworth, A. J.; Goodhew, P. J.; Singh, P.; Ruterana, P.; Cho, H. K.; Choi, R. J.; Lee, H. J., V-defects and dislocations in InGaN/GaN heterostructures. *Thin Solid Films* **2005,** 479, (1-2), 316-320.
25. Shiojiri, M.; Chuo, C. C.; Hsu, J. T.; Yang, J. R.; Saijo, H., Structure and formation mechanism of V defects in multiple InGaN/GaN quantum well layers. *Journal Of Applied Physics* **2006,** 99, (7).
26. Liu, F. D.; Collazo, R.; Mita, S.; Sitar, Z.; Duscher, G., Three-dimensional geometry of nanometer-scale AlN pits: A new template for quantum dots? *Advanced Materials* **2008,** 20, (1), 134-+.
27. LilientalWeber, Z.; Chen, Y.; Ruvimov, S.; Washburn, J., Formation mechanism of nanotubes in GaN. *Physical Review Letters* **1997,** 79, (15), 2835-2838.
28. Hangleiter, A.; Hitzel, F.; Netzel, C.; Fuhrmann, D.; Rossow, U.; Ade, G.; Hinze, P., Suppression of nonradiative recombination by V-shaped pits in GaInN/GaN quantum wells produces a large increase in the light emission efficiency. *Physical Review Letters* **2005,** 95, (12).
29. Netzel, C.; Bremers, H.; Hoffmann, L.; Fuhrmann, D.; Rossow, U.; Hangleiter, A., Emission and recombination characteristics of Ga1-xInxN/GaN quantum well structures with nonradiative recombination suppression by V-shaped pits. *Physical Review B* **2007,** 76.
30. Bright, A. N.; Sharma, N.; Humphreys, C. J., Analysis of contacts and V-defects in GaN device: structures by transmission electron microscopy. *Journal Of Electron Microscopy* **2001,** 50, (6), 489-495.
31. Lester, S. D.; Ponce, F. A.; Craford, M. G.; Steigerwald, D. A., High Dislocation Densities In High-Efficiency Gan-Based Light-Emitting-Diodes. *Applied Physics Letters* **1995,** 66, (10), 1249-1251.

32. Rudolph, P.; Jurisch, M., Bulk growth of GaAs An overview. *Journal Of Crystal Growth* **1999,** 199, 325-335.
33. Ho, I. H.; Stringfellow, G. B., Solid phase immiscibility in GaInN. *Applied Physics Letters* **1996,** 69, (18), 2701-2703.
34. Ponce, F. A.; Srinivasan, S.; Bell, A.; Geng, L.; Liu, R.; Stevens, M.; Cai, J.; Omiya, H.; Marui, H.; Tanaka, S., Microstructure and electronic properties of InGaN alloys. *Physica Status Solidi B-Basic Research* **2003,** 240, (2), 273-284.
35. Karpov, S. Y., Suppression of phase separation in InGaN due to elastic strain. *Mrs Internet Journal Of Nitride Semiconductor Research* **1998,** 3, (16).
36. Deibuk, V. G.; Voznyi, A. V., Thermodynamic stability and redistribution of charges in ternary AlGaN, InGaN, and InAlN alloys. *Semiconductors* **2005,** 39, (6), 623-628.
37. Yu, E. T.; Manasreh, M. O., *III-V nitride semiconductors: applications and devices*. Taylor & Francis: New York, 2003.
38. Pereira, S.; Correia, M. R.; Pereira, E.; Trager-Cowan, C.; Sweeney, F.; O'Donnell, K. P.; Alves, E.; Franco, N.; Sequeira, A. D., Structural and optical properties of InGaN/GaN layers close to the critical layer thickness. *Applied Physics Letters* **2002,** 81, (7), 1207-1209.
39. Chichibu, S. F.; Uedono, A.; Onuma, T.; Haskell, B. A.; Chakraborty, A.; Koyama, T.; Fini, P. T.; Keller, S.; Denbaars, S. P.; Speck, J. S.; Mishra, U. K.; Nakamura, S.; Yamaguchi, S.; Kamiyama, S.; Amano, H.; Akasaki, I.; Han, J.; Sota, T., Origin of defect-insensitive emission probability in In-containing (Al, In, Ga) N alloy semiconductors. *Nature Materials* **2006,** 5, (10), 810-816.
40. Chichibu, S.; Azuhata, T.; Sota, T.; Nakamura, S., Spontaneous emission of localized excitons in InGaN single and multiquantum well structures. *Applied Physics Letters* **1996,** 69, (27), 4188-4190.
41. Ponce, F. A.; Bour, D. P.; Gotz, W.; Wright, P. J., Spatial distribution of the luminescence in GaN thin films. *Applied Physics Letters* **1996,** 68, (1), 57-59.

42. Tomiya, S.; Hino, T.; Goto, S.; Takeya, M.; Ikeda, M., Dislocation related issues in the degradation of GaN-based laser diodes. *Ieee Journal Of Selected Topics In Quantum Electronics* **2004,** 10, (6), 1277-1286.
43. Martin, R. W.; Edwards, P. R.; O'Donnell, K. P.; Dawson, M. D.; Jeon, C. W.; Liu, C.; Rice, G. R.; Watson, I. M., Cathodoluminescence spectral mapping of III-nitride structures. *Physica Status Solidi A-Applied Research* **2004,** 201, (4), 665-672.
44. Yamamoto, N.; Itoh, H.; Grillo, V.; Chichibu, S. F.; Keller, S.; Speck, J. S.; DenBaars, S. P.; Mishra, U. K.; Nakamura, S.; Salviati, G., Cathodoluminescence characterization of dislocations in gallium nitride using a transmission electron microscope. *Journal Of Applied Physics* **2003,** 94, (7), 4315-4319.
45. Elsner, J.; Jones, R.; Sitch, P. K.; Porezag, V. D.; Elstner, M.; Frauenheim, T.; Heggie, M. I.; Oberg, S.; Briddon, P. R., Theory of threading edge and screw dislocations in GaN. *Physical Review Letters* **1997,** 79, (19), 3672-3675.
46. Orton, J. W.; Foxon, C. T., Group III nitride semiconductors for short wavelength light-emitting devices. *Reports On Progress In Physics* **1998,** 61, (1), 1-+.
47. Kisielowski, C.; Liliental-Weber, Z.; Nakamura, S., Atomic scale indium distribution in a GaN/In0.43Ga0.57N/Al0.1Ga0.9N quantum well structure. *Japanese Journal Of Applied Physics Part 1-Regular Papers Short Notes & Review Papers* **1997,** 36, (11), 6932-6936.
48. Narukawa, Y.; Kawakami, Y.; Funato, M.; Fujita, S.; Fujita, S.; Nakamura, S., Role of self-formed InGaN quantum dots for exciton localization in the purple laser diode emitting at 420 nm. *Applied Physics Letters* **1997,** 70, (8), 981-983.
49. Smeeton, T. M.; Kappers, M. J.; Barnard, J. S.; Vickers, M. E.; Humphreys, C. J., Electron-beam-induced strain within InGaN quantum wells: False indium cluster detection in the transmission electron microscope. *Applied Physics Letters* **2003**, (83).

50. Chichibu, S. F.; Abare, A. C.; Mack, M. P.; Minsky, M. S.; Deguchi, T.; Cohen, D.; Kozodoy, P.; Fleischer, S. B.; Keller, S.; Speck, J. S.; Bowers, J. E.; Hu, E.; Mishra, U. K.; Coldren, L. A.; DenBaars, S. P.; Wada, K.; Sota, T.; Nakamura, S., Optical properties of InGaN quantum wells. *Materials Science And Engineering B-Solid State Materials For Advanced Technology* **1999,** 59, (1-3), 298-306.
51. Wetzel, C.; Takeuchi, T.; Amano, H.; Akasaki, I., Piezoelectric Stark-like ladder in GaN/GaInN/GaN heterostructures. *Japanese Journal Of Applied Physics Part 2-Letters* **1999,** 38, (2B), L163-L165.
52. Morel, A.; Lefebvre, P.; Kalliakos, S.; Taliercio, T.; Bretagnon, T.; Gil, B., Donor-acceptor-like behavior of electron-hole pair recombinations in low-dimensional (Ga,In)N/GaN systems. *Physical Review B* **2003,** 68, (4).
53. Kent, P. R. C.; Zunger, A., Carrier localization and the origin of luminescence in cubic InGaN alloys. *Applied Physics Letters* **2001,** 79, (13), 1977-1979.
54. Wang, L. W., Calculations of carrier localization in $In_xGa_{1-x}N$. *Physical Review B* **2001,** 6324, (24).
55. Goldstein, J. I.; Newbury, D. E.; Joy, D. C.; Lyman, C. E.; Echlin, P.; Lifshin, E.; Sawyer, L.; Michael, J. R., *Scanning electron micrscopy and X-ray microanalysis*. Kluwer Academic/Plenum: New York, 2003.
56. Williams, D. B.; Carter, C. B., *Transmission Electron Microscopy*. Plenum Press: New York, 1996.
57. Joy, D. C., *Monte Carlo modeling for electron microscopy and microanalysis*. Oxford University Press: New York, 1995.
58. Drouin, D.; Coutre, A. R.; Gauvin, R.; Hovington, P.; Horny, P.; Demers, H. *CASINO software*, 2.42.
59. Petroff, P. M.; Logan, R. A.; Savage, A., Nonradiative Recombination At Dislocations In Iii-V Compound Semiconductors. *Physical Review Letters* **1980,** 44, (4), 287-291.
60. Leamy, H. J., Charge Collection Scanning Electron-Microscopy. *Journal Of Applied Physics* **1982,** 53, (6), R51-R80.

61. Reimer, L., *Scanning Electron Microscopy: Physics of Image Formation and Microanalysis*. Springer: Berlin, 1998.
62. Yacobi, B. G.; Holt, D. B., *Cathodoluminescence Microscopy of Inorganic Solids*. Plenum, New York: 1990.
63. Newbury, D. E.; Joy, D. C.; Echlin, P.; Fiori, C. E.; Goldstein, J. I., *Advanced Scanning Electron Microscopy and X-ray Analysis*. Plenum: New York, 1986.
64. Crewe, A. V., Possible High-Resolution Scanning Microscope. *Journal Of Applied Physics* **1964,** 35, (10), 3075-&.
65. Crewe, A. V.; Wall, J.; Welter, L. M., A High-Resolution Scanning Transmission Electron Microscope. *Journal Of Applied Physics* **1968,** 39, (13), 5861-&.
66. Strunk, H. P.; Ast, D. G. In *Combined HVTEM and EBIC studies in EFG silicon*, 38th Ann. Proc. Electron Microscopy Society of America, San Francisco, 1980; Bailey, G. W., Ed. Electron Microscopy Society: San Francisco, 1980; pp 322-323.
67. Sparrow, T. G.; Valdre, U., Application Of Scanning-Transmission Electron-Microscopy To Semiconductor-Devices. *Philosophical Magazine* **1977,** 36, (6), 1517-1528.
68. Fathy, D.; Sparrow, T. G.; Valdre, U., Observation Of Dislocations And Microplasma Sites In Semiconductors By Direct Correlations Of Stebic, Stem And Els. *Journal Of Microscopy-Oxford* **1980,** 118, (MAR), 263-273.
69. Perreault, G. C.; Ast, D. G., A Specimen Stage With No Microscope Modifications Used To Perform Ebic In A Stem. *Journal Of Physics E-Scientific Instruments* **1988,** 21, (12), 1175-1178.
70. Bunker, K. L.; Gonzalez, J. C.; Batchelor, D.; Stark, T. J.; Russell, P. E. In *Development of a High Laterial Resolution Electron Beam Induced Current Technique for Electrical Characterization of InGaN-Based Quantum Well Light Emitting Diodes*, Mat. Res. Soc. Symp. Proc., 2003; Materials Research Society: 2003; pp L10.10.1-L10.10.6.
71. Roberts, S. H. In *Cathodoluminescence spectrometer design for the TEM*, Inst. Phys. Conf. Ser., EMAG, Cambridge, 1981; Cambridge, 1981.

72. Yamamoto, N.; Spence, J. C. H.; Hazelton, D.; Higgs, A.; Bergh, M. In *A Cathodoluminescence Detection System for TEM/STEM*, Proceedings f the 41st Annual Meeting of the Electron Microscopy Society of America, 1983; 1983; pp 146-147.
73. Pennycook, S. J. In *A simple cathodoluminescence detector for the STEM*, Inst. Phys. Conf. Ser., EMAG, Cambridge, 1981; Cambridge, 1981.
74. Tanabe, T.; Muto, S.; Tohtake, S., Development of new TEM specimen holder for cathodoluminescence detection. *Journal Of Electron Microscopy* **2002,** 51, (5), 311-313.
75. Bunker, K. L. Development and Application of Electron Beam Induced Current and Cathodoluminescence Analytical Techniques for Characterization of Gallium Nitride-based Devices. North Carolina State Universtiy, Raleigh, NC, 2004.
76. Albrecht, M.; Grillo, V.; Borysiuk, J.; Remmele, T.; Strunk, H. P.; Walther, T.; Mader, W.; Prystawko, P.; Leszczynski, M.; Grzegory, I.; Porowski, S., Correlating compositional, structural and optical properties of InGaN quantum wells by transmission electron microscopy. In *Microscopy Of Semiconducting Materials 2001*, 2001; pp 267-272.
77. Boyall, N. M.; Durose, K.; Watson, I. M. In *Simultaneous TEM and Cathodoluminescence Imaging of Non-Uniformity in $In_{0.1}Ga_{0.9}N$ Quantum Wells*, Res. Soc. Symp. Proc., 2002; 2002; pp 677-682.
78. Zhang, G. Y.; Yang, Z. J.; Tong, Y. Z.; Qin, Z. X.; Hu, X. D.; Chen, Z. Z.; Ding, X. M.; Lu, M.; Li, Z. H.; Yu, T. J.; Zhang, L.; Gan, Z. Z.; Zhao, Y.; Yang, C. F., InGaN/GaN MQW high brightness LED grown by MOCVD. *Optical Materials* **2003,** 23, (1-2), 183-186.
79. Nakaji, D.; Grillo, V.; Yamamoto, N.; Mukai, T., Contrast analysis of dislocation images in TEM-cathodoluminescence technique. *Journal Of Electron Microscopy* **2005,** 54, (3), 223-230.

80. Yamamoto, N., Nanoscale Spectroscopy and its Applications to Semiconductor Research. In *Lecture Notes in Physics*, Watanabe, Y.; Heun, S.; Salviati, G.; Yamamoto, N., Eds. Vol. 588.
81. Boyall, N. M.; Durose, K.; Watson, I. M. In *An in-situ TEM-cathodoluminescence study of electron beam degredation of luminescence from GaN and $In_{0.1}Ga_{0.9}N$ quantum wells*, Materials Research Society Symposium Proceedings, Boston, MA, 2003a; Wetzel, C.; Yu, E. T.; Speck, J. S.; Rizzi, A.; Arakawa, Y., Eds. Boston, MA, 2003a.
82. Giannuzzi, L. A.; Stevie, F. A., *Introduction to focused ion beams: instrumentation, theory, techniques and practice*. Springer: New York, 2005.
83. Duscher, G. Introduction to Transmission Electron Microscopy. http://courses.ncsu.edu/mse/715/lec/001
84. Sze, S. M., *Physics of Semiconductor Devices*. John Wiley & Sons: New York, 1981.
85. Kasap, S. O., *Principles of Electronic Materials and Devices*. McGraw Hill: New York, 2000.
86. Schroder, D. K., *Semiconductor Material and Device Characterization*. Wiley: New York, 1998.
87. Hirsch, L.; Barriere, A. S., Electrical characterization of InGaN/GaN light emitting diodes grown by molecular beam epitaxy. *Journal Of Applied Physics* **2003,** 94, (8), 5014-5020.
88. Fedison, J. B.; Chow, T. P.; Lu, H.; Bhat, I. B., Electrical characteristics of magnesium-doped gallium nitride junction diodes. *Applied Physics Letters* **1998,** 72, (22), 2841-2843.
89. Yang, C. C.; Wu, M. C.; Chuo, C. C.; Chyi, J. I.; Lin, C. F.; Chi, G. C., Electrical and optical characteristics of the GaN light-emitting diodes with multiple-pair buffer layer. *Solid-State Electronics* **2000,** 44, (8), 1483-1486.
90. Dalmasso, S.; Damilano, B.; Grandjean, N.; Massies, J.; Leroux, M.; Reverchon, J. L.; Duboz, J. Y., Optoelectronic characterization of blue

InGaN/GaN LEDS grown by MBE. *Materials Science And Engineering B-Solid State Materials For Advanced Technology* **2001,** 82, (1-3), 256-258.

91. Dmitriev, V. A., GaN based p-n structures grown on SiC substrates. *Mrs Internet Journal Of Nitride Semiconductor Research* **1996,** 1, (1-46), art. no.-29.
92. Casey, H. C.; Muth, J.; Krishnankutty, S.; Zavada, J. M., Dominance of tunneling current and band filling in InGaN/AlGaN double heterostructure blue light-emitting diodes. *Applied Physics Letters* **1996,** 68, (20), 2867-2869.
93. Perlin, P.; Osinski, M.; Eliseev, P. G.; Smagley, V. A.; Mu, J.; Banas, M.; Sartori, P., Low-temperature study of current and electroluminescence in InGaN/AlGaN/GaN double-heterostructure blue light-emitting diodes. *Applied Physics Letters* **1996,** 69, (12), 1680-1682.
94. Shah, J. M.; Li, Y. L.; Gessmann, T.; Schubert, E. F., Experimental analysis and theoretical model for anomalously high ideality factors (n >> 2.0) in AlGaN/GaN p-n junction diodes. *Journal Of Applied Physics* **2003,** 94, (4), 2627-2630.
95. NI *LabView*, National Instruments.
96. Aesar, A. http://www.alfa.com/CGI-BIN/LANSAWEB?PROCFUN+WEBOEP+SRCHCHK+alf+ENG
97. Porter, L. M.; Davis, R. F., A Critical-Review Of Ohmic And Rectifying Contacts For Silicon-Carbide. *Materials Science And Engineering B-Solid State Materials For Advanced Technology* **1995,** 34, (2-3), 83-105.
98. Harris, G. L., *Properties of Silicon Carbide*. Institution of Engineering and Technology: 1995.
99. Bunker, K. L.; Russell, P. E., *Electronic Device Failure Analysis* **2002,** 4, (4).
100. Pernot, C.; Hirano, A.; Amano, N.; Akasaki, I., Investigation of the leakage current in GaN p-n junctions. *Japanese Journal Of Applied Physics Part 2-Letters* **1998,** 37, (10B), L1202-L1204.
101. Dang, G.; Zhang, A. P.; Cao, X. A.; Ren, F.; Cho, H.; Pearton, S. J.; Shul, R. J.; Zhang, L.; Hickman, R.; Van Hove, J. M., Electrical effects of Ar plasma

damage on GaN diode rectifiers. *Electrochemical And Solid State Letters* **1999,** 2, (9), 472-474.

102. Hahn, Y. B.; Hays, D. C.; Cho, H.; Jung, K. B.; Lambers, E. S.; Abernathy, C. R.; Pearton, S. J.; Hobson, W. S.; Shul, R. J., Inductively coupled plasma etching in ICl- and IBr-based chemistries. Part I: GaAs, GaSb, and AlGaAs. *Plasma Chemistry And Plasma Processing* **2000,** 20, (3), 405-415.
103. Frenkel, J., On pre-breakdown phenomena in insulators and electronic semi-conductors. *Physical Review* **1938,** 54, (8), 647-648.
104. Mitrofanov, O.; Manfra, M., Poole-Frenkel electron emission from the traps in AlGaN/GaN transistors. *Journal Of Applied Physics* **2004,** 95, (11), 6414-6419.
105. Ziegler, J. F.; Ziegler, M. D.; Biersack, J. P. *SRIM*, 2006.
106. Kato, N. I., Reducing focused ion beam damage to transmission electron microscopy samples. *Journal Of Electron Microscopy* **2004,** 53, (5), 451-458.
107. Ko, D. S.; Park, Y. M.; Kim, S. D.; Kim, Y. W., Effective removal of Ga residue from focused ion beam using a plasma cleaner. *Ultramicroscopy* **2007,** 107, (4-5), 368-373.
108. Hata, S.; Sosiati, H.; Kuwano, N.; Itakura, M.; Nakano, T.; Umakoshi, Y., Removing focused ion-beam damages on transmission electron microscopy specimens by using a plasma cleaner. *Journal Of Electron Microscopy* **2006,** 55, (1), 23-26.
109. Cao, X. A.; Zhang, A. P.; Dang, G. T.; Cho, H.; Ren, F.; Pearton, S. J.; Shul, R. J.; Zhang, L.; Hickman, R.; Van Hove, J. M., Inductively coupled plasma damage in GaN Schottky diodes. *Journal Of Vacuum Science & Technology B* **1999,** 17, (4), 1540-1544.
110. Mayer, J.; Giannuzzi, L. A.; Kamino, T.; Michael, J., TEM sample preparation and FIB-induced damage. *Mrs Bulletin* **2007,** 32, (5), 400-407.
111. Bunker, K. L.; Russell, P. E., *Current issues on multidisciplinary microscopy and education*. Formatex: 2004.
112. Grim, J. R.; Benamara, M.; Skowronski, M.; Everson, W. J.; Heydemann, V. D., Transmission electron microscopy analysis of mechanical polishing-related

damage in silicon carbide wafers. *Semiconductor Science And Technology* **2006,** 21, (12), 1709-1713.

113. Parish, C. M.; Russell, P. E., On the use of Monte Carlo modeling in the mathematical analysis of scanning electron microscopy-electron beam induced current data. *Applied Physics Letters* **2006,** 89, (19).
114. Parish, C. M. Electron and ion-beam characterization of nitride semiconductor devices. North Carolina State University, Raleigh, N C, 2006.
115. Kuroda, N.; Sasaoka, C.; Kimura, A.; Usui, A.; Mochizuki, Y., Precise control of pn-junction profiles for GaN-based LD structures using GaN substrates with low dislocation densities. *Journal Of Crystal Growth* **1998,** 190, 551-555.
116. Moldovan, G.; Kazemian, P.; Edwards, P. R.; Ong, V. K. S.; Kurniawan, O.; Humphreys, C. J., Low-voltage cross-sectional EBIC for characterisation of GaN-based light emitting devices. *Ultramicroscopy* **2007,** 107, (4-5), 382-389.
117. Cree. Inc. http://www.cree.com
118. Reshchikov, M. A.; Morkoc, H., Luminescence from defects in GaN. *Physica B-Condensed Matter* **2006,** 376, 428-431.
119. Hitachi High Technologies Americas, I. http://www.hitachi-hta.com
120. Thermo Fisher Scientific, I. http://www.thermo.com/com/cda/landingpage/1,10255,111,00.html
121. Vanroosbroeck, W., Injected Current Carrier Transport In A Semi-Infinite Semiconductor And The Determination Of Lifetimes And Surface Recombination Velocities. *Journal Of Applied Physics* **1955,** 26, (4), 380-391.
122. Donolato, C., On The Analysis Of Diffusion Length Measurements By Sem. *Solid-State Electronics* **1982,** 25, (11), 1077-1081.
123. Bonard, J. M.; Ganiere, J. D., Quantitative analysis of electron-beam-induced current profiles across p-n junctions in GaAs/Al0.4Ga0.6As heterostructures. *Journal Of Applied Physics* **1996,** 79, (9), 6987-6994.
124. Chow, T. P.; Ghezzo In *III-Nitride, SiC, and Diamond Materials for Electronic Devices*, Material Research Society Symposium Proceedings, Pttsburgh, P.A.,

1996; Gaskill, D. K.; Brandt, C. D.; Nemanich, R. J., Eds. Pttsburgh, P.A., 1996; pp 69-73.

Appendices

A.1 FIB sputter rate calculations

To get a feel for FIB milling times the following example is presented. The goal is to a volume of material bounded by the dashed box shown below in Figure A.1. The region to be removed contains a ~2 μm GaN layer on top of a SiC substrate. Including the GaN layer a total of 6 μm of material will be removed.

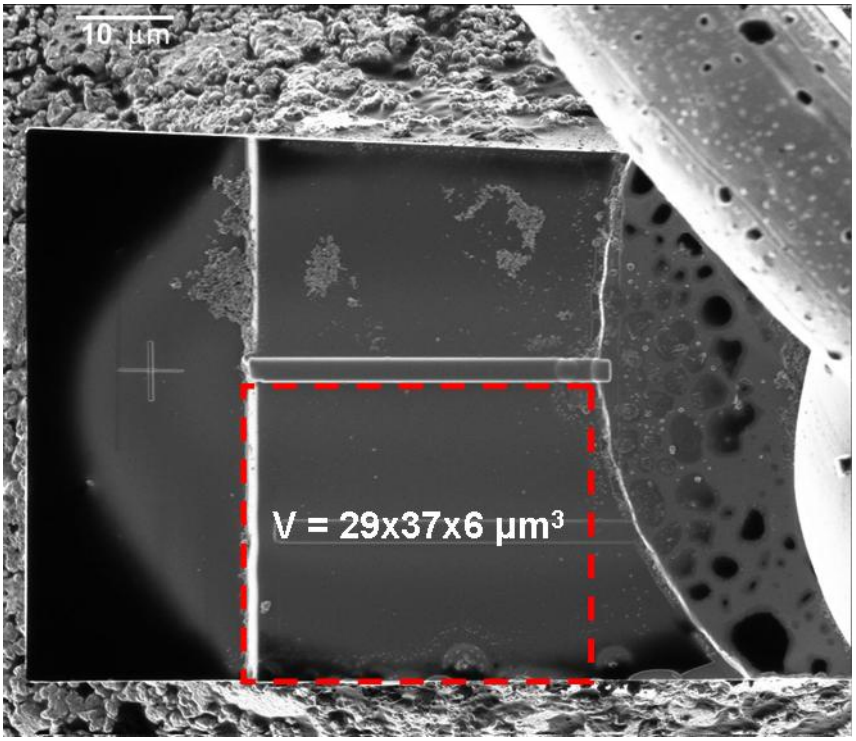


Figure A1: Region on sample to be removed by FIB milling.

SiC is harder than GaN and mills slower. Thus for this example we will simplify calculations by assuming the entire amount of material to be removed is SiC. The full set of assumptions is presented below.

Assumptions:

- SiC sample
- Volume to be removed = 6,438 μm^3
- Ga ions, 30 keV accelerating voltage → Y_{SiC} = 1.94 sputtered SiC atoms per incident Ga^+ (Y_{SiC} from SRIM simulation results[105])
- Beam current = 30 nA

In order to determine the required mill time we first must determine the sputter rate of SiC per in terms of nC. This calculation is basically a conversion from the SRIM obtained sputtered SiC atoms per incident gallium ion into a volume per charge term.

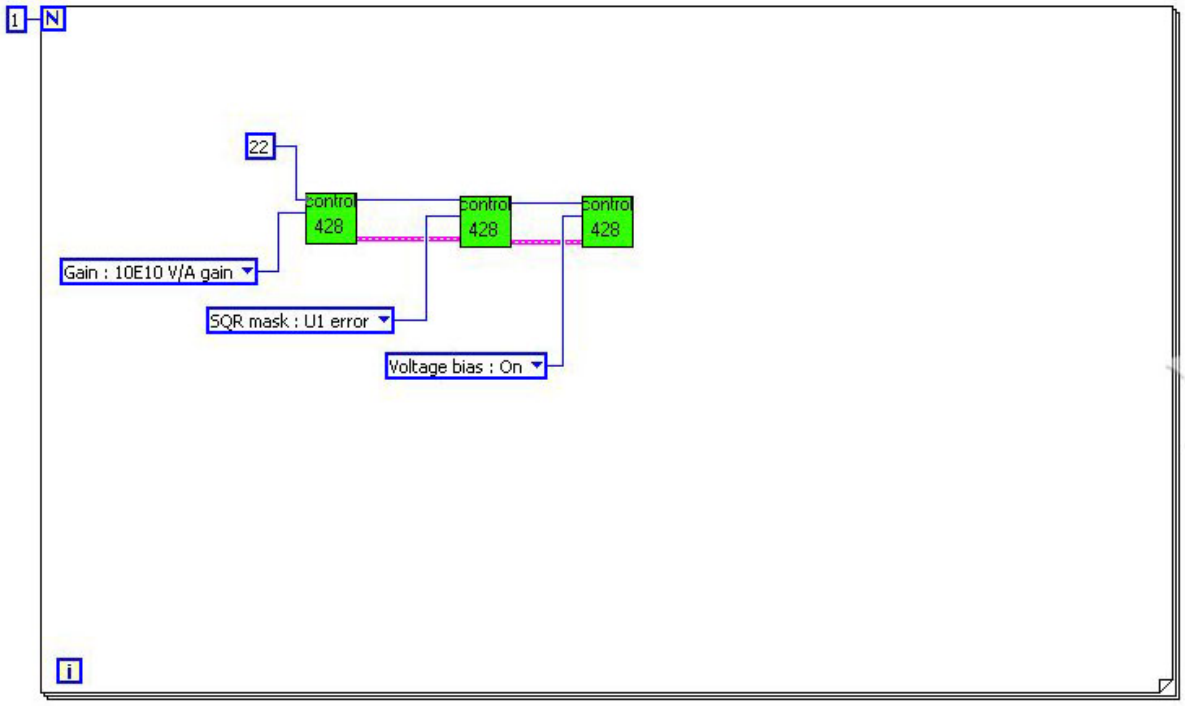
$$Y = \frac{1.94 \text{ sput'd SiC}}{\text{ion}} \left| \frac{\text{ion}}{1.602\text{x}10^{-19}\text{ C}} \right| \frac{1\text{ C}}{10^{9}\text{ nC}} \left| \frac{1\ \mu\text{m}^3}{4.8\text{x}10^{10}\text{ SiC}} \right. = 0.25\text{um}^3/\text{nC}$$

Next, we take the sputter rate, Y, and divided it into the volume of material to be removed. This yields the total required charge, which is then divided by the beam current to yield the required mill time.

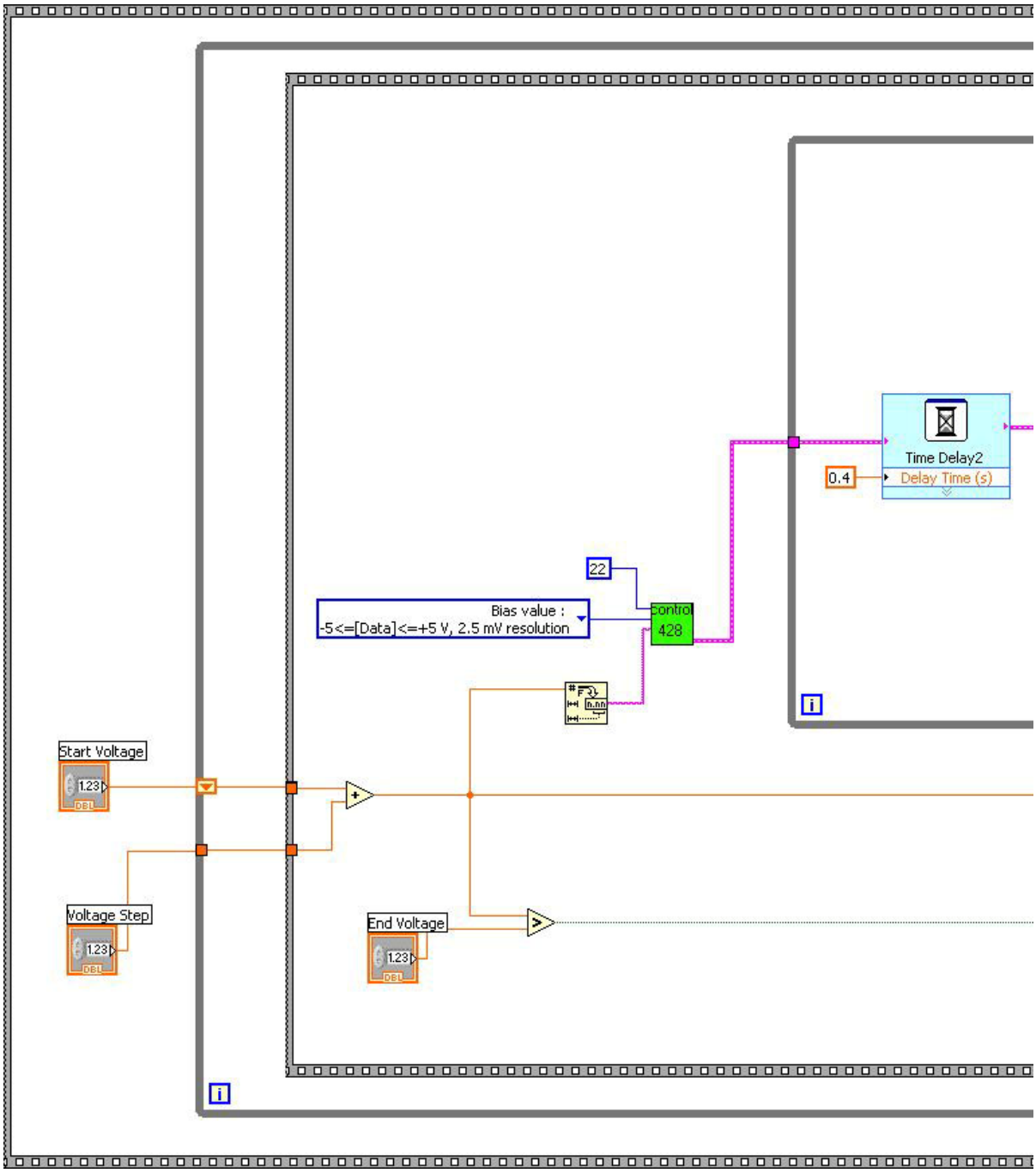
$$t = \frac{6{,}438\text{ um}^3}{} \left| \frac{\text{nC}}{0.25\text{ um}^3} \right| \frac{}{30\text{ nA}} \left| \frac{1\text{ nA•s}}{1\text{ nC}} \right| \frac{1\text{ min}}{60\text{ s}} \approx 14\text{ min/side}$$

A.2 LabView current-voltage data collection program

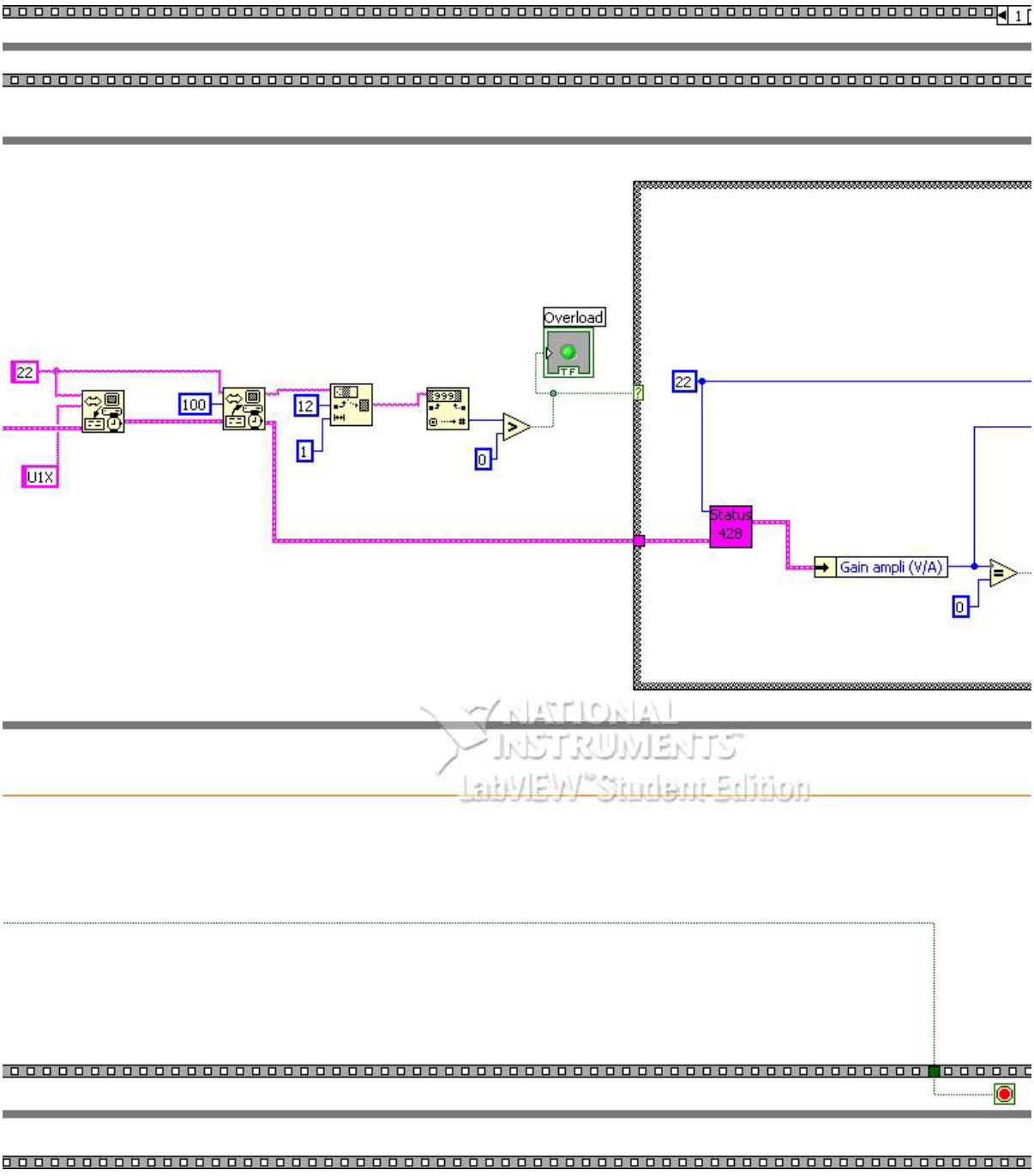
Page 1: Initiates settings of Keithley 428 current amplifier



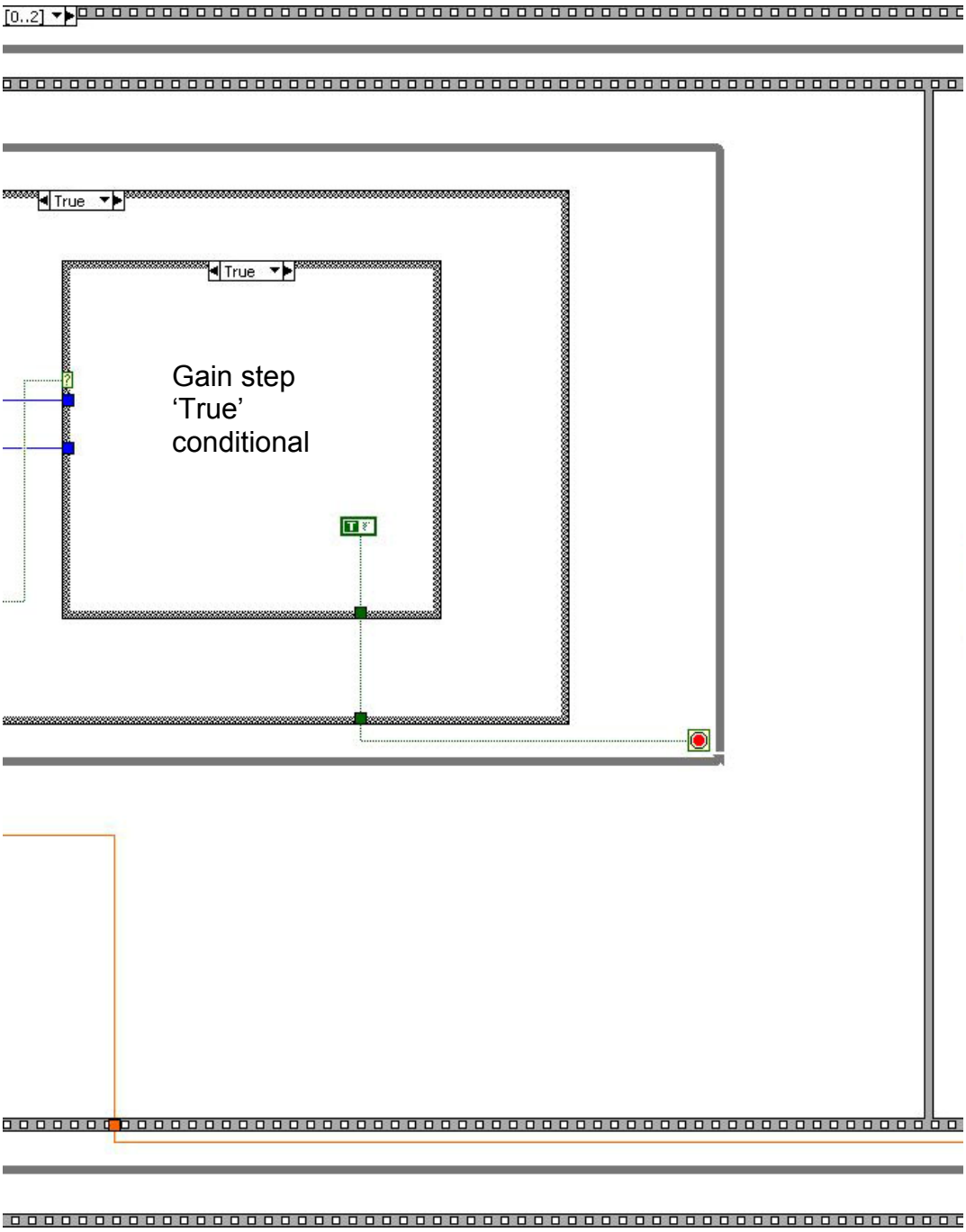
Page 2: Voltage stepping and current logging



Continued on next page

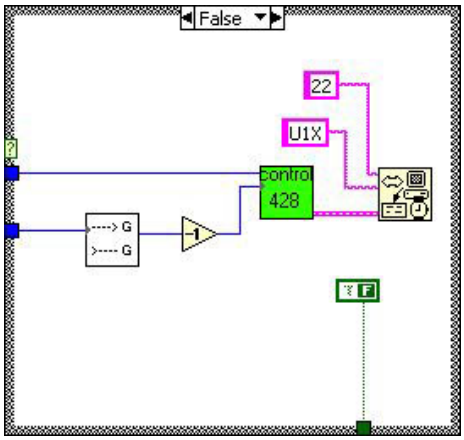


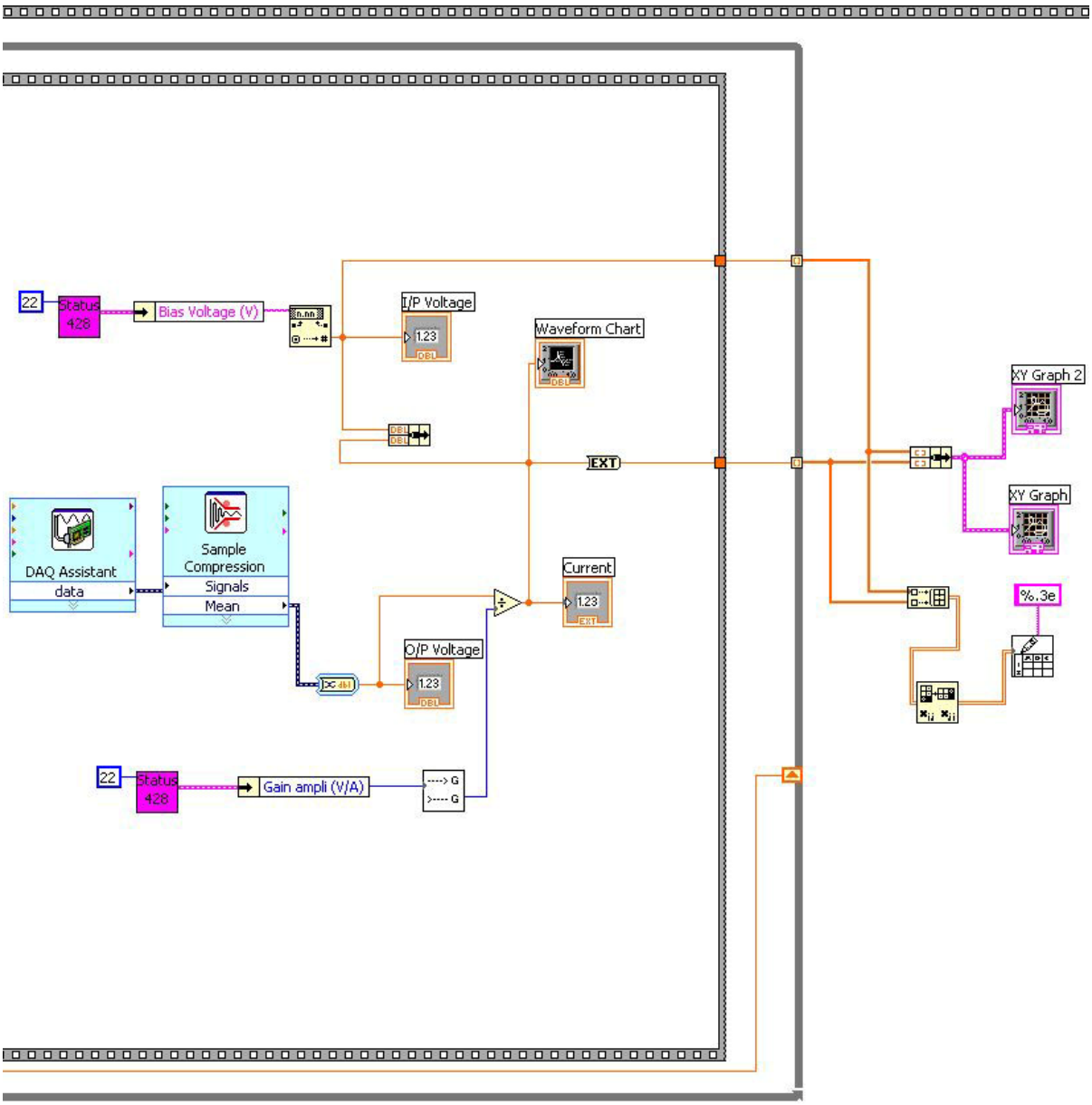
Continued on next page



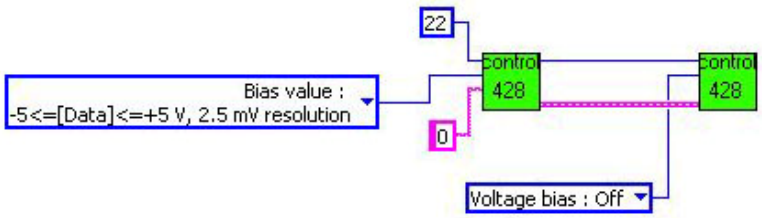
Continued on page after next

Gain step ‘False’ conditional

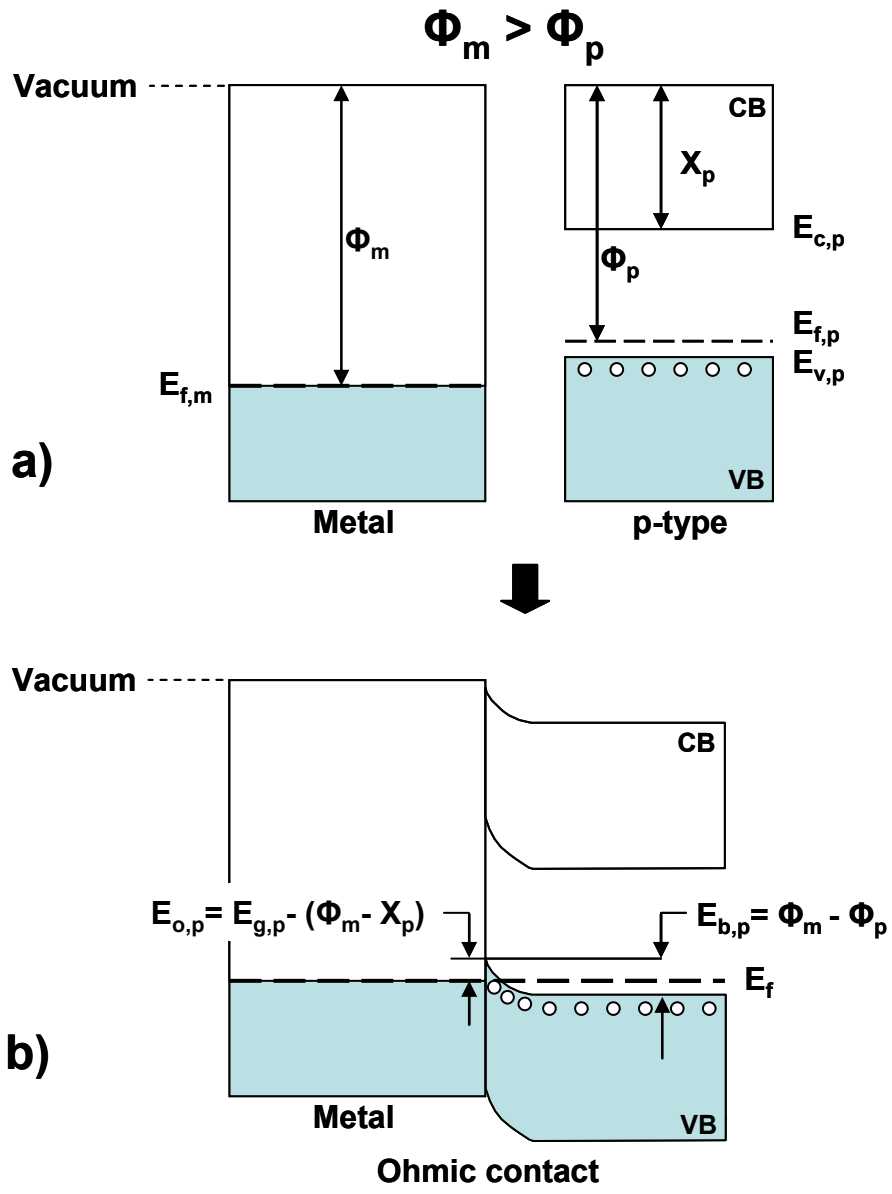


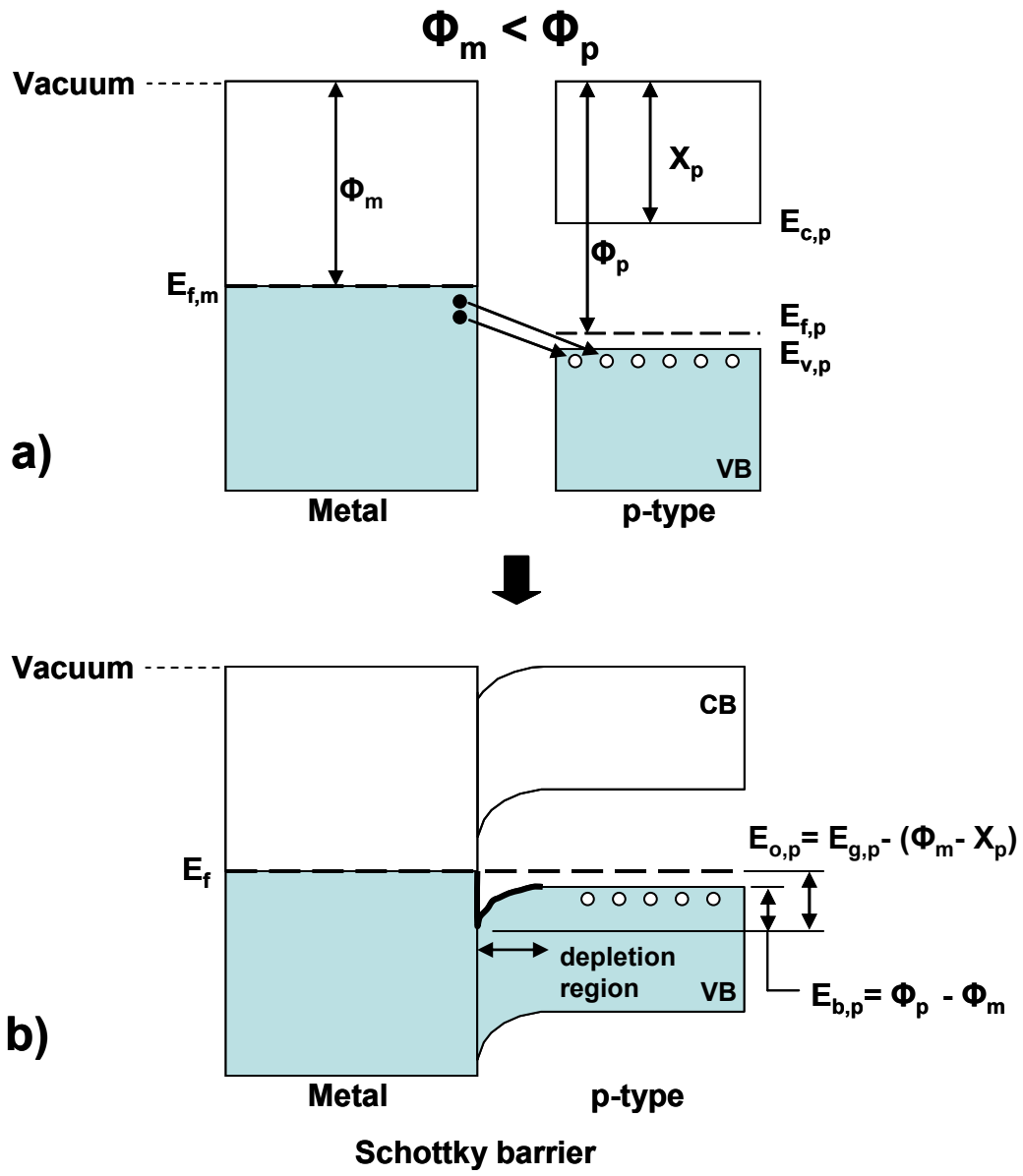

22
Status
428
Bias Voltage (V)
I/P Voltage
1.23
DBL
Waveform Chart
DBL
DBL
DBL
EXT
XY Graph 2
XY Graph
DAQ Assistant
data
Sample
Compression
Signals
Mean
Current
1.23
EXT
%.3e
O/P Voltage
1.23
DBL
22
Status
428
Gain ampli (V/A)
----> G
>---- G

Page 3: Reset Keithley 428 current amplifier - end



A.3 Metal to p-semiconductor contact




$\Phi_m < \Phi_p$
Vacuum
Φ_m
X_p
$E_{c,p}$
Φ_p
$E_{f,m}$
$E_{f,p}$
$E_{v,p}$
a)
VB
Metal
p-type
Vacuum
CB
$E_{o,p} = E_{g,p} - (\Phi_m - X_p)$
E_f
depletion region
VB
$E_{b,p} = \Phi_p - \Phi_m$
b)
Metal
p-type
Schottky barrier

A.4 Injection estimates

Low-injection conditions are an assumption for quantitative EBIC analysis for the following reasons.

- Minimum perturbation of majority carrier density allows diffusion of majority carriers to be neglected.
- Minority carriers diffuse under concentration gradient.
- The small number of excess majority carriers will drift to follow diffusive motion of minority carrier in order to maintain charge neutrality and this simplifies mathematics to determining the diffusion coefficient, D.
- If under high-injection conditions, need to use weighted value for diffusion, $D_{effective}$. In addition, excess minority carriers may saturate traps and recombination sites changing optoelectronic behavior.

To estimate injection conditions for a (S)TEM sample, start with the relativistic version of the Bethe equation to determine rate of energy loss per length. This is then multiplied by the sample thickness to estimate energy loss per incident electron.

$$\Delta E = \left(\frac{dE}{dS}\right)t = \left(831.6\frac{eV}{\mu m}\right)\left(0.25\mu m\right) = 208\,eV$$

The rate of electron-hole pair (EHP) generation is then determined by dividing the energy loss with an estimate for the EHP formation energy, E_{eh}. In this example E_{eh} = 3xBandgap for GaN. However, this is likely a conservative estimate as inelastic processes at 200 keV versus 20 keV are different. Furthermore, the equation for estimating EHP rate of generation was developed for semi-infinite sample, not a (S)TEM sample. As such it is expected that the resulting value for EHP per second will be an upper-limit bounding value.

$$\frac{EHP}{s} = \frac{\Delta E}{qE_{eh}} i_b = \frac{(208\,eV)(0.35\times10^{-9}\,A)}{(1.6\times10^{-19}\,C)(10.2\,eV)} = 4.4\times10^{10}\,\frac{EHP}{s}$$

Lastly, the EHPs per cm^3 can be calculated by making an assumption of the beam interaction volume and minority carrier lifetime, τ. In this case, the interaction volume was approximated as a cone spanning the sample cross-section, expanding from the beam spot size, ~0.5 nm to ~40 nm. Using this approach an injected carrier estimate of $3x10^{17}$ EHP/cm3 was calculated.

$$\frac{EHPs}{cm^3} = \frac{\left(\frac{EHPs}{s}\right)}{cm^3}\tau = \frac{\left(4.4\times10^{10}\,\frac{EHP}{s}\right)(1\times10^{-9}\,s)}{1.5\times10^{-16}\,cm^3} = 3.0\times10^{17}\,\frac{EHP}{cm^3}$$